UNIVERSITY OF CALIFORNIA, MERCED

A hybrid (CSP/CPV) spectrum splitting solar collector for power generation

A dissertation submitted in partial satisfaction of the requirements
for the degree of Doctor of Philosophy

in

Environmental Systems (E.S.)

by

Bennett K. Widyolar

Committee:

Professor Gerardo Diaz, Chair
Professor Elliot Campbell
Professor Yanbao Ma
Professor Roland Winston

Spring 2018

A hybrid (CSP/CPV) spectrum splitting solar collector for power generation

The dissertation of Bennett K. Widyolar, titled “A hybrid (CSP/CPV) spectrum splitting solar collector for power generation,” is approved:

Chair ________________________________ Date __________
Gerardo Diaz

________________________________ Date __________
Yanbao Ma

________________________________ Date __________
Elliot Campbell

________________________________ Date __________
Roland Winston

University of California, MERCED

Contents

Abstract

A hybrid (CSP/CPV) spectrum splitting solar collector for power generation

by

Bennett K. Widyolar

Doctor of Philosophy in Environmental Systems (E.S.)

University of California, MERCED

Professor Gerardo Diaz, Chair

This work investigates a novel form of spectrum splitting as a potential pathway for reducing the levelized cost of electricity generated by a hybrid concentrating solar power (CSP/CPV) plant for the purpose of increasing *dispatchable* solar-to-electric capacity on the grid. While the deployment of solar-to-electric capacity is occurring today at rates never before seen, most installations are *variable* generators and produce electricity while the sun is shining but have no effective means of storing this energy for nighttime or time-shifted generation. CSP systems are easily paired with cost-effective thermal energy storage (TES), but the plants themselves (solar field and power block) are still too expensive to incentivize rapid deployment. *Spectrum splitting* has been identified as a technique which would allow pairing of cheap, high efficiency PV with expensive, low efficiency CSP in a hybrid system to increase overall net electric generation efficiency and thus potentially reduce the levelized cost of electricity generated by hybrid plants below that of standalone CSP.

This dissertation is focused on the development of a novel two-stage collector which incorporates *spectrum splitting* using back-reflecting solar cells integrated into the secondary concentrator. Several different solar cell candidates are investigated as candidates and modelled against existing systems (PV, CSP, and hybrid). The economics of hybrid systems are compared to a side-by-side standalone PV and CSP plant. An early stage prototype was developed and tested on-sun up to 360 °C, after which several major challenges, obstacles, and complications were identified. The optical performance of a CPC profile approximated by segments was explored and developed, ultimately culminating in an optimized design for a secondary with integrated solar cells. Several other manufacturing and assembly techniques were developed and utilized in a second generation prototype which was assembled and tested on-sun up to 600 °C using a suspended particulate heat transfer fluid (HTF). The second generation collector had much better results and has highlighted areas for further development and research.

The concepts, designs, and experimental works in this thesis contribute to the continuous development of solar collectors and systems towards lower cost, higher efficiency, and broader applications.

Curriculum Vita

University of California, Merced

Doctoral Candidate (Ph.D) in Environmental Systems (Spring 2018)
M.S. in Mechanical Engineering and Applied Mechanics (May 17, 2013)
B.S. in Environmental Engineering (Aug 6, 2010)

During my time at the University of California, Merced, which has spanned 10 years, I have studied under Dr. Roland Winston learning the principles of optics and solar collectors. For my Master's degree I worked on an experimental solar cooling demonstration project which paired a 20 kW array of non-tracking XCPC collectors with a double-effect absorption chiller to provide space cooling. Since then I have worked on improved collector designs (for > 200 °C) and have been to Mongolia twice to install solar collectors as part of a technology transfer program and for fully off-grid space heating applications. Most of my efforts as a doctoral candidate have been toward the development of the two-stage spectrum splitting collector described in this dissertation, which is part of a 4-year project with the Department of Energy's Advanced Research Projects Agency (ARPA-E).

Journal Publications

Widyolar, B., Jiang, L., Abdelhamid, M. and Winston, R., 2018. Design and modeling of a spectrum-splitting hybrid CSP-CPV parabolic trough using two-stage high concentration optics and dual junction InGaP/GaAs solar cells. *Solar Energy*, 165, pp.75-84.

Widyolar, B., Jiang, L., Ferry, J. and Winston, R., 2018. Non-tracking East-West XCPC solar thermal collector for 200 celsius applications. *Applied Energy*, 216, pp.521-533.

Widyolar, B., Jiang, L. and Winston, R., 2018. Spectral beam splitting in hybrid PV/T parabolic trough systems for power generation. Applied Energy, 209, pp.236-250. Widyolar, B., Jiang, L. and Winston, R., 2017. Thermodynamics and the segmented compound parabolic concentrator. *Journal of Photonics for Energy*, 7(2), pp.028002-028002.

Widyolar, B., Abdelhamid, M., Jiang, L., Winston, R., Yablonovitch, E., Scranton, G., Cygan, D., Abbasi, H. and Kozlov, A., 2017. Design, simulation and experimental characterization of a novel parabolic trough hybrid solar photovoltaic/thermal (PV/T) collector. *Renewable Energy*, 101, pp.1379-1389.

Widyolar, B., Winston, R., Jiang, L. and Poiry, H., 2014. Performance of the Merced Demonstration XCPC Collector and Double Effect Chiller. *Journal of Solar Energy Engineering*, 136(4), p.041009.

Widyolar, Bennett K. *Performance Analysis of XCPC Powered Solar Cooling Demonstration Project*. Diss. University of California, Merced, 2013. (Masters Thesis).

Conference Papers

Widyolar, B., Jiang, L. and Winston, R., 2017, September. Thermodynamic investigation of the segmented CPC. In Nonimaging Optics: Efficient Design for Illumination and Solar Concentration XIV (Vol. 10379, p. 103790L). International Society for Optics and Photonics.

Widyolar, B., Jiang, L., Hassanzadeh, A., and Winston, R., 2017, November. Compound Parabolic Concentrator for Pentagon Shape Absorber. In SWC 2017 / SHC 2017

Acknowledgements

The information, data, or work presented herein was funded in part by the Advanced Research Projects Agency-Energy (ARPA-E), U.S. Department of Energy, under Award Number DE-AR0000464. The work was performed under a subcontract with the Gas Technology Institute (GTI) (Dave Cygan, Hamid Abbasi, and Joe Pondo) who developed the particle rig for high temperature testing and both Alta Devices (Eli Yablonovitch and Gregg Scranton) and MicroLink Devices Inc. (Alex Kirk and Mark Osowski) who developed and supplied the solar cells used in the prototypes.

I would also like to thank:

- The UC Merced machine shop and fabrication staff (Justin McConnel, Bryan Spielman, Brian Zimmerman, Ed Silva) for their patience in machining and then assembling/re-assembling the collector prototypes about a thousand times.
- The UC Solar support staff (Ron Durbin and Robyn Lukens) and UC Merced staff who operate behind the scenes were integral to the success of this work with regards to purchasing, ordering, and general project management.
- Brent Jerner and the guys at APG Solar, who assisted us on the ground to install, connect, and operate our equipment.
- All of the graduate and undergraduate students (Mahmoud Abdelhamid, Melissa Ricketts, Ali Hassanzadeh, Jordyn Brinkley, Yogesh Bushal, Kaycee Chang, Danny Wu) who contributed to the project at different times and in different capacities.
- Lun Jiang and Jonathan Ferry for my being partners in crime who spent many, many hours on this project over the years and shared in the victories and defeats along the way.
- And of course, Roland Winston for his guidance and mentorship.

List of Symbols

σ_{sun}	Solar half-disk angle	T_H	Hot reservoir temperature
r_{sun}	Radius of the sun	r	Rim radius
r_{earth}	Radius of the earth	ϕ	Half-rim angle
$d_{earth-sun}$	Distance between the earth and sun	$Q_{incoming}$	Incoming solar power
δ	Solar declination angle	$A_{aperture}$	Aperture area
n_{day}	Day of the year	$f_{shading}$	Unshaded fraction
t	Time	f_{window}	Fraction of solar irradiance within spectral window
ω	Hour angle	$\eta_{cell,window}$	In-band cell efficiency
$\widehat{n_s}$	Solar vector	W_{cells}	Work output by solar cells
B_λ	spectral radiance	$Q_{cell,losses}$	Thermal output from solar cells
h	Planck's constant	$\eta_{system,cells}$	CPV subsystem efficiency
c	speed of light	η_{exergy}	Solar to exergy efficiency
λ	wavelength	$\eta_{electric}$	Solar to electric efficiency
k_B	Boltzmann constant	η_{HX}	Heat exchanger efficiency
T	temperature	$\eta_{PB,net}$	Power block efficiency
C, C_x	Concentration ratio	$f_{thermal}$	Thermal fraction
A	Area	$Solar\ Field\ Cost$	Solar field installation cost
A_1	Aperture area	η_{CPV}	CPV solar-to-electric efficiency
A_2	Secondary aperture	$\$_{CPV}$	Cost of CPV in $/Watt
C_{max}	Maximum concentration	$\$_{Si}$	Cost of c-Si in $/Watt
θ	Acceptance angle	f	Focal length
G_{global}	Global irradiance	CAP	Concentration acceptance product
G_{direct}, DNI	Direct normal irradiance	$G_{absorbed}$	Fraction of radiation absorber by thermal absorber
$G_{diffuse}$	Diffuse irradiance	$G_{cell\_incident}$	Fraction of radiation incident the solar cells
ρ	Reflectance	$G_{cell\_absorbed}$	Fraction of radiation absorbed by the solar cells
τ	Transmittance	$T_{f,i}$	Inner fluid temperature
α	Absorptance	$T_{i,i}$	Inner surface temperature of inner pipe
γ	Intercept factor	$T_{i,o}$	Outer surface temperature of inner pipe
ϵ	Emittance	$T_{f,o}$	Outer fluid temperature
σ	Stefan Boltzmann constant	$T_{o,i}$	Inner surface temperature of outer pipe
h	Heat transfer coefficient	$T_{o,o}$	Outer surface temperature of outer pipe (absorber surface)

T_∞	Ambient temperature	$T_{g,i}$	Inner glass surface temperature
$\eta_{thermal}$	Thermal efficiency	$T_{g,o}$	Outer glass surface temperature
η_0	Optical efficiency	$Q_{rad,in}$	Radiation incident on each absorber node
Q_{solar}	Solar power	n	Number of nodes
$Q_{loss,rad}$	Radiative loss	$\dot{m}$	Mass flow rate
$Q_{loss,convection}$	Convective loss	c_p	Heat capacity
$Q_{thermal}$	Thermal power	k	Thermal conductivity
J_{sc}	Short circuit current	η_{energy}	Solar to energy efficiency
q	Elementary charge	T^*	Ambient and solar adjusted temperature
EQE	External quantum efficiency	T_{outlet}	Outlet temperature
η_{cell}	Cell efficiency	P	Radiative Probability Factor
V_{oc}	Open circuit voltage	F	View factor
FF	Fill factor	η	Efficiency
$\eta_{electric,PV}$	Solar to electric module efficiency	FE	Flux Efficiency
β	Temperature coefficient	$C_{x,strip}$	Concentration on a strip of cells
T_{cell}	Cell temperature	$\eta_{0,strip}$	Fraction of light incident on cell strip
T_{ref}	Reference temperature	A_{strip}	Strip area
η_{Cx}	Efficiency boost due to concentration	$\eta_{cell,strip}$	Solar to electric efficiency of cell strip
$\eta_{cell-to-module}$	Cell to module efficiency	n_{strips}	Number of strips
$\eta_{inverter}$	Inverter efficiency	$\eta_{abs,strip}$	Fraction of light absorbed by cell strip
η_{Carnot}	Carnot efficiency	I_{MPP}	Maximum power point current
T_C	Cold reservoir temperature	V_{MPP}	Maximum power point voltage

List of Figures

List of Tables

1. Introduction

1.1 Motivation

The collection and conversion of sunlight into useful energy is a potential solution to the current issues associated with fossil-fuel based power generation. Combustion of fossil fuels releases greenhouse gases and pollutants into the atmosphere which contribute to climate change. Furthermore, the global demand for energy coupled with the regional availability of fossil fuels has created a complex system of geopolitics which contributes to instability around the globe. Sunshine is both a global and renewable commodity and efficient harvesting of this energy puts us all on a path toward stability.

Human utilization of the solar resource dates back to antiquity (Perlin 2013). In 1878, conical solar reflectors were used to drive a Rankine cycle and pump water (Delgado-Torres 2009). Since then they have been developed for heating, cooling, pumping, desalination, power generation, and more. In 1954, researchers at Bell Telephone Laboratories demonstrated the first photovoltaic (PV) solar cell with an efficiency of 6% (Zondag et al. 2006).

The development of solar collectors did not become a major focus in the United States until the 1970s when the OPEC embargo caused an energy shortage and a shift in policy towards development of domestic energy resources. This resulted in the beginning of heavy R&D programs in the U.S. which culminated in the installation of solar electric generating capacity on the grid in the 1980s and 1990s.

Figure 1.1 – Solar Electric Generating Systems (SEGS) Plant

Today, solar research is driven by a growing awareness of the issue of climate change, as solar technologies represent key solutions for a 100% carbon-neutral future (Jacobson et al. 2015). Simultaneous maturation of commercial flat plate PV (which has dropped in price by more than ½ in the past 5 years) and increased state and federal response is driving unprecedented levels of installed solar generating capacity on the grid.

As this continues, a major problem becomes what to do with the excess electricity generated during daylight hours. The variable nature of solar PV has already manifested effects such as the "Duck Curve" in California where the price of energy drops during the day due to excess production and a huge ramp in electric production is required in the evening to offset the thousands of megawatts of solar PV that simultaneously go offline.

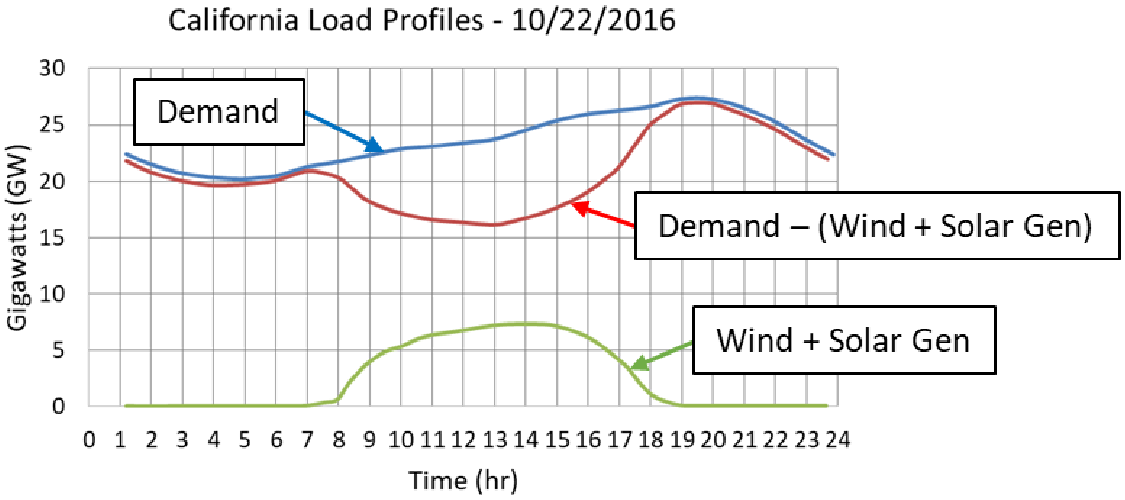

Figure 1.2 – The California "Duck" curve

Current battery systems are expensive enough to limit their economic viability, even under aggressive cost assumptions. While all this may change as industries move toward electrification and more manufacturing capacity comes online, there are other options.

Thermal energy storage (TES) systems are a cost-effective method for storing and dispatching thermal energy. When combined with concentrating solar power (CSP) plants (which use solar generated heat to produce steam and drive a Rankine power cycle), they enable nighttime or time-shifted solar electric production. The main problem preventing this solution is the high cost of the CSP plant, especially relative to the lost cost of PV which makes the two options (system + storage) roughly comparable on cost (CSP + TES is slightly lower).

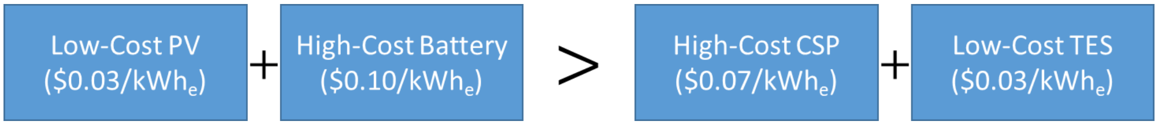

Figure 1.3 – Cost of solar-to-electric capacity and storage (Branz et al. 2015, Jorgensen et al. 2016, quoted prices at SHC / SWC 2017)

The two technologies operate on fundamentally different principles. PV systems are typically high efficiency, and spectrally dependent (i.e. only make use of a portion of the solar spectrum) whereas CSP systems are low efficiency, but spectrally *independent* (see Figure 1.4).

This disparity allows hybrid systems, through spectrum splitting techniques, to direct a portion of the solar spectrum to a PV subcomponent where it is converted at optimal efficiency and send the remaining poorly converted photons to a CSP subcomponent for additional conversion. By essentially gaining bonus solar-to-electric conversion through the addition of a low cost PV component, hybrid systems may provide low enough levelized costs of energy (LCOE) to incentivize their installation (where pure CSP has stalled) and enable the deployment of thermal energy storage systems for dispatchable power production (Branz et al. 2015). This was a motivating factor behind the U.S Department of Energy's (DOE) Advanced Research Projects in Energy (ARPA-E) release of the FOCUS solicitation, to develop advanced hybrid and spectrum splitting solar collectors for power generation.

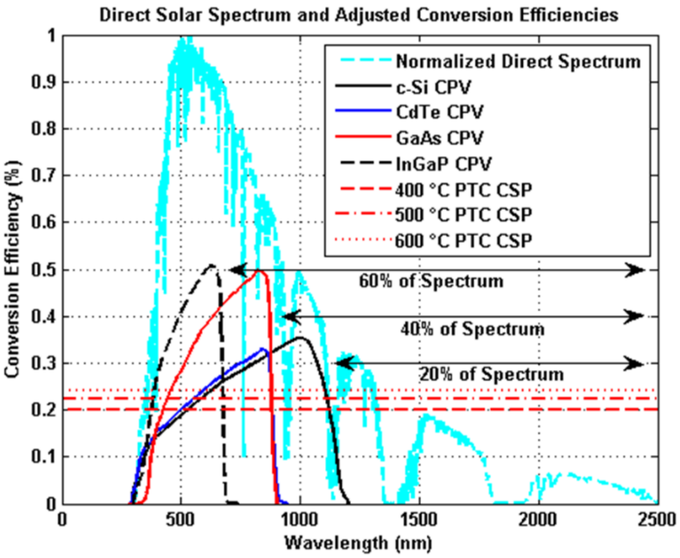

Figure 1.4 – Spectral conversion efficiencies.

In this dissertation, a novel hybrid (CSP/CPV) spectrum splitting collector is developed for the purpose of power generation which (1) integrates spectrally selective back-reflecting solar cells into a secondary concentrator to provide spectrum splitting and (2) achieves high concentration ratios on the CSP subcomponent for high temperature operation under partial (spectral) illumination.

1.1.1 Dissertation Outline

In Chapter 1, the solar resource and techniques used by collectors for efficient capture are described, followed by a literature review on CSP, PV, and spectrum splitting technologies.

In Chapter 2, a comparative model is developed to simulate performance of single and two-stage parabolic troughs incorporating ideal, typical interference, and solar cell optical filters.

In Chapter 3, a first generation prototype using GaAs cells is designed, developed, and experimentally tested up to 360 °C using Therminol VP-1.

In Chapter 4, the optics of segmented CPCs are investigated to simulate the constraint of integrated flat solar cells. A segmented (non-ideal) CPC can still achieve either (i) maximal flux concentration on the absorber or (ii) maximal optical efficiency, but not both.

In Chapter 5, a second generation prototype using dual junction InGaP/GaAs cells and an optimized secondary is designed, developed, and experimentally tested up to 650 °C using a particulate heat transfer fluid.

Chapter 6 summarizes the dissertation, novelties, and learnings to date. It also discusses future areas for research, some of which will be developed as the project continues.

1.2 The Solar Resource

1.2.1 Sun-Earth Geometry

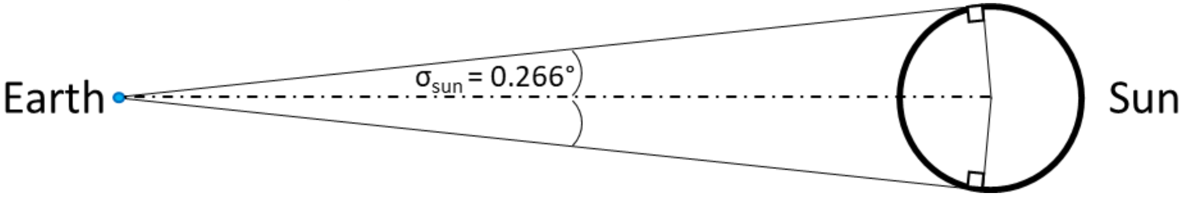

Figure 1.5 – *Solar half-disk angle*

Rays from the sun strike the Earth within the angle cone prescribed by the sun-earth geometry known as the solar half-disk angle (σ_{sun}) ~ ¼°. This has implications with regards to solar concentration and must be considered when designing the acceptance angle of solar collectors.

Radius of Sun (r_{sun})	6.96 x 10^8 meters
Radius of Earth (r_{earth})	6.40 x 10^6 meters
Distance between Sun and Earth ($d_{sun-earth}$)	1.50 x 10^{11} meters
Solar half-disk angle	±0.266°

Table 1.1 – *Sun-Earth geometries*

The angle at which these (±0.266°) ray bundles reach us here on earth is called the solar declination angle (δ) and is calculated based on the day of the year (n, where n = 1 on December 21st, the winter solstice) according to equation 1.1. The maximum angle occurs on the summer and winter solstices when the sun is +/-23.45°.

$$sin\delta = -\sin(23.45)\cos\left(360°\frac{n_{day}+10}{365.25}\right) \tag{1.1}$$

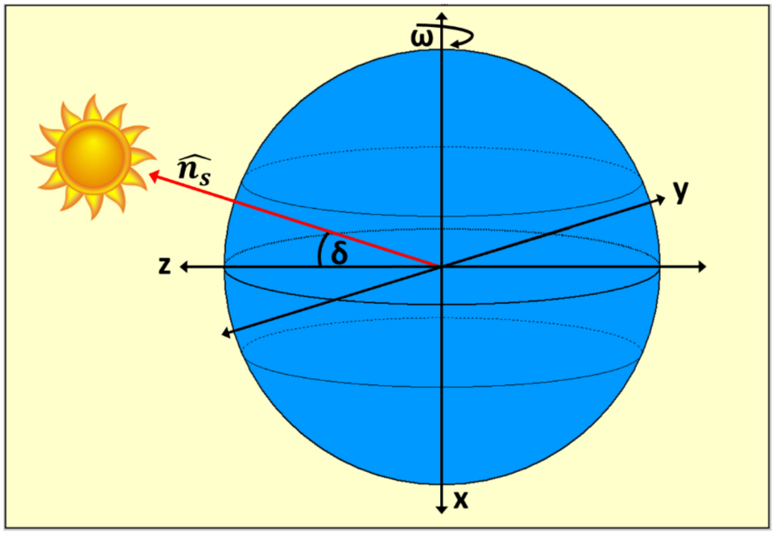

Figure 1.6 – *Sun-Earth geometry*

The hour angle (ω) accounts for the daily rotation of the Earth and is described by equation 1.2. At solar noon, the hour angle is equal to 0, which is halfway between sunrise and sunset and when shadows point due (solar) south. Here t is the hour counted from noon (t = 0 at noon, t > 0 after noon, t < 0 before noon).

$$\omega = \frac{360°}{24}t \tag{1.2}$$

With equations 2 and 3, the vector pointing from the earth to the sun ($\widehat{\boldsymbol{n_s}}$) is written as $\widehat{\boldsymbol{n_s}} = (\sin\delta, \cos\delta\sin\omega, \cos\delta\cos\omega)$.

1.2.2 Solar Spectrum

The solar resource is wavelength dependent and very closely matches the emission spectrum one would expect from a 5777 K blackbody according to Planck's law.

$$B_\lambda = \frac{2hc^2}{\lambda^5}\frac{1}{e^{\frac{hc}{\lambda k_B T}}-1} \tag{1.3}$$

As solar radiation travels through the atmosphere, certain spectral bands are absorbed by various molecules (H_2O, CO_2, O_2, O_3, CH_4, N_2O) causing portions of the extra-terrestrial solar spectrum to be missing in terrestrial measurements. Rayleigh scattering by small molecules in the atmosphere (O_2, N_2) preferentially scatters light at shorter wavelengths, causing the sky to appear blue. Because of these effects, by the time the solar radiation reaches the surface of the Earth it has a direct (directional) component and a scattered (non-directional) diffuse component.

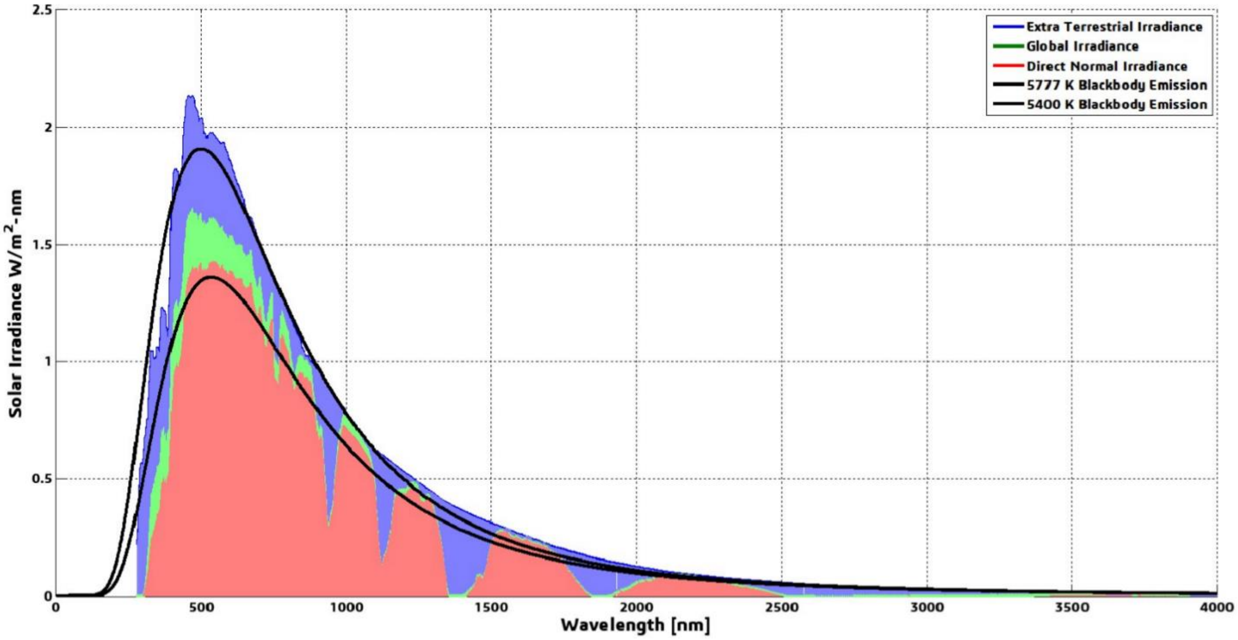

Figure 1.7 – *Solar Spectra*

The direct component (direct normal irradiance, or DNI) strikes the Earth at the angle based on the sun-earth geometry and within an angle cone given by the solar half disk angle. The diffuse component is a combination of light which is scattered by the atmosphere (gases, aerosols, clouds) and has no strong directional or angular component. Global irradiance is used to describe the combination of direct and diffuse components.

$$G_{global} = DNI + G_{diffuse} \tag{1.4}$$

The American Society for Testing and Materials (ASTM) G173-03 reference solar spectra are plotted in Figure 1.7. You can clearly see the atmospheric absorption bands which are present in extra-terrestrial (satellite) measurements but not in ground-based measurements. Most of the difference between global and direct irradiance is at shorter wavelengths due to Rayleigh scattering. Also plotted the blackbody emission curves for a 5777 K and 5400 K blackbody using Eq. 1.3.

DNI	900 W/m^2
Global	1000 W/m^2
Extra-Terrestrial	1348 W/m^2

Table 1.2 – *Relative solar fluxes*

Integrating over these spectra from 1-4000 nm yields the different fluxes in Table 1.2. The solar resource is commonly quantified as 1 kW/m^2.

1.2.3 Potential

The total solar power reaching the top of the earth's atmosphere at any given moment is ~174,000 TW with about ~129,000 TW reaching the surface. Typically a good portion of the globe is shrouded by clouds and even assuming 75% cloud cover, 32,000 TW global solar flux is available at the surface.

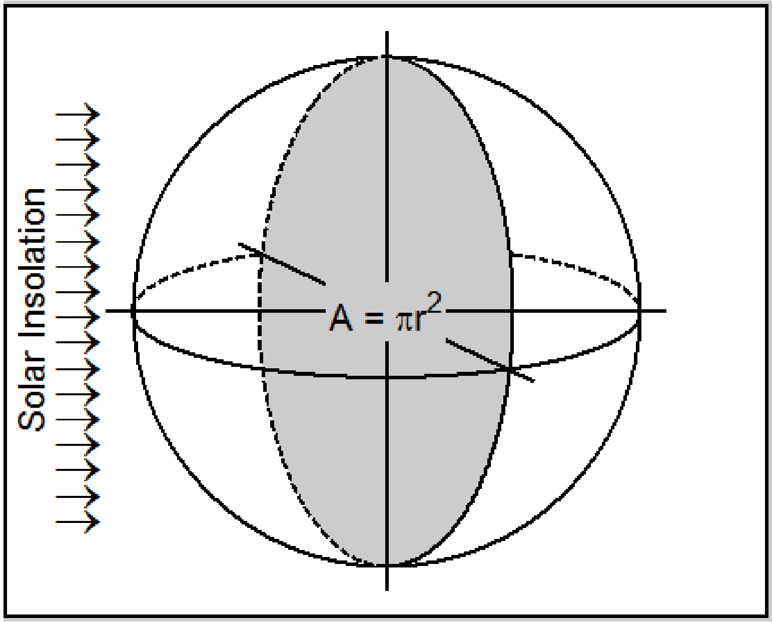

Figure 1.8 – *Cross-section of Earth*

In 2015, annual global primary energy consumption reached 161,507 TWh, equivalent to an annually averaged (24/7) power consumption of 18.4 TW. Assuming 20% solar to electric conversion (achievable by both PV and thermal systems), harvesting less than 0.3% of global irradiance (even under 75% cloud cover) would more than satisfy current global power demand. Thus it should not be impossible for a significant portion of the world's energy to be generated by clean, renewable solar.

In 2016 the United States consumed about 28,545 TWh. A similar 20% solar to electric system installed under ~3000 kWh/m^2 annual solar irradiance in the American Southwest would generate 680 kWh/m^2. Assuming a packing factor of ½ to account for effects such as shading and land-use (i.e. power block stations, roads, facilities), meeting the U.S. domestic energy demand would require a solar plant 308 x 308 km, or ~1% of the total U.S. land area. A 300 km x 300 km square is drawn in Figure 1.9 for illustration.

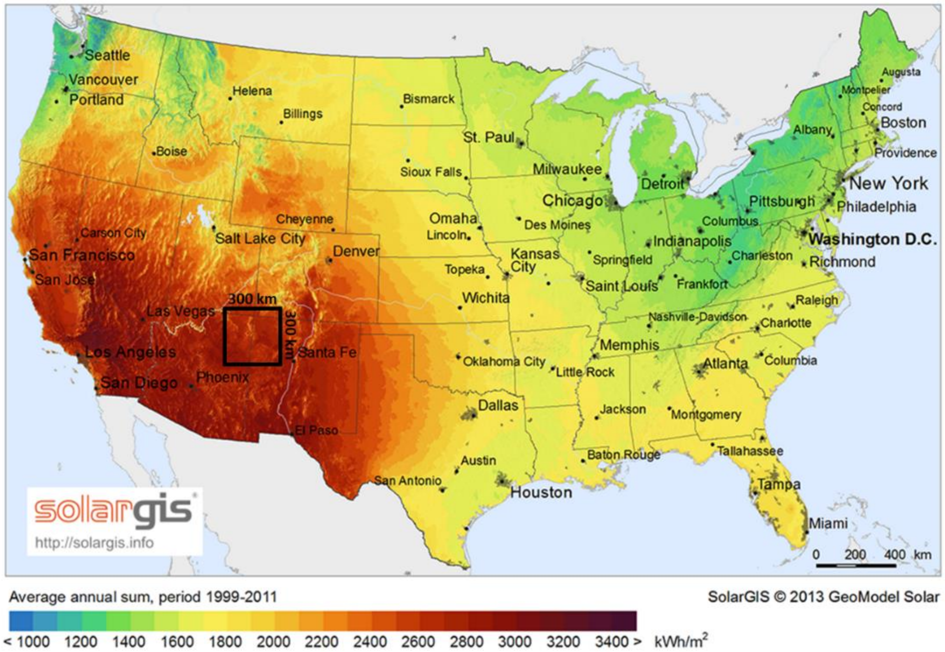

Figure 1.9 - *Direct solar resource in the United States and land area required for 100% solar generation.*

There are three main techniques for converting solar irradiance to electric power: (1) Concentrating Solar Power (CSP), (2) Photovoltaics (PV), and (3) Concentrating Photovoltaics (CPV). The solar resource is variable by nature. As solar energy systems are becoming more developed, an emerging need is the ability to *store* the captured solar energy for later use. This *dispatchability* is a major motivating factor for this work.

1.3 Solar Collectors

As seen in the previous chapter, the solar flux has an angular component (σ_{sun}), a directional component ($\widehat{\boldsymbol{n}_s}$) which is also tied to the direct and diffuse components of the solar resource, and a spectral component ($G(\lambda)$). A solar collector's job is to take advantage of these properties for the collection and conversion of solar irradiance (radiation flux) into a more useful form of energy (light, heat, electricity).

In this section we discuss the principle of concentration (1.2.1), the principles governing efficient operation of solar thermal collectors (1.2.2), and the spectrally dependent properties of photovoltaic solar cells (1.2.3).

1.3.1 Concentration

Optical devices can be used to concentrate the relatively dilute solar flux (~1000 W/m^2) to a much higher flux density. The concentration ratio (C) of a device is simply the ratio of its entrance aperture area to its exit aperture area.

$$C = \frac{A_{entrance\ aperture}}{A_{exit\ aperture}} \tag{1.5}$$

The limiting case for maximum concentration is given by conservation of etendue, which is a geometric quantification of the angular and spatial extent of an aperture. It is based on the principle that physical space can be broken into a finite number of discrete positions, each with a finite number of discrete directions (ray bundles). For two-dimensional systems, etendue is the product of angular extent ($\sin\theta$) and spatial extent (A) and since etendue is conserved, any lossless optical device which provides *constriction* of the spatial extent (concentration) must provide a corresponding *expansion* in the angular extent. This is described in much more detail in the book *High Collection Nonimaging Optics* by W.T. Welford and R. Winston.

$$A_1 \sin\theta_1 = A_2 \sin\theta_2 \tag{1.6}$$

$$\frac{A_1}{A_2} = \frac{\sin\theta_2}{\sin\theta_1} \tag{1.7}$$

Since the maximum angular extent exiting an optical concentrator is ±90° (i.e. $\sin\theta_2 = 1$) and

$$C = \frac{A_1}{A_2} \tag{1.8}$$

The maximum concentration allowed for a two-dimensional system is given by

$$C_{max} = \frac{1}{\sin\theta} \tag{1.9}$$

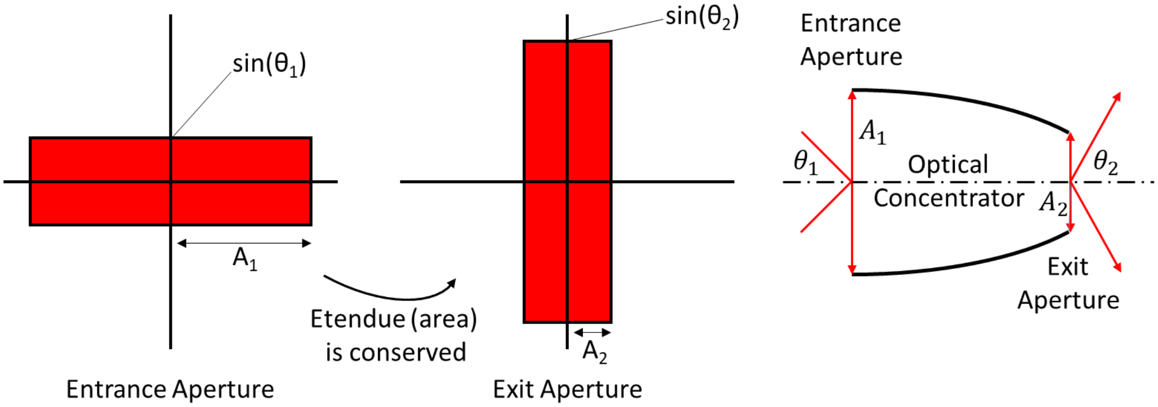

Figure 1.10 – *Conservation of etendue*

This is the maximum concentration allowed by the 2nd law of thermodynamics, and prevents an optical device from increasing the temperature of a receiver above the source. As a result, the limit to solar concentration (for an index of refraction = 1) on earth (σ_{sun}=0.266°) for a line-focus (two-dimensional) concentrator is 215X, and 46,396X for a point-focus (three-dimensional) concentrator (which turns out to be the square of equation 1.9).

In real applications the acceptance angle of a collector ($\pm\theta$) is enlarged over the solar disk angle to accommodate angular error introduced to the optical system from manufacturing tolerances and installation misalignment which reduces the concentration ratios achieved in practice.

Furthermore, not all concentrators are capable of reaching maximal concentration. *Imaging* concentrators produce an image of the source at the exit aperture. While this is incredibly useful for many applications, it is an unnecessary constraint (image mapping) when it comes to pure radiation transfer. *Nonimaging* concentrators are thermodynamically efficient and can reach maximal concentration through optimal utilization of phase space. They are, however, very non-compact for small acceptance angles which limits their practical use.

The most common concentrators used in the collection of solar energy are imaging systems, such as parabolic trough (2D), dish (3D), or Fresnel-based linear reflector / lens (2D) or solar tower / lens (3D) systems. Typical concentration ratios for 2D systems are on the order of 20-30X and 500-1000X for 3D systems, much lower than the thermodynamic limit.

Concentration of the solar flux is desirable in both thermal and photovoltaic applications, but is achieved by restricting the acceptance angle (θ) of a collector which has two important implications:

1. Since the sun follows a daily prescribed motion $(\widehat{\boldsymbol{n_s}})$, restricting the acceptance angle requires the collector be placed on a tracking device to follow this motion. Tracking systems add complexity and cost (installation and O&M) to solar collector systems.
2. The solar resource is made of direct (directional) and diffuse (isotropic) components. Limiting the acceptance angle of a collector reduces the amount of sky the collector "sees". This eliminates availability of the diffuse component for high concentration collectors, which in some places can be quite high.

1.3.2 Thermal Collectors

The "game" of a solar thermal collector is to collect and convert incoming solar flux into useable heat without losing it to the environment. There are several techniques for accomplishing this, namely

- Insulation (vacuum, aerogel)
- Optical concentration
- Selective coatings

The complexity of a solar thermal collector is a function of the desired operating temperature, and the number of techniques required for efficient operation.

$$\underbrace{A_1 DNI}_{Q_{solar}} * \underbrace{\rho\tau\alpha\gamma}_{\eta_0} - \underbrace{A_2 \epsilon\sigma T^4}_{Q_{loss,rad}} - \underbrace{A_2 h(T - T_\infty)}_{Q_{loss,convection}} = \underbrace{\eta_{thermal} * A_1\, DNI}_{Q_{thermal}} \tag{1.10}$$

Generally speaking the performance of a solar thermal collector can be described by equation 1.10. Incoming solar power (Q_{solar}) multiplied by the optical efficiency (η_0) and subtracting the thermal losses from radiation and convection $(Q_{loss,rad}, Q_{loss,convection})$ is equal to the net thermal power produced $(Q_{thermal})$. Here A_1 is the primary aperture area in m^2, DNI is the incoming solar power in W/m^2, $\rho, \tau, \alpha, \gamma$ are the reflectance, transmittance, absorptance, and intercept factor, A_2 is the absorber area in m^2, ϵ is the emittance of the selective coating at the operating temperature, σ is the Stefan-Boltzmann constant, T is the operating temperature in Kelvin, h is the heat transfer coefficient in W/m^2-K and T_∞ is the environmental temperature. $\eta_{thermal}$ is the effective thermal efficiency of the collector.

Vacuum insulation is a standard technique for eliminating convective loss $(h \rightarrow 0)$ from a hot absorber surface to the environment. It is applied to almost all solar collectors with the exception of low temperature flat plate and rubber pool heating systems. If we eliminate the convective loss term in equation 1.10, divide both sides by Q_{solar}, and substitute the concentration ratio $C_x = \frac{A_1}{A_2}$, we can describe the thermal efficiency of a collector much more compactly using equation 1.11.

$$\eta_{thermal} = \underbrace{\rho\tau\alpha\gamma}_{\eta_0} - \underbrace{\frac{\epsilon\sigma(T_{abs}^4 - T_{amb}^4)}{C_x DNI}}_{radiative\ loss} \tag{1.11}$$

The optical efficiency (η_0) is the *maximum* possible efficiency of a collector in which all losses are the result of the optical system alone. This occurs when the collector is at ambient temperature and there is no temperature gradient to drive thermal loss mechanisms. High optical efficiency is achieved through the use of highly reflective (ρ) reflectors, highly transparent (τ) envelopes, and highly absorptive (α) absorbers. The intercept factor (γ) is a measure of the shape efficiency of real systems which accounts for geometric losses (rays that miss the absorber) due to angular/tracking tolerance and collector design (non-idealities).

As a collector heats up, a temperature gradient between the absorber and the environment is established and, in an evacuated collector, results in absorber radiation loss. Optical concentration (C_x) reduces these losses by reducing the absorber surface area (A_2). The use of selective coatings imparts both a high absorptance (α) for high optical efficiency and a low emittance (ϵ) which reduces radiation loss at high temperatures.

	Evacuated Tube Collector (ETC)	**Evacuated Flat Plate (VFP)**	**Compound Parabolic Concentrator (XCPC)**	**Compact Linear Fresnel (CLFR)**	**Parabolic Trough Collector (PTC)**	**Two-Stage Parabolic Trough (PTC w/ secondary)**	**Solar Tower (STC)**
C	1/π	1	1.4	20	25	50	1000
η_0	0.85	0.85	0.77	0.77	0.77	0.73	0.625

Table 1.3 – *Approximate concentration ratio and optical efficiency of solar collectors*

Equation 1.11 is plotted for some approximated solar thermal collectors in Figure 1.11 based on the parameters in Table 1.3. Also plotted in Figure 1.11 are the performance ratings of some commercial collectors.

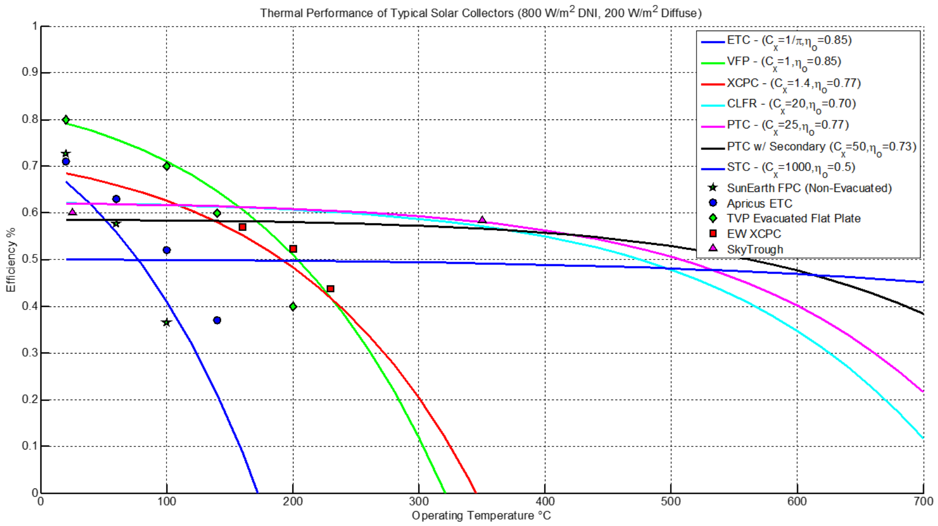

Figure 1.11 – *Thermal performance of typical solar collectors*

Several collectors exist and can operate efficiently at ≤200 °C without tracking. To reach higher temperatures with any reasonable efficiency requires concentration. The main players in the field are line-focus Fresnel and parabolic trough systems and point-focus parabolic dish and power tower systems.

1.3.3 Photovoltaics

PV systems generate electricity by a different, wavelength-dependent quantum process. A PV semiconductor is responsive to sunlight photons with energy greater than or equal to its bandgap energy. Photons with energy greater than the bandgap that are absorbed generate electrons and holes, thus producing a usable current and voltage (or chemical potential difference). Sub-bandgap energy photons are either not absorbed or else they may be absorbed in non-reflective metal electrodes and end up generating waste heat. The excess energy of the electrons (holes) created by absorption of the above bandgap photons is also converted to heat through a process known as hot carrier relaxation, which is a result of carrier-phonon scattering. Thus, there is a tradeoff: for a given solar spectrum there is an optimal bandgap energy that results in the best power conversion efficiency in the context of a single bandgap device (single quantum threshold). When the bandgap energy is too small, the photogenerated current density is large but the voltage is too small whereas when the bandgap energy is too large, the voltage is large but the current density is too small. Solar cell power conversion efficiency is a function of both the current density and voltage and so this is why an optimal choice of bandgap energy emerges. Fortunately, this optimum is not a delta function and thus near-peak power conversion efficiency under the polychromatic sunlight spectrum is relatively broad. Under the internationally accepted air mass 1.5 global (AM1.5G) simulated solar spectrum at 25 °C, the peak theoretical power conversion efficiency is 33.7% (corresponding to a bandgap energy of ~1.35 eV) (Shockley & Queisser 1961). Today, the limit for single-junction (single bandgap) solar cells is closely approached by 1.42 eV GaAs and 1.12 eV silicon (Si) solar cells which have demonstrated laboratory efficiencies of 28.8% and 26.7% respectively (Green et al. 2017 Good quality commercially available Si *modules* are typically about 20% efficient (Smith et al. 2013).

Multi-junction solar cells (more than one quantum threshold) under sunlight concentration have achieved flash lamp-tested efficiencies up to 46% [7], a feat which is made possible by stacking cells with incrementally larger bandgaps (from bottom to top) in order to more optimally convert the polychromatic solar radiation into electricity. This technique may be thought of as a type of spectral beam splitting (SBS); each subcell in the multi-junction stack more effectively converts a relatively small portion of the incident sunlight into electricity thus mitigating hot carrier relaxation loss.

The solar spectra are plotted in Figure 1.12 along with the bandgap wavelengths of some common cells.

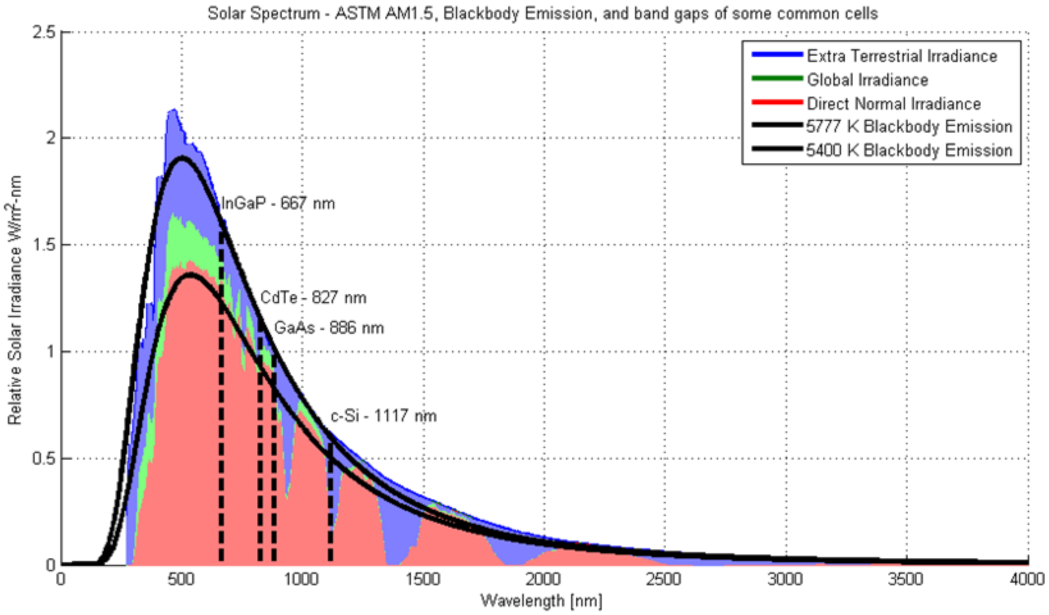

Figure 1.12 – *Solar Spectra and Solar Cell Bandgaps*

The spectral response (External Quantum Efficiency) curves, open circuit voltages, and fill factors for champion cells under the global AM1.5 spectrum at 25 °C (Green et al. 2013, 2016, 2017) and temperature coefficients (β) (Silverman et al. 2013, Virtuani et al. 2010, Nishioka et al. 2005) are summarized in Table 1.4 for crystalline silicone (c-Si), cadmium telluride (CdTe), gallium arsenide (GaAs), and indium gallium phosphide (InGaP).

Semiconductor material	Bandgap	β	V_{oc}	*FF*	η_{cell}
c-Si	1117 nm	0.41 %/°C	0.74	0.83	26.26%
CdTe	827 nm	0.21 %/°C	0.87	0.79	20.61%
GaAs	886 nm	0.08 %/°C	1.12	0.86	28.96%
InGaP	667 nm	0.04 %/°C	1.49	0.87	21.83%

Table 1.4 – *Characteristics of some common solar cells*

When testing the performance of a solar cell, a cell is exposed to monochromatic light and the short circuit current response ($J_{sc}(\lambda)$) is measured. This is then converted to the external quantum efficiency (EQE) according to equation 1.12 which is commonly reported as it allows quick comparison between cells. Here q, h, c, and λ are the elementary charge, Planck's constant, speed of light, and wavelength, respectively. The EQEs of 4 common cells are plotted in Figure 1.13 and the short circuit spectral response is plotted in Figure 1.14 against the global AM1.5 solar spectrum.

$$J_{sc}(\lambda) = q\frac{\lambda}{hc}EQE(\lambda) \tag{1.12}$$

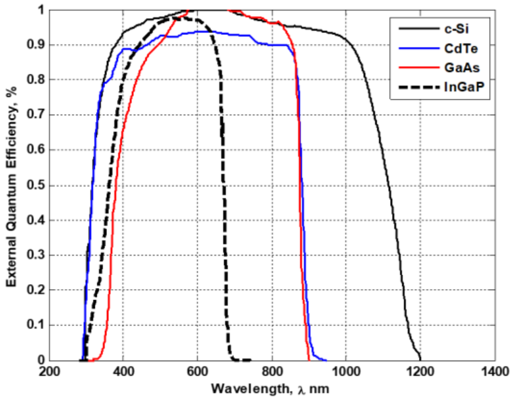

Figure 1.13 - *External Quantum Efficiency of champion cells as a function of wavelength*

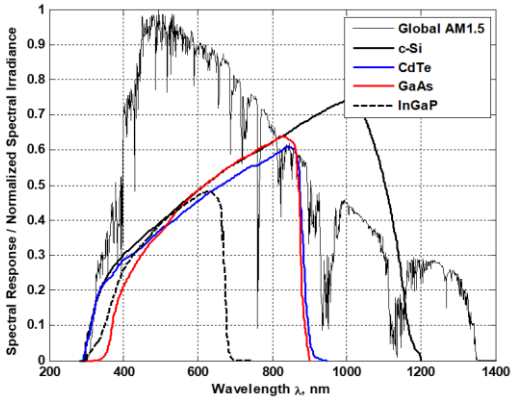

Figure 1.14 - *Short circuit current density of each cell as a function of wavelength*

The spectral efficiency of a cell ($\eta_{cell}(\lambda)$) is determined by multiplying the short circuit current with the open circuit voltage (V_{OC}) and fill factor (*FF*) of the cell and is the cell's effective efficiency as a function of wavelength. These are plotted in Figure 1.15.

$$\eta_{cell}(\lambda) = J_{sc}(\lambda)\, V_{oc}\, FF \tag{1.13}$$

The efficiencies of the cells in Table 1.4 are calculated from equation 1.14. These are within 0.1% of the efficiencies reported in the solar cell efficiency tables (Green et al. 2017) with error introduced by extracting the curve data.

$$\eta_{cell} = \frac{\int \eta_{cell}(\lambda) G_{direct}(\lambda)}{\int G_{direct}(\lambda)} \tag{1.14}$$

As a solar cell heats up its efficiency is reduced based on its temperature coefficient (β). Concentration tends to improve the efficiency of a solar cell.

These results are for small area cells. To get the current out, typical commercial cells are covered in grid contact "fingers" to reduce the diffusion distance of an electron through the semiconductor material. The metallic grid contact fingers are in contact with tabbing wires, which are then in contact with bus wires, all of which incrementally increase in size to reduce electronic resistance. Grid contact "fingers" prevent irradiance from reaching small portions of the cell and contact, tabbing wire, and bus wire resistance adds some voltage drop and reduces the ultimate power output of a module. Finally, an inverter must convert the DC output to AC output which adds another efficiency to the total equation.

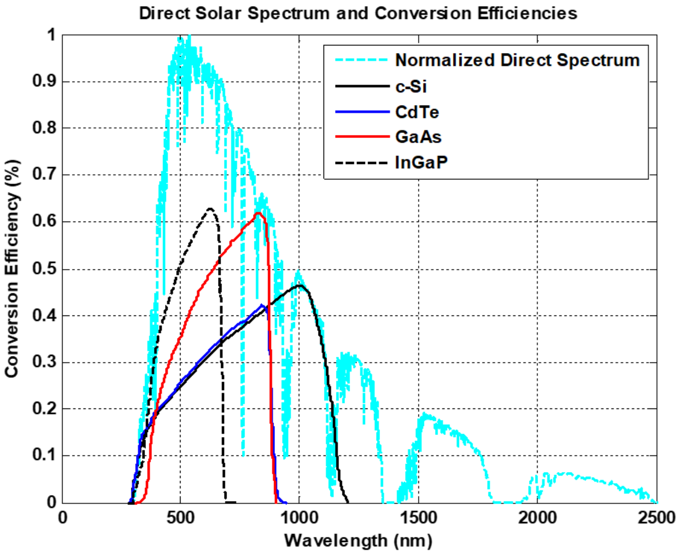

Figure 1.15 – *Spectral efficiencies*

The total solar-to-electric (AC) efficiency of a module can be described by equation 1.15, which incorporates these effects.

$$\eta_{electric,PV} = \eta_{cell}(1 - \beta(T_{cell} - T_{ref}))\eta_{Cx}\eta_{cell-to-module}\eta_{inverter} \tag{1.15}$$

Crystalline silicone (c-Si) is the most commercially mature technology, followed by Cadmium Telluride (CdTe) which has a lower efficiency but performs better in hotter environments (low temperature coefficient). Gallium Arsenide (GaAs) and Indium Gallium Phosphide (InGaP) cells are still quite expensive to produce, but are used in satellite and concentrating photovoltaic applications for their high efficiency.

1.4 Solar to Electric Conversion (Literature Review)

There are two main methods for converting solar energy into electricity, including (1) Concentrating Solar Power (CSP) and (2) Photovoltaics (PV) or Concentrating Photovoltaics (CPV).

1.4.1 Concentrating Solar Power (CSP)

CSP systems generate electricity in a similar fashion to typical power plants, using concentrated solar radiation to generate useful temperatures in a heat transfer fluid (HTF) which is delivered to a steam Rankine cycle.

Historically, most plants have used parabolic trough collectors (PTCs) (Zhang et al. 2013) operating with thermal oils near 400 °C to achieve instantaneous solar to electric conversion efficiencies around 20% (Price et al. 2002). Between 1984 & 1990, 9 CSP plants (SEGS I-IX) were built in the California Mojave Desert which were until recently the largest installed CSP capacity (354 MW) in the world. The feasibility of the technology has been demonstrated since the 1980s with hundreds of megawatts in operation (Fernández-Garcia et al. 2010) and due to this extensive track record is considered the most bankable solar technology.

The technical limitation of these systems comes from the mineral oil HTF, which reaches a maximum operating temperature of 400 °C (Therminol VP-1) and requires the power cycle to operate at less than ideal efficiencies (~37%) (Price et al. 2002). More recent systems employing molten salt HTFs are able to reach higher temperatures (580 °C) (Maccari et al. 2016) and power block efficiencies (~42%), but are still temperature limited by the molten salt chemistry and the thermal efficiency of the parabolic collector itself (Kearney et al. 2003).

The conversion of heat to work in a CSP plant is limited by the maximum Carnot efficiency (η_{Carnot}), described by equation 1.16, which increases with the temperature difference between the hot (T_H) and cold (T_C) reservoirs.

$$\eta_{Carnot} = 1 - \frac{T_C}{T_H} \tag{1.16}$$

As a result, the main drive in CSP research today is toward the development of high concentration systems (power towers with concentration ratios > 1000) capable of generating temperatures > 700 °C, where power blocks (specifically dispatch-ready supercritical CO_2 Brayton cycles) achieve high (>50%) thermo-electric conversion efficiencies (Mehos et al. 2017). The champion technology behind this push is the solar power tower, which harnesses thousands of heliostats to concentrate sunlight (in some cases more than 1000X) on a high temperature centralized receiver (Behar et al. 2013). In 2014, the Ivanpah (tower) power plant was commissioned and is now the world's largest CSP plant (392 MW).

Operation at elevated temperatures (>580 °C) requires new HTFs of which the most likely candidates are molten salt, solid particles, and CO_2 or Helium gases. None of these, however, exist without unique technical challenges (corrosive attack, poor heat transfer, high temperature and pressure fatigue) and unique receiver designs (Mehos et al. 2017).

Though today such systems are more expensive than their photovoltaic (PV) counterparts, they provide an opportunity to integrate cost-effective thermal energy storage (TES) systems which add value by allowing time-shifted renewable electric generation (Denholm et al. 2013). During my most recent conference (Solar World Congress / Solar Heating and Cooling, October 2017) in Abu Dhabi, the lowest quoted levelized cost of energy for CSP including molten salt storage was \$0.073/kWh (for a plant with 300 MW PTC capacity and 100 MW Tower capacity).

1.4.2 Photovoltaics (PV)

Early work for practical solar to electric conversion focused on CPV systems since the solar cells themselves were too expensive to be used for non-concentrating PV.

In the 1990s two-dimensional parabolic trough concentrators focusing to silicon cells were actively studied. These efforts culminated in the EUCLIDES prototypes (several generations) in Spain which ultimately reached 14% efficiency (Sala et al. 1996) at a projected install cost of \$3.40/W_e (Vivar et al. 2012). This was approximately half the cost of flat plate silicone at the time (Luque et al. 1997). The cells were passively cooled and thermal contact between the cells and heat sink was identified as a critical component to maintaining efficiency (Vivar et al. 2006).

In 2005, a similar system (CHAPS) using active water cooling was demonstrated in Australia and achieved solar to electric efficiencies between 10-13% depending on the water temperature (Coventry et al. 2005). A major problem identified was non-uniform flux incident on cells in series which caused a current bottleneck in the least-illuminated cell.

The 2000s also saw an interest in three-dimensional concentrating systems which could reach much higher concentrations and enable the use of expensive but high efficiency triple junction solar cells. The first systems using point-focus Fresnel lenses demonstrated efficiencies ~14% with silicon solar cells (70X Bentley et al. 2010, 250X Stone et al. 2004). The use of triple junction cells quickly improved solar to electric efficiencies to 25% (Kinsey et al. 2011) and projected costs dropped to less than \$2/W_e (Kurtz 2009).

In the late 2000s and early 2010s, the race toward higher concentration systems began. A 460X Fresnel lens (28% efficiency, van Riesen et al. 2011), 500X cassegrian (26% efficiency, Horne et al. 2006), and finally a 1100X dual stage refractive optical system were all demonstrated, with the latter reaching 35% solar to electric efficiency (Ghosal et al. 2014).

Systems reported in the literature are summarized in Table 1.5. By 2010, a cumulative capacity of 21 MW of CPV had been installed globally and the lowest reported installed cost was \$3/W_e (Mokri and Emziane 2011).

System	Concentrator Type	Solar Cell Type	Efficiency (%)*	Reference
EUCLIDES	PTC (32X)	mono c-Si	14%	Sala et al. 1996
CHAPS	PTC (37X)	mono c-Si	13%	Coventry et al. 2005
Whitfield	Fresnel Lens (70X)	mono c-Si	13%	Bentley et al. 2010
AMONIX	Fresnel Lens (250X)	mono c-Si	14%	Stone et al. 2004
AMONIX	Fresnel Lens (250X)	Triple Junction	25%	Kinsey et al. 2011
SolFocus	Cassegrian (500X)	Triple Junction	26%	Horne et al. 2006
Concentrix	Fresnel Lens (460X)	Triple Junction	28%	van Riesen et al. 2011
SEMPRIUS	Glass Lens (1100X)	Triple Junction	35%	Ghosal et al. 2014
Solar Systems Dish	Dish (500X)	Triple Junction	22.8%	John Lasich, 2009
Multi-Focus Dish	Multi-Focus Dish (1375X)	Triple Junction	23.2%	Max Schmitz 2017

Table 1.5 – *CPV Efficiencies*

Though CPV systems achieve high efficiencies, they are limited to direct light and thus are confined to regions of high DNI where they can exhibit significant performance increases compared to traditional silicon flat plate systems (Mikami et al. 2016). CPV systems are also sensitive to the effects of soiling in the field (Vivar et al. 2008), which increase linearly with concentration and are higher in reflective systems due to an increased number soil-able layers in the optical system (Vivar et al. 2010). Substantial efforts to improve cell efficiency by a few percentage points in the lab can easily be wasted if care is not taken to minimize soiling in the field and several different techniques, such as nighttime stowing of panels upside down, were investigated for improving output and reducing O&M costs associated with cleaning (Mikami et al. 2016).

Despite their high efficiencies, a review of installed systems in Spain concluded CPV systems typically produced the same output as fixed systems, and less than tracking flat plate systems (Gomez-Gil et al. 2012). While CPV systems have higher efficiencies, they have reduced input irradiance (direct only) and higher performance losses due to degradation whereas flat plate systems suffer from cosine losses but gain diffuse radiation and have minimal effects from soiling.

From 2010 to 2013, price of utility scale fixed flat plate PV dropped from \$4.57 to \$2.04 and is today <\$1.03 in the United States (Fu et al. 2017). Today, most (if not all) CPV companies which formed during the 2000s are gone as they are unable to compete with the low cost of flat plate PV. During my most recent conference (Solar World Congress / Solar Heating and Cooling, October 2017 in Abu Dhabi) current levelized energy costs for new flat plate systems installed in Dubai were \$0.024/kWh for 800 MW_{PV}.

1.4.3 Hybrid (CSP/CPV) Spectral Beam Splitting (SBS) Systems

Hybrid systems combine photovoltaic and thermal technologies into a single device. Most hybrid systems operate on the principle of waste heat recovery (WHR) and capture the waste heat generated by the solar cell. In doing so most of the solar energy can be harvested, but these systems are typically limited to low temperatures since the conversion efficiency of a solar cell decreases with temperature.

Spectral beam splitting (SBS), in which the solar spectrum is selectively controlled through an optical filter, thermally *decouples* the cell and thermal subsystems in a hybrid PV/T collector. This decoupling enables each subsystem to operate at optimal conditions for conversion without hindering the other, and more specifically allows the thermal subsystem to operate at high temperature where it can be used to provide dispatchable thermal power.

Spectral beam splitting allows control over the solar spectrum and can be accomplished using a number of techniques. The most common technique is through the use of interference filters, where thin layers of dielectric material provide constructive or destructive interference to selectively reflect or transmit different spectral regions. Absorptive filters have also been developed which selectively absorb certain spectral regions typically in a flowing HTF and transmit the remainder to a solar cell component. Beam splitting can also be performed by solar cells (as in the multi-junction cell) which are absorptive of photons with energies above the band gap and transmissive of low energy photons.

Early work on beam splitting systems began in the 1980s, with theoretical and experimental investigations into the basic approaches to beam splitting (Osborn et al. 1986, Soule et al. 1986). Thin-film multilayer filters were easily tailored to match the spectral response window of silicon, but were sensitive to incidence angle (DeSandre et al. 1985). Liquid absorptive filters were identified as a potentially lower cost approach but required further investigation to identify materials with proper spectral matches (Chendo et al. 1987). In simulations, band-pass configurations (Soule et al. 1985) performed better than single-pass systems (D. Johnson 1983) since poorly utilized high energy photons could be redirected to the thermal subsystem. Most of this early work is summarized in the review by Imenes and Mills (2004).

In the 2000s SBS research expanded with the development of high concentration dish (Laisch et al. 1994) and tower (Segal et al. 2004), (Mills et al. 2002) configurations, and the introduction of high efficiency III-V cells (Vorobiev et al. 2006). Different materials were explored for the fabrication of interference filters (Wang et al. 2013, Shou et al. 2012, Peters et al. 2010), and new design methods enabled wider angle incidence (Imenes et al. 2006). More sophisticated models looked at optimal filter placement location for dish (Jiang et al. 2009) and trough systems (Jiang et al. 2010). The addition of nano-particles allowed spectral tuning in absorptive fluid filters (Otanicar et al. 2009) and several different materials were investigated (Taylor et al. 2012, 2013). Detailed simulations explored new and optimized absorptive filter receiver designs (Zhao et al. 2010, Otanicar et al. 2011). This phase of beam splitting research is reviewed by Mojiri et al (2013).

In the past 5 years the price of installed solar PV in the US has dropped by a factor of two (Fu et al. 2016), increasing solar penetration and manifesting effects such as the “Duck Curve” in California which reduces the value of additional PV (and variable) capacity on the grid (Palmintier et al. 2016). Time-shifted energy production is possible through the deployment of battery banks, but current costs and even aggressive research targets may not economically viable. Thermal energy storage (TES), on the other hand, is a relatively cheap addition to a CSP plant which enables dispatchable renewable electricity generation (Mehos et al. 2016) and increases the value of additional capacity on the grid (Denholm et al. 2013). Deployment of these systems on a meaningful scale, however, requires reductions to the currently high capital costs of CSP systems.

In 2013, ARPA-E released the FOCUS solicitation to develop advanced hybrid solar converters which, by employing SBS, could more optimally exploit the solar spectrum and reach higher conversion efficiencies. By doing so they could reduce the levelized electricity cost from hybrid plants to a point where such plants would be economically competitive, thus enabling the deployment of TES systems (Branz et al. 2015). The program has revitalized research on SBS systems with an emphasis on experimental work. It has also generated publications on various system level and experimental works on beam splitting systems using interference filters (Raush et al. 2014, Yu et al. 2015, Orosz et al. 2016, Weinstein et al. 2018), liquid absorptive filters (DeJarnette et al. 2015, 2016, Otanicar et al. 2016), semi-transparent (Xu et al. 2016), and back-reflecting solar cells (Cygan et al. 2016, Abdelhamid et al. 2016, Widyolar et al. 2016).

Research into absorptive filter systems continued concurrently with investigations into fluids (Vivar & Everett 2014, Looser et al. 2014, Joshi et al. 2016), nano-particles (Crisostomo et al. 2015, 2017, Hjerrild et al. 2016, An et al. 2015, 2016), and the development of more detailed absorptive receiver designs (Mojiri et al. 2015, 2016, Stanley et al. 2016, Saroha et al. 2015). Additional research explored alternative interference filter materials (Crisostomo et al. 2014, Hu et al. 2013, Sibin et al. 2017), and novel system designs (Liu et al. 2014, Crisostomo et al. 2015). General performance models for absorptive fluids were developed (Otanicar et al. 2015), along with methods for optimizing filter windows according to the band-gap of a solar cell (Bierman et al. 2016).

Most beam splitting systems use either interference or liquid absorptive filters which are tuned to match the spectral response of the solar cells being used. Silicon cells are by far the most common solar cells studied due to their low cost and availability, but the qualities that make them ideal as one-sun cells (low, broad-band conversion efficiency) make them less so for spectrum splitting systems (Widyolar et al. 2018). Linear Fresnel reflectors (Liu et al. 2014) and lenses (Yeh et al. 2018), parabolic trough (Stanley et al. 2016), dish (Shou et al. 2011, Xu et al. 2016), and tower configurations (Segal et al. 2004) have all been described with design solar-to-electric efficiencies between 20-30%, and the economics of trough systems (drop-in retrofit and new) has been calculated to be somewhere between $\$1.0 - 2.30/W_{electric}$ (Duquette et al. 2012, Orosz et al. 2016).

Remaining challenges for interference filters include cost reduction, the ability to produce large-area filters, and angular spectral control, whereas absorptive filter systems require further development with regards to stability and high temperature operation. Spectrum splitting tends to reduce the operating temperature of the thermal component, which limits the ability to charge thermal storage systems and brings into question its usefulness if storage is a major selling point. The most recent review of SBS systems (Ju et al. 2017) highlighted these issues, indicating the need for higher temperature designs, standardized metrics, and a better understanding of the economics of hybrid SBS systems.

The collector developed in this dissertation implements a novel form of spectrum splitting through the use of back-reflecting solar cells. In this way the current challenges associated with interference and absorptive filters are bypassed. Furthermore, a new two-stage optical design provides high concentration on the thermal absorber for high temperature operation and TES.

In the next chapter, a baseline model for comparing the different technologies and the new collector type are developed. The economics of a hybrid beam splitting system are also compared to the economics of side-by-side standalone PV and CSP plants.

2. Spectrum Splitting in Parabolic Troughs

The contents of this chapter have been published in-part as the journal article:

Widyolar, B., Jiang, L. and Winston, R., 2018. Spectral beam splitting in hybrid PV/T parabolic trough systems for power generation. *Applied Energy*, 209, pp.236-250.

In this chapter, a set of models are developed to provide a broad outlook on the net solar-to-electric conversion potential in parabolic trough systems which incorporate spectrum splitting. Parabolic troughs are specifically selected as they represent the most mature and bankable CSP technology to date. Several different beam splitting techniques are investigated including:

- ideal (lossless) optical filter
- typical interference filter
- semi-transparent cell
- back-reflecting cell

Both single and two-stage parabolic trough systems are simulated. Four different solar cells are examined including:

- Crystalline silicon (c-Si)
- Cadmium Telluride (CdTe)
- Gallium Arsenide (GaAs)
- Indium Gallium Phosphide (InGaP)

The spectral window (top and bottom window cutoffs) are optimized for each solar cell for the ideal optical filter and typical interference cases. The operating temperature of the CSP subsystem for maximum combined solar to electric efficiency is determined. The results provide a standardized comparison between different configurations and show a range of conversion efficiencies which are likely achievable in real systems. Lastly, the economics of a hybrid SBS system are examined as a case study and compared to the economics of a side-by-side PV and CSP plant.

2.1 Optics of Parabolic Trough Systems

2.1.1 Single Stage

The geometric concentration ratio of a typical parabolic trough system concentrating to a cylindrical absorber is described geometrically (Figure 2.1) by equation 2.1. Where ϕ is the half-rim-angle of the parabola and θ is the half-acceptance-angle.

$$C_{PTC} = \frac{\sin\phi}{\pi \sin\theta} \tag{2.1}$$

Parabolic systems are typically designed with half-rim angles close to 90° to maximize their concentration. Any further concentration is limited by the amount of angular error which can be tolerated before a significant amount of concentrated solar flux is de-focused. Although the solar half-disk angle is ~0.27°, the half-acceptance angle (θ) of systems is enlarged in practice to the range of 0.6° - 0.8° to allow for tracking error, mirror surface inaccuracies, and relaxation of manufacturing tolerances (Fernandez-Garcia 2010). The half-acceptance angle, for example, of the widely adopted LS3 system is 0.68° (Gee et al. 2010) and 0.8° for the SkyTrough collector (Adrian Farr and Randy Gee, 2009). For a typical (single-stage) system the effective concentration is somewhere in the range of 20-30X for a half-acceptance angle of θ = 0.6° - 0.8°.

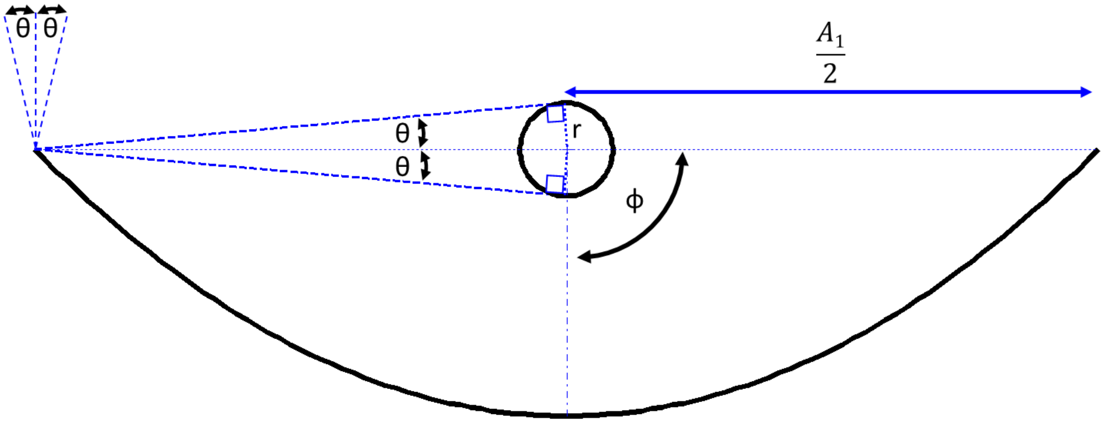

Figure 2.1 – *Geometry of a typical parabolic trough and cylindrical absorber.*

The thermodynamic limit to concentration for a 2D system with a faraway source, however, tells us that it should be possible to increase the geometric concentration ratio of typical parabolic trough systems by a factor of π.

2.1.2 Two-Stage

One option for increasing the concentration ratio is to use of a secondary concentrator. A number of secondary designs for pairing with primary parabolic troughs have been developed and are reported in the literature review in Appendix A1. For this exercise we will assume the secondary is an ideal CPC concentrator.

The concentration ratio of a first stage (C_1) parabolic trough concentrating to a horizontal secondary aperture is defined geometrically (Figure 2.2) by equation 2.2, where $A_1$and A_2 are the primary and secondary aperture areas in m^2 and r is the rim radius in meters.

$$C_1 = \frac{A_1}{A_2} = \frac{2r \sin\phi \cos\phi}{2r\theta} = \frac{\sin\phi \cos\phi}{\theta} \tag{2.2}$$

Since the secondary is an ideal concentrator, the concentration ratio of the second stage (C_2) is given by equation 2.3 where the half-acceptance angle of the CPC is the half-rim angle of the primary.

$$C_2 = \frac{A_2}{A_3} = \frac{1}{\sin\phi} \tag{2.3}$$

The concentration ratio of the entire optical system (C_{total}) is the ratio of the primary aperture to the absorber area, and equivalent to the multiplication of the each stage's concentration ratio (Equation 2.4).

$$C_{total} = \frac{A_1}{A_3} = C_1 C_2 = \frac{\cos\phi}{\theta} \tag{2.4}$$

From equation 2.4 we can see the combined concentration ratio maximizes for small half-rim (ϕ) and half-acceptance (θ) angles. In practice, small half-rim angle configurations have very long focal lengths and anything larger than ϕ=45° are likely not practical. Assuming a half acceptance angle θ = ±0.8°, similar to commercial PTCs, a two-stage trough-CPC collector can reach 50X solar concentration or about double a typical trough.

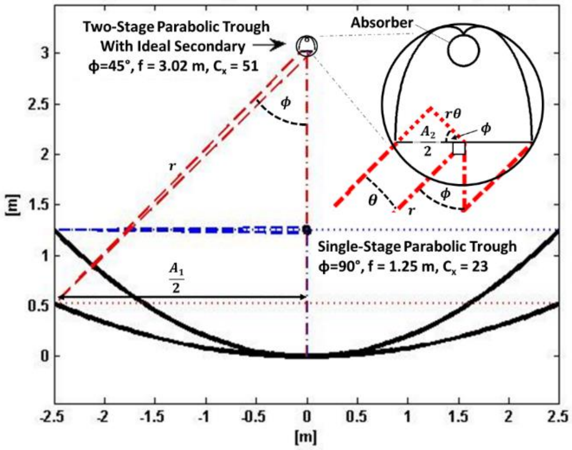

Figure 2.2 - *Geometries of a typical (blue) and two-stage (red) parabolic trough for ($\theta = \pm 0.8°$ and $A_1 = 5\ m$)*

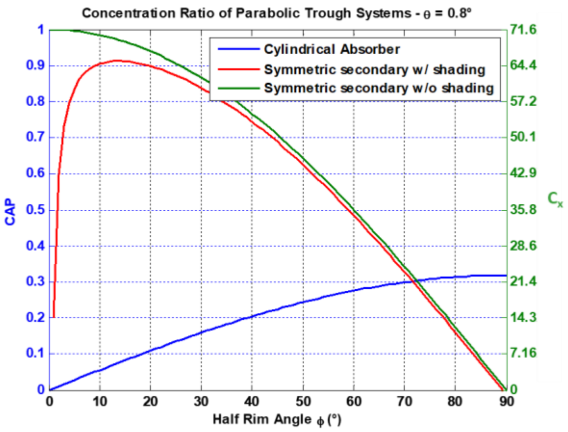

Figure 2.3 – *Limits to solar concentration in single (blue) and two-stage (red) parabolic troughs.*

The dimensions of a single and two-stage system are drawn to scale in Figure 2.2 and the theoretical limits to concentration for single and two-stage systems (Equations 2.1 & 2.4) are plotted in Figure 2.3. The concentration acceptance product (CAP) is the ratio of a system's concentration ratio relative to the maximum.

$$CAP = \frac{C}{C_{max}} = C \sin\theta \tag{2.5}$$

2.2 Modelling Approach

A schematic of the variables involved in the modelling approach is presented in Figure 2.4 and the model flow diagram is presented in Figure 2.5. The power at each interface (Q_{A1}, Q_{A2}, …) is calculated in watts based on optical, spectrum splitting, photovoltaic conversion, and thermal losses. The solar cells are modelled under partial spectral illumination to estimate net AC power production from the cell subsystem. The thermal stream is also modelled under partial illumination to estimate the net AC generation from the thermal subsystem. These two are combined for a net solar-to-electric efficiency of the system.

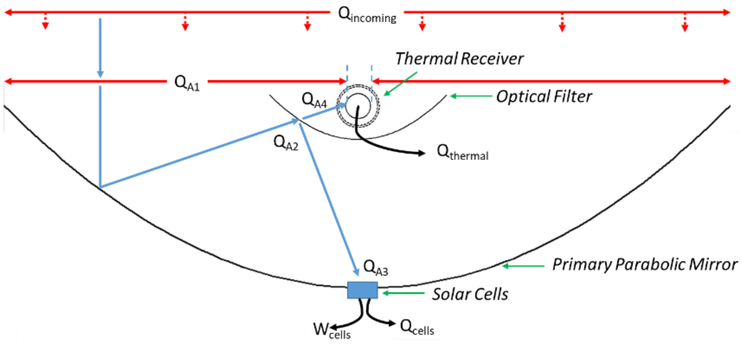

Figure 2.4 – *Model Diagram*

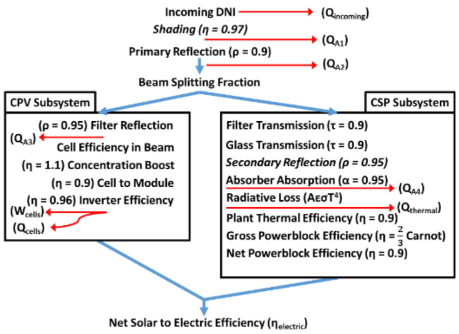

Figure 2.5 – *Model flow diagram*

2.1.1 Primary Optics and Spectrum Splitting

The incoming power to the system ($Q_{incoming}$) is calculated based on the ASTM G173-03 Direct reference spectrum (G_{direct}) and the unshaded aperture area of the collector ($A_{aperture}$) which is selected to be 5 m^2 (5 m wide x 1 m long).

$$Q_{incoming} = A_{aperture} G_{direct} \tag{2.6}$$

A_2 is calculated based on the concentration ratio and the primary aperture area. For a single stage system A_2 is the absorber area, and for a two stage system A_2 is the aperture area of the secondary concentrator.

$$\begin{aligned} A_2 &= A_{aperture}/C_{PTC} \text{ for a typical single stage system} \\ A_2 &= \frac{A_{aperture}\sin\theta}{\sin\phi\cos\phi} \text{ for a two-stage system} \end{aligned} \tag{2.7}$$

The fraction of unshaded incoming radiation ($f_{shading}$) is calculated based on A_2.

$$\begin{aligned} f_{shading} &= \frac{A_{aperture} - \frac{A_2}{\pi}}{A_{aperture}} \text{ for a single stage system with cylindrical absorber} \\ f_{shading} &= \frac{A_{aperture} - A_2}{A_{aperture}} \text{ for a two-stage system with secondary aperture } A_2 \end{aligned} \tag{2.8}$$

The total radiant power striking the parabolic mirror (Q_{A1}) is calculated from the shading factor.

$$Q_{A1} = Q_{incoming} f_{shading} \tag{2.9}$$

For these simulations, the optical filter is assumed to lie between the parabolic mirror and the thermal receiver, but does not provide any shading of the trough. The amount of power incident on the optical filter (Q_{A2}) is based on the reflectivity of the primary mirror ($\rho_{primary}$).

$$Q_{A2} = Q_{A1} \rho_{primary} \tag{2.10}$$

At this point the spectrum is split into a spectral window bound by an upper (λ_2) and lower (λ_1) cutoff wavelength. The fraction of incident power within the spectral window (f_{window}) is calculated as follows

$$f_{window} = \frac{\int_{\lambda_1}^{\lambda_2} G_{direct}(\lambda)}{\int G_{direct}(\lambda)} \tag{2.11}$$

2.1.1 CPV Subsystem

The amount of power incident on the solar cells (Q_{A3}) is the fraction of the spectrum within the window multiplied by the reflectivity of the optical filter (ρ_{filter}) within the window.

$$Q_{A3} = Q_{A2} f_{window} \rho_{filter} \tag{2.12}$$

To quantify the performance of a cell under partial illumination, the short circuit current density $J_{sc}(\lambda)$ generated by a solar cell at each wavelength is determined from the external quantum efficiency (EQE) of the cell.

$$J_{sc}(\lambda) = q \frac{\lambda}{hc} EQE(\lambda) \tag{2.13}$$

The spectral efficiency of the cell ($\eta_{cell}(\lambda)$) is determined by multiplying the short circuit current with the open circuit voltage (V_{OC}) and fill factor (FF) of the cell.

$$\eta_{cell}(\lambda) = J_{sc}(\lambda)\, V_{oc}\, FF \tag{2.14}$$

The efficiency of the solar cell inside the spectral window ($\eta_{cell,window}$) is determined by integration.

$$\eta_{cell,window} = \frac{\int_{\lambda_1}^{\lambda_2} \eta_{cell}(\lambda) G_{direct}(\lambda)}{\int_{\lambda_1}^{\lambda_2} G_{direct}(\lambda)} \tag{2.15}$$

Power output from the cells (W_{cells}) is calculated from the cell efficiency within the spectral window, adjusted for operating temperature (T_{cell}) using the temperature coefficient (β) and the reference cell temperature where the EQEs were taken (T_{ref}), cell to module efficiency (η_{module}), inverter efficiency ($\eta_{inverter}$), and efficiency gain from concentration (η_{Cx}).

$$W_{cells} = Q_{A3}\eta_{cell,window}(1 - \beta(T_{cell} - T_{ref}))\eta_{Cx}\eta_{cell-to-module}\eta_{inverter} \tag{2.16}$$

All of the incident power that is not converted into electricity is assumed to be converted into heat in the term Q_{cells}.

$$Q_{cells} = Q_{A3} - W_{cells} \tag{2.17}$$

2.1.2 CSP Subsystem

The amount of power absorbed by the thermal absorber (Q_{A4}) is calculated according to the optical filter and glass envelope transmittance (τ_{filter},τ_{glass}) and absorptance of the selective coating on the absorber ($\alpha_{absorber}$). Single stage systems capture non-concentrated light which is incident on the absorber from above, whereas two-stage systems lose this portion of light due to shading from the secondary reflector and incur an additional reflection loss ($\rho_{secondary}$).

$$Q_{A4} = (Q_{A2}(1 - f_{window})\tau_{filter} + Q_{incoming}(1 - f_{shading}))\tau_{glass}\alpha_{absorber}$$

for a single stage system or

$$Q_{A4} = Q_{A2}(1 - f_{window})\tau_{filter}\tau_{glass}\rho_{secondary}\alpha_{absorber} \tag{2.18}$$

for a two stage system,

Net thermal generation ($Q_{thermal}$) is determined by subtracting the radiative loss (since the thermal absorber is assumed to be encased in an evacuated glass tube).

$$Q_{thermal} = Q_{A4} - A_{abs}\varepsilon\sigma T_{abs}^4 \tag{2.19}$$

2.1.4 Combined Performance

Thermal and system cell efficiencies ($\eta_{thermal}$,$\eta_{system,cells}$) are calculated according to the total unshaded incoming light,

$$\eta_{thermal} = \frac{Q_{thermal}}{Q_{incoming}} \tag{2.20}$$

$$\eta_{system,cells} = \frac{W_{cells}}{Q_{incoming}} \tag{2.21}$$

When analyzing hybrid systems we must select a metric to evaluate the combined electric and thermal generation. Cogeneration efficiency has been used in the past, but does not take into account the different qualities of the electric and thermal energies produced. Since the Carnot efficiency limit applies to the conversion of heat into useful work (or electricity), solar-to-exergy efficiencies have been proposed as a more practical measure of hybrid solar systems, especially for the purpose of power generation (Branz et al. 2015). Exergy, defined as $Q(1-T_C/T_H)$, is the thermodynamic limit to the amount of useful work that can be extracted from a quantity of heat Q at a temperature T_H. The energy and exergy content of electricity are identical since there is no limit to the amount of electricity which can be converted into useful work. In this way, the solar-to-exergy efficiency calculated in equation 2.22 is the maximum possible efficiency of the hybrid system at converting the incoming solar energy into useful work. For these calculations the cold reservoir temperature of the Carnot cycle T_C is assumed to be 37 °C and T_H is the operating temperature of the thermal subsystem.

$$\eta_{exergy} = \frac{W_{system,cells}+Q_{thermal}(1-T_C/T_H)}{Q_{solar}} = \eta_{system,cells} + \eta_{Carnot}\cdot\eta_{thermal} \tag{2.22}$$

In practice, inverter losses will reduce the CPV subsystem electric output during DC-to-AC conversion, and additional plant, power block, and generator losses will reduce conversion of the CSP subsystem into electricity. To account for these, a more realistic solar-to-electric efficiency of the system ($\eta_{electric}$) is calculated with equation 2.23. A 2/3 term is included since actual power block turbines typically reach only ~66% of the Carnot efficiency. Two additional losses are considered to account for plant thermal, storage, and heat exchange losses (η_{HX} = 0.9), and for parasitic losses ($\eta_{PB,net}$ = 0.9).

$$\eta_{electric} = \eta_{system,cells} + \frac{2}{3}\eta_{Carnot}\eta_{thermal}\eta_{HX}\eta_{PB,net} \tag{2.23}$$

This net solar-to-electric efficiency is the metric by which the solar windows are optimized. The thermal fraction ($f_{thermal}$) is the fraction of solar-to-electric conversion efficiency contributed by the thermal subsystem.

$$f_{thermal} = \frac{\eta_{electric}-\eta_{system,cells}}{\eta_{electric}} \tag{2.24}$$

2.1.5 Parameters, Constants, and Optimization

The constants used in the model are listed in Table 2.1. The secondary reflector is assumed to be inside the evacuated tube envelope, and since it is protected from the elements a reflectivity ($\rho_{secondary}$) of 95% is assumed. The emissivity of the selective coating in Table 2.1 is estimated as a function of temperature from commercially available selective coatings reported by Selvakumar & Barshilia (2012).

A_1	5 m^2	$\rho_{primary}$	0.9
θ	0.8°	$\rho_{secondary}$	0.95
T_c	37 °C	τ_{glass}	0.9
T_{cells}	40 °C	$\alpha_{absorber}$	0.95
T_{ref}	25 °C	ε	$2e^{-7}(T_{abs}^2)+5e^{-5}T_{abs}+0.05$
$\eta_{cell-to-module}$	0.90	η_{HX}	0.9
$\eta_{inverter}$	0.96	$\eta_{PB,net}$	0.9
η_{Cx}	1.10		

Table 2.1 - *Constants*

In addition to the $\frac{2}{3}\eta_{Carnot}$ generic power block used in this model, Steam-Rankine and CO_2 recombination Brayton power cycles are simulated according to the relationships determined by Dunham

& Iverson (2014) and are displayed for reference in the resulting efficiency graphs as $\eta_{Rankine}, \eta_{Brayton}$. All power block cycles are assumed to be wet cooled with a cold reservoir temperature of 37 °C.

Spectral conversion efficiencies calculated from Eq. 2.14 are presented for each cell in Fig 2.6 after being adjusted to the modelling assumptions from Figure 2.5. Also shown are the rough percentages of solar power at post-bandgap wavelengths for each cell, and the conversion efficiency for a PTC CSP system operating at different temperatures (assuming an overall optical and thermal efficiency of 70% and adjusted according to the modelling assumptions from Figure 2.5).

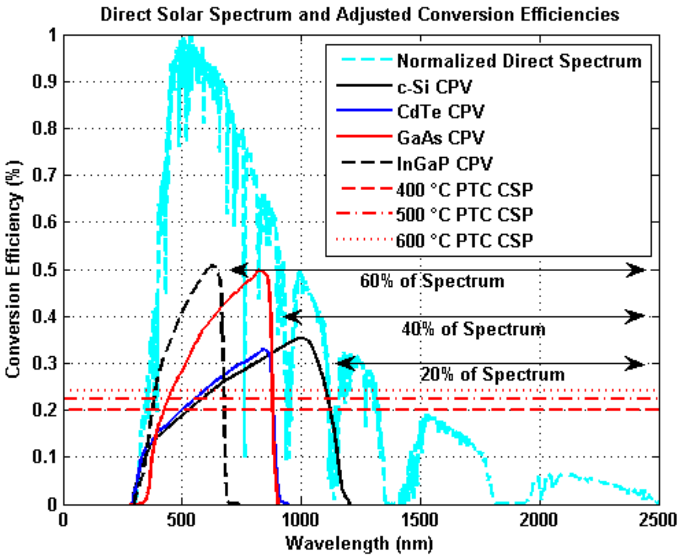

Figure 2.6 – *Normalized direct solar spectrum (teal). Spectral efficiencies for each cell are plotted after being adjusted according to the modelling assumptions. Also plotted are the conversion efficiencies of a pure CSP system operating at different temperatures under the current model assumptions. The greater conversion efficiency of the solar cells within certain spectral windows highlights the potential of beam splitting systems.*

Optimization is performed by running the simulation multiple times and adjusting the upper and lower spectral window boundaries. These are initially set to be the upper and lower limits of the solar cell spectral response (i.e. full cell response). The program is iterated while slowly squeezing the limits (first the lower limit, then the upper limit) until a maximum is reached. The spectral windows are optimized for both solar to exergy efficiency and solar to electric efficiency.

2.3 Simulation Results

2.2.1 Pure CSP Troughs

For pure CSP troughs, the fraction of power in the spectral window (f_{window}) is set to 0 and the transmission of the optical filter (τ_{filter}) set to 1. The performance results for a typical 90° half rim angle PTC are shown in Figure 2.4a, and for a two-stage 45° half rim angle PTC with an ideal secondary in Figure 2.4b. Also plotted are the optical efficiency, thermal efficiency, exergy efficiency, and electric efficiency of the system as well as the solar to electric efficiencies using the estimated Rankine and Brayton cycles.

An optical efficiency (η_o) of 77% is consistent with optical efficiencies reported elsewhere for typical parabolic trough collectors (Fernández-García et al. 2010, Price et al. 2002, Blair et al. 2014). The performance with temperature is slightly conservative (~53% @ 600 °C here compared to 57% @ 600 °C in the state of the art – Mason and Reitze 2014). The system reaches a maximum solar-to-exergy efficiency of 39% and solar-to-electric efficiency of 21% at 455 °C. Electric efficiencies near 20% are consistent with instantaneous solar-to-electric conversion efficiencies of typical parabolic trough plants operating at 390 °C.

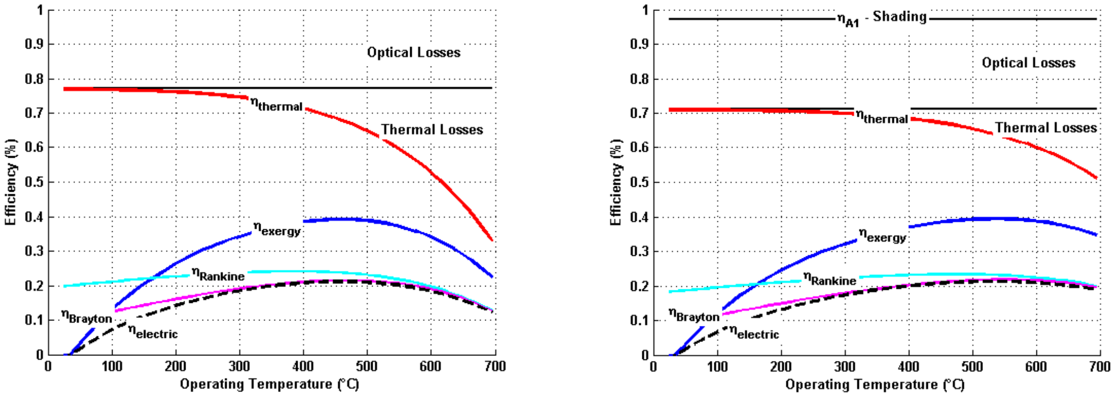

a) b)

Figure 2.7 – *Non-spectrum splitting troughs. Single (a) and Two-Stage (b).*

For the two-stage system, a half-rim angle of 45° enables secondary concentration while maintaining practical focal lengths. The two-stage system reaches a maximum exergy efficiency of 39% and solar-to-electric efficiency of 21% at 535 °C.

2.2.2 Ideal Optical Filters

The spectral window in each system is optimized for maximum overall electric efficiency ($\eta_{electric}$). Results for the ideal optical filter configuration (τ_{filter}, ρ_{filter} = 1) are presented in Table 2.2. These are the maximum achievable solar-to-electric efficiencies for a SBS PTC system under the current model assumptions with no optical loss introduced by the beam splitter. The optimized spectral window and overall conversion efficiencies are presented in Figure 2.8 for the c-Si case. The text in Figure 2.8(a) describes the fraction of the spectrum within the spectral window and compares the efficiency of the champion silicon cell under the full direct spectrum to the efficiency in the window.

Single Stage ($C_x = 23$)			
	λ_{window} (f_{window})	$\eta_{electric}$ (T)	$f_{thermal}$
CSP	(100%)	0.21 (455 °C)	1
c-Si	541-1117 nm (57%)	0.25 (375 °C)	0.33
CdTe	517-879 nm (46%)	0.24 (405 °C)	0.45
GaAs	431-877 nm (58%)	0.31 (375 °C)	0.26
InGaP	380-674 nm (39%)	0.29 (415 °C)	0.41

Table 2.2 - *Ideal optical filter* (τ_{filter}, ρ_{filter} = 1)

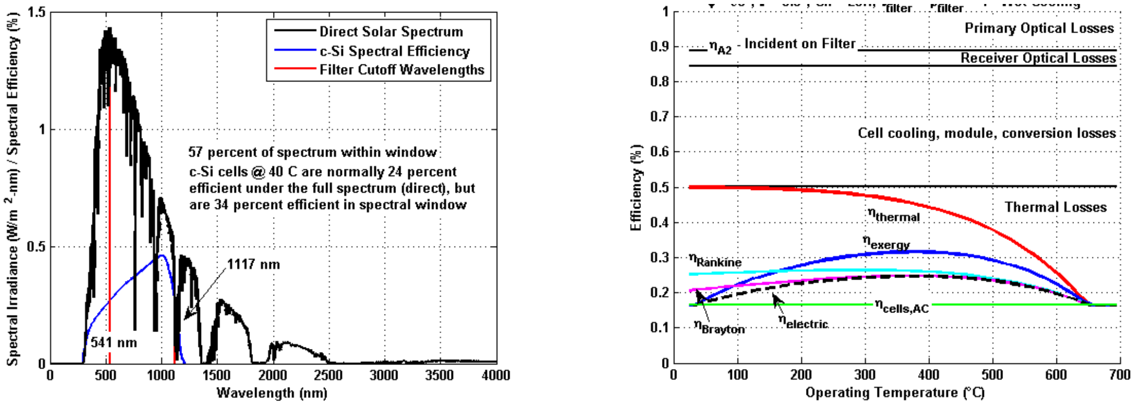

a) *Maximized spectral window (red)*

b) *A maximum conversion efficiency ($\eta_{electric}$) of 25% is reached at 375 °C.*

Figure 2.8 – *SBS by an ideal (lossless) optical filter in a single stage PTC.*

2.2.3 Typical Interference Filters

To better simulate typical interference filters (dichroic mirrors), a spectrally selective transmission τ_{filter} = 0.9 and reflection ρ_{filter} = 0.95 were used. These values are typical of interference filters reported in the literature. The performance of the c-Si SBS system is presented in Figure 2.9 and the results for all cell types are presented in Table 2.3.

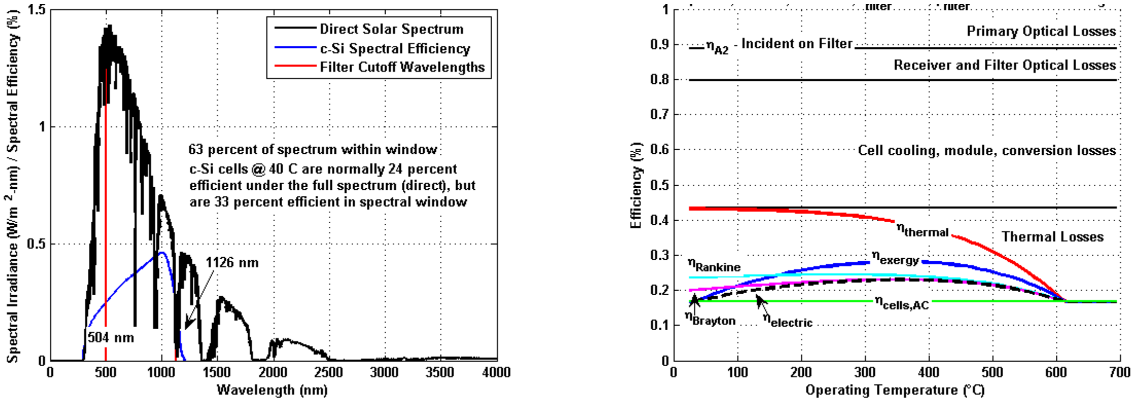

a) *Maximized spectral window (red)*

b) *A maximum conversion efficiency ($\eta_{electric}$) of 23% is reached at 355 °C.*

Figure 2.9 – *SBS by a typical interference filter in a single-stage system.*

The optimized spectral window and efficiencies for the two-stage c-Si SBS system are plotted in Figure 2.10.

	Single Stage ($C_x = 23$)			**Two Stage** ($C_x = 51$)		
	λ_{window} (f_{window})	η_{electric} (T)	f_{thermal}	λ_{window} (f_{window})	η_{electric} (T)	f_{thermal}
CSP	(100%)	0.21 (455 °C)	1	(100%)	0.21 (535 °C)	1
c-Si	504-1126 nm (63%)	0.23 (355 °C)	0.27	527-1122 nm (60%)	0.23 (425 °C)	0.30
CdTe	486-881 nm (51%)	0.22 (385 °C)	0.39	496-880 nm (49%)	0.22 (455 °C)	0.41
GaAs	420-878 nm (59%)	0.29 (365 °C)	0.24	420-877 nm (59%)	0.29 (435 °C)	0.24
InGaP	375-674 nm (40%)	0.27 (405 °C)	0.39	375-674 nm (40%)	0.27 (475 °C)	0.42

Table 2.3 – *Performance with a typical interference filter (τ_{filter} = 0.9, ρ_{filter} = 0.95)*

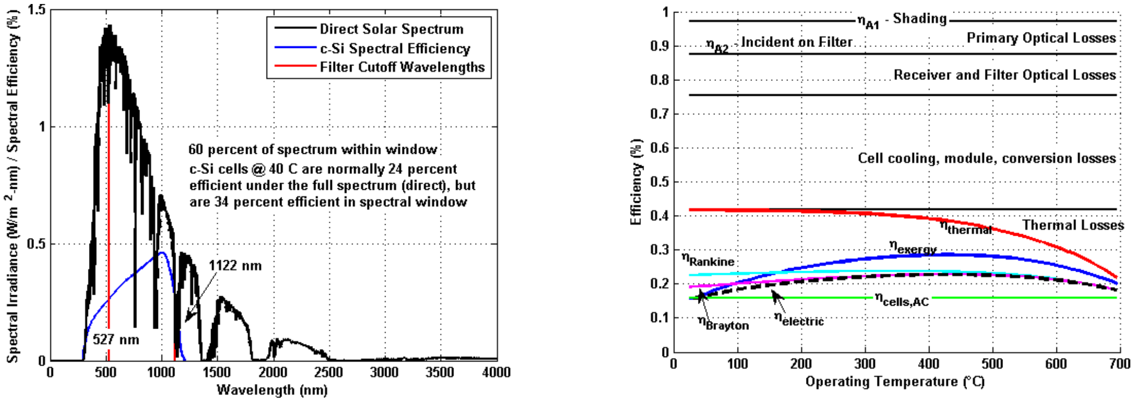

a) Maximized spectral window (red)

b) A maximum conversion efficiency ($\eta_{electric}$) of 23% is reached at 425 °C.

Figure 2.10 – *SBS by a typical interference filter in a two-stage system*

2.2.4 Integrated Solar Cell Filters

A PV semiconductor material is transparent to low energy photons and absorptive of sub-bandgap photons. This allows the material to act as a semi-transparent/reflective optical interface (Figure 2.11). In these configurations, the solar cell acts as the optical filter and any additional losses associated with the optical filter are eliminated.

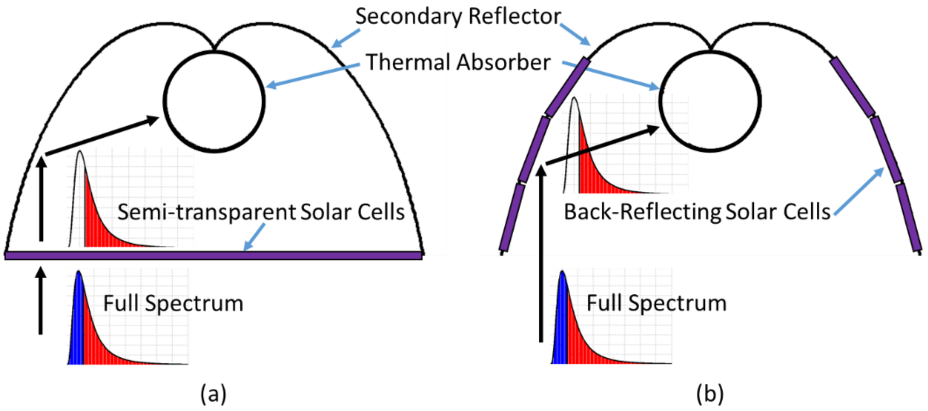

Figure 2.11 – *Spectral beam splitting by solar cells (purple) in semi-transparent (a) and back-reflecting (b) configurations as part of a secondary concentrator. These method split the solar spectrum at the semiconductor bandgap wavelength. High energy photons are absorbed and low energy photons are either (a) transmitted into the secondary concentrator or (b) reflected towards the thermal absorber.*

Although a semiconductor material is theoretically 100% transparent to low energy photons, this is not the case for real PV modules since cells are mounted on substrates, covered in grid-contacts, and encapsulated. Out-of-band transmission in a semi-transparent triple junction cell was reported to be 87% after ignoring grid contact shading losses (Ji et al. 2015) and out-of-band reflectance of a bare GaAs cell was measured to be 92%, (probably closer to 83% with encapsulent losses). These properties are used to simulate performance for a two-stage system with semi-transparent or back-reflecting solar cells (GaAs, InGaP). Typical c-Si and CdTe cells maintain high absorption at post-bandgap wavelengths (Sun et al. 2017) making them unusable as spectrum splitting devices in their current production forms and as a result are not included in the following simulations.

In the first scenario, semi-transparent solar cells are assumed to cover the entrance aperture of the secondary concentrator. All of the light striking the secondary aperture is incident on the cells, with 87% of out-of-band light transmitted. Simulation results for the transmitting two-stage SBS system using GaAs cells are shown in Figure 2.12.

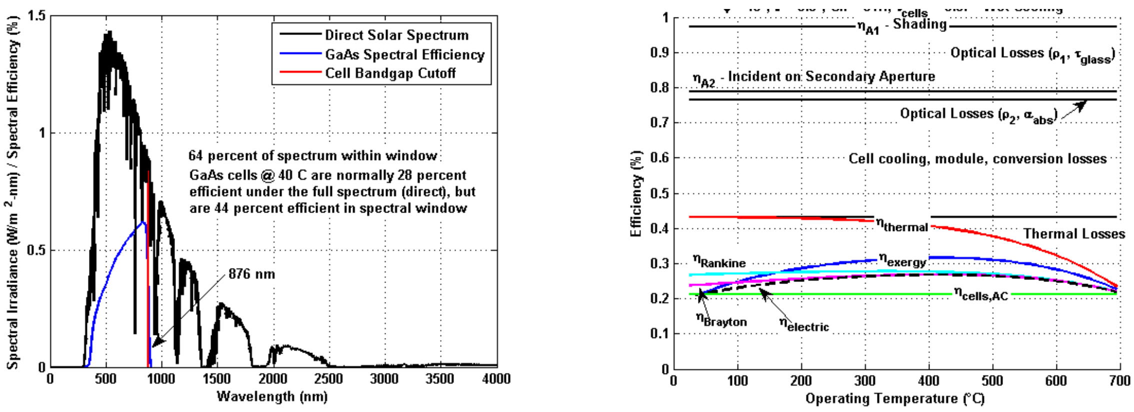

a) Cell spectral window (red)

b) A maximum conversion efficiency ($\eta_{electric}$) of 27% is reached at 415 °C.

Figure 2.12 – *SBS by semi-transparent GaAs cells in a two-stage PTC*

In the second scenario, back-reflecting solar cells are assumed to make up a portion of the secondary reflector. Since some of the light will directly strike the absorber, only 50% of the light incident on the secondary aperture is assumed to strike the solar cells. The back-reflecting solar cells are 83% reflective for sub-bandgap light and results for a two-stage back-reflecting InGaP SBS system are shown in Figure 2.13. The InGaP semiconductor bandgap of 672 nm (red) absorbs 41% of the solar resource and converts it according to its spectral efficiency (blue). The remaining 59% of solar power is redirected to the thermal subsystem. Simulated results for each configuration are presented in Table 2.4.

	Transparent Solar Cells ($\tau_{cells,sub\_bandgap} = 0.87$)			**Back-Reflecting Solar Cells** ($\rho_{cells,sub\_bandgap} = 0.83$)		
	λ_{window} (f_{window})	$\eta_{electric}$ (T)	$f_{thermal}$	λ_{window} (f_{window})	$\eta_{electric}$ (T)	$f_{thermal}$
CSP	(100%)	0.21 (535 °C)	1	(100%)	0.21 (535 °C)	1
GaAs	876 nm (64%)	0.27 (415 °C)	0.21	876 nm (64%)	0.24 (485 °C)	0.56
InGaP	672 nm (41%)	0.25 (465 °C)	0.39	672 nm (41%)	0.23 (505 °C)	0.67

Table 2.4 – *Solar cells as integrated beam splitters in two-stage PTCs ($C_x = 51$)*

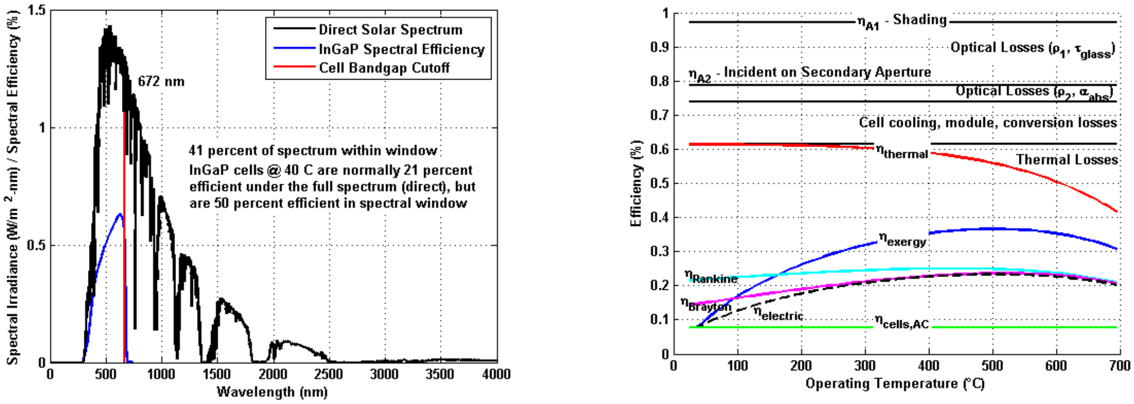

a) Cell spectral efficiency

b) A maximum conversion efficiency of $\eta_{electric}$ = 23% is reached at 505 °C.

Figure 2.13 – SBS by back-reflecting InGaP cells in a two-stage PTC

2.4 Discussion

Regardless of configuration, SBS systems show improvement over non-SBS systems. It was initially believed that integration of the solar cell into the beam splitting device would improve efficiencies by reducing optical losses associated with the added interference filter, but it turns out that reflection / transmission of out of band light can be worse in a solar cell than in an interference filter. Furthermore, band-pass configurations which are enabled by interference filters allow poorly utilized UV photons to be directed to the thermal stream, whereas single-pass configurations where the spectrum is split by a solar cell bandgap are stuck converting these poorly utilized (high energy) photons mostly into waste heat.

The spectral windows directed to each cell remained fairly independent regardless of system configuration (single and two-stage, ideal and typical filter, and even between interference filter and solar cell beam splitting methods). This is especially true for systems using high efficiency III-V cells and indicates standardized filters could be manufactured for pairing with each solar cell. When optimized for solar to exergy efficiency, all spectral windows revert to 0, favoring a pure CSP system.

The baseline PTC CSP system operates with ~20% solar to electric efficiency under full spectrum illumination. This decreases linearly under partial illumination as shown in Figure 2.14(a). As a result, partial illumination has the effect of reducing the effective operating temperature of the CSP subsystem. While two-stage systems incur additional losses over single stage systems due to partial shading and an additional secondary reflection loss, these losses are compensated for by a reduction in radiation loss which extends their operation into higher temperatures (see Figure 2.7). The improved conversion efficiency of power blocks at higher temperatures results in equivalent conversion efficiencies between single and two-stage systems (both non-SBS and SBS systems). Although there is no performance gain, the operation of two-stage systems at elevated temperatures has important implications. High temperatures enable the use of thermal energy storage systems (TES) which require temperature gradients to transfer heat into the power block HTF. Additionally high temperatures allow the power block to be switched from a baseload Rankine turbine to a peaker Brayton turbine, which can quickly ramp up and allow stored thermal energy to be quickly dispatched as electricity on demand.

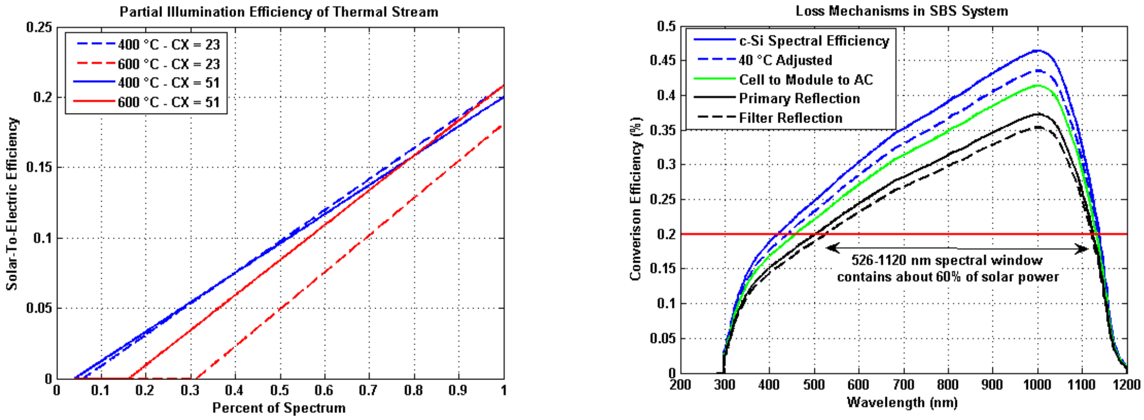

a) *CSP Subsystem. Partial illumination of the CSP subsystem with a single (dash) and two-stage (solid) systems at 400 °C (blue) and 600 °C (red). At 400 °C the benefits of secondary concentration are essentially nonexistent, but at 600 °C improve conversion efficiency by several percent regardless of illumination.*

b) *CPV Subsystem.*
The raw spectral efficiency (blue), adjusted for 40 °C operation (dash blue), adjusted for module and inverter efficiencies (green), and accounting for primary (black) and interference filter (dashed black) reflection losses. The result is approximately 80% of the raw spectral efficiency.

Figure 2.14 – *Subsystem conversion*

The conversion efficiency of a c-Si solar cell in the beam splitting systems modelled here is roughly 80% of its spectral efficiency due to the various losses shown in Figure 2.14(b). A crystalline silicon cell is approximately 34% efficient in the spectral window from 526-1120 nm. Adjusting this by 80% for system losses and multiplying by the fraction of the spectrum within the spectral window (60%) results in a 16% solar-to-electric efficiency of the CPV subsystem. The solar-to-electric efficiency of the CSP subsystem under partial illumination (40%) and multiplied by a filter transmission of 90% yields about 7%. The combined solar-to-electric conversion efficiency is therefore approximately 23%, similar to that reported in Table 2.3 for a c-Si SBS system of nearly the same spectral window.

While all SBS systems modelled in this paper reach greater overall efficiencies than a PTC CSP system, it is perhaps more interesting to compare them to their champion *module* efficiencies as listed in Table 2.5. The module efficiencies are corrected for 40 °C operation and the SBS simulation results are multiplied by 0.9 to account for the global solar resource.

Solar Cell	Best PV Module Efficiency under Global Spectrum *	Best modelled SBS Efficiency under Global Spectrum**	Efficiency Change
c-Si	22%	21%	-1%
CdTe	18%	20%	+2%
GaAs	23%	26%	+3%
InGaP	19%	24%	+5%

Table 2.5 – *Comparison w/ PV Modules*

*Adjusted to 40 °C and multiplied by a 0.96 inverter efficiency.

**Efficiencies modelled in this paper multiplied by 0.9 to compare against module efficiencies under global spectrum.

Here the combined performance of a SBS PTC system using c-Si cells actually underperforms a flat plate c-Si module, due to the reduced available solar irradiance under the direct spectrum and the additional optical losses introduced by the SBS system. In a broader sense the poor performance of the c-Si SBS system can be attributed to the wide-band nature and the low conversion efficiency of c-Si cell which tends to make it more applicable for full-sun applications. CdTe has a similarly low conversion efficiency but demonstrates gains when paired with a SBS PTC system due to a narrower spectral response band since a greater percentage of the spectrum can be directed toward thermal stream. GaAs has a similar spectral response band but much higher overall conversion efficiency, resulting in the greatest net conversion efficiency of the SBS systems modelled. InGaP has both a small spectral response band and high conversion efficiency, allowing efficient utilization of the spectrum by the cell while also sending a generous portion of the spectrum towards the thermal stream. As such the InGaP SBS-PTC system sees the greatest efficiency gain over its standalone PV module. Since the additional fraction of the spectrum sent to the thermal stream is converted with lower efficiency than by a GaAs cell, the overall efficiency is still lower efficiency than the GaAs SBS system.

2.5 Economics

To estimate the economics of a SBS system, individual component costs were pulled from the parabolic trough and photovoltaic performance models in NREL's System Advisor Model (SAM). For this exercise we chose to estimate the cost of a SBS single-stage PTC plant using interference filters and c-Si cells.

Such a plant would have the same costs as a typical state-of-the-art PTC CSP plant using molten salt HTF and storage, but with power block and thermal storage capacities reduced according to thermal fraction. The additional cost of the interference filter is estimated to be \$20/m^2 and to take up 20% of the solar field aperture area.

The costs associated with the PV module are reduced under concentration (assuming 30X). Inverter costs remain the same, but the balance of system, installation, and overhead for the CPV subsystem are overlapping costs and are considered zero since they are already paid for by the PTC field (solar field cost includes installation). Land purchase, environmental inspection, permitting are also overlapping with the PTC field and considered zero. A summary of the costs used for estimating the economics of a c-Si SBS single-stage PTC system are presented in Table 2.6 and Figure 2.15.

According to NREL's System Advisor Model (SAM 2017.1.17), a 100 MW PTC CSP plant with a solar multiplier of 2 and 6 hours of storage can be built today for \$5.72/W_{AC} (\$3.8/W_{exergy}) on a footprint of 890 acres. A c-Si SBS PTC system built over the same footprint with the same aperture area generates 130 MW of variable PV capacity and 24 MW of thermal capacity with 6 hours of storage and costs \$2.39/ W_{AC} (\$2.2/W_{exergy}). The reduced thermal fraction of the SBS system yields major cost reductions for the thermal storage and power block components, but results in only 1/4 of the dispatchable capacity of the pure CSP plant. Building the same capacity power plant with side by side PV and CSP (130 MW flat plate PV and 24 MW PTC CSP with 6 hours storage), however, is cheaper than a hybrid system and costs only \$2.33/ W_{AC} (\$2.15/W_{exergy}). If we assume the cost of the 24 MW CSP subsystem is the same as a for a standalone plant of the same capacity and the remaining cost of the oversized site, solar field, and HTF system, as well as the dichroic filter, modules under concentration, inverters, grid connection, and transmission is associated with the CPV subsystem, the added install cost of the CPV subsystem is \$1.77/W_{AC}, which is 4% higher than the install cost of flat plate PV.

	Item	Cost	Units	Qty	Units	Total Cost
CSP Subsystem	Site Improvements	$ 25.00	$/m^2	858768.00	m^2	$ 21,469,200.00
	Solar Field	$ 150.00	$/m^2	858768.00	m^2	$ 128,815,200.00
	HTF System	$ 60.00	$/m^2	858768.00	m^2	$ 51,526,080.00
	Molten Salt Storage – 6 hrs	$ 65.00	$/kW$_{th}$	520.54	MWh$_t$	$ 33,835,244.51
	Power Plant	$ 1,150.00	$/kW$_e$	26.36	MW$_e$ gross	$ 30,312,466.72
	BOP	$ 120.00	$/kW$_e$	26.36	MW$_e$ gross	$ 3,163,040.01
	Dichroic Filter	$ 20.00	$/m^2	171753.60	m^2	$ 3,435,072.00
					Subtotal	$ 272,556,303.24
				7%	Contingency	$ 19,078,941.23
					Total Direct CSP Cost	**$ 291,635,244.46**
	EPC and Owner Cost			0.11	of direct thermal cost	$ 32,079,876.89
	Total Land Cost	$ 10,000.00	$/acre	890.00	acres (3.6 km^2)	$ 8,900,000.00
	Sales Tax	5%	applies to	0.80	of direct thermal cost	$ 11,665,409.78
					Total Indirect CSP Cost	**$ 52,645,286.67**
CPV Subsystem	Modules under 30X concentration	0.02133333	$/W$_{DC}$	135.50	MW$_{DC}$	$ 2,890,613.09
	Inverter	0.1	$/W$_{DC}$	135.50	MW$_{DC}$	$ 13,549,748.85
	Balance of System Equipment	0	$/W$_{DC}$	135.50	MW$_{DC}$	$ -
	Installation	0	$/W$_{DC}$	135.50	MW$_{DC}$	$ -
	Installer Margin and Overhead	0	$/W$_{DC}$	135.50	MW$_{DC}$	$ -
					Total Direct CPV Cost	**$ 16,440,361.94**
	Permitting and Environmental	0	$/W$_{DC}$	135.50	MW$_{DC}$	$ -
	Engineering/Developer Overhead	0	$/W$_{DC}$	135.50	MW$_{DC}$	$ -
	Grid Interconnection	0.03	$/W$_{DC}$	135.50	MW$_{DC}$	$ 4,064,924.66
	LandPurchase	0	$/W$_{DC}$	135.50	MW$_{DC}$	$ -
	Land Prep & Transmission	0.02	$/W$_{DC}$	135.50	MW$_{DC}$	$ 2,709,949.77
	Sales Tax	5%	applies to	100%	of direct PV cost	$ 822,018.10
					Total Indirect CPV Cost	**$ 7,596,892.52**
					Total CSP Cost	**$ 344,280,531.13**
					Total CPV Cost	**$ 24,037,254.46**
					Total Hybrid SBS Cost	**$ 368,317,785.59**
					Total Cost ($/kW$_{e,AC}$)	**$ 2,394.78**

Table 2.6 – *Associated costs for a c-Si SBS PTC plant (130 MW$_{CPV}$ + 24 MW$_{CSP}$ w/ 6 hrs molten salt storage)*

The primary incentive of a hybrid system is to fully utilize the solar spectrum to achieve maximum economic value. This is most exemplified when the infrastructure between the PV and thermal subsystems can be shared without significantly inhibiting the performance of either. A reduction in one subsystem's efficiency as a result of beam splitting must be compensated by the added economic value of the other subsystem, otherwise a beam splitting system is not justifiable.

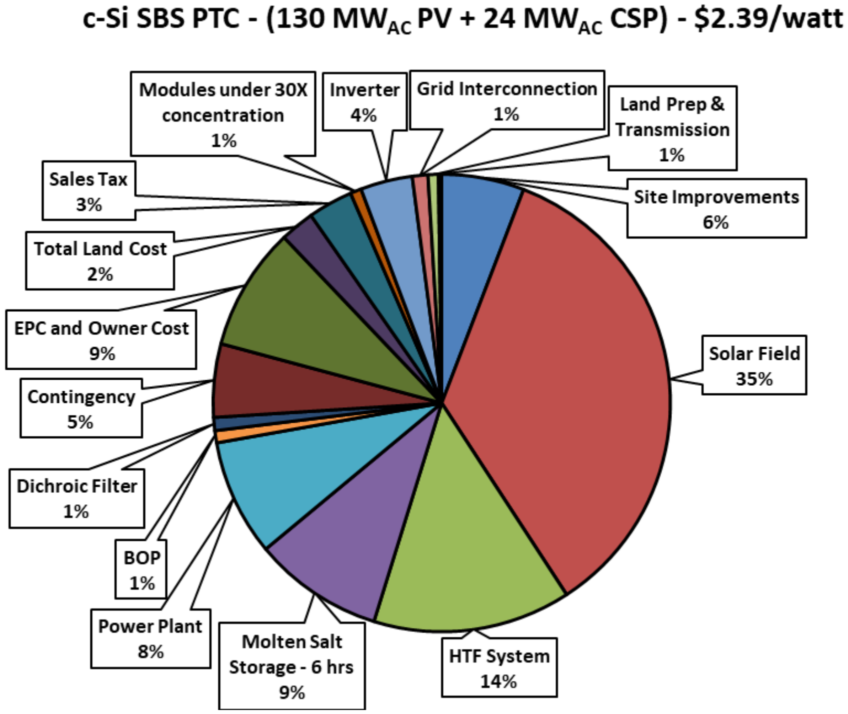

Figure 2.15 – *SBS PTC c-Si Plant Cost Breakdown (130 MW PV, 24 MW Thermal w/ 6 hrs of molten salt storage)*

In order to achieve this cost efficiency, the install cost of the SBS CPV subsystem must be effectively cheaper than the install cost of a flat plate PV module. The condition comparing the relative cost of the two systems is shown in equation 2.25. Here $Solar\ Field\ Cost$ is in \$/m^2, η_{CPV} is the efficiency of the CPV module, η_0 is the optical efficiency of the CPV subsystem, $\$_{CPV}$ is the cost of the CPV cell in \$/Watt, C is the concentration on the CPV cell, DNI is the Direct Normal Irradiance (~900 W/m^2), η_{Si} is the efficiency of a flat plate silicon PV module (~0.18), and $\$_{Si}$ is the module + installation cost of flat plate silicon (~\$0.80/Watt).

$$\frac{Solar\ Field\ Cost}{DNI * \eta_{CPV}\eta_0} + \frac{\$_{CPV}}{C} < \ \$_{Si} \tag{2.25}$$

An 18% efficient c-Si panel installed today for about \$0.80/watt (module + installation) or \$144/m^2, however, is already cheaper than the \$150/m^2 install cost of the PTC solar field. This means the CPV subsystem must have improved efficiency over flat plate c-Si to add economic value. Since CPV systems incur additional optical losses (η_0~0.85) and only accept direct beam radiation ($\frac{DNI}{GTI}$~0.9), a CPV subsystem using c-Si will not have an economic case until the solar field cost is reduced.

Looking instead at a 25% efficient GaAs cell, the efficiency of the CPV subsystem is enhanced over flat plate c-Si enough to overcome the current cost of the PTC solar field. If the cell costs are ignored, the system would install for slightly less than PV at roughly \$0.78/watt. Current cell prices (~\$13.6/W Woodhouse and Goodrich 2013), however, indicate higher concentration configurations are necessary to reduce the cost contribution of the cell.

2.6 Summary

In this chapter, several different beam splitting approaches (ideal, interference filter, and novel integrated semi-transparent / back-reflecting solar cell filters) with different solar cells (c-Si, CdTe, GaAs, InGaP) and parabolic trough configurations (single stage and novel two stage design) were simulated and optimized (spectrally and with temperature) for the purpose of power generation.

Ideal (lossless) optical filters improved the solar-to-electric conversion efficiency over standard PTC CSP plants by 25% when paired with c-Si and by 50% when paired with GaAs. Conversion efficiencies up to 31% are achieved by typical interference filter systems paired with GaAs.

An important result is the recovery of operating temperature in two-stage systems without a loss in conversion efficiency. The main purpose of a hybrid CPV/CSP system is to efficiently utilize the solar spectrum and by doing so produce dispatchable thermally-generated electricity at a lower cost than current CSP. Since higher temperature enable TES and gas turbines, both of which improve the dispatchability and hence the value of the CSP subsystem, methods for improving the concentration of trough systems should be investigated further.

An economic assessment using individual component costs from NREL’s SAM 2017 model indicates a hybrid c-Si SBS PTC plant with 130 MW variable PV generation and 24 MW thermal power with 6 hours of dispatchable storage can be installed today for \$2.39/W_e. This is still currently higher than the side-by-side cost of PV/CSP and indicates the economic case will be limited for systems using c-Si due to the cost of the PTC solar field. III-V cells are more ideal for pairing in SBS systems and are not limited in the same way c-Si systems are, but are instead limited by the solar cell cost.

While spectrum splitting systems do enhance the net solar-to-electric conversion of a hybrid CPV/CSP plant above both traditional PTC CSP and flat plate PV, further reductions to the PTC solar field, III-V cell cost, and improvements to solar cell efficiency are still required before hybrid CPV/CSP beam splitting plants become cost competitive with side-by-side flat plate PV-CSP.

In the next chapter, a novel spectrum splitting prototype collector (using back-reflecting solar cells) is modelled in more detail and developed into a prototype for testing.

3. Generation 1 Prototype Development & Testing

The contents of this chapter have been published in-part in the following journal articles:

Widyolar, B.K., Abdelhamid, M., Jiang, L., Winston, R., Yablonovitch, E., Scranton, G., Cygan, D., Abbasi, H. and Kozlov, A., 2017. Design, simulation and experimental characterization of a novel parabolic trough hybrid solar photovoltaic/thermal (PV/T) collector. *Renewable Energy*, 101, pp.1379-1389.

Abdelhamid, M., Widyolar, B.K., Jiang, L., Winston, R., Yablonovitch, E., Scranton, G., Cygan, D., Abbasi, H. and Kozlov, A., 2016. Novel double-stage high-concentrated solar hybrid photovoltaic/thermal (PV/T) collector with nonimaging optics and GaAs solar cells reflector. *Applied Energy*, 182, pp.68-79.

This chapter discusses the design, manufacturing, and performance testing of the first-generation novel two-stage (PTC / CPC) hybrid converter with integrated spectrum splitting GaAs solar cell mirrors. A nonimaging CPC secondary optic in the receiver is transformed into a spectrum-splitting device through the integration of back-reflecting GaAs solar cells. Their sharp band gap cutoff allows them to produce electricity from high energy photons while reflecting low energy photons to the thermal absorber. High concentration on the thermal absorber allows high temperature operation despite partial (spectrum splitting) illumination. The solar cells (GaAs) were originally designed to operate at 200 °C to add to the exergy production.

3.1 Collector Design

The main components of the two-stage collector are outlined in Figure 3.1.

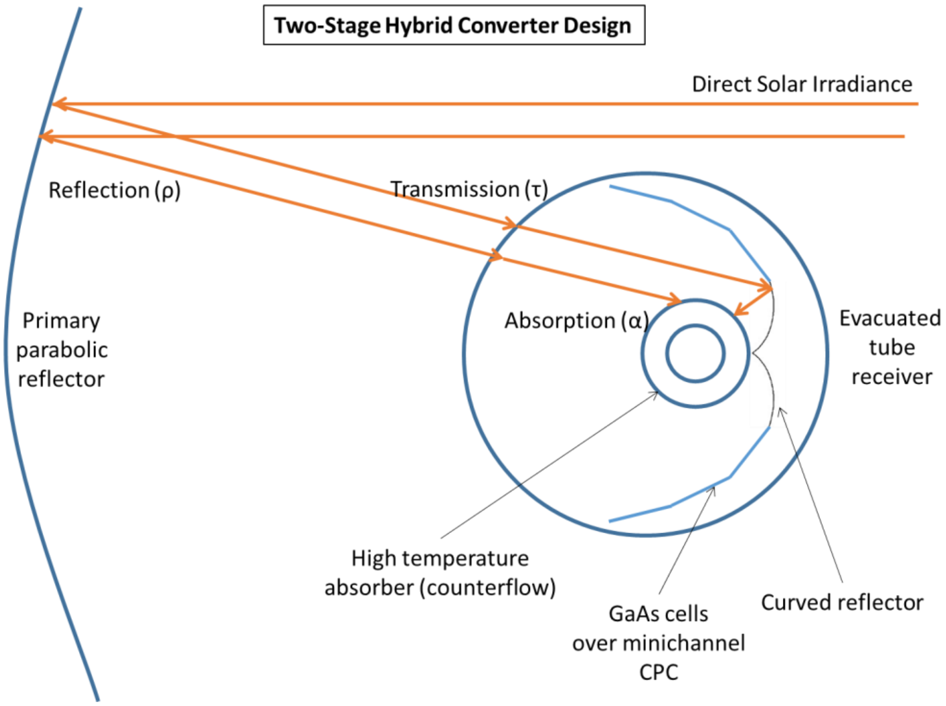

Figure 3.1 – *Two-stage hybrid collector design*

The receiver contains a CPC secondary which provides additional concentration on the thermal absorber. Aluminum minichannels approximate the “wings” of the CPC and serve as both the solar cell substrate and fluid channels to provide active cooling of the cells. Thin film GaAs cells are applied directly to the aluminum minichannels, and curved mirrors form the involute portion of the CPC where the minichannels are unable to effectively approximate the profile. A selectively coated absorber receives concentrated light from the primary and secondary and serves as the high temperature fluid channel. The entire receiver is encased in an outer glass tube to allow the inside to be evacuated for heat loss reduction.

3.1.1 Two-Stage Optical Design

The optics of a two-stage design incorporating a parabolic primary are outlined in Figure 3.2.

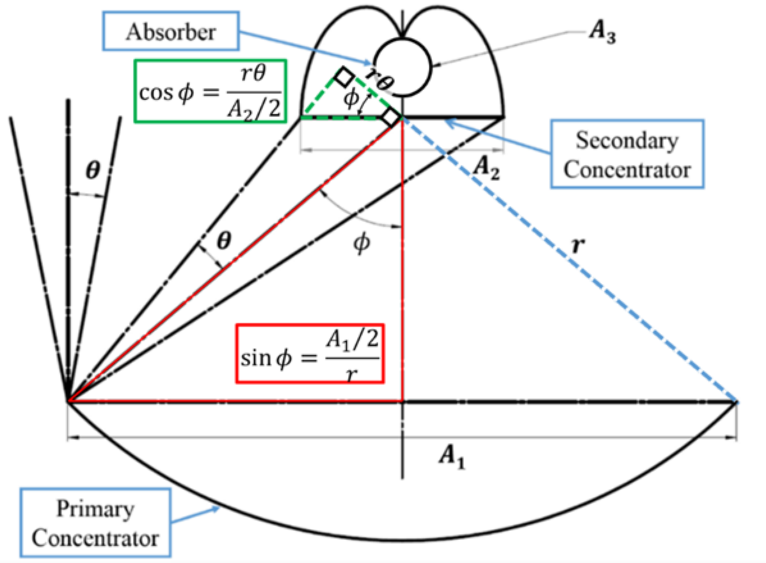

Figure 3.2 - *Two stage concentrator design (parabolic primary, CPC secondary)*

The concentration ratio of the first stage is described geometrically by equation 3.1, where A_1 is deduced from the red triangle and A_2 from the green triangle in Figure 3.2.

$$C_1 = \frac{A_1}{A_2} = \frac{\sin\phi\cos\phi}{\theta} \tag{3.1}$$

The second stage concentration is given by Compound parabolic concentrators (CPCs) are a class of ideal wide-angle concentrators for infinite light sources and compound elliptical concentrators (CECs) are a similar class of concentrators for finite light sources. Both are able to concentrate light from the parabolic primary since both have the qualities of accepting wide-angle light (from the primary parabola, i.e. ϕ). Being ideal maximally concentrators, both follow the law of maximum concentration. In this case, the half-acceptance angle of the CPC / CEC is equal to the half-rim angle ϕ of the parabola and therefore

$$C_2 = \frac{A_2}{A_3} = \frac{1}{\sin\phi} \tag{3.2}$$

The total concentration ratio of the system is given by

$$C_{total} = C_1C_2 = \frac{\cos\phi}{\theta} \tag{3.3}$$

Simple investigation of this formula reveals the concentration maximizes for small half-acceptance angles (θ) and small half-rim angles (ϕ).

Small half-rim angles are technically possible, but generate parabolas with long focal lengths which become unwieldy. A 45° half-rim angle was selected as a compromise between achieving high concentration and practical design. With such a half-rim angle, the focal length relative to the secondary reflector aperture is so great that the CPC and CEC solutions converge to almost the same profile. From this point on the secondary is chosen to be a CPC.

A primary mirror width of 5 meters was selected to be comparable with existing trough systems. The sun disk half-angle is approximately 0.27°, which represents the minimum angular acceptance a concentrator can reach. Several other factors contribute to system optical error including mirror slope error (0.17°), receiver misalignment (0.11°), tracking error (0.06°), and imperfect specularity of real surfaces (0.11°). Angular headroom is required to prevent in-field reductions in optical efficiency and in most parabolic trough plants the half-acceptance angle is close to 0.85°. The ultimate goal is to reduce the acceptance angle as much as possible without going below the total optical error of the real system.

For this design, a somewhat ambitious half-acceptance angle of 0.6° was selected. This generates a 105 mm wide beam at the focus of the parabolic mirror. For a secondary CPC with an acceptance angle of 45° to match the half-rim angle of the primary parabolic mirror, the concentration ratio is about 1.41X, which yields an absorber diameter of 23.57 mm. For simplicity, we chose to scale up the absorber diameter to a nominal ¾" standard pipe with an outer diameter of 26.67 mm. The CPC was then truncated to 94% of the original aperture width (66% original height) to fit within the 120 mm glass tube. The final CPC aperture width is 111 mm.

While the maximum possible concentration for such a system according to equation 3.3 is 95.49X, the actual concentration ratio of the system (due to the aforementioned modifications) is 59.67X.

$$C_{1st} = \frac{A_1}{A_2} = \frac{5000\,mm}{111.12\,mm} = 45X \tag{3.4}$$

$$C_{2nd} = \frac{A_2}{A_3} = \frac{111.12\,mm}{\pi * 26.7\,mm} = 1.324X \tag{3.5}$$

$$C = C_{1st} \cdot C_{2nd} = 59.6\text{X} \tag{3.6}$$

After all the design considerations, the final concentration ratio of the system is 59.6 or about 60X and the CAP is 0.62. The main parameters of the two-stage optical design are listed in Table 3.1.

Half-rim angle (ϕ)	45°
Half-acceptance angle (θ)	0.6°
Primary aperture width (A_1)	5 m
Focal length (f)	3.02 m
Concentration ratio	59.6X
CAP	0.62

Table 3.1 – *Optical characteristics of (Generation 1) two-stage collector design*

3.1.2 Hybrid Receiver Design

The hybrid receiver and a typical parabolic trough absorber tube are shown side-by-side in Figure 3.3. High concentration reduces the absorber in the hybrid receiver by almost one third compared to a standard absorber.

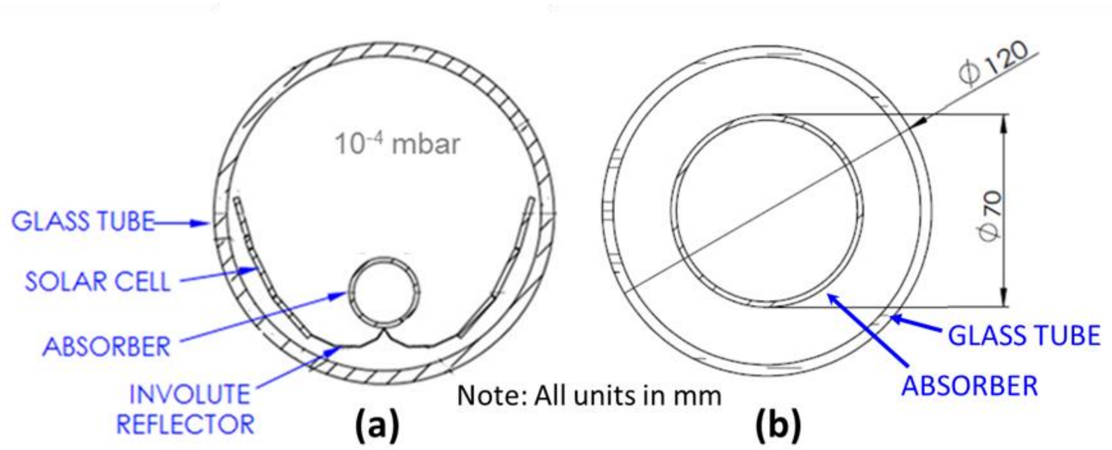

Figure 3.3 – *(a) Hybrid receiver (b) standard PTC receiver*

Single junction GaAs solar cells are to be manufactured by Alta Devices for use in the hybrid receiver. A spectral reflectance curve of a bare cell is shown in Figure 3.4. The sharp bandgap cutoff at 870 nm, with 90% absorption at sub-bandgap wavelengths and 92% reflectance at wavelengths above the bandgap, allows them to operate as efficient spectrally selective reflectors. The cells occupy only 2.4% of the primary aperture area, allowing the system to be more affordable.

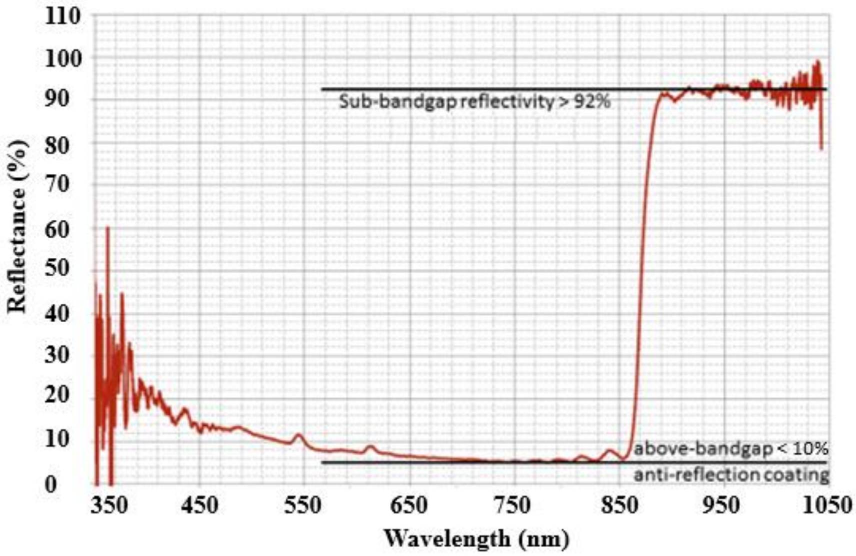

Figure 3.4 - *Spectral reflectance of Alta Devices' GaAs cell (Source: Alta Devices).*

The wings of the CPC are approximated by three segments of aluminum minichannel. The involute portion of the CPC is formed using Alanod Miro-Sun which has a total solar reflectance of approximately 89%.

3.2 Performance Modelling

3.2.1 Optical Model

The optical system was modelled and simulated using the ray-tracing program LightTools. Initial simulations were performed using ideal optical surfaces (ignoring reflection, transmission, and absorption losses) to determine the geometric efficiency. Ray tracing with the parabolic mirror focusing to an ideal CPC is shown in Figure 3.5 for a perfectly collimated light source to show the optical system setup and CPC performance for on-axis and 0.6° off-axis light.

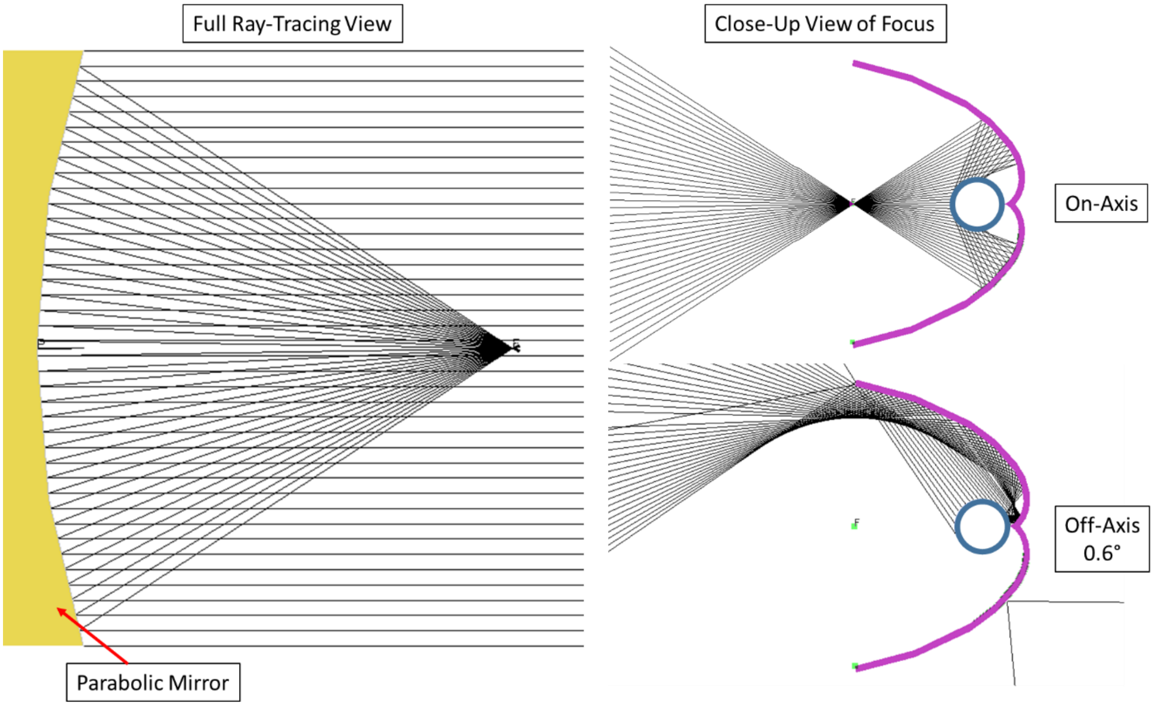

Figure 3.5 – *Ray tracing on ideal CPC secondary*

The CPC was originally to be constructed from flexible GaAs cells, but after discussion was determined to be a high risk factor. Instead, flat cells would be provided and as a result the CPC profile had to be approximated by flat segments. Placement of these cells was done manually by locating the start and end point of each segment along the ideal CPC profile. The involute portion of the CPC (closest to the absorber) could not be easily approximated by a segment and it was decided to use a pure reflector for the involute portion. Thus the CPC was made partially of an involute reflector and partially from flat GaAs cells (see Figure 3.6).

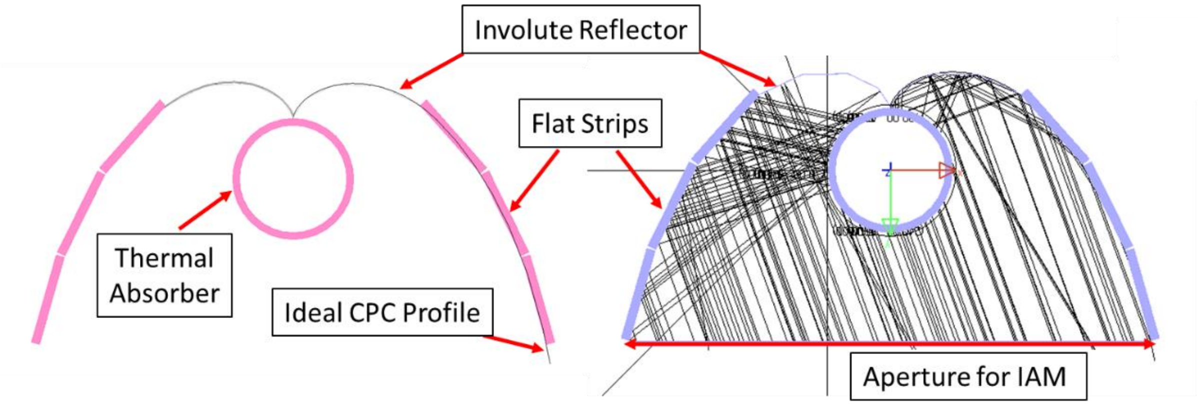

Figure 3.6 – *Secondary CPC with integrated flat solar cell strips*

The optical effects introduced by the partially segmented and truncated secondary CPC were investigated using ray tracing software. The incidence angle modifier of the newly approximated CPC profile was calculated by sweeping a light source from 0° (normal incidence) to 65° and recording the fraction of light captured by the absorber. The resulting profile (Figure 3.7) has a geometric efficiency of 0.91 at normal incidence with approximately 10% of light between 0° and 45° rejected.

The full system (primary and secondary) incidence angle modifier is shown in Figure 3.8 which verifies an acceptance angle of about 0.6°.

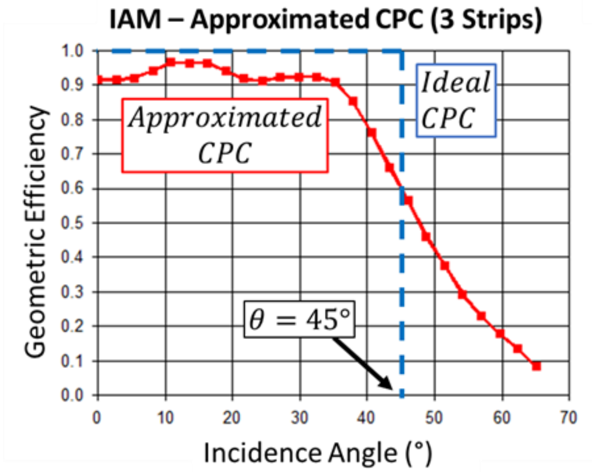

Figure 3.7 – *Incidence Angle Modifiers (IAM) of the approximated CPC (red) plotted against an ideal CPC (blue)*

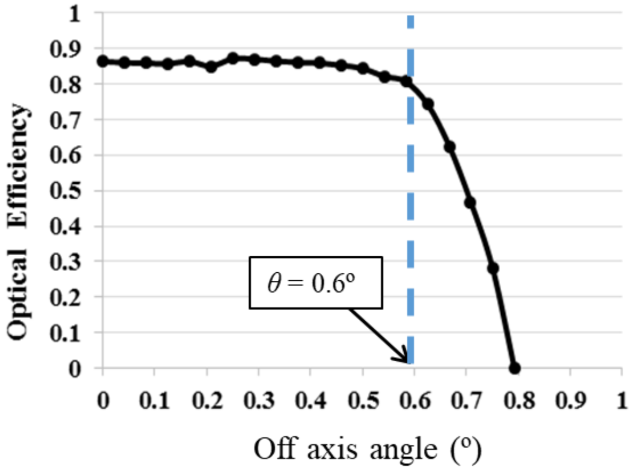

Figure 3.8 – *Full system incidence angle modifier (IAM).*

A full optical model of the system was developed to include spectral surface properties of all components (see Figure 3.9). The GaAs cells were assumed to have a UV reflectance of 0.27 and an infrared reflectance of 0.906 outside of the supplied spectral data. The primary and involute reflectors were assumed to have a reflectance of 0.92, and the glass envelope was modelled with Fresnel losses at each interface (~4% at each interface, or 92% total transmission). The AM 1.5 and 500 °C blackbody emission curves presented in Figure 3.9 are unified, meaning values at all wavelengths are divided by the maximum value to adjust the data to be between 0 and 1.

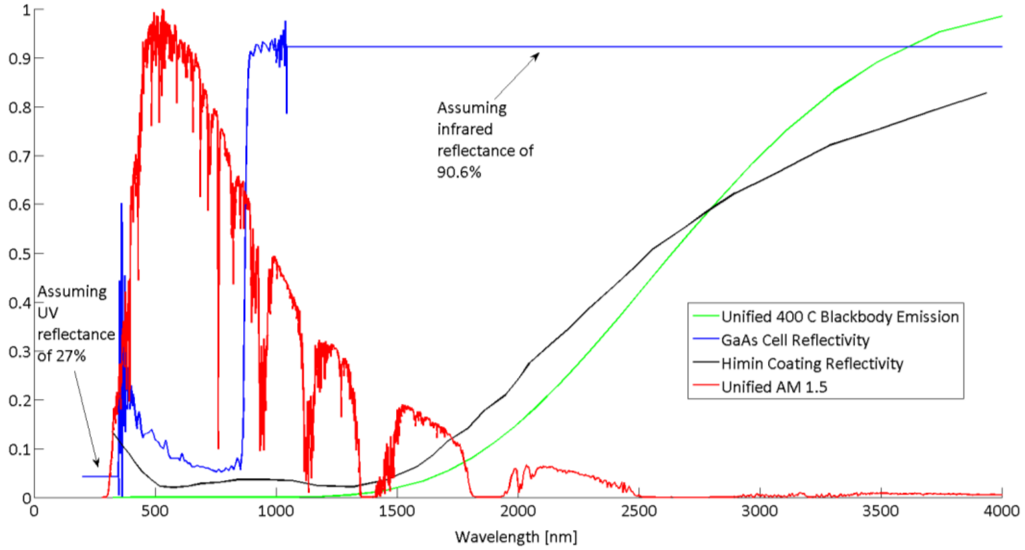

Figure 3.9 - *Hybrid receiver material spectral properties.*

Virtual receivers were placed on each cell strip and the thermal absorber to determine the amount of light incident and absorbed by each component. Optical modelling of the full system was performed using uniformly distributed rays within a 0.6° cone to simulate the effects of sun disk angle, tracking error, and optical misalignment of the system. Of the total incoming solar flux to the system, 82% is incident on the aperture of the secondary (losses from reflection and glass transmittance). Of the incoming DNI, 47% is captured at the absorber and 26% is absorbed by the solar cells and converted into either electricity or low grade heat. The results of these simulations are presented in Table 3.2.

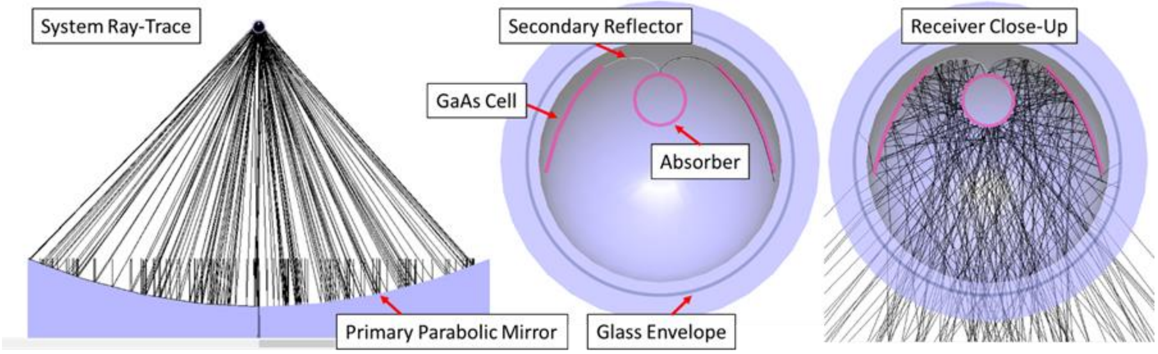

Figure 3.10 – *Full System Ray Tracing*

The optical model generates three key performance parameters which are used to calculate the thermal performance of the system: radiation absorbed by the absorber ($G_{absorbed}$), radiation incident on the GaAs cells ($G_{cell\_incident}$), and the amount of radiation absorbed by the GaAs cells ($G_{cell\_absorbed}$).

	Incident	**Absorbed**
Secondary Aperture	82%	-
Solar Cells	42% ($G_{cell\_incident}$)	26% ($G_{cell\_absorbed}$)
Involute Reflector	15%	1%
Thermal Absorber	50%	47% ($G_{absorbed}$)

Table 3.2 – *Optical model results*

3.2.2 CPV Subsystem Model

The temperature coefficient of GaAs is well documented (Silverman et al. 2013). Their solar to electric efficiency is calculated based on their operating temperature (T_{cell}). The cells are estimated to operate with 14.8% efficiency at 200 °C.

$$\eta_{GaAs} = 0.308 - 0.0008 * T_{cell} \tag{3.7}$$

Total electric output of the CPV subsystem (W_{cells}) is calculated based on the amount of radiation incident upon the cells as determined by the optical model.

$$W_{cells} = \eta_{GaAs} * G_{cell\_incident} \tag{3.8}$$

And the total solar to electric efficiency from the CPV subsystem is given by equation 3.9.

$$\eta_{system,cells} = \frac{W_{cells}}{GA_1} \tag{3.9}$$

Thermal gain by the low temperature stream (Q_{cells}) is calculated with the assumption that all light absorbed by the GaAs cells that is not converted to electricity is converted to heat. Bulk radiative losses (Q_{bulk_loss}) from the low temperature thermal stream based on the estimated area and emittance (Table 3.3) of all components (minichannels, GaAs cells, and all piping) at 200 °C are included in this model and the output is calculated according to equation 3.10.

$$Q_{cells} = (G_{cell\_abs} - W_{cells}) - Q_{bulk\_loss} \tag{3.10}$$

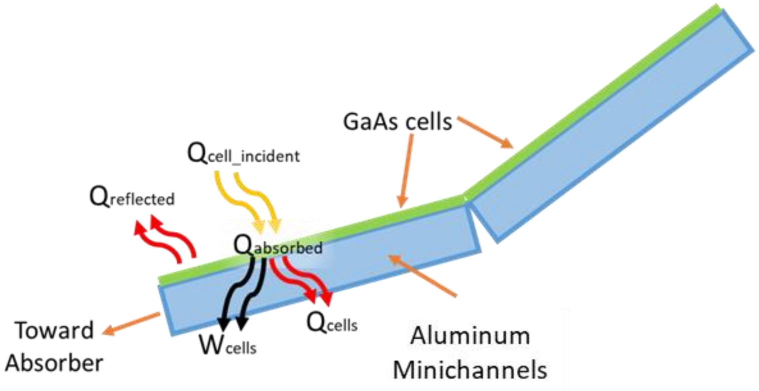

Figure 3.11 – *CPV subsystem model diagram*

3.2.3 CSP Subsystem Model

The emissivity of the selective coating at different temperatures was estimated by comparing blackbody emission at with the spectral emissivity data provided a coating provider (Himin Solar). As an example, the red line in Figure 3.12 depicts the spectral emissivity of the coating while the blue line represents the emission curve of a blackbody at 500 ºC. Multiplication of the two produces a spectral emission curve for the coating at 500 ºC, represented by the green line. The area under the green curve divided by the total area under the blue curve gives an estimate of the emissivity at this new temperature. The total emissivity of this coating at 500 ºC is estimated to be 0.14.

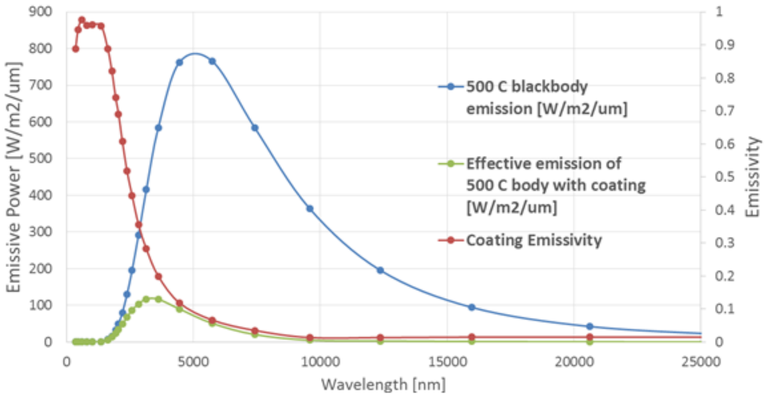

Figure 3.12 – *Estimation coating emissivity at 500°C.*

The results of the optical model are used as inputs to the thermal model. Heat transfer in the counterflow thermal absorber is determined by finite element analysis (FEA). The 1 meter length of the absorber is divided into 50 nodes, with temperatures determined at the incoming fluid ($T_{f,i}$), inner pipe inner surface ($T_{i,i}$), inner pipe outer surface ($T_{i,o}$), outgoing fluid ($T_{f,o}$), outer pipe inner surface ($T_{o,i}$), outer pipe outer surface ($T_{o,o}$), glass inner surface ($T_{g,i}$), and glass outer surface ($T_{g,o}$). Uniform irradiance is assumed around the absorber pipe.

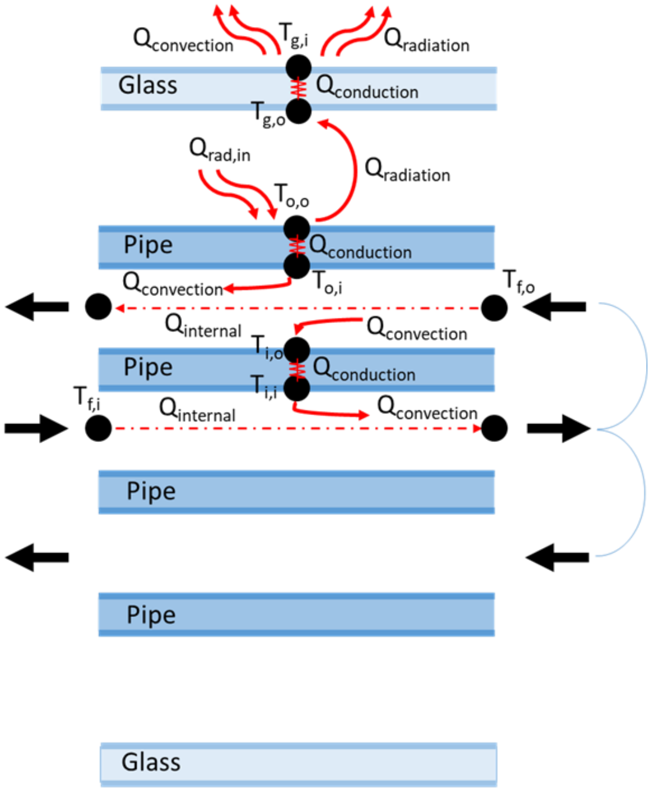

Figure 3.13 – *Finite element analysis of counterflow pipe in hybrid receiver.*

Each surface node ($T_{o,o}$) sees $Q_{rad,in} = \frac{G_{DNI} A_1 G_{absorbed}}{n}$ and is in radiative contact with the inner glass surface and thermally conducts to the inner surface of the outer counterflow pipe ($T_{o,i}$). The inner surface of the outer pipe conducts thermally to the outer surface and is in contact with ($T_{f,o}$) by convection. The outoing fluid ($T_{f,o}$) is in convective contact with both wall surfaces ($T_{o,i}$) and ($T_{i,o}$) and also carries heat internally ($\dot{m} C_p T$). The outer wall of the inner pipe ($T_{i,o}$) is in convective contact with the outer fluid ($T_{f,o}$) and conducts to the inner surface of the inner pipe ($T_{i,i}$). The inner wall of the inner pipe ($T_{i,i}$) conducts to the outer wall of the inner pipe ($T_{i,o}$) and is in convective contact with the inner fluid ($T_{f,i}$). And lastly, the inner fluid ($T_{f,i}$) is in convective contact with the inner wall of the inner pipe ($T_{i,o}$), and carries heat internally. The inner glass surface ($T_{g,i}$) is in radiative contact with the outer counterflow pipe surface ($T_{o,o}$) and conducts to the outer glass surface ($T_{g,o}$). The outer glass surface ($T_{g,o}$) conducts to the inner glass surface ($T_{g,i}$) and exchanges heat via radiation and convection with the ambient environment which is assumed constant at 300 K.

The heat transfer fluid used is Therminol VP-1 and thermal properties are referenced at each temperature from the manufacturer's specifications. For simplicity it is assumed that the radiation emitted by the counterflow absorber is only absorbed by the glass and not by the GaAs cells (probably a valid assumption considering they are highly reflective in the infrared region). The temperatures at each node are solved by matrix inversion and this process is iterated until the temperature change between iterations is < 0.01 °C. The initial conditions for the program are the inlet temperature of the fluid and the solar irradiance G, both of which are varied from 0-500 °C and 500-1000 W/m2 respectively. The heat transfer parameters used in the model are listed in Table 3.3.

$$\eta_{thermal} = \frac{\dot{m} c_p (T_{out} - T_{in})}{G A_1} \tag{3.11}$$

The efficiency of the high temperature thermal stream is calculated according to equation 3.11 and the results of the simulation are presented in Figure 3.14.

$D_{o,o}$	26.7 mm
$D_{o,i}$	23.4 mm
$D_{i,o}$	17.2 mm
$D_{i,i}$	13.9 mm
$k_{Stainless\ Steel}$	20 W/m-K
$\varepsilon_{300°C}$	0.08
$\varepsilon_{500°C}$	0.14
ε_{GaAs}	0.10
$\varepsilon_{Aluminum}$	0.08
k_{glass}	1.005 W/m-K
$\alpha_{glass,infrared}$	1
$\dot{m}$	100 g/s
T_{amb}	310 K
h_{amb}	10 W/m^2-K

Table 3.3 – *Heat transfer model parameters*

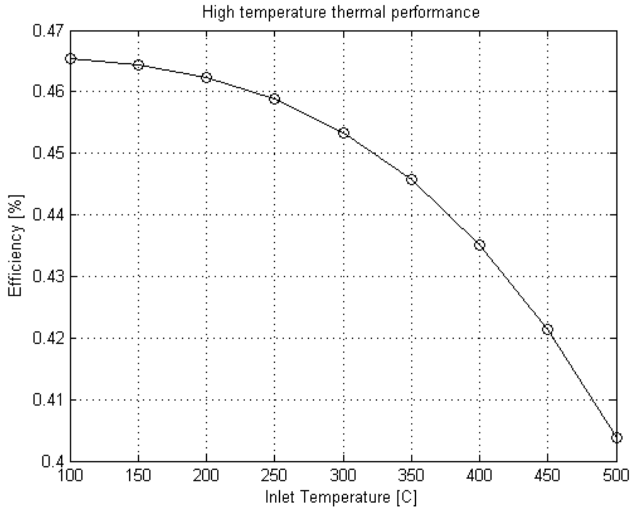

Figure 3.14 – *High temperature stream efficiency*

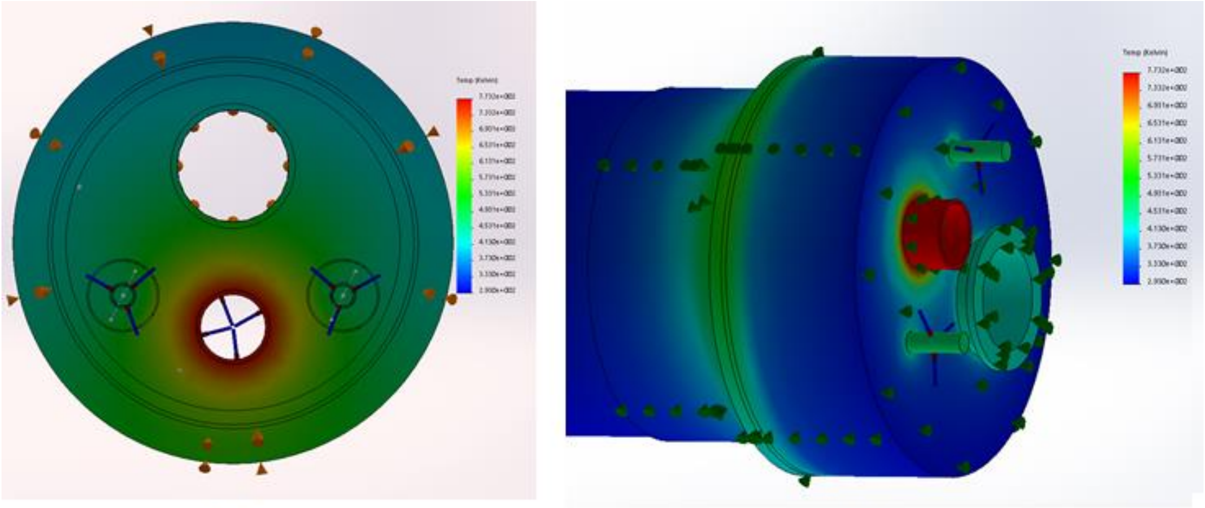

(a) (b)

Figure 3.15 - *(a) Radiative heat loss from interior stainless steel end cap, (b) Heat loss through 50.8 mm (2") Fiberglass Insulation.*

Heat loss from the receiver end cap was calculated in SolidWorks and incorporated into our model (see Figure 3.15). All losses were taken from the high temperature stream. For a high temperature inlet of 500 °C and low temperature inlet of 200 °C, radiative loss from the inside of the receiver end cap was 42 Watts, and conductive/convective heat loss through two inches of fiberglass insulation on the exterior of the cap was 51 Watts.

3.2.4 Combined System Performance

The total energy efficiency of the system is calculated from equation 3.12, including the waste heat generation by the solar cells which are assumed to operate around 200 °C.

$$\eta_{energy} = \eta_{thermal} + \eta_{system,cells} + \frac{Q_{cells}}{GA_1} \tag{3.12}$$

And the total exergy efficiency can be calculated using the Carnot efficiency.

$$\eta_{exergy} = \eta_{Carnot}\eta_{thermal} + \eta_{system,cells} + \eta_{Carnot}\frac{Q_{cells}}{GA_1} \tag{3.13}$$

The outputs of the full system performance model are listed in Table 3.4 for varying solar irradiance. A DNI greater than about 750 W/m^2 is required to achieve an exergy efficiency above 40%.

Direct Solar Input (W/m^2)	**Electricity Produced (W/m^2)**	**Thermal Output at 200 °C (W/m^2)**	**Thermal Output at 400 C ° (W/m^2)**	**Exergy Efficiency**
1000	130.20	295.27	320.73	40.4%
900	117.18	263.91	286.51	40.3%
800	104.16	232.54	252.29	40.1%
700	91.14	201.18	218.06	39.7%
600	78.12	169.81	183.84	39.3%
500	65.10	138.45	149.62	38.7%

Table 3.4 - *Outputs of heat transfer model*

The exergy efficiency of the system is also plotted for varying solar irradiance and high temperature inlet temperatures. The main result of this plot is that for low DNI, the exergy peaks at lower operating temperatures of the thermal stream.

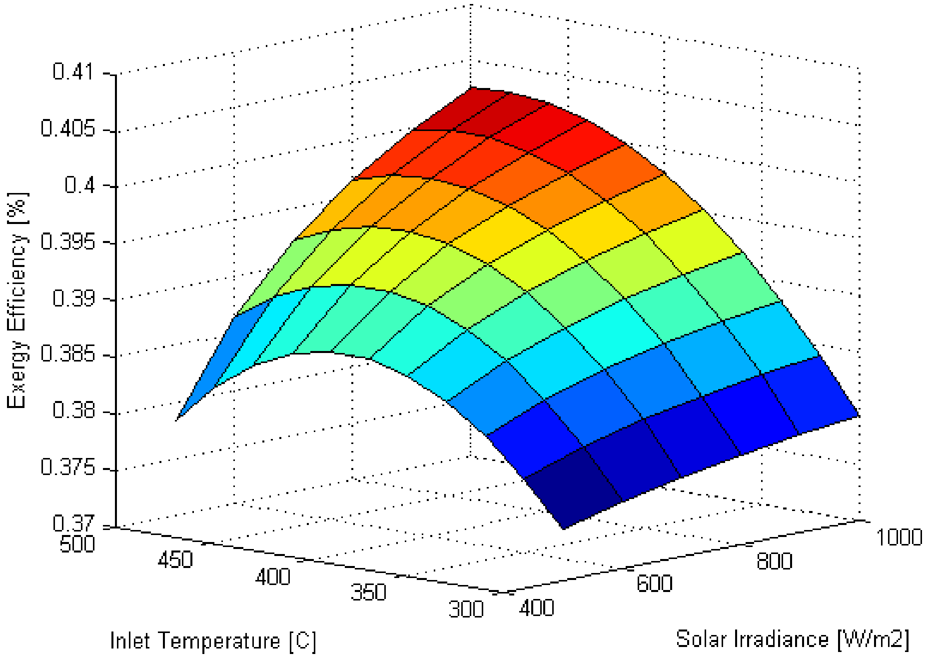

Figure 3.16 – *Solar-to-exergy efficiency as a function of high temperature thermal stream inlet temperature and solar irradiance.*

3.3 Prototype Development

3.3.1 Primary Mirror

The primary mirror is a 45° half-rim angle parabola. It is designed with an aperture width of 5 m and a length of 1 m. The primary mirror and frame were constructed by a local furniture company. The mirror frame was made out of wood and the reflective surface was formed by a plastic laminate, overlaid with the highly reflective ReflecTech film. The frame holding the receiver was constructed of welded aluminum to reduce the weight load on the elevation actuator of the tracker.

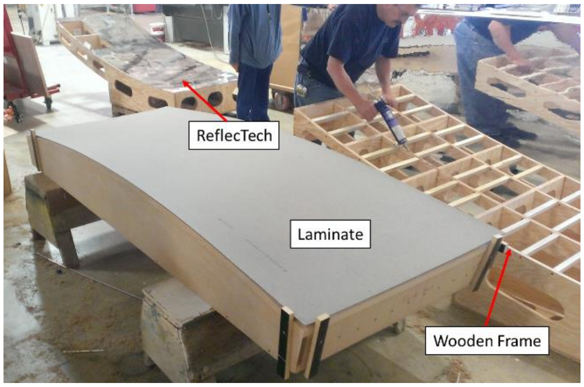

Figure 3.17 – *Primary mirror construction*

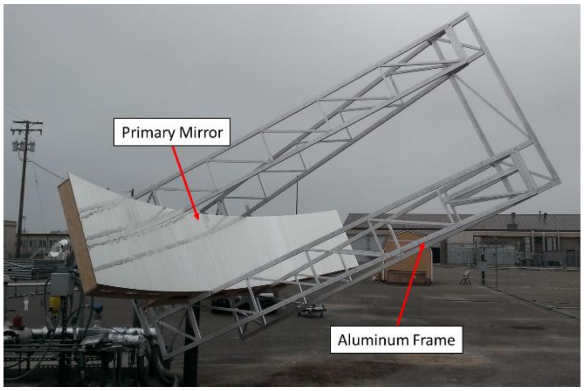

Figure 3.18 – *Assembled mirror and frame*

3.3.2 GaAs Cells

The Two live GaAs solar cells were manufactured by Alta devices, and one of them is shown in the image below.

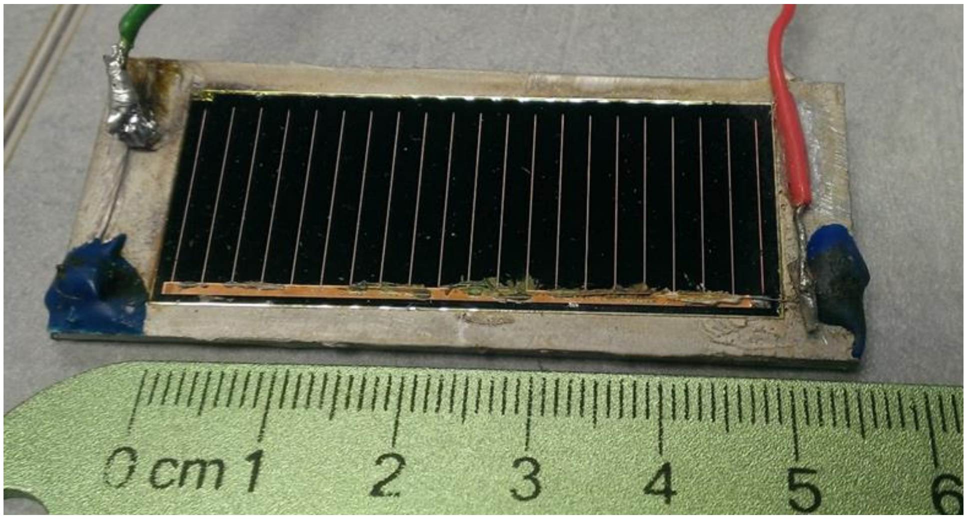

Figure 3.19 – *Live GaAs cell from Alta Devices*

Since only two live cells were produced, one live cell was used in the hybrid receiver prototype with the other saved as a spare. The rest of the minichannels were covered by "dummy" GaAs cells which were grown but did not have any grid contacts. These "dummy" cells were applied to aluminum substrates like the live cells using OmegaTherm, and glued to the minichannels using OmegaTherm as well (see Figure 3.20).

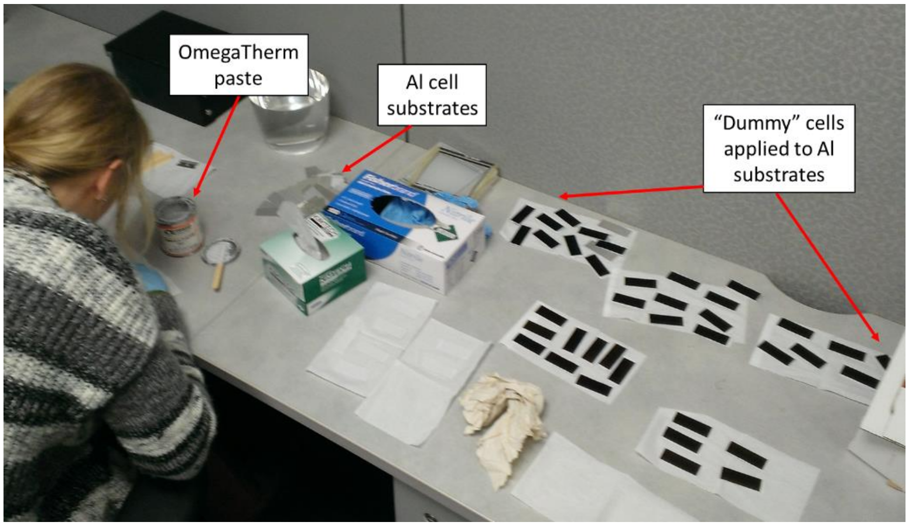

Figure 3.20 – *Cell assembly*

Early experimental tests indicated the OmegaTherm lost its adhesive qualities and dried out over time under heated evacuated conditions, causing the cells to fall from the aluminum minichannels. As a quick fix, the cells were then tied to the minichannels using enameled wire (see Figure 3.21).

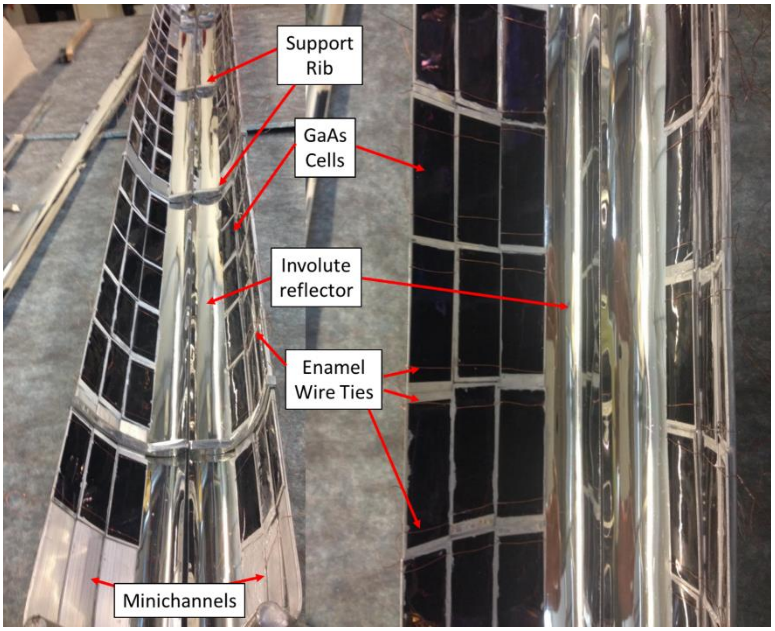

Figure 3.21 – *Solar cell and secondary reflector assembly*

3.3.3 Thermal Absorber

The selective coating was produced by the Chinese company Himin and coated on a stainless steel pipe. It has a solar-weighted absorptance of 95% as calculated by the spectral reflectance in Figure 3.22.

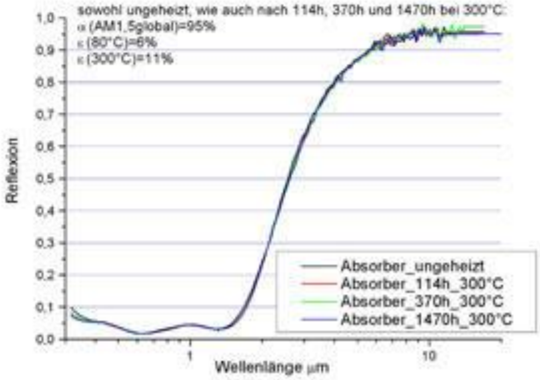

Figure 3.22 – *Spectral reflectance of Himin selective coating*

The emissivity of the selective coating at temperature was back-calculated based on the spectral data provided by Himin (tested at Fraunhoffer). At 500 °C, this is approximately 18%. At 80 °C and 300 °C the back-calculation produces an emissivity of 6% and 11% which is equal to the values measured by Fraunhoffer, thus indicating this method to be a decent approximation.

3.3.5 Involute Reflectors

The involute reflectors were produced from Alanod Miro-SUN and matched the curved profile between the bottom-most minichannel and the center of the CPC. The spectral reflectance profile is shown in Figure 3.23.

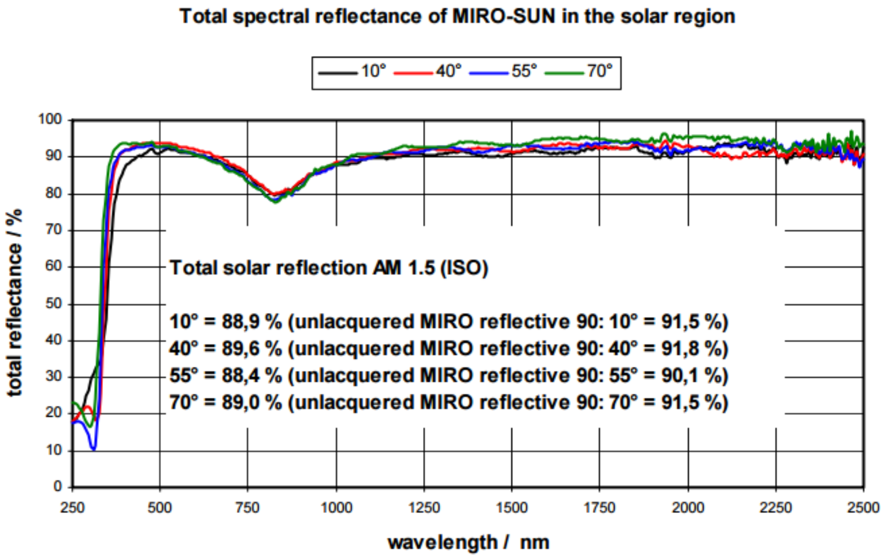

Figure 3.23 – *Alanod MIRO-SUN reflectance.*

3.3.6 Glass Tube

The glass tube was manufactured by a Berkeley-based scientific glass company (AdamsChittenden) who also provided the quick sealing clamp, end cap, and supporting structure drawn in Figure 3.24. The glass tube was produced by Schott.

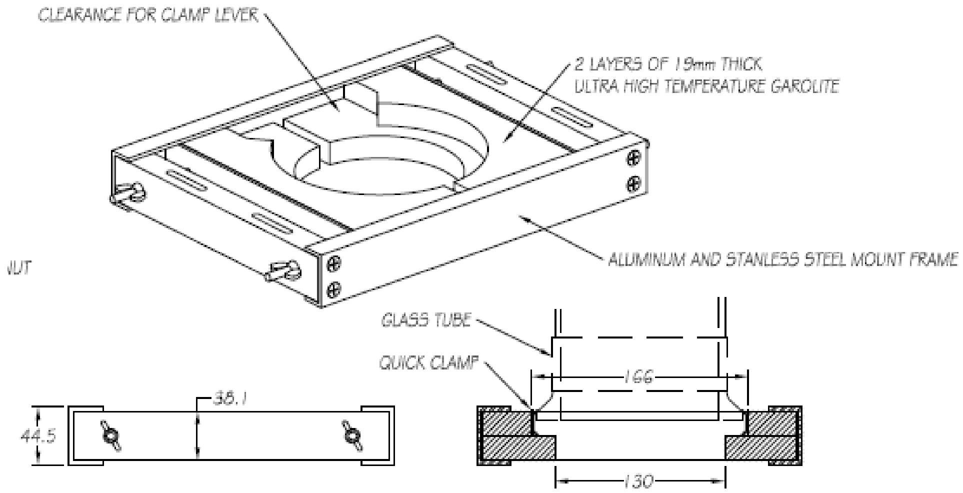

Figure 3.24 – *Glass tube end cap, clamp, and supporting structure.*

3.3.7 Hybrid HCE Assembly

The hybrid heat collection element (HCE) contains the selectively coated thermal absorber, the minichannels covered in solar cells, and the involute reflector, all of which are contained in an evacuated glass tube. This entire assembly is referred to as the HCE or the receiver.

The HCE was assembled at the University of California, Merced. Many supplemental and supporting parts were machined by the UCM machine shop (reflector ribs, absorber end support, end cap) and all welds were performed by the on-campus special projects fabricator.

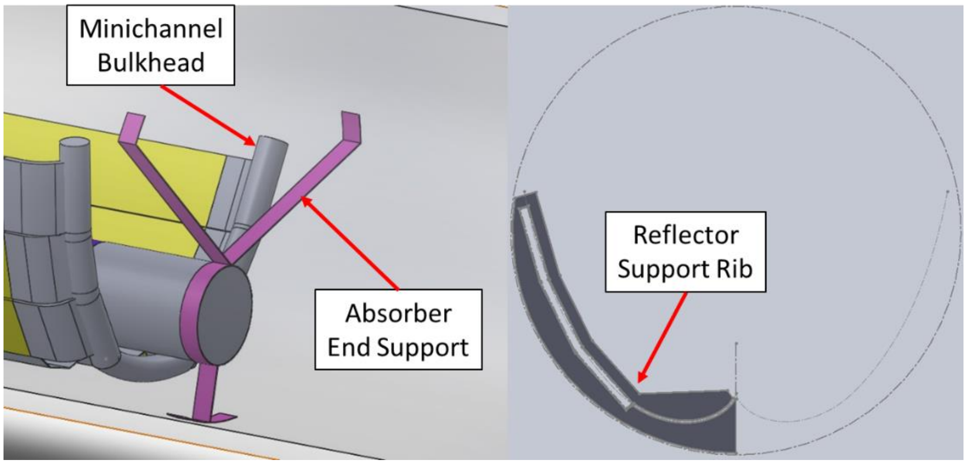

Figure 3.25 – *Absorber and reflector supports*

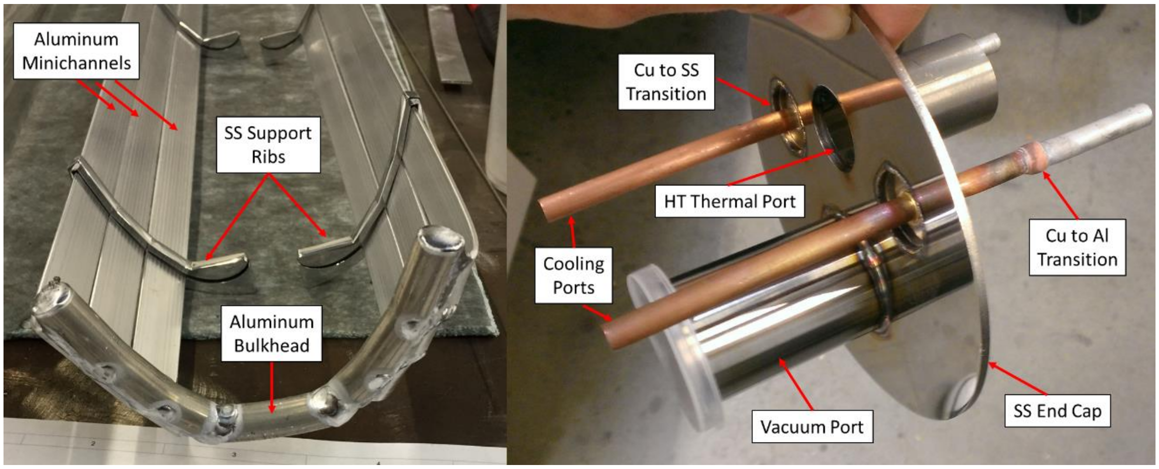

Figure 3.26 – *(left) Minichannel assembly used to exhaust waste heat from the solar cells, and (right) HCE end cap.*

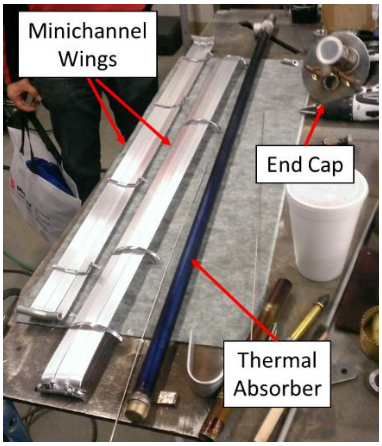

Figure 3.27 – *Assembled parts*

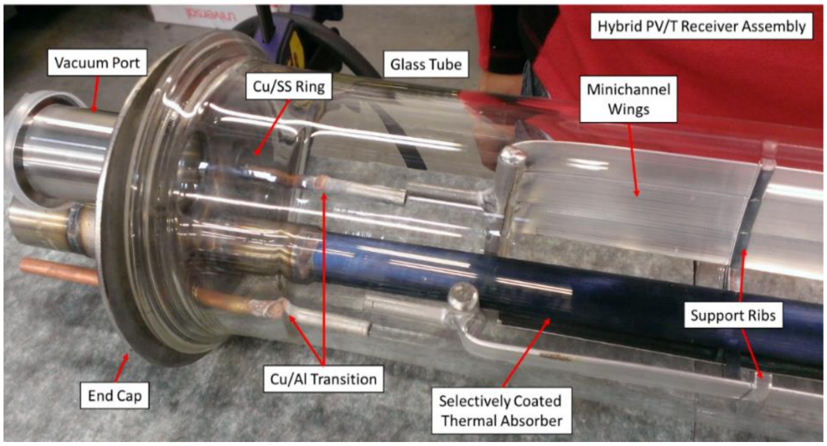

Figure 3.28 – *Partially assembled HCE*

Since the only minichannels found at the time were made from Aluminum, a solution was needed to transition to stainless steel to allow for vacuum sealing (welding) with the end-cap. This was done through the use of an intermediate copper pipe, which was welded to a stainless steel transition ring which could be welded to the stainless end cap, and had a transition to aluminum which allowed the minichannels to be connected to it on the other end.

A DN 40 vacuum port welded onto the end cap allowed the entire HCE to be evacuated.

3.4 Experimental Tests

3.4.1 High Temperature Loop Design and Fabrication

The high temperature loop was constructed from Schedule 80 SS 304 using 300 lb flanges for all connections. It was designed to allow the entire loop to be drained into a single drain-back tank at the end of the day, which contained an immersion heater for pre-heating the Therminol and to prevent in-line freezing.

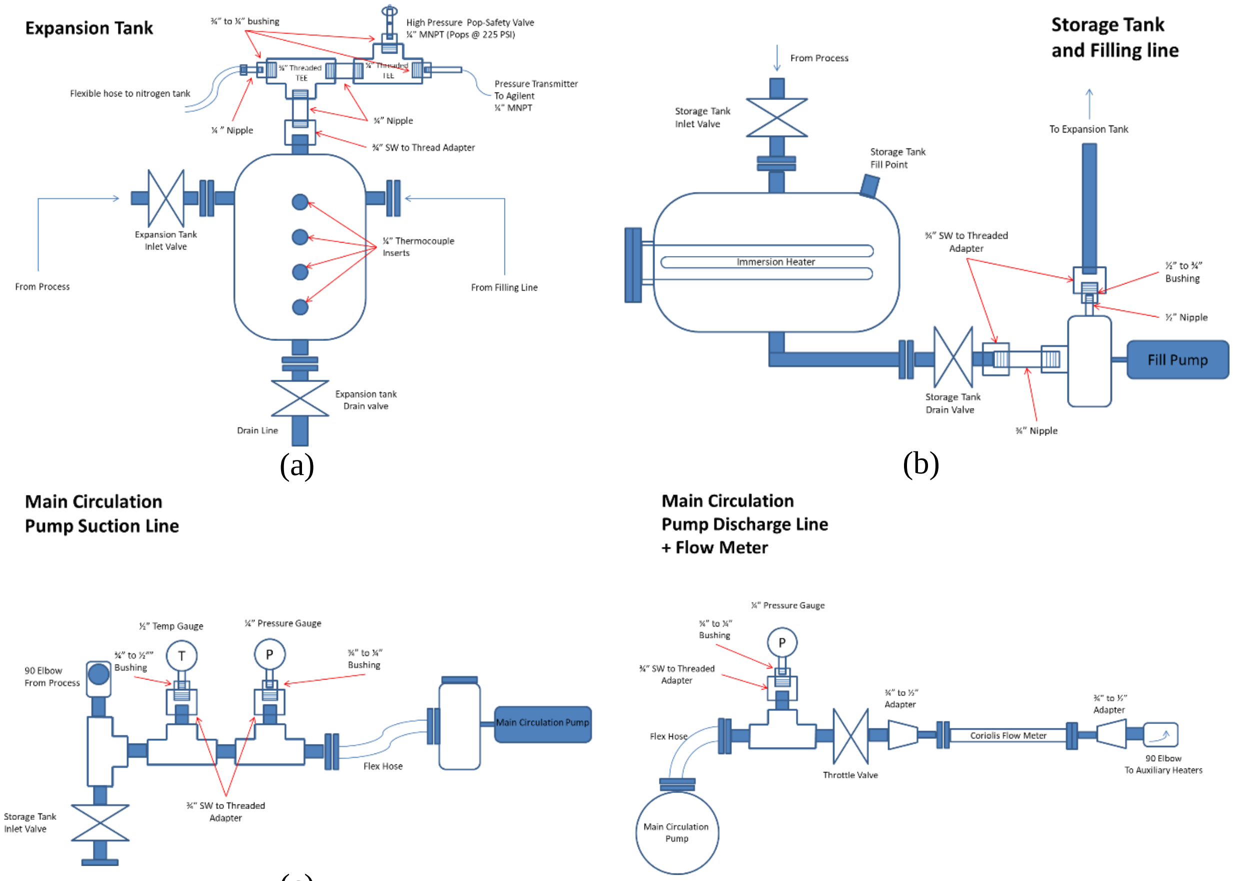

(a)

(b)

(c)

(d)

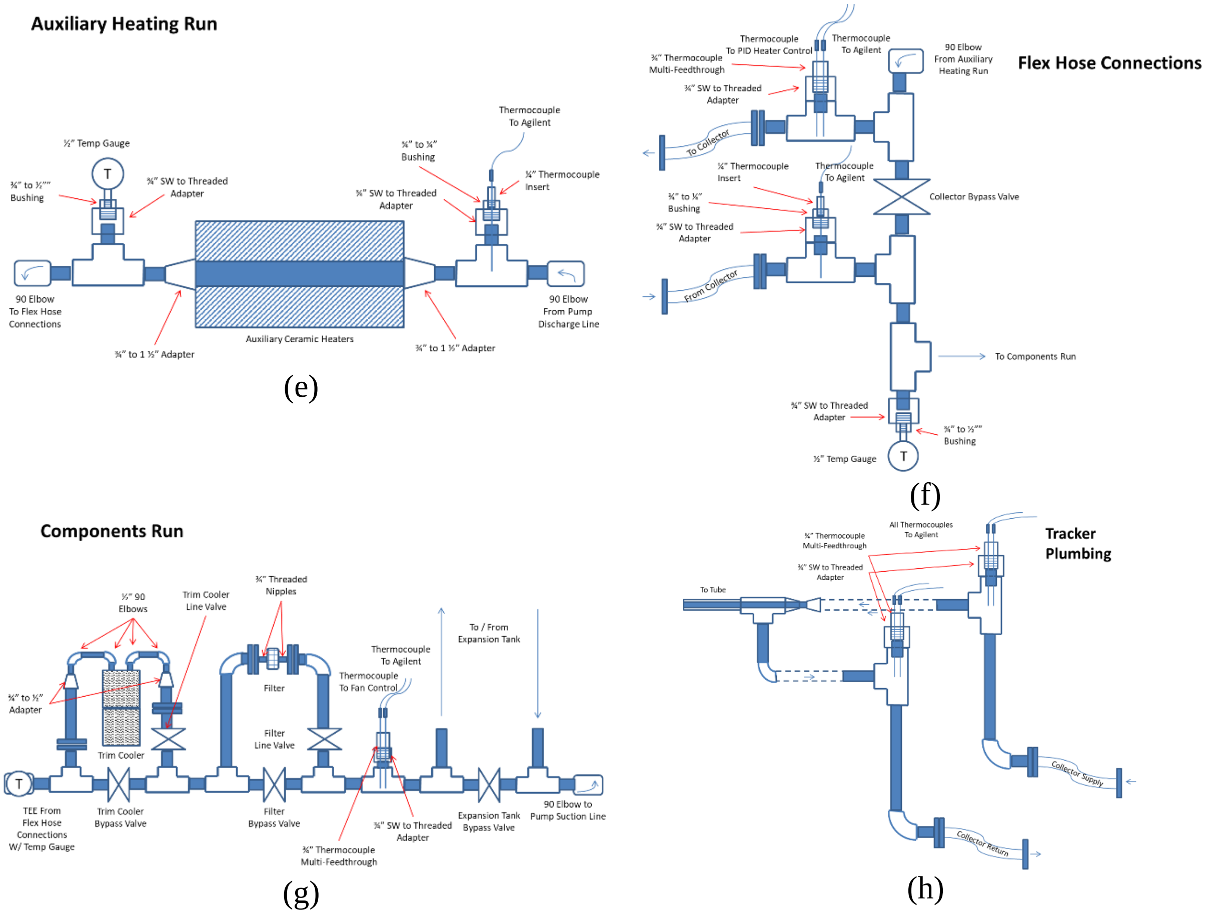

Figure 3. 29 – *High temperature test loop design schematics*

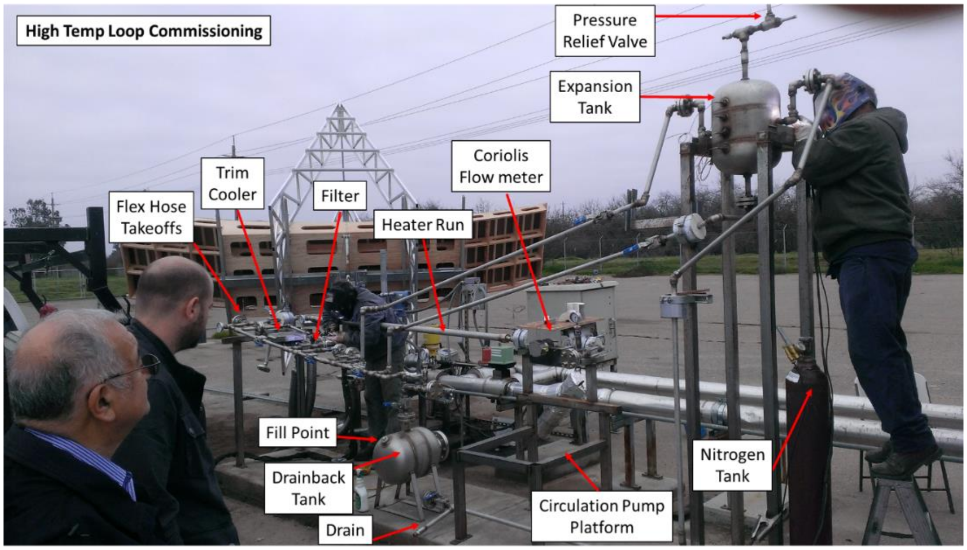

Figure 3.30 – *High temperature loop commissioning*

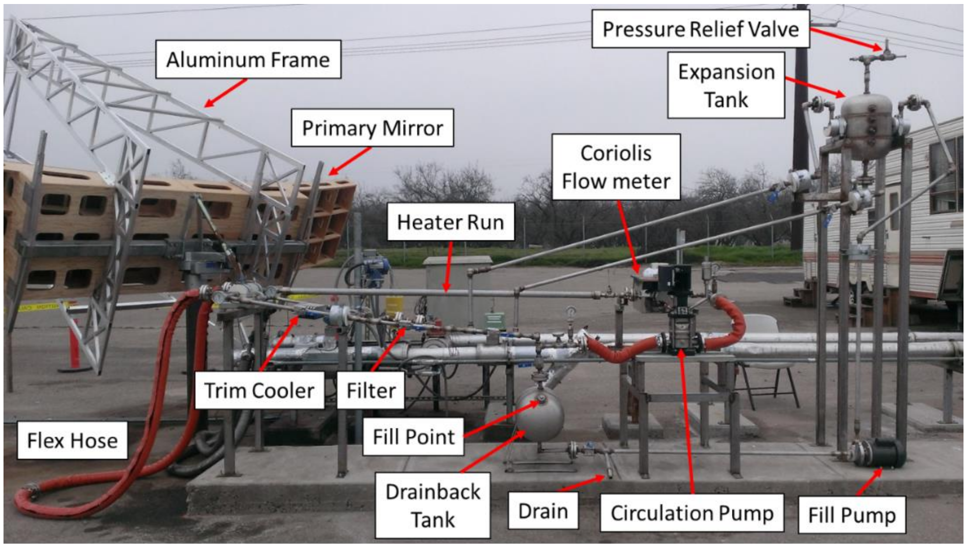

Figure 3.31 – *High temperature loop, primary mirror, and tracker.*

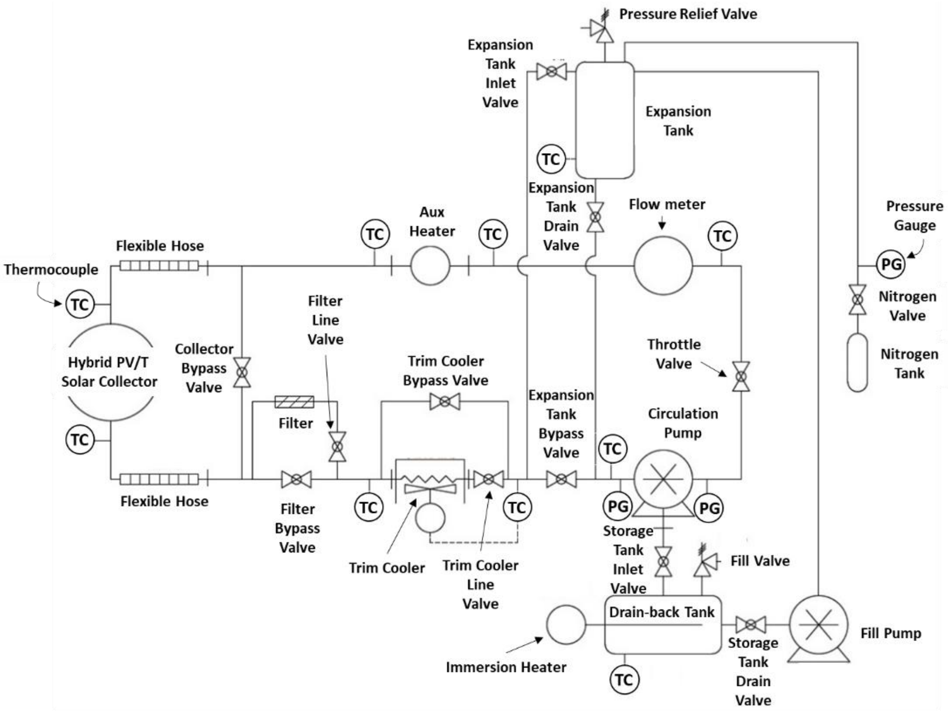

Figure 3.32 – *High temperature loop design*

3.4.2 Experimental Test Platform

The experiment was performed at the University of California, Merced Castle Research Center. The solar resource was measured by a normal incidence pyrheliometer (NIP) mounted on a separate tracker. Flowrate was measured by a coriolis flow meter. Auxiliary heaters were used to heat the Therminol-VP1 up to desired temperatures before on-sun testing. A combination benchtop roughing/turbopump was connected to the receiver vacuum port. A vacuum "tee" allowed us to also install a vacuum gauge to measure the vacuum pressure just outside the receiver. A secondary oil test loop which used Duratherm 600 mineral oil was connected to the minichannel cooling loop. In a similar fashion, thermocouple clusters measured the inlet and outlet temperatures and the flowrate was measured by a coriolis flow meter.

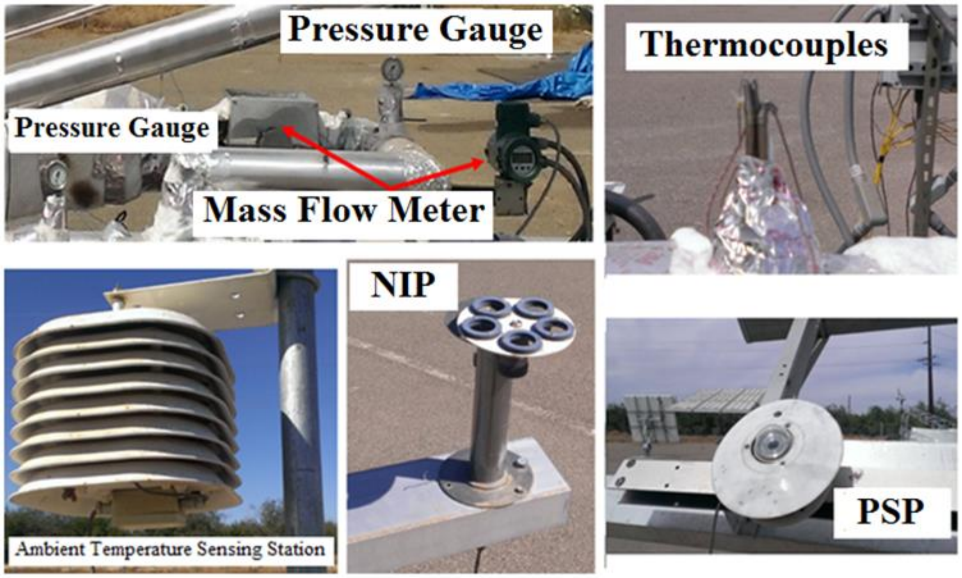

Figure 3.33 – *Solar and environmental sensors.*

Measurement	Quantity	Sensor	Calibration Range	Instrument Uncertainty	Manufacturer
Ambient temperature	1	Thermocouple, Type k	Up to 1335°C	Less than 2.8°C in 25 week	Omega
System Pressure	2	Pressure Gauge	15,000 psi	+/- 1% full scale	Ashcroft
Fluid temperature	18	Thermocouple, Type k	Up to 1335°C	Less than 2.8°C in 25 week	Omega
Mass flow rate	1	Coriolis mass flow meter	0-7 gallon/minute	0.35-0.38% of rate	Yokogawa
Direct normal irradiance (DNI)	1	Normal Incidence Pyrheliometer	Field of View 5° and sensitivity approx. 8 μV / Wm^{-2}	less than 1%	Eppley
Global horizontal solar irradiance	1	Precision Spectral Pyranometer	approx. 8 μV / Wm^{-2} 0–2000 W/m^{2}	less than 1%	Eppley

Table 3.5 – *Sensor specifications.*

The pressure required to keep Therminol VP-1in a liquid state at 400 °C is approximately 170 psi. Pressure was applied using nitrogen via the expansion tank which blanketed the system to prevent oxidation of the oil at elevated temperatures. The system was designed for a flow rate of 50 g/s, or about 1 gallon per minute. At this flow rate, the oil was expected to rise by 10 °C through the solar collector (at 400 °C and 800 W/m^2 DNI)

The fluid used in the low temperature loop to cool the cells was Duratherm 600. It was circulated and temperature-regulated by a Chromalox micro-therm temperature control system. Flowrate was measured by a Coriolis mass flow meter and temperature was measured via thermocouple clusters positioned as close as possible to the inlet and outlet connections at the receiver.

Early on we realized we could not lift the optical system using our current elevator actuator due to the heavy weight of the mirror, frame, receiver, and plumbing. To get data we manually lifted the tracker using wooden 2”x4” support struts (see Figure 3.34).

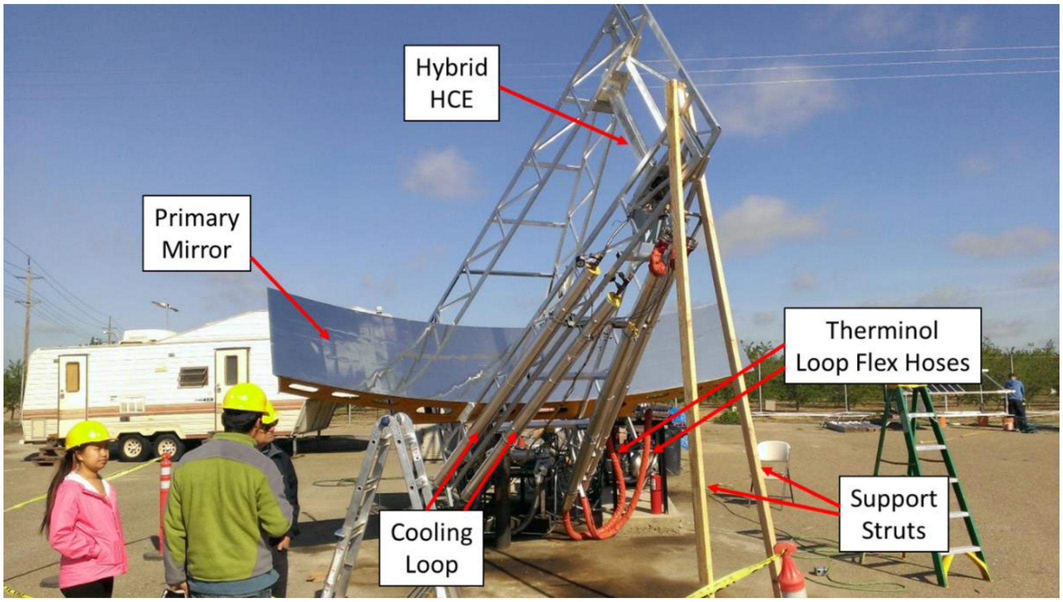

Figure 3.34 – *Hybrid HCE On-Sun*

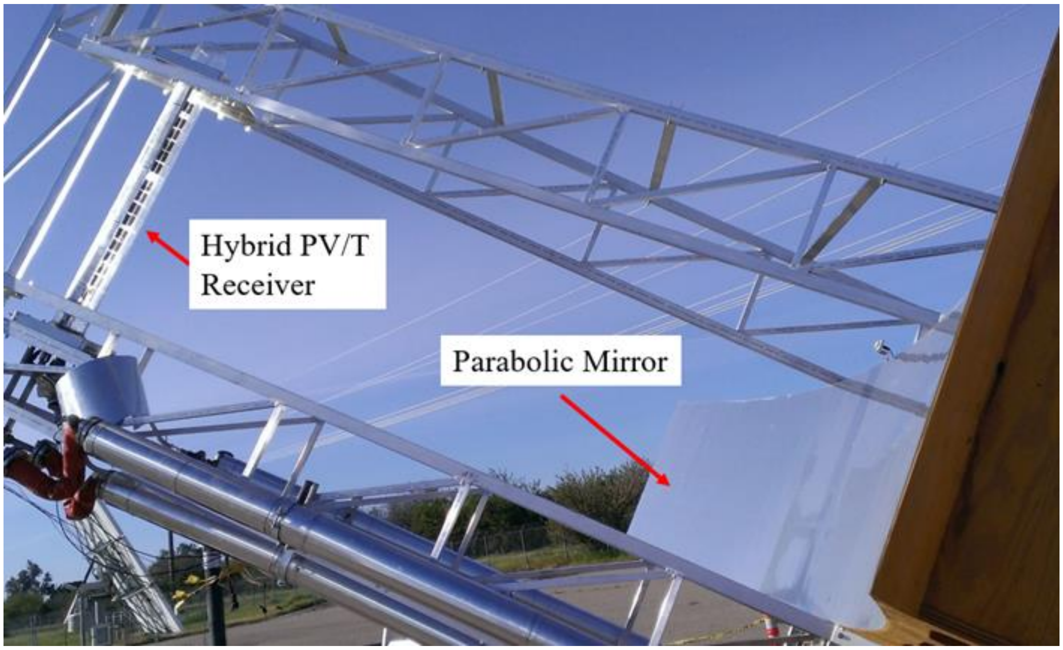

Figure 3.35 – Hybrid HCE On-Sun

3.4.3 Test Results

In this section are the individual day-by-day test data and some pictures to qualify the quality of the DNI. These figures are not numbered. This sections is presented as a log of experimental testing and the events that occurred.

<u>February 13th 2015 – Optical Efficiency Test – Thermal HCE</u>

Initial tests were performed on the thermal-only receiver (no solar cells) to establish a baseline efficiency.

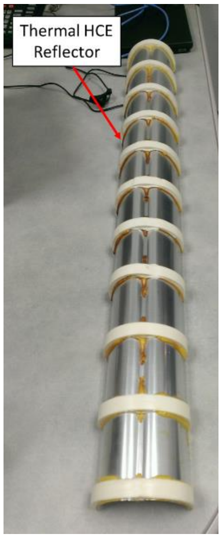

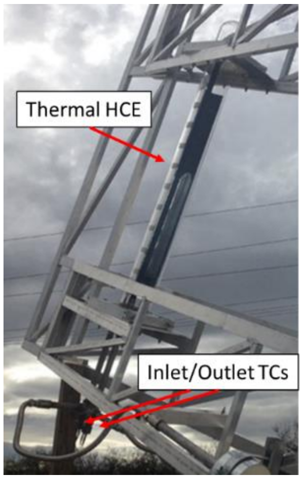

Picture NOT taken on same day as test.

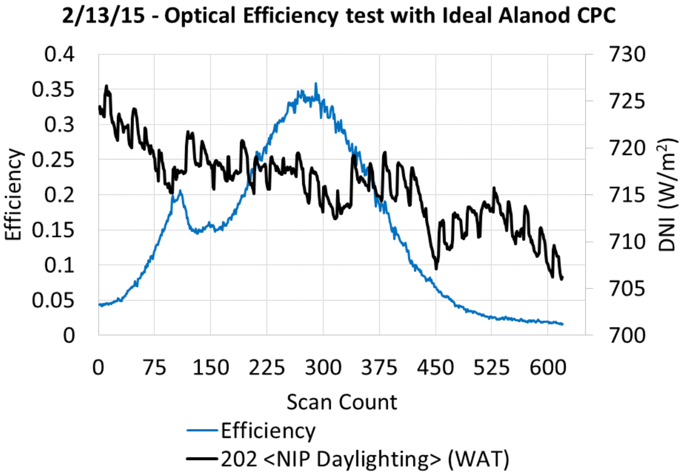

Tracker accuracy and receiver positioning are uncertain.

<u>March 9th 2015 – Optical Efficiency Test (70 °C)</u>

This was the first test of the Hybrid HCE. The tracker angle was too low during the sun-sweep, resulting in only two-thirds of the receiver being illuminated (see picture below). The efficiency was corrected for this to assume full illumination. Since it was an optical efficiency test at low temperature, the tube was not evacuated.

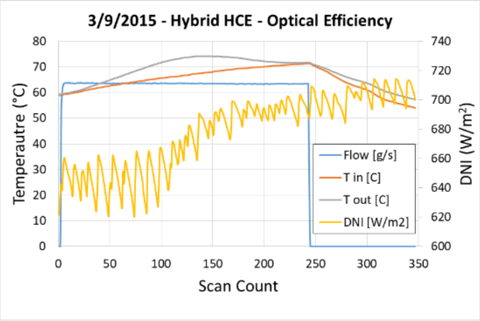

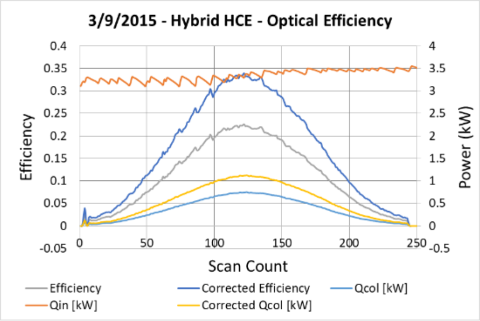

March 10th 2015 – Optical Efficiency Test (55 °C)

The tracker was manually adjusted to a higher elevation using longer wooden struts, but the angle was still too low to fully illuminate the receiver during the sun sweep (see picture). Since it was close the efficiencies are not corrected for full illumination. They are corrected for heat loss which was measured off-sun to be about 50 watts at 50 °C. During this test, the cell connections were fixed and the open circuit voltage (V_{oc}) of the cell was connected to the datalogger. The test occurred during cloudy conditions and the tube was non-evacuated.

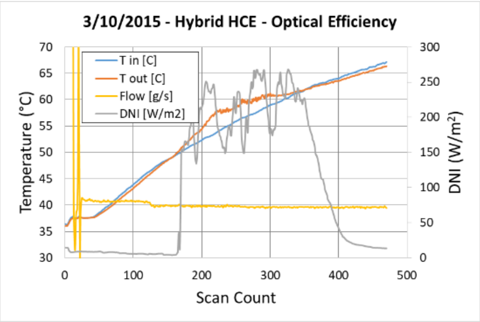

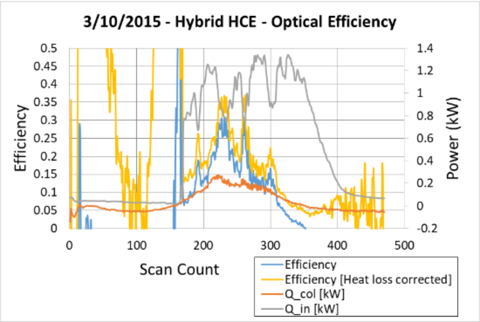

March 12th 2015 – Optical Efficiency Test

This test took place during sunny conditions. The tube was non-evacuated and our IV curve measurements using the arduino were tested.

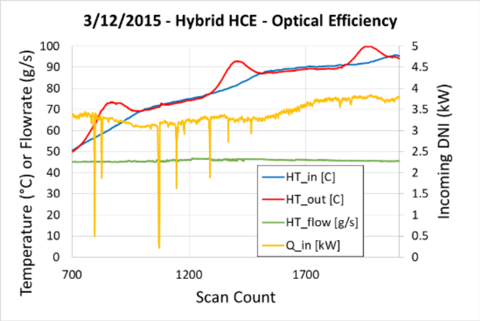

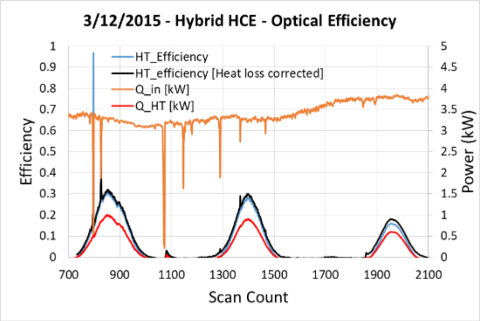

March 13th 2015 – Optical Efficiency Test

This test took place under clear sunny conditions.

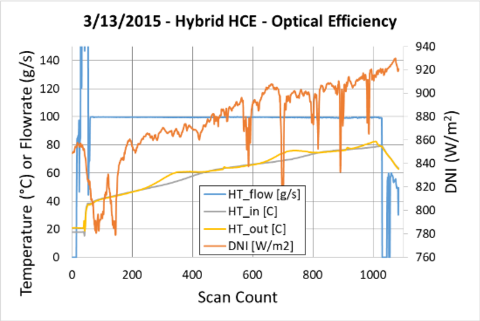

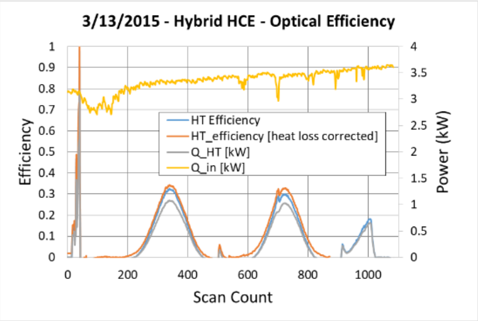

March 14th 2015 – 170 C Test, High DNI

This test was performed under high-DNI sunny conditions. During the test, however, the solar cell electrical connection was broken.

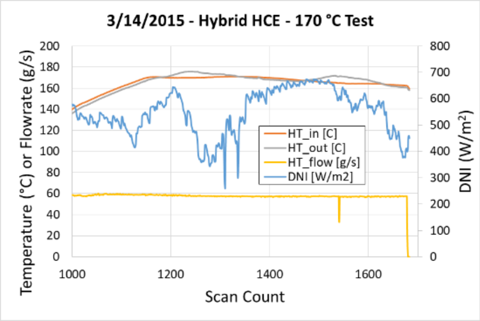

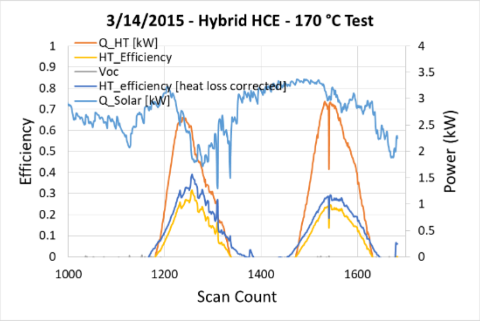

March 15th – 19th, 2015

On Sunday March 15th, the tube was left in place at the focus of the mirror without operating the loop. Without any fluid to remove the heat, the receiver tube was cooked by the concentrated beam which focused on the receiver for a short period of time due to the sun path. Some of the solar cells developed bubbles in their plastic covers and some of the plastic covers were burned completely and the solar cells were crinkled. Some of the thermal paste turned brown and the live cell connections were destroyed (solder was melted).

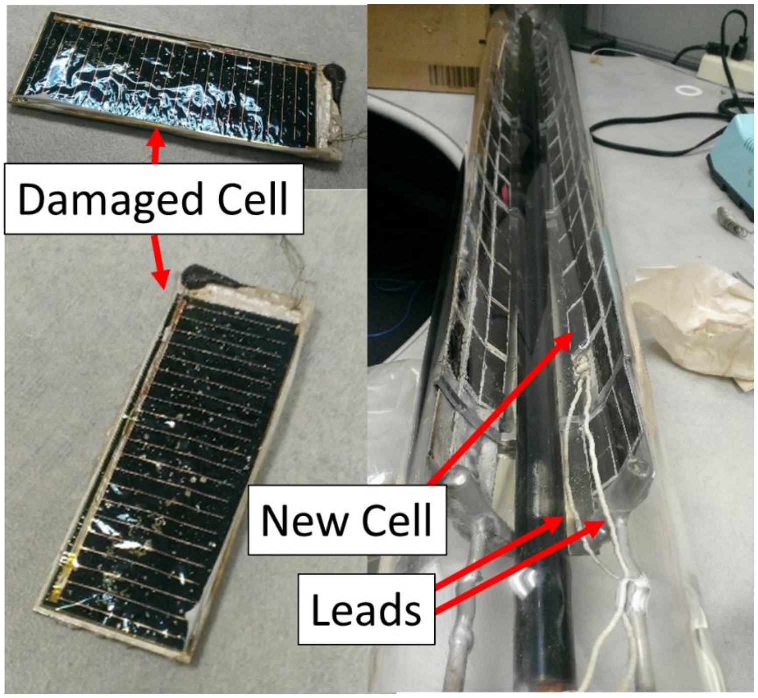

Figure 3.36 – *Cooked cell*

The following week, the tube was removed and the following repairs were made: (1) a small minichannel leak was fixed, (2) a new solar cell was installed in place of the old one, and (3) the glass tube was cleaned inside and out. None of the dummy cells were replaced, and the tube was re-installed 302 cm from the reflector.

March 20th 2015 – 50 C and 70 C test, Low DNI

This test was performed during cloudy conditions. The vacuum pump was turned on during the first test but did not reach steady state until the second test at 0.14 mbar. During the second test, the tracker angle was too low so about ¼ of the tube was shadowed. Efficiency data is corrected for this to assume full illumination.

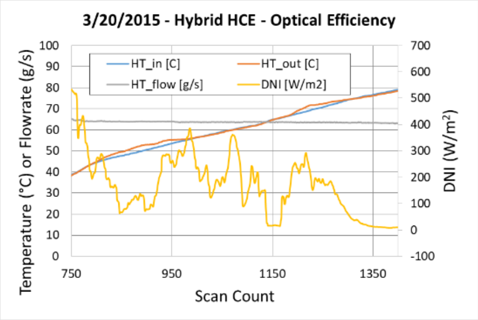

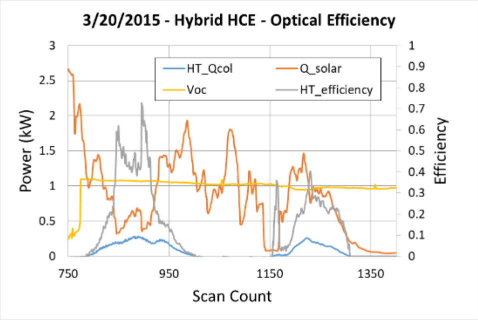

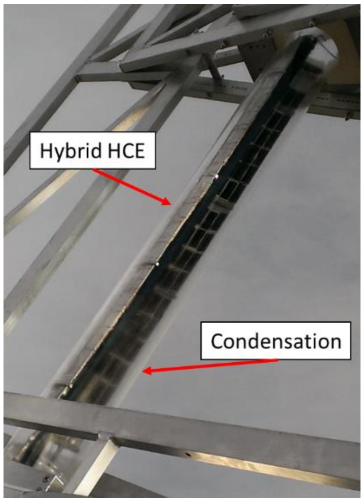

Figure 3.37 – Condensation formed on inside of hybrid HCE

At the end of the second test, it looked like condensation had formed on inside of the tube at a pressure about 0.14 mbar.

March 23rd 2015 – 80-160 C Test, High DNI

This test was performed under clear sunny conditions. The vacuum pump turned on 30 minutes prior to testing and achieved a pressure of 8.6E-2 mbar at the start of testing. This test was performed slightly differently than the previous tests. Instead of letting the sun “sweep” across the tube for each point, the east-west angle was manually tracked over an hour long period. The projected shadow of the receiver on the mirror surface was recorded during this time for data correction. The efficiencies below are corrected to assume full illumination. Dips in the efficiency are caused by manual tracking error (sometimes it was left a little too long and the receiver was de-focused). The average efficiency during operation was 0.304 and the max efficiency was 0.356.

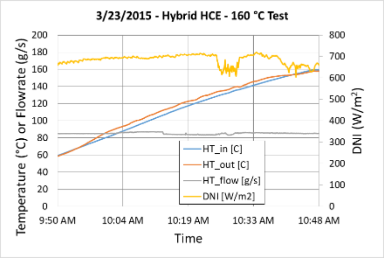

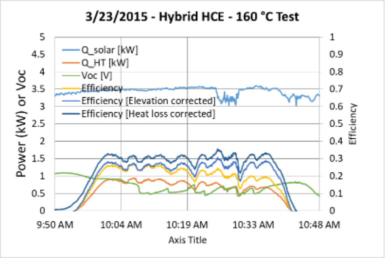

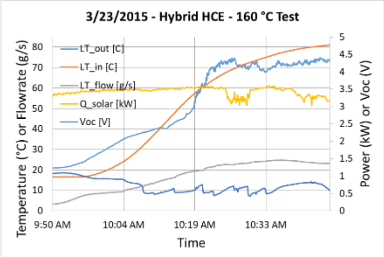

At the start of the test, condensation was visible on the inside of the glass. As we tested, the condensation slowly evaporated from the base of the tube upwards. There is likely a vacuum gradient between the gauge and the far side of the tube (i.e. the gauge reads 8.6E-2 mbar, but the inside of the tube is at the vapor pressure of gaseous water).

Primary Mirror Surface is slightly dusted, causing scattering of light on its way to the receiver

Condensation formed on inside of tube

Condensation causes significant reflection / scattering when illuminated

Figure 3.38 – *Optical loss mechanisms*

<u>March 24th 2015 – 200 C Test, Low DNI</u>

This test was performed under hazy and slightly cloudy conditions, which caused the DNI to be low. The primary mirror was cleaned with water and windex prior to testing. This test was performed the same way as the previous test, manually tracking in the E/W direction over an hour long period while recording the projected shadow of the receiver on the mirror surface for data correction. Efficiencies are corrected to assume full illumination and full vacuum (heat loss is added). Dips in the efficiency are caused by off-axes data due to manual tracking error. Condensation is still present inside the glass tube, and the vacuum gauge measured 4.6E-2 at its lowest. It took about 3 hours to reach 200 °C which is near the temperature limit for the loop. At 200 °C there is about 3 Watts of heat loss from the HT loop in the receiver. The average on-sun efficiency was 0.249 with a maximum efficiency of 0.342.

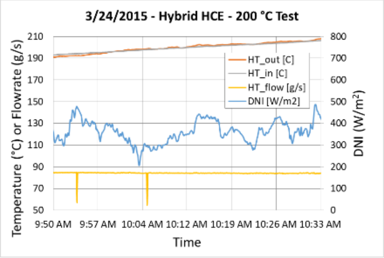

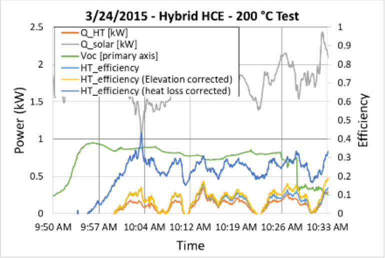

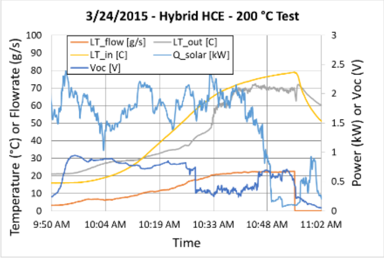

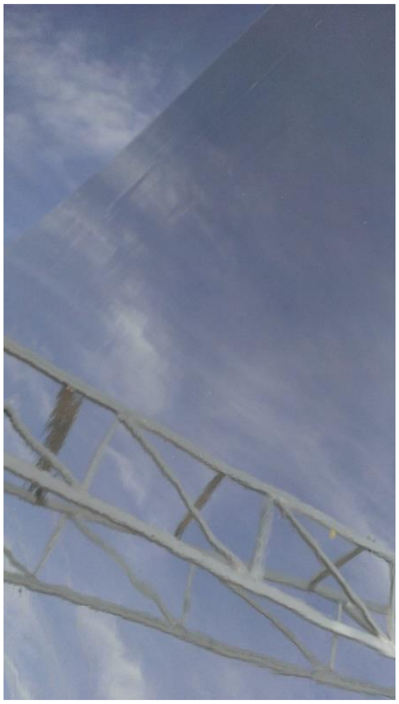

Clean primary mirror surface

Condensation still present

March 25th 2015 – 200 °C Test, High DNI

This test was performed under clear conditions. Efficiencies are corrected to assume full illumination and full vacuum (heat loss is added). Dips in the efficiency are caused by off-axes data due to manual tracking error. Condensation is still present inside the glass tube and the vacuum gauge measured 4.6E-2 during testing. It took about 2 hours to reach 200 °C, during which insulation was added to the high temp receiver inlet/outlet, mains pump, Coriolis flow meter, flex hoses, and small areas of exposed pipe to increase heat retention in the loop. Shortly prior to testing the AUX heaters short circuited and stopped functioning.

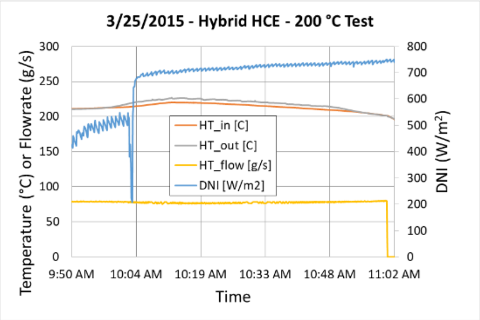

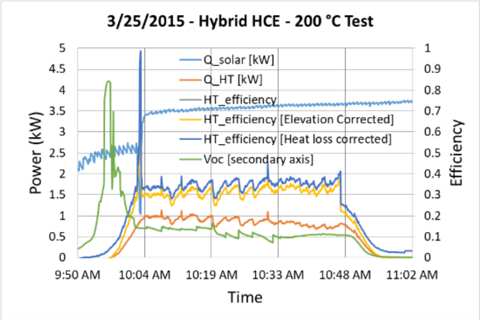

At 200 °C with the new insulation there is about 0.12 kW of heat loss from the HT loop in the receiver. No open circuit voltage was measured from the cell, indicating it is again somehow disconnected. The NIP tracker eye was adjusted just at the start of testing. It was under-reading the DNI and its adjustment caused a spike in the data around 10 am.

March 26th 2015 – 160-220 °C Test, High DNI

This test was performed under clear sunny conditions. The vacuum gauge measured 3.4 E-2 mbar during testing, despite the fact that condensation is still present in the tube. The average on-sun efficiency was 0.333 with a maximum of 0.374.

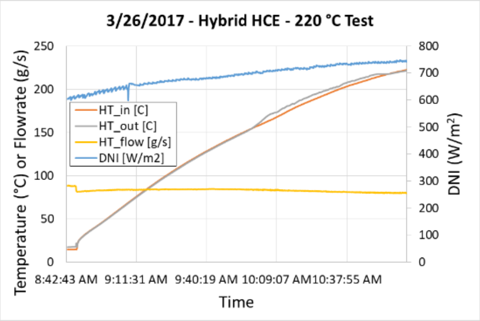

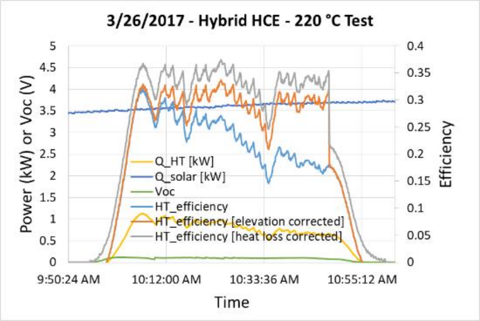

March 27th 2015 – 320-350 C Test, High DNI

This final test was performed under clear sunny conditions. Condensation was still present and the vacuum gauge read 2.2 E-2 mbar during the test. More insulation was added to the loop and receiver prior to testing.

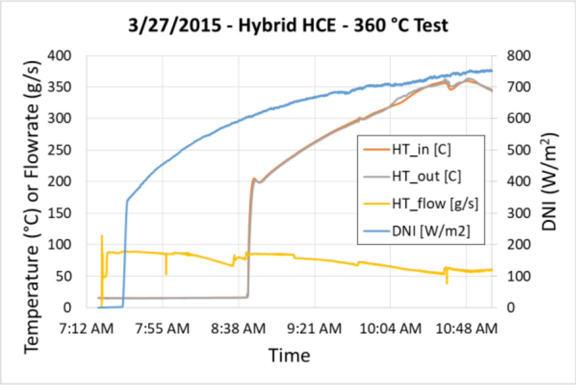

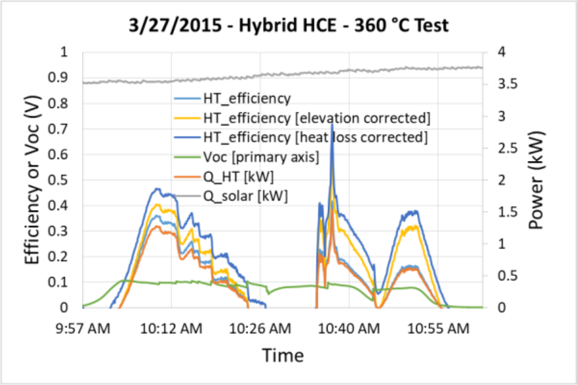

3.4.4 Experimental Performance Summary

After testing the Hybrid PV/T receiver was taken down and photographed. A composite image along the length of the tube is shown below, followed by an image of the end connections.

Figure 3.39 – *Hybrid HCE after experimental testing*

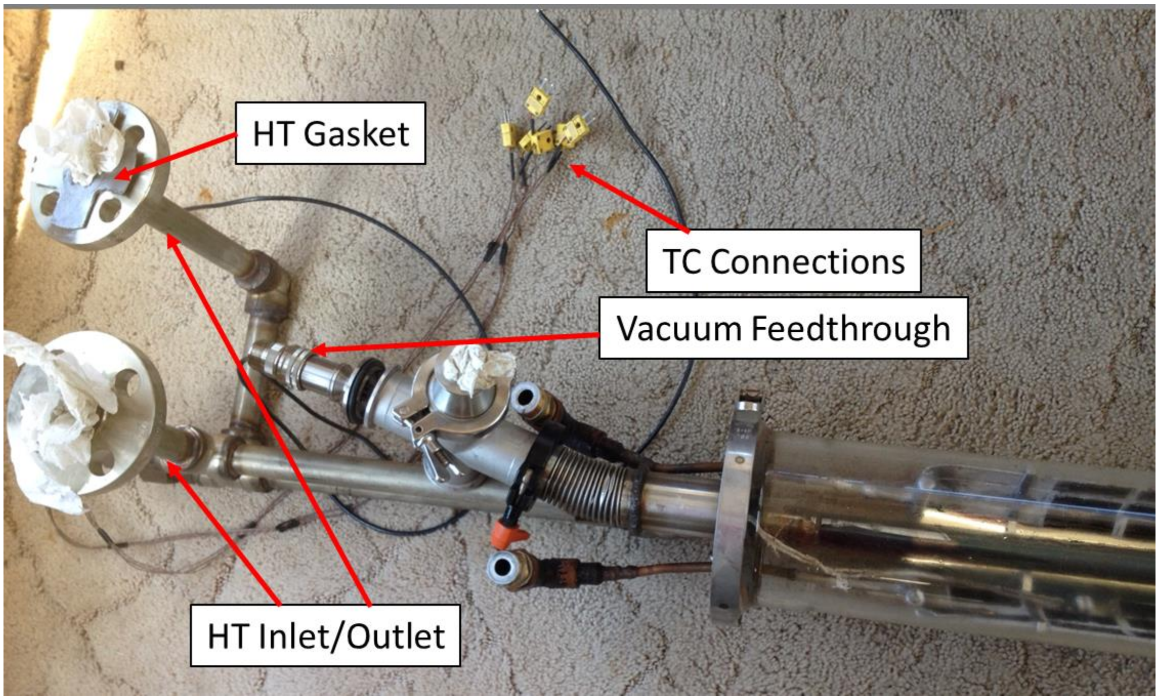

Figure 3.40 – *Hybrid HCE end connections*

The results of all performance tests are summarized and compiled into Table 3.6 and Figure 3.41.

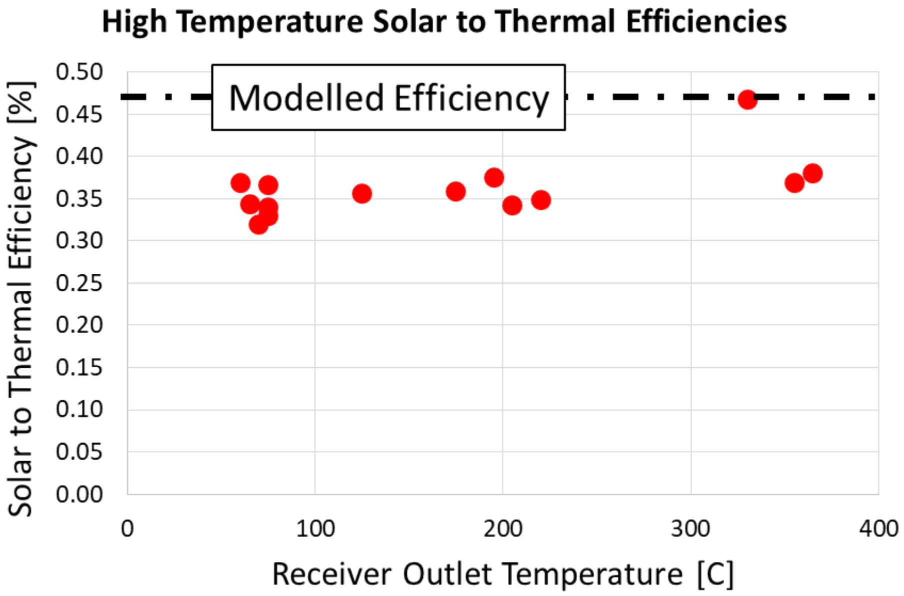

Figure 3.41 – *Thermal performance results*

Test Date	Outlet Temp [C]	Corrected Efficiency	DNI [W/m2]	Flowrate [g/s]	Ambient Temp [C]
9-Mar-15	75	0.339	650	65	18
10-Mar-15	60	0.369	250	40	20
12-Mar-15	70	0.320	650	45	14
13-Mar-15	65	0.344	660	100	15
13-Mar-15	75	0.330	680	100	16
14-Mar-15	175	0.359	370	60	18
20-Mar-15	75	0.367	200	65	19
23-Mar-15	125	0.356	700	85	15
24-Mar-15	205	0.342	350	85	14
25-Mar-15	220	0.348	750	80	14
26-Mar-15	195	0.375	700	80	18
27-Mar-15	330	0.467	750	55	18
27-Mar-15	355	0.368	750	55	20
27-Mar-15	365	0.380	750	55	20

Table 3.6 – Thermal performance results

The best direct electrical efficiency data obtained was on March 20th under highly cloudy conditions. The output voltage of the PV cell was measured and electrical efficiency calculated and the results are shown in Figure 3.42. The maximum solar to electric efficiency of the CPV subsystem was around 8%, the short circuit current (I_{sc}) was 230 mA and the fill factor (FF) was determined to be 84.3%.

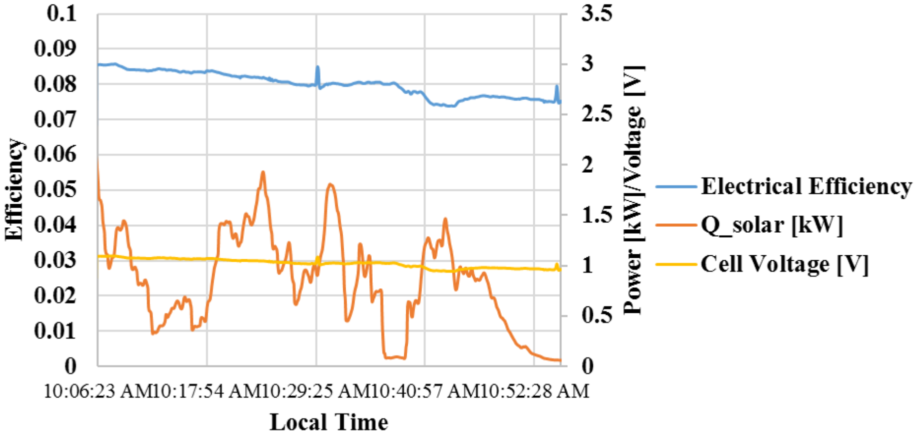

Figure 3.42 - *Direct solar to electric efficiency of GaAs cells (March 20, 2015).*

3.4.5 Discussion

The high temperature thermal performance tests produced efficiencies which were lower than the simulated 47% optical efficiency. The receiver operates with efficiencies around 37% at 360 °C under 750 W/m^2 DNI conditions. Reduced performance is at least partially due to a number of aspects of the prototype receiver that deviate from the ideal design, including:

- The reflector formed by the 3 flat minichannel surfaces is not an ideal CPC.
- The minichannel reflector is not entirely covered by GaAs cells. Approximately 80% is covered, with 20% of it being exposed aluminum from the minichannels, bulkheads, or dried thermal paste, which are less reflective.
- Alignment of the CPC reflector and high temperature absorber within the glass tube are prone to adjustment after mounting.
- Light bleed (missing target) and aberrations from primary mirror.

One of the problems we had with the high temperature test loop was an inability to pull a strong vacuum in the receiver tube, even after evacuating constantly for several days. Just outside the receiver cap, where our vacuum gauge was located, we measured a vacuum as low as 2.2e^{-2} mbar. Condensation was still formed on the inside surface of the glass tube indicating a lower vacuum inside the tube itself. To account for heat loss caused by an inadequate vacuum, all thermal efficiencies were heat loss corrected. The heat loss measured prior to the on-sun test was added to the thermal gain during test to adjust to zero heat loss. As a result of these corrections, the efficiency vs. temperature graph is flat and does not decrease with temperature as you would expect in a non-corrected evacuated system due to increased radiative loss. In fact, due to these corrections, the efficiencies at temperature are simply measurements of the optical efficiency. The fact that they all lie along the same line is indicative that these adjustments and corrections are fair and consistent even under varying test conditions.

Over time the condensation in the glass tube slowly disappeared (likely due to high test temperatures). This is one explanation for why the efficiencies increase slightly with temperature, since the highest temperatures were tested last.

The 47% efficiency at 330 °C is sort of an anomaly. After looking at the data for that test, there is no clear reason for the increased efficiency (DNI and flow rate were very stable). It is included for completeness.

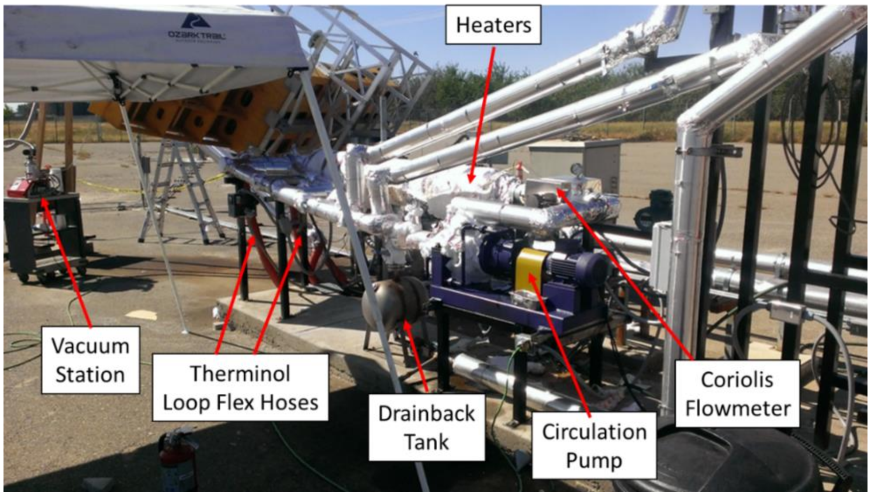

Figure 3.43 - *Back end of the test setup, heavily insulated to reach 360 °C.*

Fully illuminated receiver

Fully illuminated receiver

Light bleed from primary mirror

Figure 3.44 – *On-sun tests*

3.5 Summary

In this chapter, a novel two-stage hybrid CPV/CSP solar collector designed to simultaneously generate electricity and high temperature dispatchable heat was fabricated and tested. While the technical targets were not reached, this phase of the project (generation 1 prototype testing) resulted in the acquisition of experimental experience, resulting in several major lessons learned:

- **Cell Adhesive**: The OmegaTherm (thermal paste) did not maintain its adhesive properties at elevated temperatures and in a partially evacuated environment. Over time, many solar cells fell off the minichannels and had to be tied using enameled copper wire. For this application a better adhesive needs to be found.
- **Vacuum Subsystem**: Vacuum systems are incredibly challenging and we were never able to pull a proper vacuum inside the receiver during testing. This could be from a number of things:
    - Outgassing from the OmegaTherm under partial vacuum
    - Internal leaks: the minichannels may not have been 100% sealed since there were many difficult welds.
    - Assembly leaks: the end cap may not have been fully sealed since there are a number of components that feed through (cooling, vacuum, thermal, and electric). The end cap may also not have been fully secured since a number of heavy components weigh it down.
    - Improper placement of the vacuum gauge in the installation never allowed us to accurately monitor the pressure inside the tube.
- **Cooling Subsystem**: The cooling loop never worked as we were never able to get any flow of Duratherm 600 oil through the minichannels. This indicates either clogged minichannels or an incredibly high pressure drop which prohibited the flow of cold oil.
- **Electrical Subsystem**: Pulling the electrical leads out of the receiver was a challenge. The lead wires disconnected several times during testing, perhaps due to poor connection to the cell (lead wires from cell were extremely thin). Furthermore, connection to the feed through is challenging and especially cumbersome when the entire assembly needs to be disassembled / reassembled multiple times.
- **Secondary shape**: Maintaining the shape of the CPC using minichannels is a challenge. The use of ribs meant that several sections could not be covered by dummy cells, reducing overall reflectivity.
- **Number of subsystems**: The sheer number of components that are involved in a spectrum splitting receiver makes the entire assembly a challenge as there are a high number of risks and failure points. Getting them all to work at the same time is an impressive feat.
- **Temperature:** Reaching 360 °C using Therminol VP-1 in a small prototype system was also a challenge and required large heaters, significant insulation, and high pressure. Small pumps capable of these temperatures do not typically exist. High temperature components are trickier and more expensive to source.
- **Tracking**: Tracking a 45° parabolic mirror is a challenge for 2 reasons:
    - The long focal length means any sun-tracking sensor must be highly accurate. Most commercially available systems do not achieve the required accuracy
    - The long focal length acts as a boom arm, making it very difficult for the elevation actuator to lift the entire setup. This caused our elevation arm to not work and we had to support the entire setup using wooden 2x4 wooden planks. This limited our on-sun

testing by requiring us to wait until the sun passed over to do a “sun-sweep”. Our receiver was rarely fully illuminated requiring us to correct for partial illumination.

- **Fire Safety**: Having a large focusing mirror outdoors is dangerous. Not only did we accidentally destroy our Hybrid HCE do to inadvertent weekend illumination with no flow or cooling, but several wooden support struts and other components were inadvertently scorched over time. Care must be taken to properly stow the mirror in the correct position or always move things out of the potential focus area during the day.

These modifications were incorporated into the generation 2 design discussed in Chapter 5. In the next chapter, optimization of the secondary shape under the constraint of flat solar cell segments is investigated.

4. Segmentation of the CPC

The contents of this chapter have been published in-part as conference proceedings and a journal article:

Widyolar, B., Jiang, L. and Winston, R., 2017, September. Thermodynamic investigation of the segmented CPC. In *Nonimaging Optics: Efficient Design for Illumination and Solar Concentration XIV* (Vol. 10379, p. 103790L). International Society for Optics and Photonics.

Widyolar, B.K., Jiang, L. and Winston, R., 2017. Thermodynamics and the segmented compound parabolic concentrator. *Journal of Photonics for Energy*, *7*(2), p.028002.

In the previous prototype demonstration, a CPC was approximated by flat solar cell strips which had the effect of dropping the geometric efficiency (with perfect optical surfaces) of the secondary to 91%. In this chapter, the optics behind segmented CPCs are investigated and their characteristics uncovered to assist in the design of the generation 2 secondary CPC.

The efficiency of a 3D CPC approximated by facets was first discussed by Segal et al. (1994) for use as a secondary concentrator from a heliostat field. Optimization was explored by Timinger et al. (2000) for both homogeneous and non-homogeneous input radiation, and further developed by Cooper et al. (2013) who investigated the additional effects of circumferential faceting. Jafrancesco et al. (2012) described different methods for approximating a 2D CPC with flat absorber.

To date there has been no research into the effect of profile segmentation for CPCs with tubular absorbers. The traditional figures of merit (optical efficiency, concentration ratio) are adequate when describing ideal concentrators, but fall apart when dealing with non-ideal concentrators because the geometric optical efficiency is not directly correlated with flux. As a result, geometric concentration ratios *can* be larger than the theoretical limit by having optical efficiencies less than one (Benitez et al. 1997).

In this chapter, the concept of Flux Efficiency (FE) is developed. It is a parameter which combines the optical efficiency and concentration ratio and is capable of fairly comparing collectors, both ideal and non-ideal, based on the universal maximum flux achievable according to the laws of thermodynamics. This allows further investigation into the relationship between the number of segments and optical transmission of a CPC with cylindrical absorber approximated by equal length segments whose start and end points lie along the CPC profile. A separate method for generating CPC-like profiles by adjusting the angle of each segment to satisfy the edge-ray principle is also investigated.

The results are used to optimize the secondary CPC in the generation 2 prototype.

4.1 Non-ideal nonimaging systems

4.2.1 Reciprocity Theorem

Consider a typical problem in radiation concentration (Figure 4.1): a radiation source 1 passes its energy through the aperture 2 of an unknown optical concentrator and arrives at absorber 3.

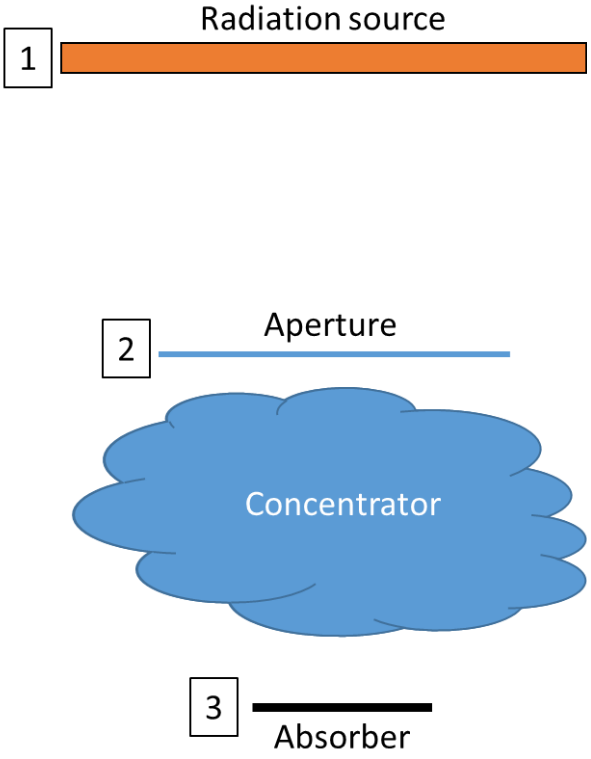

Figure 4.1 - *A typical radiation concentration problem*

We define the probability of radiation leaving one surface and hitting a second surface as

$$P_{12} = \frac{radiation\ from\ 1\ to\ 2}{total\ radiation\ emitted\ from\ 1} \tag{4.1}$$

Here P_{12} is different from the conventional view factor used in radiative heat transfer, F_{12}, because where F is simply geometric, P includes radiation that is indirectly transferred through reflection, refraction, and other ideal, lossless optical mechanisms (i.e. light transferred through the geometry of some optical system).

Assuming black body radiation, the radiant power transferred from 1 to 3 (Q_{13}) can be described as

$$Q_{13} = A_1 \sigma T_1^4 P_{13} \tag{4.2}$$

Here σ is the Stefan-Boltzmann constant and T is temperature of the emitting surface in degrees Kelvin. Using the principles of reciprocity (Modest, 2013), we can write the following equation, where A is the area of the surface.

$$A_1 P_{13} = A_3 P_{31} \tag{4.3}$$

In order to know the radiative flux from 1 to 3 at the surface of the absorber (q_{13}), we divide Q_{13} by the area of the absorber surface (A_3).

$$q_{13} = \frac{Q_{13}}{A_3} = \frac{A_1 P_{13}}{A_3} \sigma T_1^4 = P_{31} \sigma T_1^4 \tag{4.4}$$

Because $P_{31} \leq 1$, the radiative flux arriving at 3 cannot exceed the surface flux of the radiation source. Consequently, the temperature of surface 3 will not exceed the temperature of the radiation source.

Notice that the flux q_{13} at the absorber surface is proportional to P_{31}. This is a counter-intuitive conclusion in that the intensity of radiative flux received by 3 is directly related to where the virtual radiation leaving 3 would end up. This allows for a new paradigm in the optical design of concentrators, which focuses on the radiation leaving the absorber rather than radiation leaving the source.

4.2.2 Solving for P_{31}

To quantify the optical loss in the concentrator, we define the optical efficiency (η) as the amount of light leaving the source and striking the absorber divided by the amount of light leaving the source and striking the aperture.

$$\eta = \frac{P_{13}}{P_{12}} \tag{4.5}$$

Using the reciprocity theorem as before we can write the relationship between surface 1 and surface 2:

$$A_2 P_{21} = A_1 P_{12} \tag{4.6}$$

Using equations (4.3), (4.5), and (4.6), and introducing the geometric concentration ratio C of the concentrator (A_2/A_1), we arrive at:

$$P_{31} = \frac{\eta A_2}{A_3} P_{21} = \eta C P_{21} \tag{4.7}$$

As shown in previous work (Winston 2012), P_{21} is directly related to the maximum concentration ratio according to the 2nd law of thermodynamics, where

$$C_{max} = \frac{1}{P_{21}} \tag{4.8}$$

Therefore equation 4.7 is transformed into

$$P_{31} = \frac{\eta C}{C_{max}} \tag{4.9}$$

P_{31} as shown in eq. (4.4) and (4.9) is essentially the Flux Efficiency (FE), which describes the energy density (W/m^2) relative to the maximum achievable at the absorber surface through the laws of thermodynamics.

$$FE = P_{31} = \frac{\eta C}{C_{max}} \leq 1 \tag{4.10}$$

The FE is directly related to the flux the absorber receives from the source and quantifies how close the concentrated flux is, to the theoretical maximum. A concentrator with an FE of 1 will allow the absorber to reach the highest temperature according to the 2nd law, equal to the temperature of the source. The FE multiplied by the flux at the source will determine the flux at the absorber.

4.2.3 P_{31} in a two-dimensional system

In the application of radiative energy collection, the maximum concentration ratio of a collector under the assumption of no optical loss has been demonstrated according to both the conservation of etendue and the 2nd law of thermodynamics as $C_{max} = 1/sin(\theta)$, for a 2-D system of half-acceptance angle θ_a.

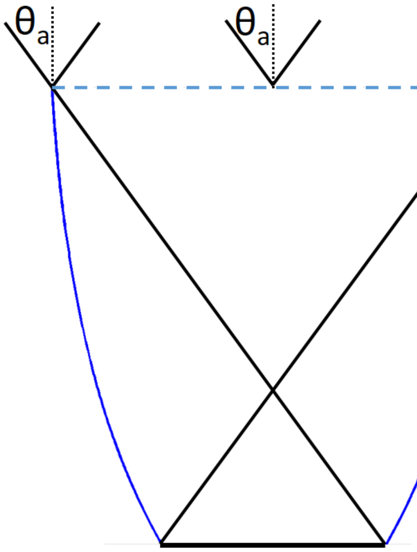

Figure 4.2 - *Simple CPC accepts incoming light which subtends half acceptance angle* θ_a.

The efficiency η can be calculated from its definition (4.5).

$$\eta = \frac{P_{13}}{P_{12}} = \frac{Radiation\ from\ 1\ arriving\ at\ 3 / \cancel{Radiation\ from\ 1}}{Radiation\ from\ 1\ arriving\ at\ 2 / \cancel{Radiation\ from\ 1}} = \frac{\int_0^{\theta_a} \eta_o\, cos\theta\ d\theta}{\int_0^{\theta_a} cos\theta\ d\theta} \tag{4.11}$$

Here η_0 is the optical efficiency of the concentrator at a specific incidence angle θ and the cos θ term accounts for the cosine effect.

$$\eta = \frac{\int_0^{\sin\theta_a} \eta_m\, d(\sin\theta)}{\int_0^{\sin\theta_a} d(\sin\theta)} \tag{4.12}$$

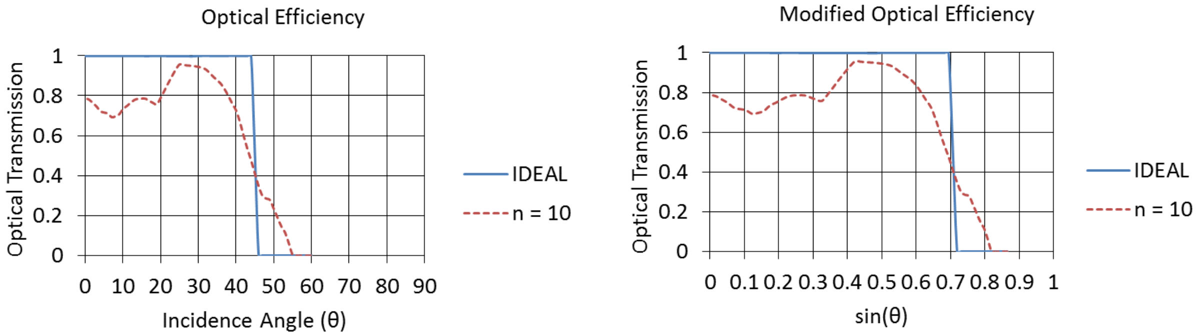

a) b)

Figure 4.3 *a) Optical efficiency vs b) Modified optical efficiency for two 45 degree concentrators, one ideal and one arbitrarily chosen non-ideal concentrator constructed from 10 segments using the segment approximation method.*

To have a better visual understanding of the integral which includes the cosine effect, the modified optical efficiency η_m, which is a function of $\sin\theta$ instead of θ, is used.

The difference is visually demonstrated in Figure 4.3, where we show results for an ideal maximally concentrating concentrator and an arbitrarily chosen non-ideal concentrator made from n = 10 segments. Both of these concentrators have an acceptance angle of 45° and perfect reflective surfaces (i.e. 100% reflectance). Figure 4.3 (a) depicts the traditional optical efficiency as a function of incidence angle (incidence angle modifier – IAM) for an ideal concentrator and a non-ideal concentrator (n = 10 segments). Figure 4.3 (b) depicts the modified optical efficiency as a function of sin θ for the same two concentrators.

Since the traditional IAM is a function of θ, the areas under the curves have no physical meaning because they do not account for the cosine effect. The areas under the curves in Figure 4.3 (b), however, are exactly the integrals described in equation 4.12 and thus can be used to visually gauge the optical efficiency of a collector.

4.2 Segmentation of the CPC

Now that we have described the flux efficiency (FE) we can properly compare non-ideal collectors. In this section we systematically analyze several different methods for approximating CPC reflector profiles with flat segments.

4.2.1 Ideal CPC Profile Generation

The ideal CPC with half-acceptance angle θ is generated by numerical approximation of the string method (Winston and Hinterberger, 1975) as outlined in Figure 4.4.

Starting at the base of the receiver and stepping along the circumference by one degree at a time, the unraveled string length ($r\phi$) is projected tangent to the step point (A) on the receiver to produce the involute curve (B). Once 90° + θ is reached, a virtual slider is created (at C) and the lengths of string from the receiver to reflector profile (AB) and from the reflector profile to the slider (BC) are stored. With each additional step the new unraveled length is added to the length of AB and the total length of string (AC). The reflector point (B) and the position where the string meets the slider (C) are projected based on their respective string lengths. If point C is above the slider, a small amount of string is moved from BC to AB and vice versa if it is below until point C is within a specified tolerance from the true slider position. This process continues until 270° - θ is reached.

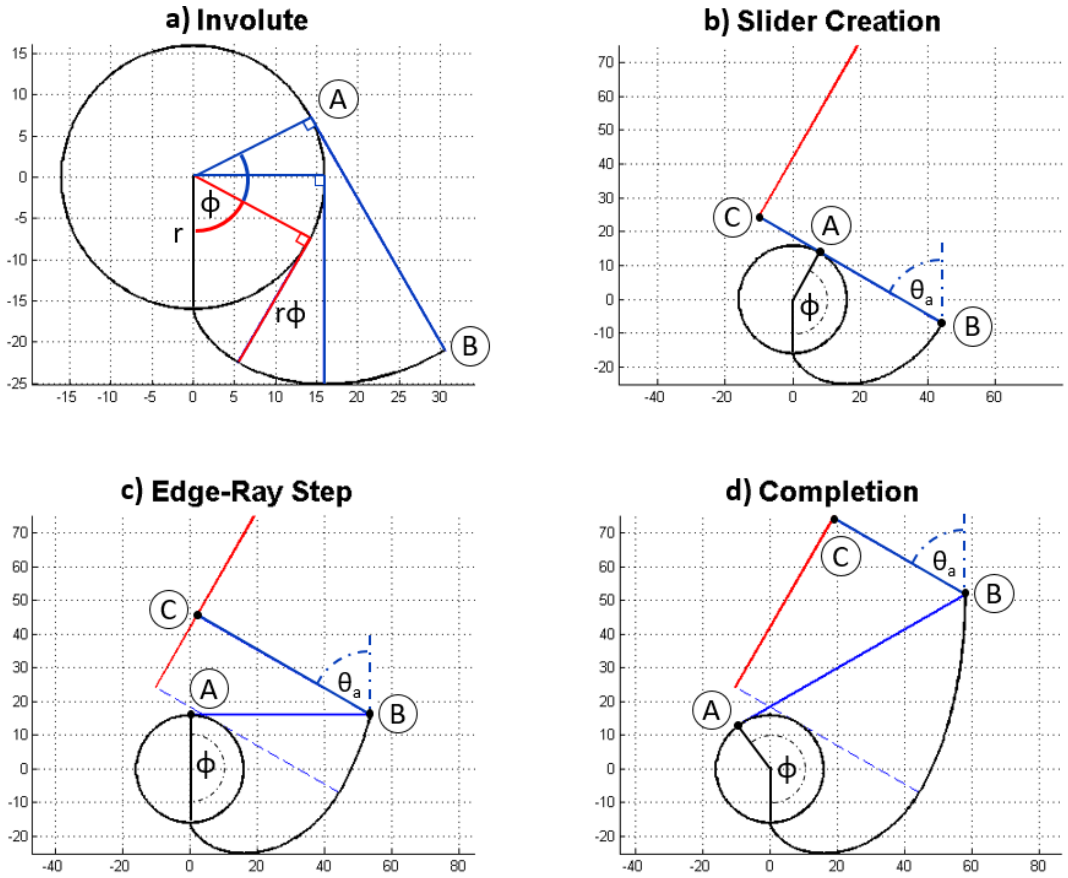

Figure 4.4 – *Numerical approximation of CPC using the string method by unravelling from the absorber starting at $\varphi = 0°$. The beginning of the CPC is approximated by an involute (top left) where the length AB is projected tangent to A at a length $r\phi$. Then a virtual slider is created (top right) to simulate edge rays entering at the extreme angle θ. The total string length (AB + BC) becomes a constant, with each step adding ($r\phi$) to the total string length. The point B is found by adjusting the string lengths under the constraints that AB is always tangent to A, and C always lies on the virtual slider. This continues until $270° + \theta$, or until the reflector profile curves back in on itself.*

With this method there is no propagation of error as each point is determined from the receiver and not based on the previous point. The CPCs generated using this method are displayed in Figure 4.5 with blue and red rays representing the edge rays for the involute and wing parts of the profile.

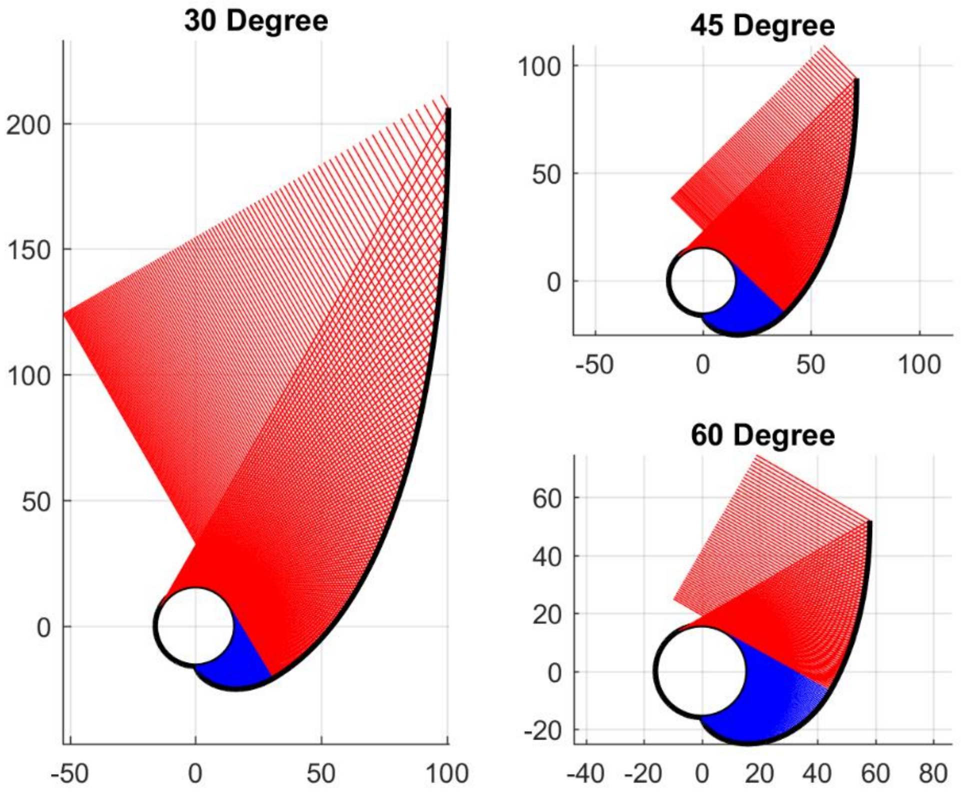
30 Degree

45 Degree

60 Degree

Figure 4.5 – *Numerically approximated CPCs for* θ *= 30° (left), 45° (top right), and 60° (bottom right). Rays within the involute region are drawn in blue and edge-rays for the "wing" portion of the CPC are drawn in red. The X and Y coordinates represent real dimensions.*

The ideal CPC guarantees the most extreme-angle ray (Ries and Rabl, 1994) is directed towards the most extreme edge of the absorber. This is known as the edge ray principle (Winston et al. 2005) and is valid at all points along the ideal reflector profile. A segmented CPC, however, cannot guarantee the edge ray principle at all points along the segment and therefore one faces the choice of how to choose the location on a particular segment where edge ray principle is satisfied.

4.2.1 Simple Segment Approximation

The easiest method is to approximate the reflector profile by n equal length segments whose start and end points lie on the ideal reflector profile. Since the slope of each segment is somewhere between the slope of the ideal reflector at the start and end points of the segment, the edge ray principle must be satisfied at some location along the segment.

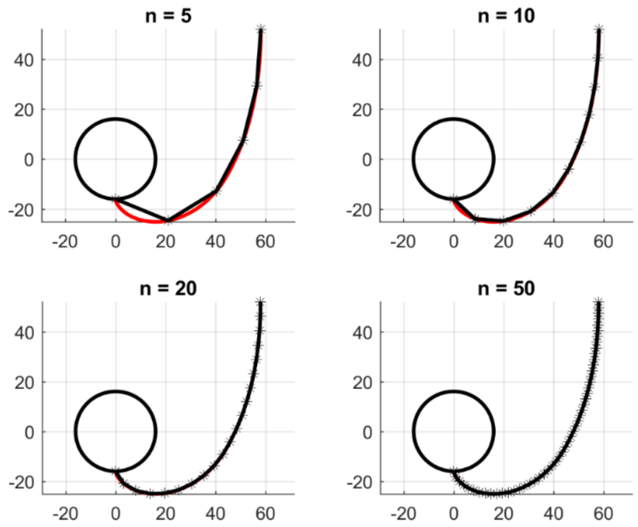

Figure 4.6 – *Profiles of ideal 60° CPC approximated by n equal length segments. The ideal CPC is drawn in red and overlaid by the segmented approximation in black. * indicates segment endpoints. The X and Y coordinates represent real dimensions.*

4.2.2 Projection Angle Approximation

Another way to approximate the ideal CPC is to project a small segment at an angle that guarantees the edge ray principle is satisfied. As you increase the number of segments you approach the ideal profile. At smaller numbers of larger segments, the profiles can be substantially different and depend greatly on the position along the segment the edge ray principle is enforced. For this analysis, three variations are investigated where the edge ray principle is enforced at the start, middle, and end of each segment.

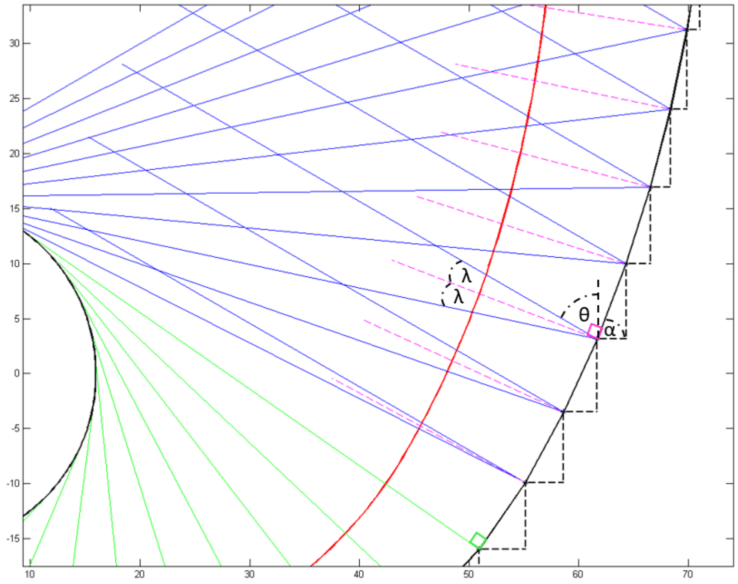

Figure 4.7 – *Profile generation for start, mid, end point projection methods. α is the projection angle of the segment, θ is the incoming edge ray angle, and λ is the half angle that guarantees the incoming edge ray is directed tangent to the absorber.*

Using the start point projection method as an example, each segment in the involute portion is projected orthogonal to the tangent angle to the receiver. This method guarantees that the first segment is vertical. Past the involute, the projection angle α for the segment is orthogonal to θ + λ, where theta is the acceptance angle and lambda is the half angle between theta and the line tangent to the receiver (see Fig 4.7). This method guarantees that any ray leaving the edge of the absorber is reflected back to itself within the involute, and any ray entering at the acceptance angle is reflected tangent to the absorber. Results for a 60° ideal CPC approximated using the start point method are shown in Figure 4.8.

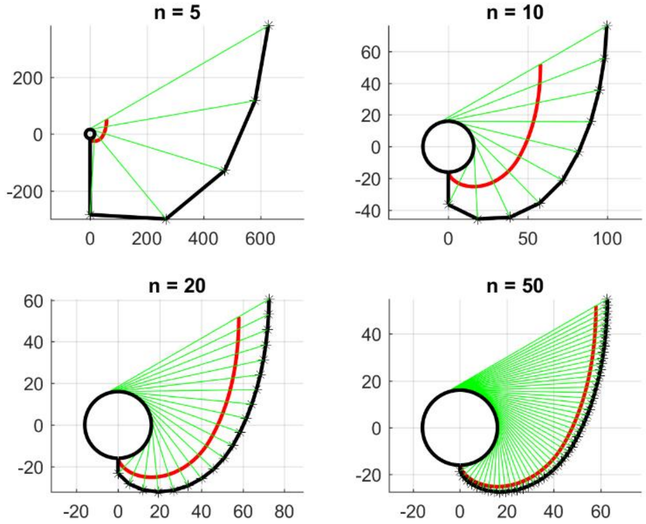

Figure 4.8 – *Profiles of ideal 60° CPC approximated by n equal length segments using the start point projection method. The ideal CPC is drawn in red and overlaid by the segmented approximation in black. * indicates segment endpoints. Green rays indicate the tangent ray, from which the segments are projected perpendicularly. In the start point projection method the tangent ray is taken at the starting point of the segment. X and Y coordinates represent real dimensions.*

For the midpoint and end point projection methods, a projection angle is guessed to locate the midpoint and end point for tangent calculations. Once the projection angle is adjusted, the point where the edge ray condition is evaluated is in a different location so the adjustment process is iterated until the change in projection angle between iterations is below a prescribed tolerance. Results for a 60° ideal CPC approximated using the midpoint method are shown in Figure 4.9 and for the same CPC approximated using the end point method in Figure 4.10.

When the desired number of segments is reached, the program checks to see if the endpoint of the final segment is above or below the tangent line from the last point of the ideal CPC to the receiver, adjusts the segment lengths accordingly, and repeats the entire process until the final segment point is within tolerable limits.

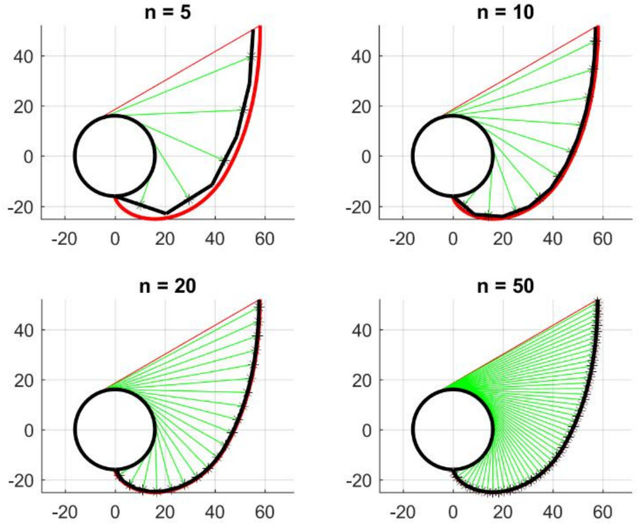

Figure 4.9 – *Profiles of ideal 60° CPC approximated by n equal length segments using the midpoint projection method. The ideal CPC is drawn in red and overlaid by the segmented approximation in black. * indicates segment endpoints. Green rays indicate the tangent ray, from which the segments are projected perpendicularly. In the midpoint projection method the tangent ray is taken at from the middle of the segment. X and Y coordinates represent real dimensions.*

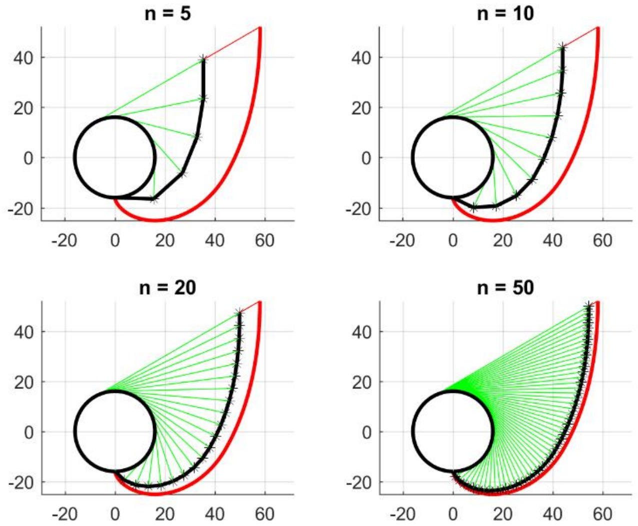

Figure 4.10 – *Profiles of ideal 60° CPC approximated by n equal length segments using the end point projection method. The ideal CPC is drawn in red and overlaid by the segmented approximation in black. * indicates segment endpoints. Green rays indicate the tangent ray, from which the segments are projected perpendicularly. In the end point projection method the tangent ray is taken at from the end of the segment. X and Y coordinates represent real dimensions.*

4.2.3 Summary

Multiple CPCs were generated using each method for acceptance angles 30°, 45°, and 60° and for various n numbers of segments. Examples of these methods for the case of n = 10 segments and θ_a = 60° are shown in Figure 4.11 where the ideal profiles are shown in red, the segmented profiles are shown in black, and the edge ray used for projections are shown in green. All profiles are produced for a cylindrical receiver with a 32 mm outer diameter with tolerated distances < 1/100th mm, and angles < 1/100th degree.

For all cases, approximating with the simple segment method maintains the aperture of the ideal CPC while the start point projection method produces profiles with larger apertures and the remaining two methods generate profiles with smaller apertures.

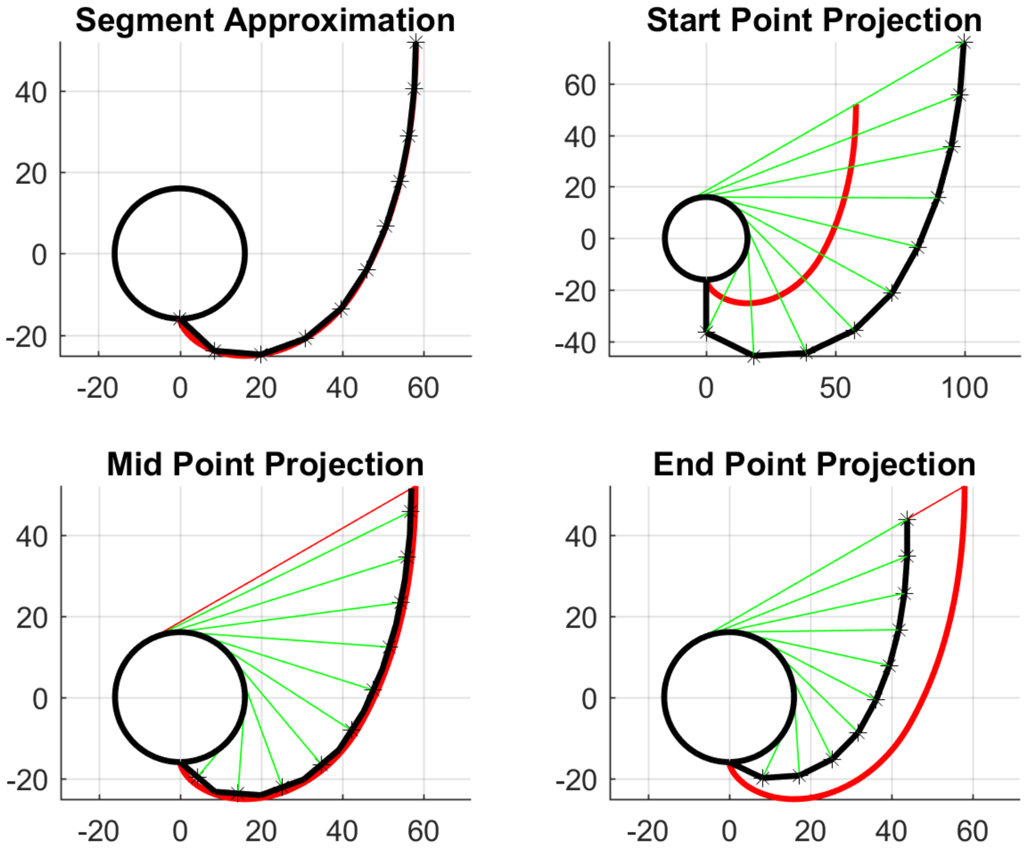

Figure 4.11 - *Approximated Profiles (n = 10, θ_a = 60°). Ideal CPC shown in red, segmented CPC shown in black, with rays used for edge ray calculation shown in green.*

4.3 Results

The numerically approximated versions of the ideal CPC used in this analysis reach flux efficiencies over 99%. This is to validate the ray tracing software's inaccuracies to be within tolerance.

	30 Degree	**45 Degree**	**60 Degree**
FE	99.5%	99.7%	99.8%

Table 4.1 – Flux efficiency of numerically approximated ideal CPCs

Incident Angle Modifier (IAM) curves for each of the approximated profiles are shown in Figure 4.12 below for varying number of segments. For all profiles, as the number of segments increases, the IAM curve becomes more like the ideal. The segment approximation and midpoint projection methods produce IAM curves similar to truncated CPCs with some light within the acceptance angle being rejected and some light outside the acceptance angle being accepted. The start point projection method guarantees that no light outside the acceptance angle is accepted, whereas the end point projection method guarantees optical transmission within the acceptance angle. Both of these conditions exist in the ideal concentrator, but by faceting with these different methods they are separated.

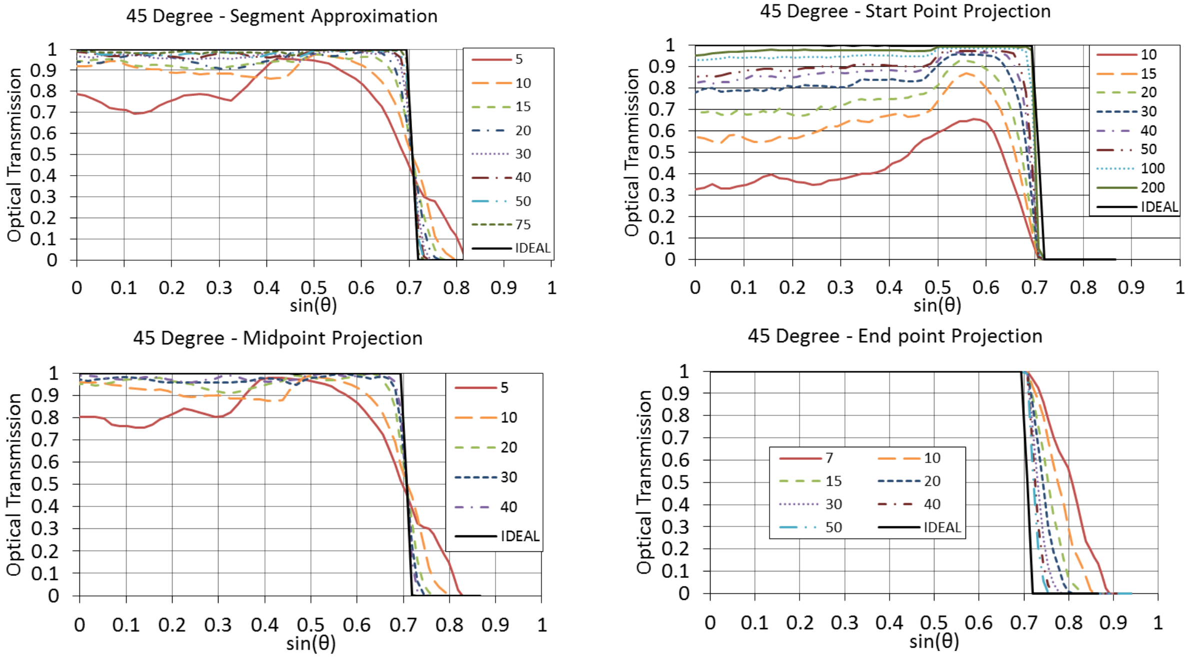

Figure 4.12 - *Modified IAM Curves of each method for different n numbers of segments*

The relationship between the flux efficiency (FE) and segment length is displayed for each approximation method in Figure 4.13. For all cases, as the segment length is decreased, the flux efficiency approaches 100%. The segment approximation and midpoint projection method producing similar trends for the FE, reaching > 95% when the ratio of segment length to receiver circumference is < 0.05. For a 32 mm diameter cylindrical absorber, this is a segment length of about 5 mm.

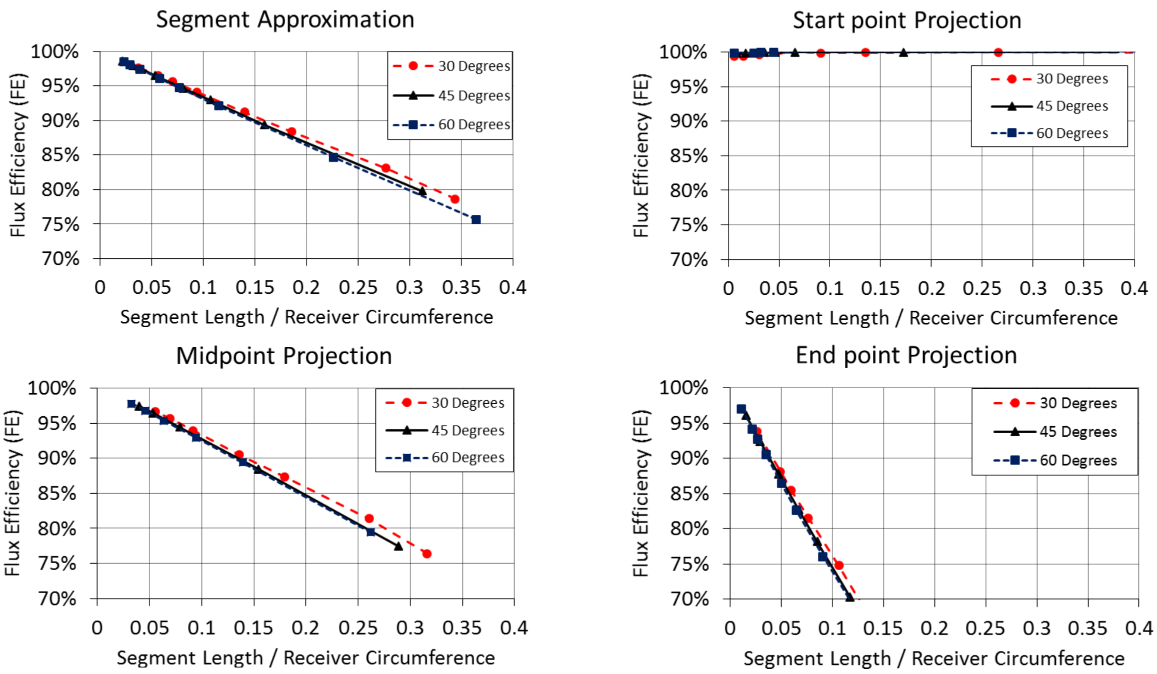
Segment Approximation

Start point Projection

Midpoint Projection

End point Projection

Figure 4.13 – *Flux efficiency versus segment length for all cases.*

4.2.5 Discussion

End point projection guarantees optical transmission within the acceptance angle and therefore all rays within the acceptance angle reaching the aperture are transmitted onto the absorber. This ensures optimal utilization of the aperture.

Start point projection guarantees that no light outside the acceptance angle is transmitted onto the absorber. This produces a flux efficiency (FE) of 100% regardless of segment size and guarantees optimal utilization of the absorber.

Recalling equation (4.10), the flux efficiency (FE) is a relationship between the optical efficiency (η, as defined in equations (4.11) and (4.12)) and the concentration ratio relative to the maximum (C/C_{max}).

$$FE = (\eta) \times \left(\frac{C}{C_{max}}\right) \leq 1 \qquad (4.13)$$

In the end point method, the concentration ratio is sacrificed for an optimization of optical efficiency, resulting in 100% optical efficiency at the expense of flux efficiency. In the start point method, however, all sacrifices in optical efficiency are compensated by increases in the geometric concentration ratio, guaranteeing a 100% flux efficiency.

With segmented profiles, either optical efficiency or flux efficiency can be chosen to be 100%, but not both. Both optical efficiency and flux efficiency are only guaranteed to be 100% in the ideal case.

Lastly the relationship between reflector length and the flux efficiency is shown in Figure 4.15 for all cases. At equal flux efficiency, end point projection requires the least reflector area, followed by midpoint projection and simple segment approximation. Start point projection guarantees a FE of 1 regardless of the segment size, but is impractical with larger segments since it requires significantly more reflector material.

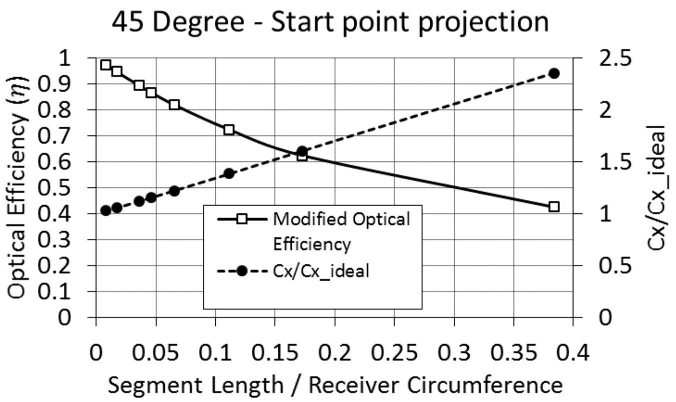

Figure 4.14 - *Tradeoff between concentration and modified optical efficiency in start point projection method*

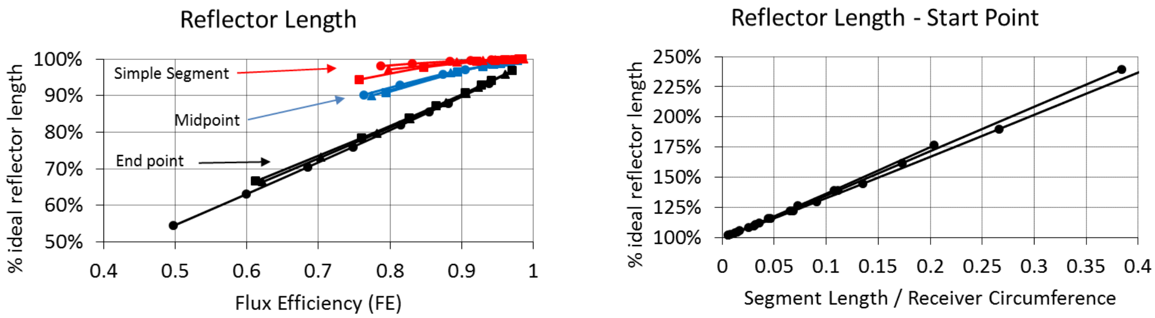

Figure 4.15 - *Reflector Lengths*

4.4 Summary

In this chapter, a new metric (Flux Efficiency) is developed which relates traditional optical efficiency and geometric concentration ratio to the maximum achievable flux allowed by a concentrator as set forth by the 2nd law of thermodynamics. This allows for fair comparison between ideal and non-ideal concentrators. Equipped with this tool, 4 different methods for approximating a 2D CPC profile using flat segments are outlined, simulated and analyzed.

Of the 4 methods described, two guarantee specific qualities of interest, i.e. 100% optical efficiency (end point method) and 100% flux efficiency (start point method). The ideal CPC will guarantee both 100% flux efficiency and 100% optical efficiency as it optimizes spatial and directional utilization of both the aperture and absorber. With segmented profiles, a compromise must be made favoring either optimization of the aperture or the absorber.

For the two-stage concentrators described in this dissertation, the concentration ratio of the primary is ~ 45X (5 meter parabolic aperture to ~ 110 mm secondary aperture). Since the secondary provides a maximum additional 1.4X concentration (45° CPC), we want to ensure optimal utilization of the secondary aperture so as not to waste the already highly concentrated light from the primary. Thus, the optimized secondary design discussed in the next chapter is developed using the endpoint projection method which guarantees that all light entering the aperture of the secondary will be transmitted to the absorber.

5. Generation 2 Prototype Development & Testing

The contents of this chapter section have been partially published in the following journal article, with the remaining contents pending publication:

Widyolar, B., Jiang, L., Abdelhamid, M. and Winston, R., 2018. Design and modeling of a spectrum-splitting hybrid CSP-CPV parabolic trough using two-stage high concentration optics and dual junction InGaP/GaAs solar cells. *Solar Energy*, *165*, pp.75-84.

In this chapter, the design, development, and experimental testing of a second generation hybrid CSP/CPV prototype is described. It is similar to the system described in Chapter 3, but with four main differences:

1. Dual junction InGaP/GaAs cells are used instead of GaAs
2. The secondary profile is optimized for geometric efficiency based on Chapter 4
3. The cells are operated at low temperature (~ 40 °C)
4. The thermal stream is operated at 600 °C using a particulate heat transfer fluid

Furthermore, a thermal-only (non-hybrid) HCE is also produced and tested for comparison.

5.1 Collector Design

5.1.1 Spectrum Splitting

The spectral efficiency of InGaP (dashed blue) and GaAs (dashed red) are plotted against the direct-beam solar spectrum in Figure 5.1. The in-band efficiency (η_{band}) of each cell is shown above the x-axis.

The Carnot efficiency (η_{Carnot}) is the thermodynamic limit for converting thermal energy into useful work calculated and is calculated using equation 1, where T_H is the hot reservoir temperature and T_C is the cold reservoir temperature. Real engines typically only reach 2/3 of this thermodynamic limit and this is plotted in Figure 6 (dashed red) for a target operating temperature (T_H) of 600 °C and cold reservoir temperature (T_C) of 37 °C, and listed as η_{band} for the thermal junction in Figure 6. Also listed below the x-axis are the fractions of the direct beam solar spectrum within each spectral region from 0-670 nm, 670-875 nm, and 875-2500 nm.

The in-band efficiency of each junction multiplied by the fraction of the solar spectrum in each band yields a total solar-to-electric conversion efficiency of 49.1%. This is higher than what is achieved by any of the subsystems under full spectrum alone. While optical, thermal, and conversion losses will reduce this number in practice, this demonstrates the potential of beam splitting systems to achieve higher conversion efficiencies through optimal utilization of the solar spectrum.

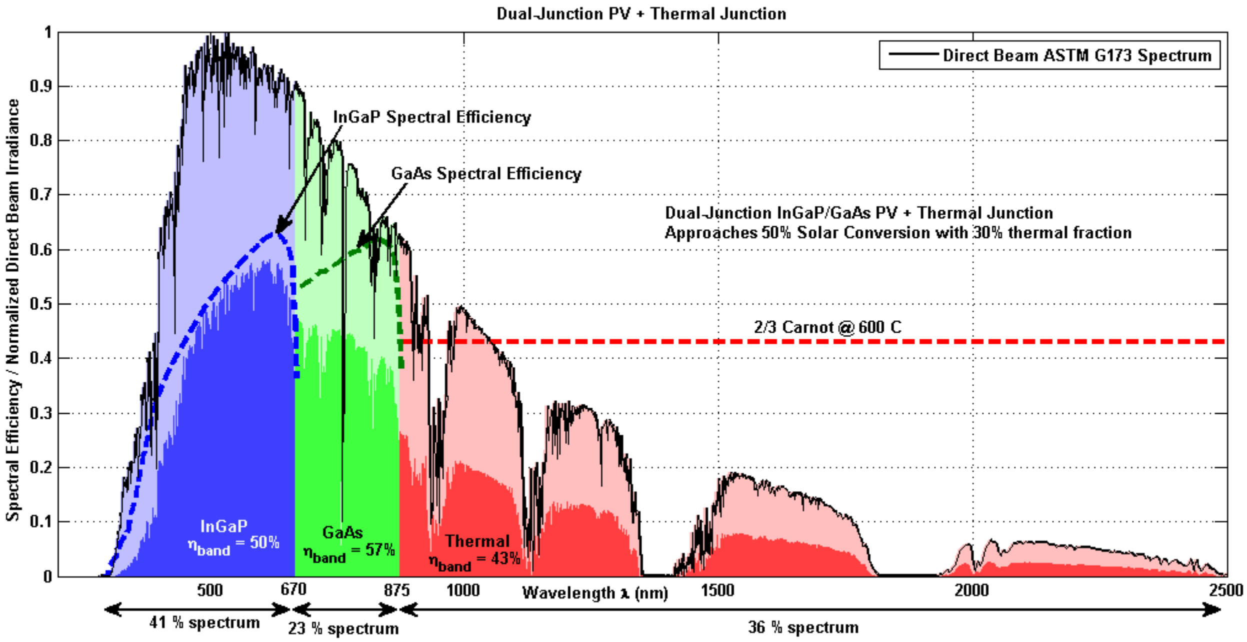

Figure 5.1 – *Spectral beam splitting with dual junction PV and third thermal junction. InGaP and GaAs spectral efficiency curves (dashed blue and green) are adapted from the solar cell efficiency tables. The in-band efficiencies (η_{band}) are calculated according to Eq. 5.2 for the solar cells and assuming 2/3 Carnot efficiency for the thermal junction. The fraction of the solar spectrum within each band is listed below the graph. Adding all of these together yields a solar-to-electric conversion efficiency which approaches 50% with a thermal fraction of 30%.*

5.1.2 Two Stage Optical Design

The main design parameters are the same as before. The geometry of the proposed two stage parabolic concentrator is plotted against a typical parabolic trough collector system in Figure 5.2.

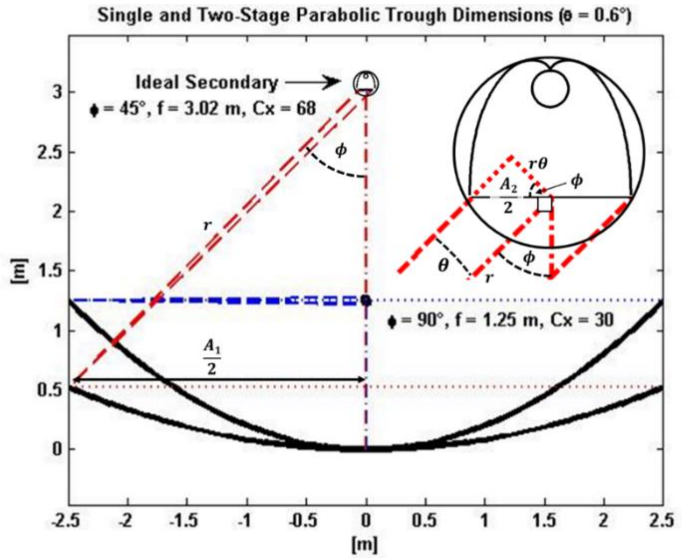

Figure 5.2 – *Proposed two stage parabolic trough collector (PTC) design (red) overlaying typical single-stage PTC design (blue) with listed half-rim angles (ϕ), focal length (f), and concentration ratio (C_x).*

5.1.3 Optimization of the Secondary

Sections of the secondary CPC are to be replaced with high efficiency back-reflecting solar cells (see Figure 5.3) which generate electricity from sub-bandgap photons and reflect remaining photons to the thermal absorber.

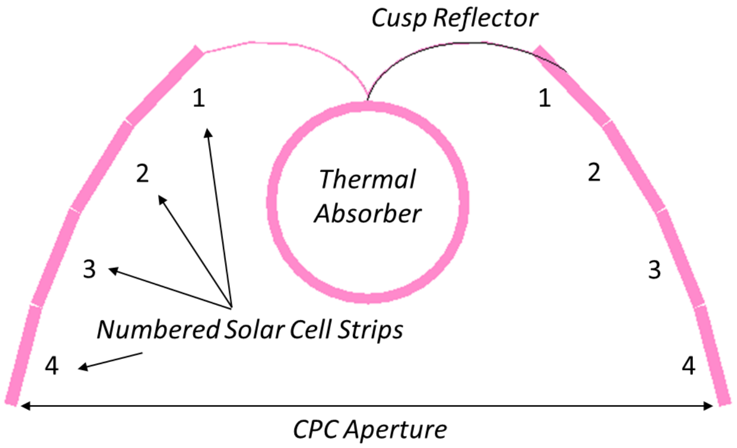

Figure 5.3 – *Secondary CPC*

Ray trace simulations generated the intensity profile along the CPC reflector in Figure 5.4. A high intensity band located 10 mm from the center of the CPC and extending approximately 50 mm represents the ideal location for the cell placement.

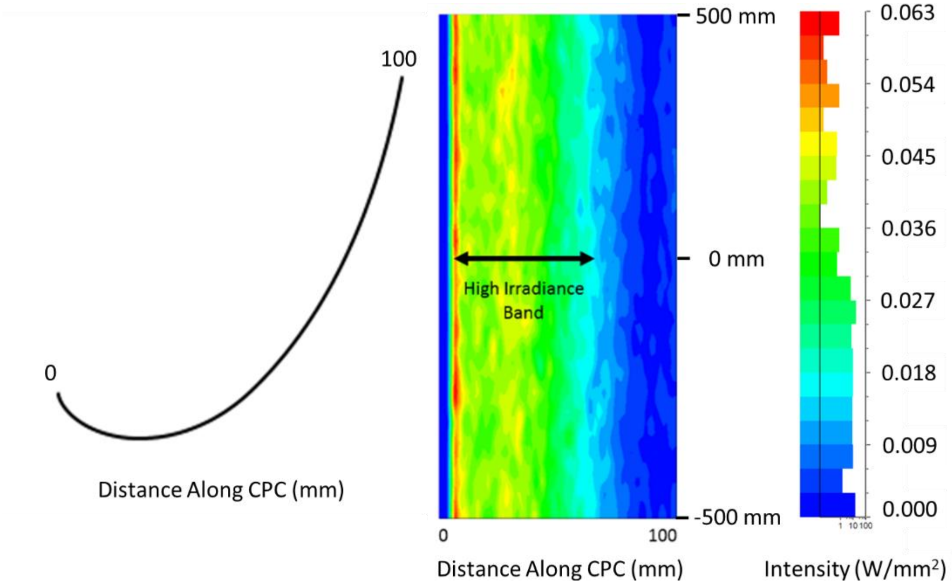

Figure 5.4 – *Local light intensity on ideal secondary CPC reflector as reflected from 45° primary parabolic trough. The high irradiance band begins roughly 10 mm from the center of the CPC and extends roughly 50 mm.*

Since the cells are not flexible, portions of the CPC profile must be approximated by flat segments. Ray tracing on a CPC approximated by 4 strips, however, reduced the geometric efficiency to 90%. To recover this loss a new design was developed to guarantee edge ray incidence on the absorber (see Figure 5.5). In doing the geometric efficiency was fully recovered, but at the expense of a 13% reduction in aperture area (concentration ratio). To maintain the required secondary aperture, the entire secondary design was scaled up to an absorber outer diameter of 32 mm. After these changes the system has a final geometric concentration ratio of $Cx = \frac{5000\ mm}{\pi * 32\ mm} = 50$, approximately 52% of the theoretical limit.

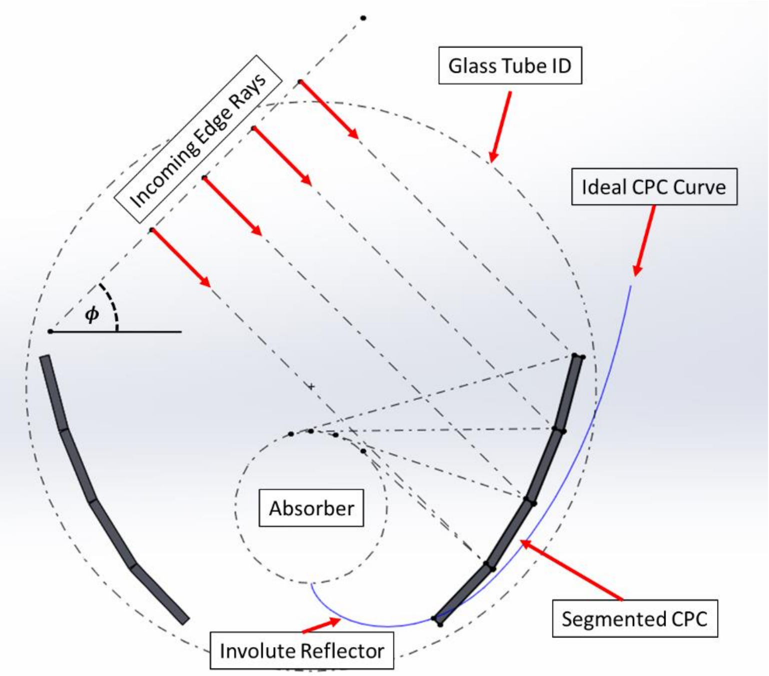

Figure 5.5 – *Optimized secondary CPC shape where portions of profile are approximated by flat segments. The optimized profile has 100% geometric efficiency despite its non-ideal shape.*

5.1.4 Final Two-Stage Optical Design Parameters

The final parameters of the two-stage optical system are listed in Table 5.1.

Design Parameter	Value
ϕ	45°
θ	0.6°
A_1	5 m
C_1	45X
C_2	1.1X
C_{total}	50X
CAP	0.52

Table 5.1 – *Two-stage concentrator parameters.*

Full system simulations with perfect optical surfaces and no shading for incoming light with a uniform ±0.25° angle spread produce the incidence angle modifier for the two-stage system shown in Figure 5.6. This verifies an intercept factor >0.9 for incoming angles up to 0.6°.

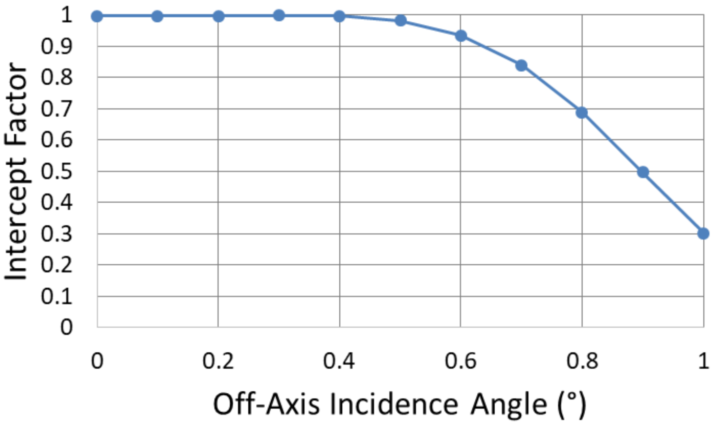

Figure 5.6 – *Geometric efficiency on thermal absorber using optimized CPC from Figure 5.5*

5.2 Modelling

In this sections, several HCE configurations are simulated for the purpose of down-selecting an optimal design. Varying numbers of strips (from 2-4 on each wing) of different solar cells (single junction, dual junction) are simulated for solar-to-exergy and solar-to-electric output. The optimal design is selected based on simultaneously maximizing solar-to-exergy (>40%) and solar-to-electricity efficiency.

5.2.1 Optical Model

Full optical simulations with relevant material properties were performed using 1 million rays with the ASTM direct-beam solar spectrum as the input to the collector system. Shading from the 110 mm wide secondary aperture results in a 2.2% loss from the primary aperture. The parabolic mirror has a standard glass-silver mirror reflectance (ρ) of 0.92. The secondary concentrator, absorber, and solar cells are encased in a glass tube which is evacuated to 10^{-4} mbar to eliminate convective heat loss and isolate the hot absorber surface from the cells in close proximity. The glass has a transmittance (τ) of 0.95 after the assumed application of anti-reflective coatings to each surface.

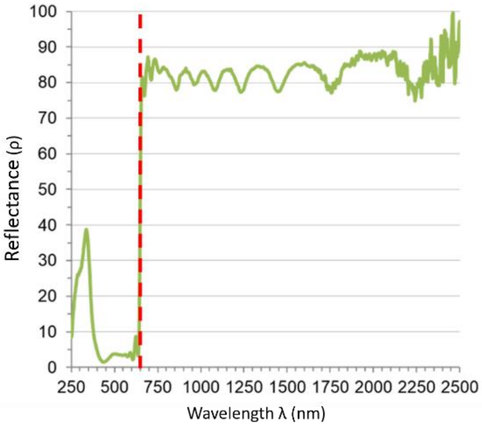

Figure 5.7 – *Measured InGaP cell reflectance with bandgap at 670 nm shown by dashed line.*

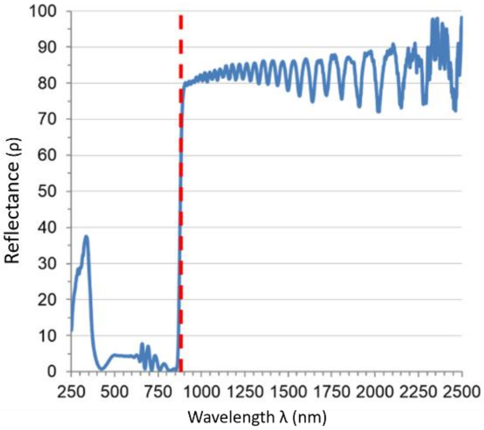

Figure 5.8 – *Measured InGaP/GaAs cell reflectance with bandgap at 875 nm shown by dashed line.*

Characteristic spectral reflectance curves for a single junction InGaP and a dual junction InGaP/GaAs cell were measured at MicroLink Devices, using a spectrophotometer. The resulting curves (Figures 5.7 and 5.8) were incorporated into the optical model to determine the amount of light reflected or absorbed by the cells. The remaining portion of the CPC profile which is not made from solar cells is assumed to be a polished aluminum mirror with a reflectance (ρ) of 95%. The solar-weighted absorptance (α) of the selective coating on the absorber is assumed to be 95%.

Optical performance is simulated for a thermal only receiver (no cells) and for a hybrid PV/T receiver with varying (4-8) numbers of solar cell strips. Simulations are performed for both single (InGaP) and dual junction (InGaP/GaAs) cells, with the cells always placed on the closest available strip to the absorber where they experience the highest flux.

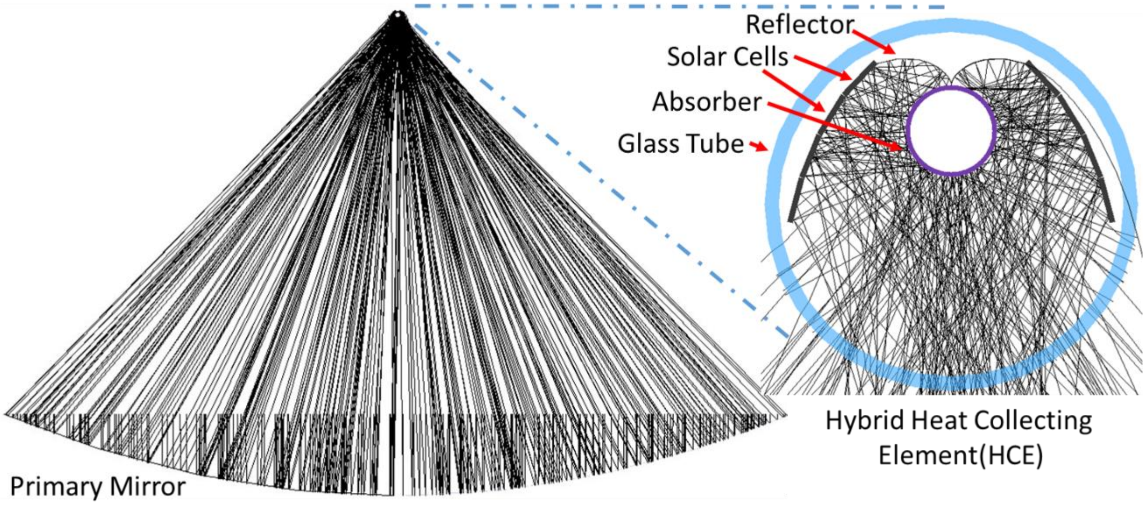

Figure 5.9 – *Ray tracing*

The optical simulations generate several key parameters which are used later as inputs to the solar cell and thermal performance models: light absorbed by the high temperature absorber ($\eta_{0,thermal}$) and the light incident upon ($\eta_{0,strip}$) and absorbed ($\eta_{abs,strip}$) by each cell strip. Relevant optical parameters from the model are summarized in Table 5.2.

Parameter	Value
$\rho_{primary}$	0.92
τ_{glass}	0.95
$\rho_{secondary}$	0.95
$\alpha_{absorber}$	0.95

Table 5.2 – *Optical simulation parameters*

5.2.2 Solar Cell Model

The solar cells are modelled using the properties listed in Table 5.3. Cell efficiency is calculated as a function of concentration at an operating temperature of 40 °C.

	η_{cell} **(%), 25 °C**	β **(%/°C)**
InGaP Solar Cell	0.14	0.0002
InGaP/GaAs Solar Cell	0.23	0.0005

Table 5.3 – *Solar cell properties*

The solar concentration on each strip $C_{x,strip}$ is estimated from equation 5.1 to determine the increase in efficiency according to Figure 5.10. Here A_1 is 5 m and the combined length of a strip pair (A_{strip}) is 0.032 m (each minichannel strip is 16 mm wide).

$$C_{x,strip} = \eta_{0,strip} \frac{A1}{A_{strip}} \tag{5.1}$$

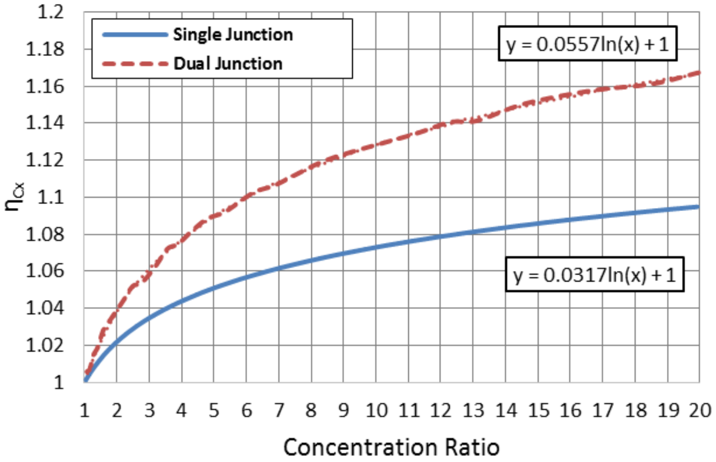

Figure 5.10 – *Improvement in cell efficiency due to increased concentration with the single junction InGaP cell drawn solid blue and dual junction InGaP/GaAs cell drawn dashed red.*

The electric output of each strip ($\eta_{cell,strip}$) is calculated based on the amount of incident light and cell efficiency at temperature.

$$\eta_{cell,strip} = \eta_{cell}\eta_{Cx}(C_{x,strip}) - \beta(T - 25°C) \tag{5.2}$$

The net efficiency of the CPV subsystem ($\eta_{system,cells}$) is calculated by summing the efficiency of each individual strip.

$$\eta_{system,cells} = \sum_{1}^{n_{strips}} \eta_{0,strip}\, \eta_{cell,strip} \tag{5.3}$$

All light absorbed by the solar cells but not converted to electricity is exhausted from the system as waste heat ($\eta_{cell\_cooling}$).

$$\eta_{cell\_cooling} = \sum_{1}^{n_{strips}} \eta_{abs,strip} - \eta_{system,cells} \tag{5.4}$$

5.2.3 Thermal Model

The emittance of the selective coating on the absorber is estimated based on several coatings reported by Selvakumar and Barshilia (2012) and plotted in Figure 5.11. Its variation with temperature is arbitrarily chosen so that it performs slightly better than the best available commercial coatings and within the realm of current research coatings. As a result the modelled emittance is representative of improved selective coatings which can be expected in the near future.

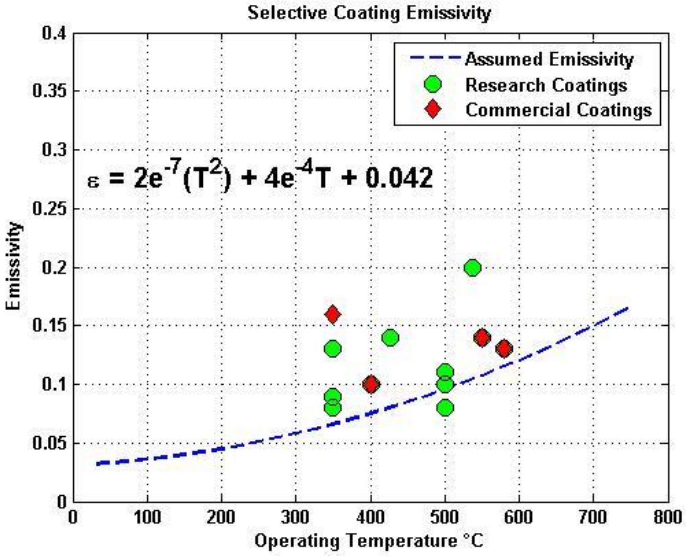

Figure 5.11 – *The assumed emissivity profile of the selective coating used in this model plotted (dashed blue) against some selected commercial (red diamond) and research (green circle) coatings reported by Selvakumar and Barshilia (2012).*

A finite element model was developed based off Figures 5.12-5.13 to analyze the heat transfer within the absorber pipe and calculate thermal performance. The model includes the interaction between the internal particulate fluid, the inner pipe surface, and outer pipe surface which radiates to the environment, and divides the 1 meter length absorber into 50 nodes (n = 50). The particulate HTF is treated as a standard fluid with a heat transfer coefficient calculated based on the correlation with particle temperature in equation 5.5. The temperatures at each node are solved by matrix inversion and iterated until the temperature change between iterations of all nodes is < 0.0001 °C.

$$h = 328.75T^{0.2025} \tag{5.5}$$

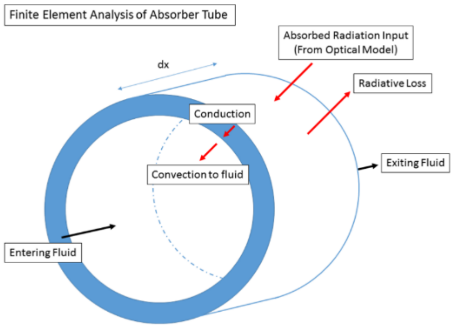

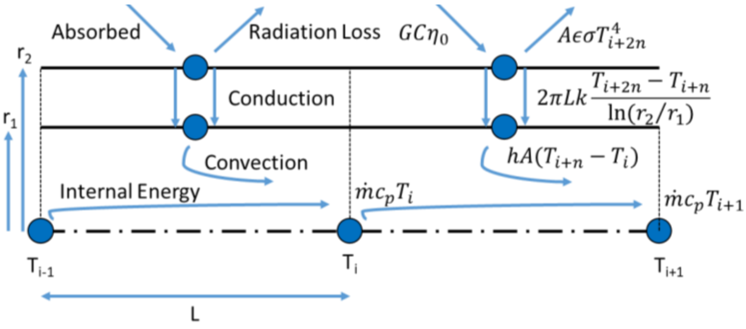

Figure 5.12 – *Finite element analysis (FEA) schematic.*

Figure 5.13 – *Finite element analysis node schematic and defining equations.*

The temperatures of all nodes are plotted for a particle inlet temperature of 650 °C and a DNI of 900 W/m^2 in Figure 5.14, showing approximately a 30° rise in temperature between the particles and the absorber surface and a 20° rise along the length of the absorber.

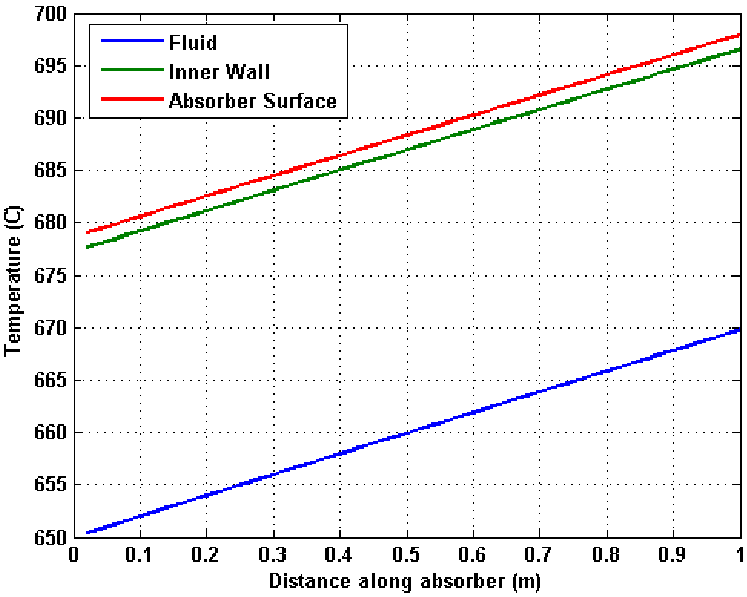

Figure 5.14 – *Simulated temperature profile along absorber pipe length based on the finite element analysis.*

Thermal efficiency ($\eta_{thermal}$) is calculated according to equation 5.6 where A_1 is the aperture of the collector in m^2, DNI is the incoming direct normal irradiance in W/m^2, $\dot{m}$ is the mass flow rate of the HTF in kg/s, c_p is the heat capacity of the fluid in kJ/kg-K, and ΔT is the temperature difference between the outlet and inlet of the HCE in °C.

$$\eta_{thermal} = \frac{Thermal\ Output}{Solar\ Input} = \frac{\dot{m}c_p\Delta T}{A_1 DNI} \tag{5.6}$$

5.2.4 System Exergy and Electric Efficiencies

As a hybrid system, we must select a metric by which we can evaluate the combined electric and thermal generation. Cogeneration efficiency has been used in the past, but does not take into account the different qualities of the electric and thermal energies produced. Since the Carnot efficiency limit applies to the conversion of heat into useful work (or electricity), solar-to-exergy efficiencies have been proposed as a more practical measure of hybrid solar power generation systems (Branz et al. 2015). Exergy, which is defined as $Q(1 - T_C/T_H)$, is the thermodynamic limit to the amount of useful work that can be extracted from a quantity of heat Q at a temperature T_H. The energy and exergy content of electricity are identical since there is no limit to the amount of electricity which can be converted into useful work. In this way, the solar-to-exergy efficiency calculated in equation 5.7 is the maximum possible efficiency of the hybrid system at converting the incoming solar energy into useful work. For these calculations the cold reservoir temperature of the Carnot cycle T_C is assumed to be 37 °C and T_H is the operating temperature of the thermal subsystem.

$$\eta_{exergy} = \frac{W_{system,cells}+Q_{thermal}(1-T_C/T_H)}{Q_{solar}} = \eta_{system,cells} + \eta_{Carnot}\cdot\eta_{thermal} \tag{5.7}$$

In practice, inverter losses will reduce the CPV subsystem electric output during DC-to-AC conversion, and additional plant, power block, and generator losses will reduce conversion of the CSP subsystem into electricity. To account for these, a more realistic solar-to-electric efficiency of the system ($\eta_{electric}$) is calculated with equation 5.8. A 2/3 term is included since actual power block turbines typically reach only ~66% of the Carnot efficiency. Two additional losses are considered to account for plant thermal, storage, and heat exchange losses (η_{HX} = 0.9), and for parasitic losses ($\eta_{PB,net}$ = 0.9).

$$\eta_{electric} = \eta_{system,cells} + \frac{2}{3}\eta_{Carnot}\eta_{thermal}\eta_{HX}\eta_{PB,net} \tag{5.8}$$

5.2.5 Economic Analysis

System cost is estimated using the costs already listed in NREL's parabolic trough System Advisor Model (SAM). Solar field costs were updated to include the current cost of cold-bent glass-silver mirrors, structural components, and trackers. The hybrid receiver cost was based on the current production cost of parabolic trough receivers with the additional cost of the solar cells. Power block and thermal energy storage (TES) costs were based on estimates of a 100 MW plant using a powder-based HTF and handling system (Cygan et al. 2016).

5.2.6 Simulated Performance Results

84.5% of light is incident on the secondary aperture after shading, primary reflection, and transmission losses. The fraction of light incident on each pair of cell strips ($\eta_{0,strip}$) in Figure 5.15 is presented in Table 5.4 and shows an illumination pattern that validates previous ray tracing.

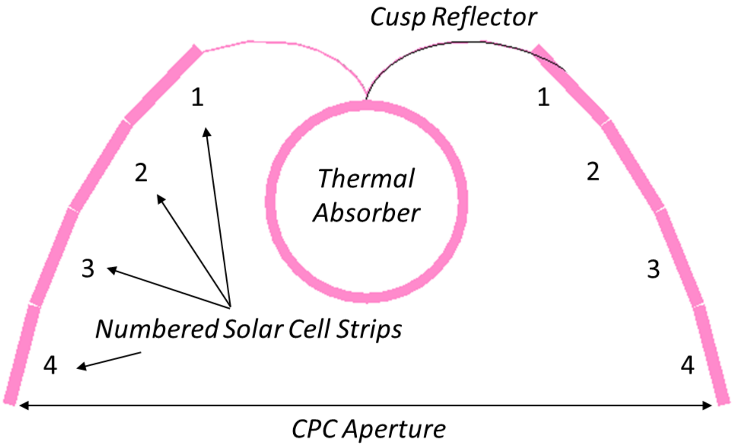

Figure 5.15 – *Hybrid HCE schematic with numbered solar cell strips.*

	1st strips	2nd strips	3rd strips	4th strips
$\eta_{0,strip}$	13.45%	13.3%	8.32%	3.98%

Table 5.4 - *Total illumination on strip pairs*

The fraction of light absorbed by the thermal absorber ($\eta_{0,thermal}$) for each scenario (Table 5.5) increases with the use of fewer or single rather than dual-junction cells since more light is reflected.

	Thermal Only	2 Strips	3 Strips	4 Strips
$\eta_{0,thermal,InGaP/GaAs}$	77.51%	61.98%	57.12%	54.97%
$\eta_{0,thermal,InGaP}$	77.51%	66.92%	63.60%	62.15%

Table 5.5 – *Thermal absorption*

The thermal and full system performance models were evaluated up to operating temperatures of 700 °C and the results for all configurations at 600 °C are listed in Table 5.6.

	$\eta_{thermal}$ **@ 600 °C**	$\eta_{system,cells}$	η_{exergy} **@ 600 °C**	$\eta_{electric}$ **@ 600 °C**
Dual Junction Solar Cells – 4 Strips	45.9%	9.1%	38.9%	23.7%
Dual Junction Solar Cells – 3 Strips	47.9%	8.2%	39.3%	23.5%
Dual Junctions Solar Cells– 2 Strips	52.5%	6.2%	40.4%	23.0%
Single Junction Solar Cells – 4 Strips	52.6%	5.8%	40.1%	22.6%
Single Junction Solar Cells – 3 Strips	54.0%	5.2%	40.4%	22.5%
Single Junction Solar Cells – 2 Strips	57.1%	4.0%	41.2%	22.3%
Thermal Only	67.1%	0.0%	43.8%	21.5%

Table 5.6 – *Performance results summary*

5.2.7 Modelled Cost-Performance Metrics

Cost-performance metrics were calculated as a result of the performance models at 600 °C and estimated collector costs. The hybrid converter is expected to reach $< \$1/W_{exergy}$ for a 2 strip hybrid and thermal only configuration.

5.2.8 Discussion and Down-Selection

The ultimate difference in full system cost between two strips of single junction or dual junction was negligible and since the dual junction cells provide greater total power output per square meter, the two-strip configuration was selected as the optimal design. The various efficiencies for the thermal-only and hybrid collectors are presented in Figures 5.16 and 5.17, respectively. The solid black lines indicate shading and optical losses, with the net thermal efficiency shown in red and the exergy efficiency in blue. Also drawn in these plots are the net system efficiencies assuming the 2/3 Carnot power block used in this model (dashed black), steam Rankine (cyan), and CO_2 recombination Brayton (magenta) power blocks (Dunham and Iverson 2014). The balance between increasing Carnot efficiency and increasing heat loss at higher temperatures yields optimal thermal operating temperatures between 500-600 °C. A rendering of the final thermal-only and hybrid HCEs are shown in Figures 5.18, 5.19.

Thermal HCE

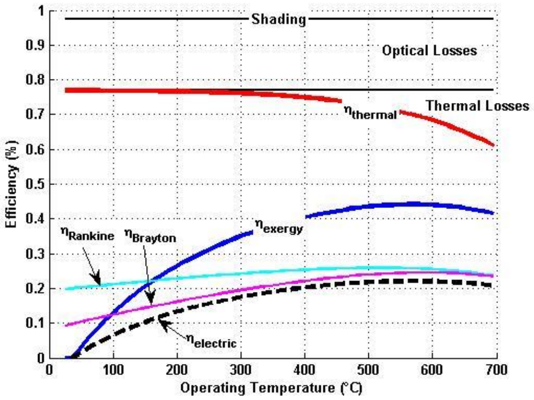

Figure 5.16 – *Simulated performance of thermal-only collector.*

Hybrid HCE

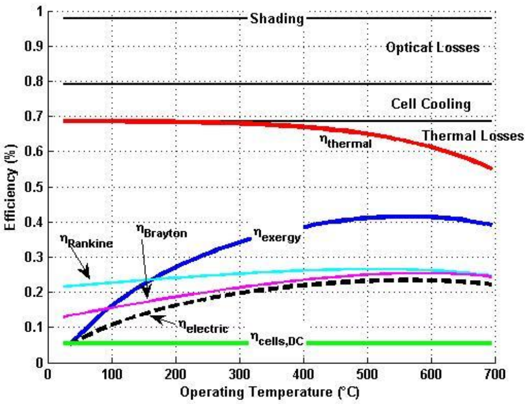

Figure 5.17 - *Simulated performance of hybrid collector with 2 strips of InGaP/GaAs cells.*

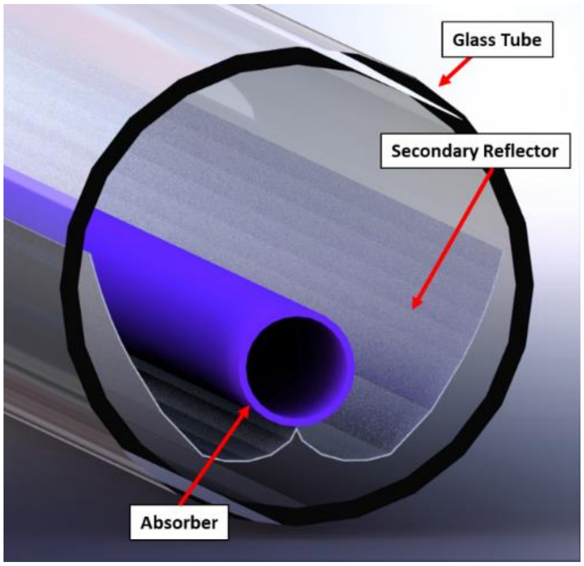

Figure 5.18 – *Rendering of thermal HCE design*

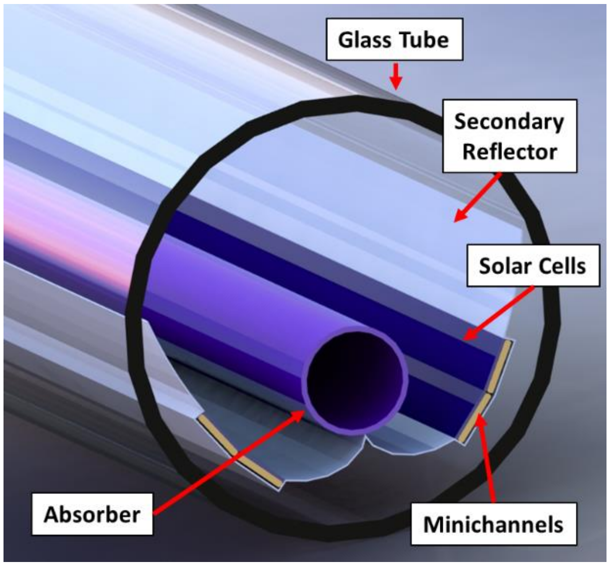

Figure 5.19 – *Rendering of final down-selected hybrid HCE design with 2 mirrored strips of dual junction InGaP/GaAs solar cells integrated into the secondary reflector.*

5.3 Prototype Development

5.3.1 Primary Mirror

The primary reflector is made from 5 glass-silver mirror panels which are combined together to make up the 5 x 1 meter, 45° half-rim angle parabola.

5.3.2 HCE Design

The cross section of the hybrid heat collecting element (HCE) is shown in Figure 5.20. The entire assembly is encased in a glass tube for evacuation (to 10^{-4} mbar). This prevents heat loss and provides thermal isolation between the absorber, solar cells, and secondary reflector. The secondary is shaped to guarantee geometric efficiency with incorporated solar cell segments. The solar cells are mounted above minichannel substrates which provide active water cooling of the cells under concentrated sunlight. The thermal absorber at the focus of the secondary collects the concentrated/spectrally-split light reflected by the secondary/solar cells. Spectral reflectance of an actual cell is shown in Figure 5.21, indicating the absorption of photons below 875 nm and reflection (80-90%) of longer wavelength photons.

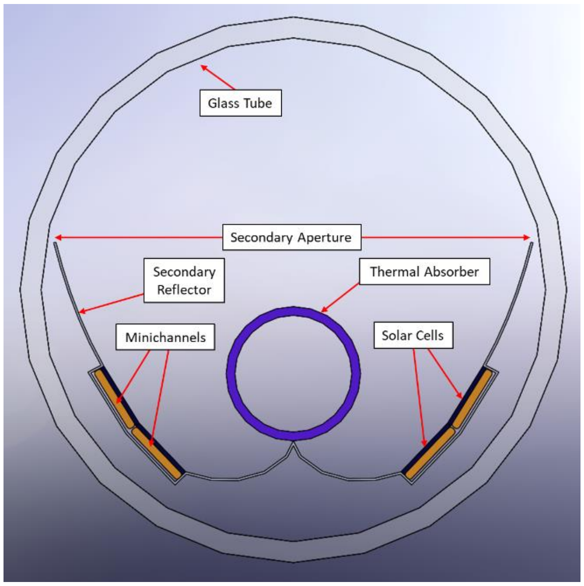

Figure 5.20 – *Hybrid heat collecting element (HCE) schematic (to scale).*

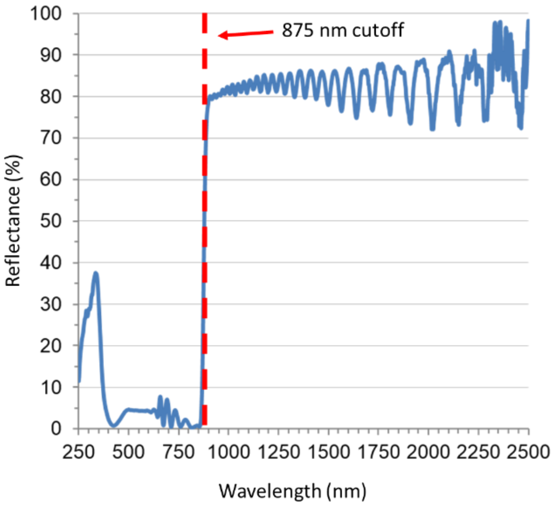

Figure 5.21 – *Spectral reflectance curve of an actual dual junction InGaP/GaAs cell. The dashed red line indicates a bandgap wavelength cutoff of 875 nm.*

The entire HCE is encased in a borosilicate glass tube. Stainless steel end caps with silicone O-rings provide a vacuum-tight seal with the glass. The end caps are bolted to aluminum U-clamps which are assembled around the tube on the opposite side of a 45° glass flange and Teflon gasket which prevents hard contact between the aluminum and glass. The bellows and vacuum ports were welded to each end cap.

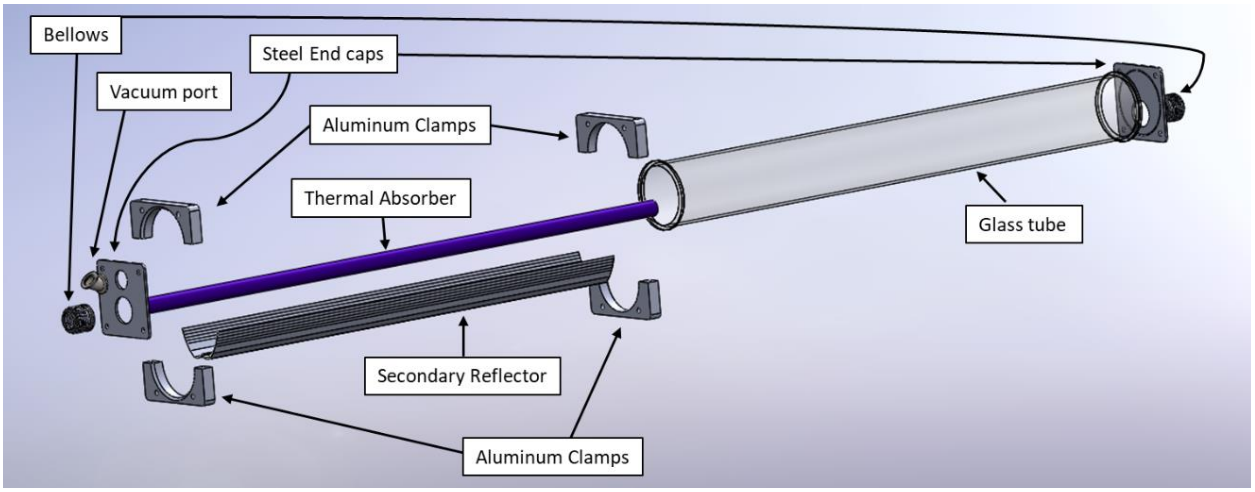

Figure 5.22 – *Rendered thermal HCE (exploded view).*

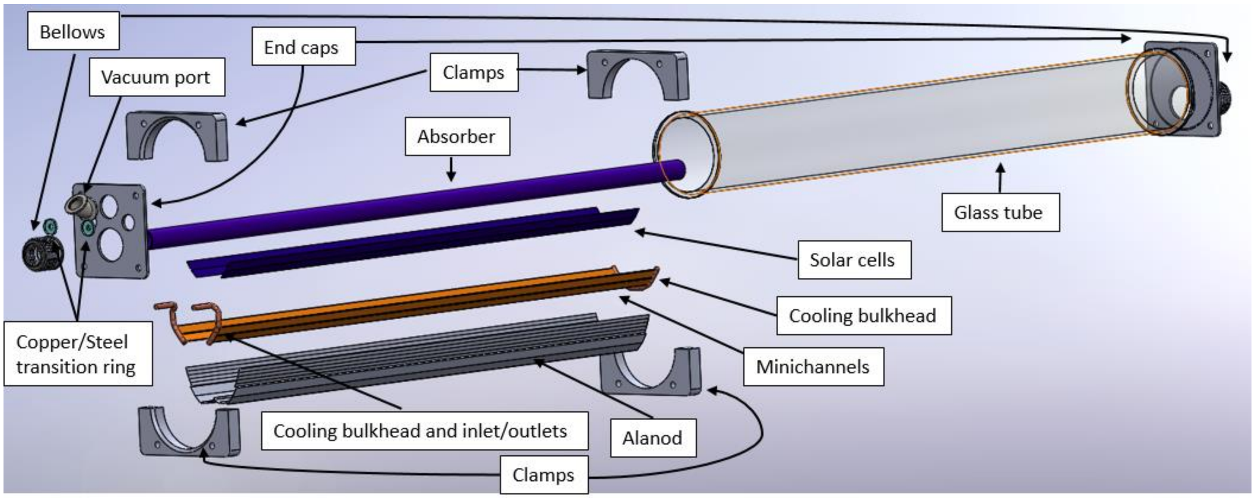

Figure 5.23 – *Rendered hybrid HCE (exploded view).*

5.3.3 Secondary Reflector

The secondary reflector is made from Alanod MIRO-Silver with a solar-weighted reflectance of 95%. The profile shape is produced by controlled bending and includes indentations for the solar cell and minichannel subcomponents. The two halves of the CPC are produced independently and joined together by riveting to a central connecting bridge.

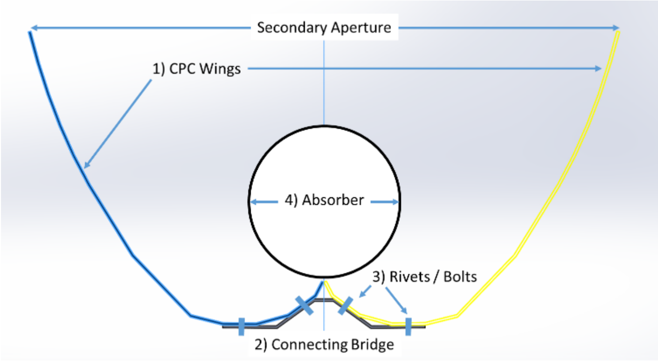

Figure 5.24 – *Secondary design*

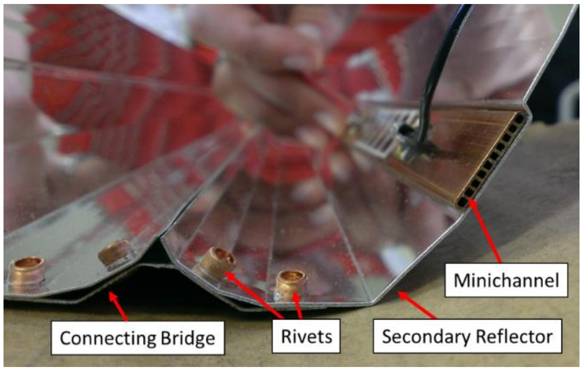

Figure 5.25 – *Secondary reflector and minichannel*

5.3.4 Minichannels and Cooling Circuit

Extruded copper minichannels were produced using a technique developed by the Center for Advanced Materials Processing at Ohio University (see Figure 5.26).

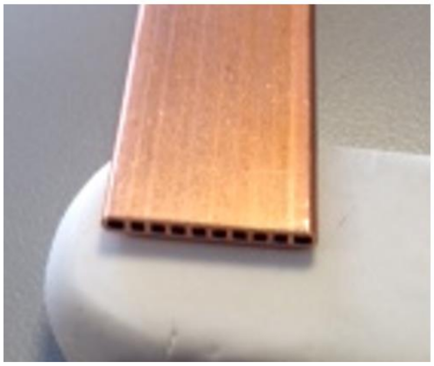

Figure 5.26 – *Copper minichannel*

Figure 5.27 – *Minichannel connections at U-bend (left) and cap end (right).*

The two strips of minichannels on each wing flow in parallel to each other and are connected in series to the strips on the opposite wing. In this way they form a U-tube in the hybrid HCE and the inlet and outlets are both made on the same side of the HCE (Figure 5.27). These connections are made using low temperature solder which transition through the stainless steel end caps by a copper-to-stainless transition ring.

5.3.5 Solar Cells

The dual junction InGaP / GaAs solar cells were supplied by MicroLink Devices (see Figure 5.28). They adhere to the minichannels by a two-sided electrically insulating silicone tape, and the same tape is used to join the minichannel strips to the secondary reflector. A rough thermal analysis indicates the cells should see a 4-8 °C rise in temperature over the cooling water circulating in the minichannels.

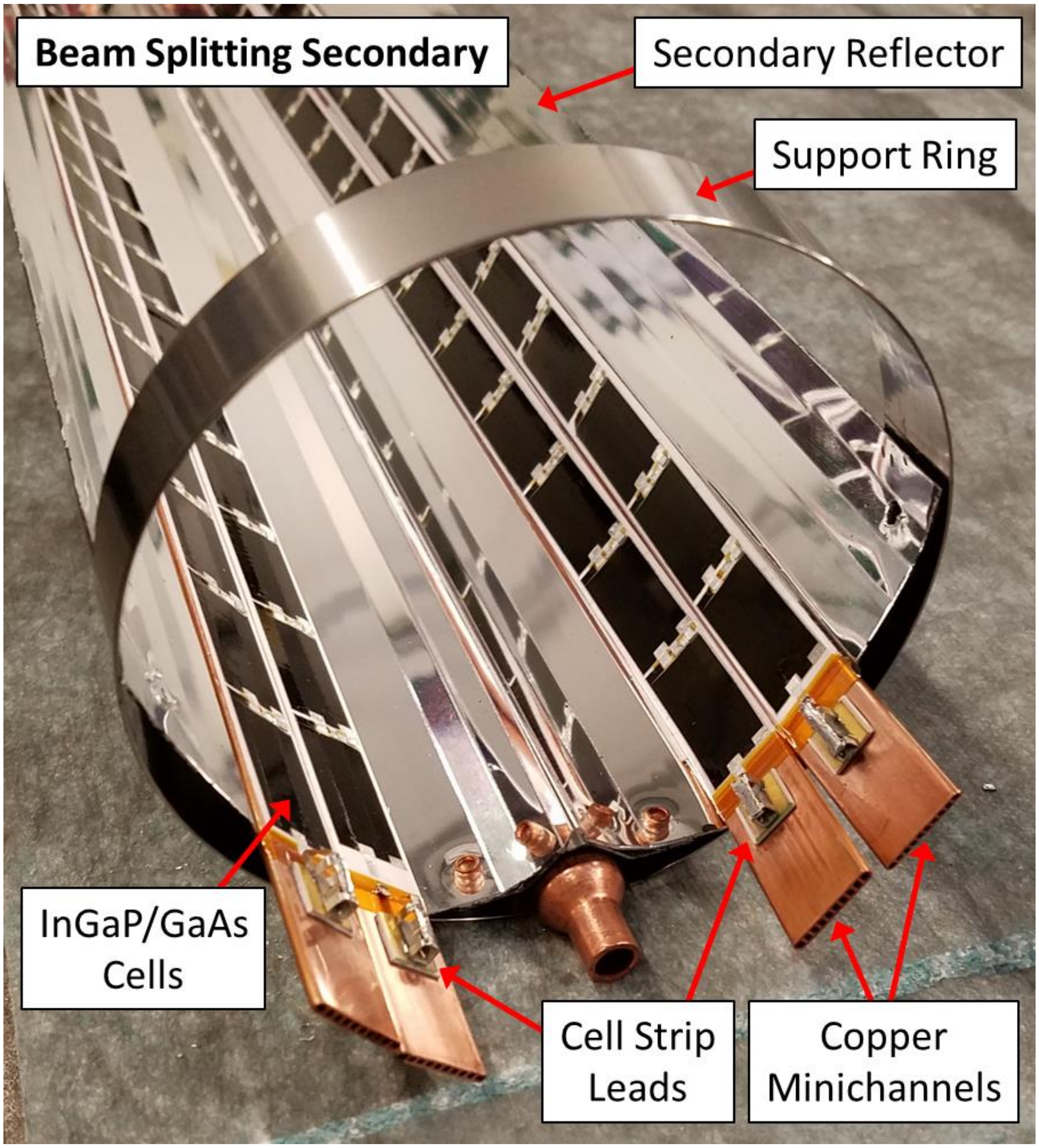

Figure 5.28 – *Secondary reflector shown with integrated InGaP/GaAs and minichannel subassemblies.*

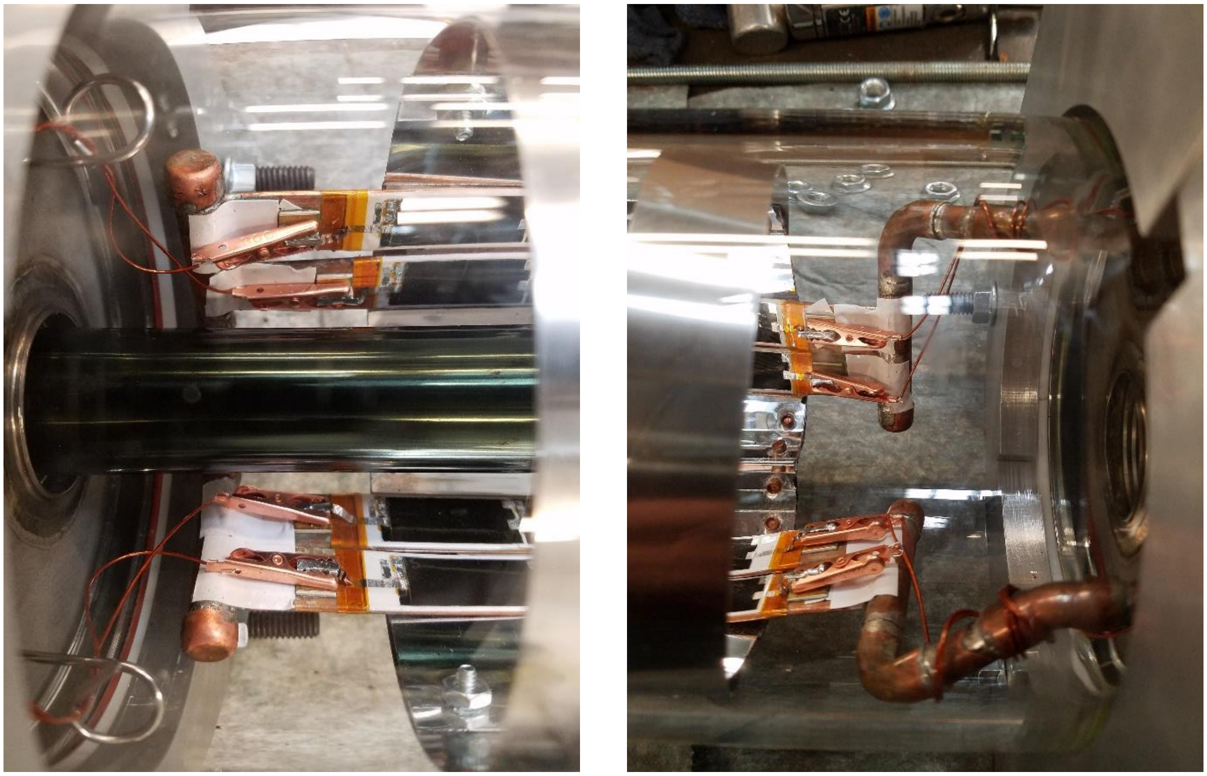

Figure 5.29 – *Cell wire connection methods at u-bend end (left) and transition end (right).*

The strip leads were contacted using copper alligator clips. Vacuum stable wire was used to connect these leads with to a vacuum feed through on either end of the HCE. In this way, each strip is wired individually.

5.3.5 Absorber

The absorber is made from Schedule 5 SS 316 pipe. 4 selectively coated absorbers were acquired from the Non-Ferrous Metals Institute in Beijing who were able to coat the custom-size absorber (Figure 5.30). The coating has a solar-weighted absorptance of 95% and an estimated emissivity of 15% at 600 °C. The absorber passes through the stainless steel end-caps with a bellows on each side to accommodate thermal expansion as the absorber is raised to 600 °C.

Figure 5.30 – *Selectively coated thermal absorber*

5.3.8 Glass Envelope, End Caps, Vacuum Subsystem

The CPC and absorber are both encased in a glass tube with the characteristics in Table 5.7. This allows the entire HCE to be evacuated to eliminate convective heat loss and provide thermal isolation between the absorber and CPC reflector.

Length	1160 mm
End connection	45° tapered flange
Material	Borosilicate
Transmittance (τ)	0.92

Table 5.7 – *Glass tube specifications*

At each end of the hybrid HCE end-cap is welded a DN 25 vacuum port for active vacuum pumping on one end and vacuum measurement on the other.

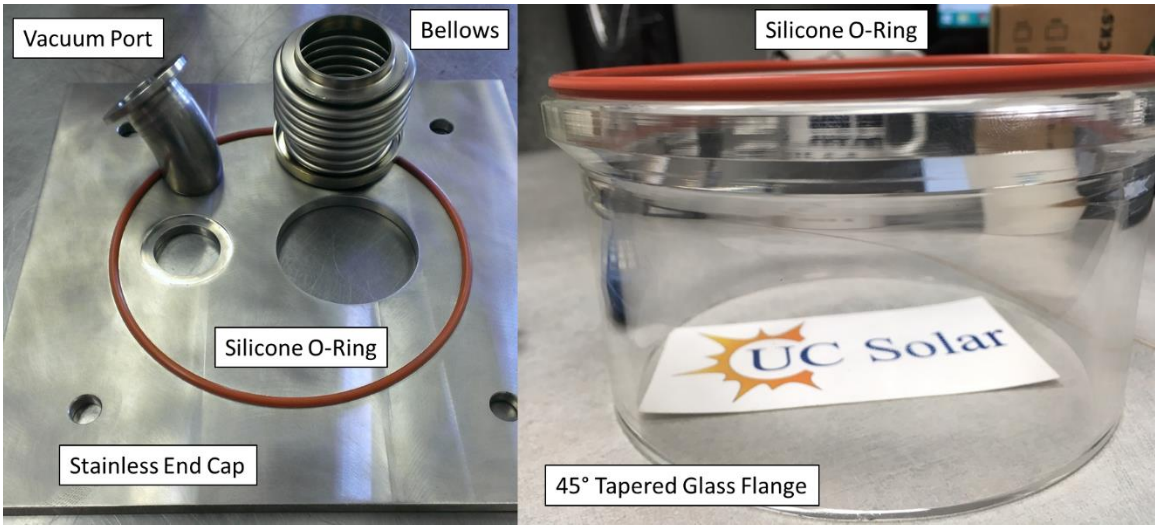

Figure 5.31 – *End cap, o-ring, bellows and vacuum port (left) and tapered glass flange (right).*

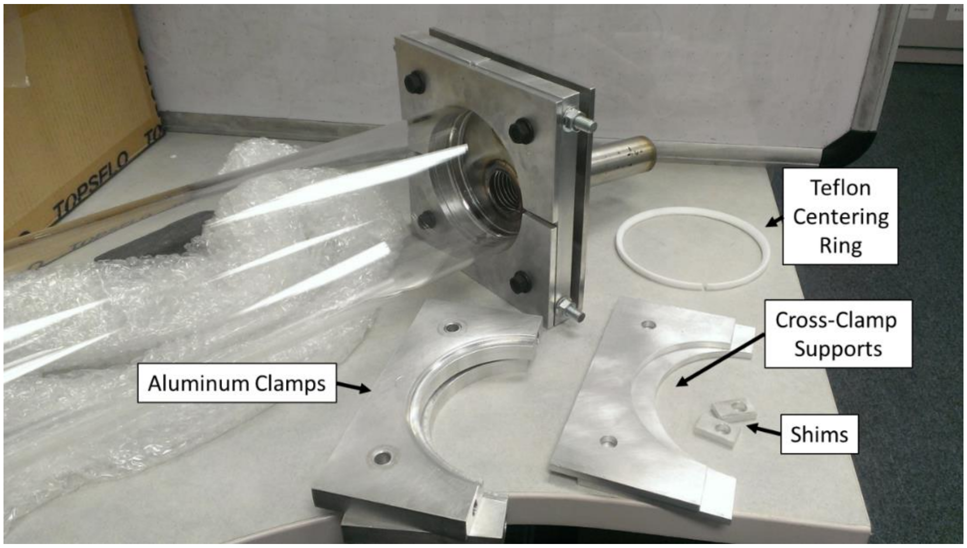

Figure 5.32 – *Partially assembled end-cap with aluminum clamps, shims, and Teflon centering ring.*

5.3.9 Assembled HCE Prototypes

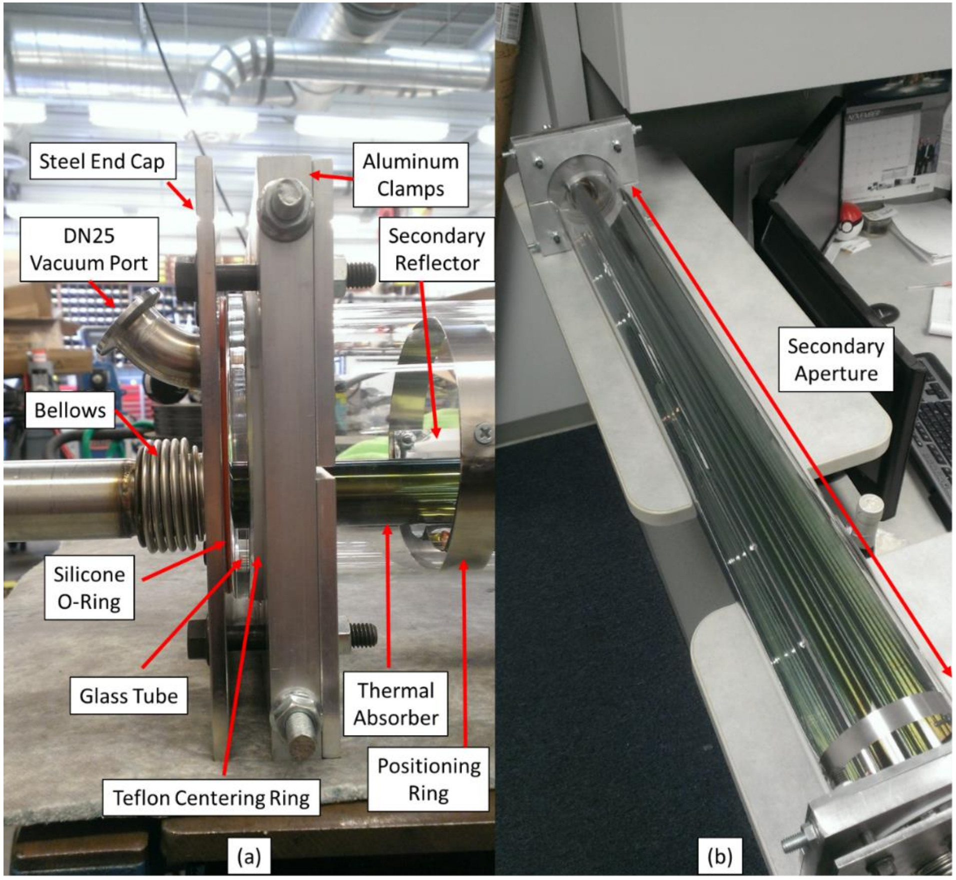

Figure 5.33 – *Assembled receiver. The various components of the receiver are labelled in (a). Positioning rings are used to maintain the shape and location of the secondary reflector in the receiver. The entire assembly is shown in Figure (b). The entire aperture appears to be the same green color as the thermal absorber which is indicative of functioning optics.*

Figure 5.34 – *(above) 3-piece assembly for the Hybrid HCE. Step 1-insert secondary reflector/end cap and secure to glass tube. Step 2-insert absorber/end cap from other side and secure to glass tube. Make cell connections and weld absorber. The fully assembled hybrid HCE is pictured on the right.*

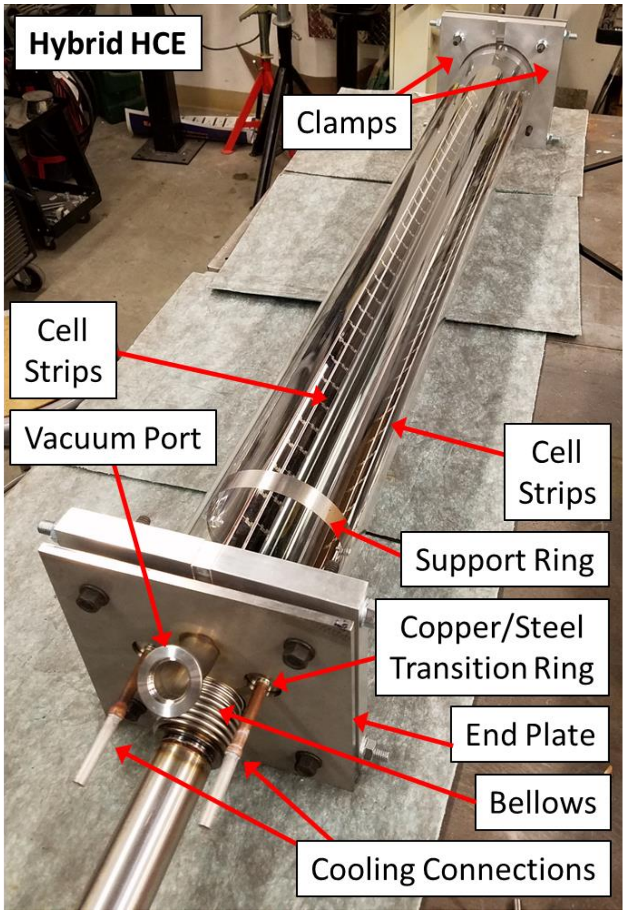

5.3 Experimental Test Platform and Pre-Performance Tests

5.3.1 Vacuum Bakeout Test

A vacuum bakeout test was performed to verify integrity of the HCE assembly at operating temperature.

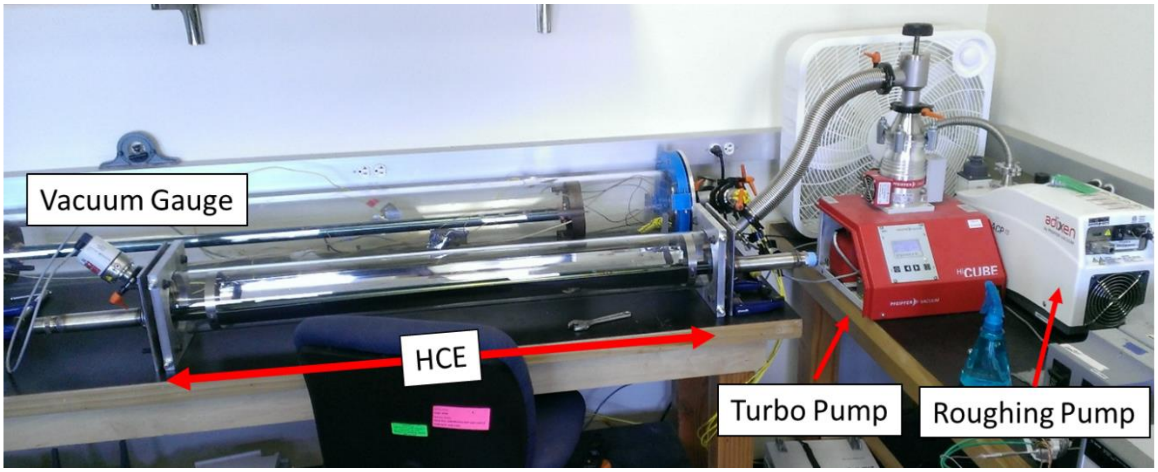

Figure 5.35 – *Vacuum bakeout testing.*

Thermocouples were spot welded at various locations on the end cap (near the O-ring, bellows, and vacuum port) and taped along the top (above absorber) and bottom (behind reflector) of both the middle and ends of the glass tube. A thermocouple was also spot-welded to the center of a 1 meter long heating element, which was then inserted inside the HCE's absorber tube to measure the temperature inside the absorber. Power to the heating element was controlled manually by adjusting a variable A/C transformer while simultaneously measuring voltage and current.

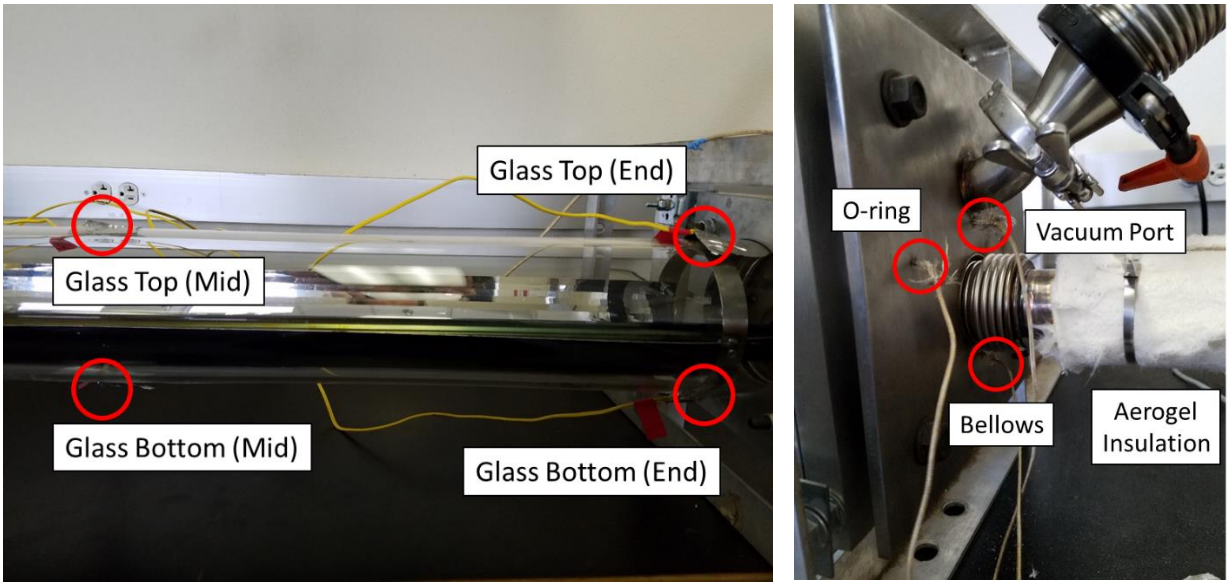

Figure 5.36 – *Thermocouple positioning on glass (left), and end cap (right).*

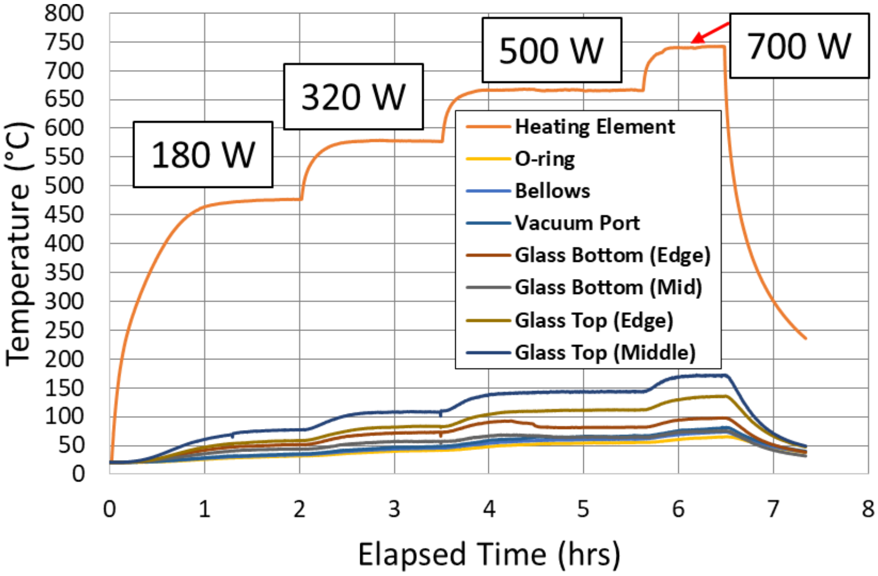

Figure 5.37 – *HCE vacuum bakeout test results. The temperatures at various locations in the HCE and on the heating element are shown throughout the duration of the test. The amount of power supplied to the heater is incrementally increased and listed in Watts above the temperature curves.*

The test was run for a little over 6 hours during which the internal heater temperature was raised incrementally to 750 °C and the vacuum inside the HCE maintained at 10^{-4} mbar. The temperatures during this test and the heating power (from voltage and current clamp measurements) are presented in Figure 5.37. Maintaining an internal temperature of 650 °C and 750 °C required approximately 500 and 700 watts, respectively. This corresponds to an emittance of roughly 13-15% at temperature which is consistent with both commercially available coatings and the previously modelled emittance.

5.3.2 IV Curve Testing

All 4 strips of solar cells were IV-curve tested on 11/15/2017. After reassembling, one of the strips had lost contact (the bottom left strip in Figure 5.39). An image of an illuminating strip during IV-curve tracing is shown in Figure 5.38.

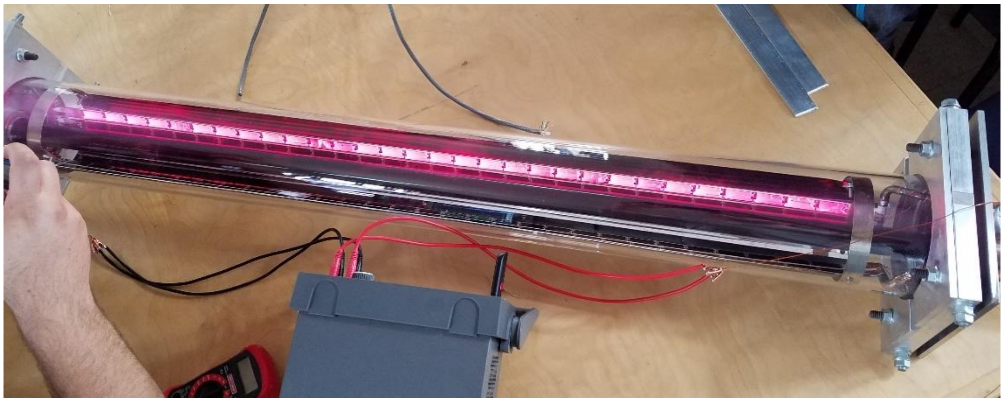

Figure 5.38 – *IV curve strip illumination.*

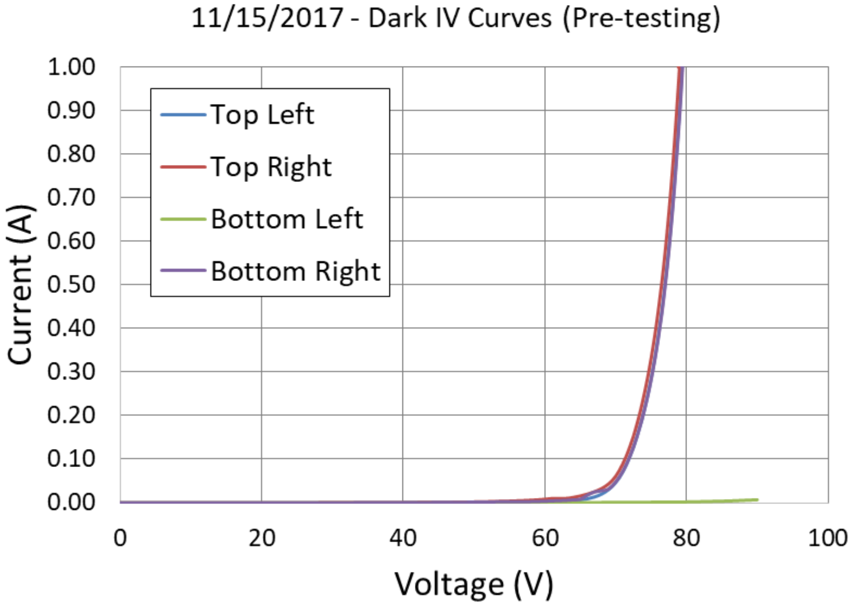

Figure 5.39 – *Dark IV Curve test results*

5.3.3 On-Sun Test Platform

Experimental performance tests were carried out at the University of California, Merced Castle Research Facility (37.3 °N, 120.6 °W) together with GTI. Optical efficiency tests were performed using city water as the HTF, after which high temperatures tests were carried out using a particulate HTF. An image of the researcher is shown in Figure 5.40, and the collector and testing apparatus are labelled in Figure 5.41.

Figure 5.40 – *The researcher*

The primary mirror is mounted on a dual axis tracker. Tracking is controlled by an array of 4 solar cells which are located on the primary mirror in the shadow of the HCE. As the shadow moves due to the movement of the sun, different solar cells are shaded or unshaded. Their current outputs are monitored by an arduino microcontroller which then engages the proper tracking actuators to maintain the shadow in the correct position. A normal incidence pyranometer (NIP) sensor mounted on the frame measures the direct normal irradiance.

Particle circulation is accomplished by moving particles between 3 hoppers (see Figure 5.41). A continuous particle flow through the receiver is maintained by periodically replenishing the feed hopper so it does not fall below a minimum set lever. Carrier air and pressure differentials are used to move the particles between the hoppers. The carrier air is vented, but this has minimal effect on the overall efficiency because of the very high particle to air weight ratios employed. The particle HTF system was developed by GTI, and the rig was designed to allow the HCE to simulate any 1 m length of a full scale commercial absorber, from its inlet to its outlet. Meaning the rig could deliver particle HTF at any temperature from ambient up to 625 °C at the absorber inlet.

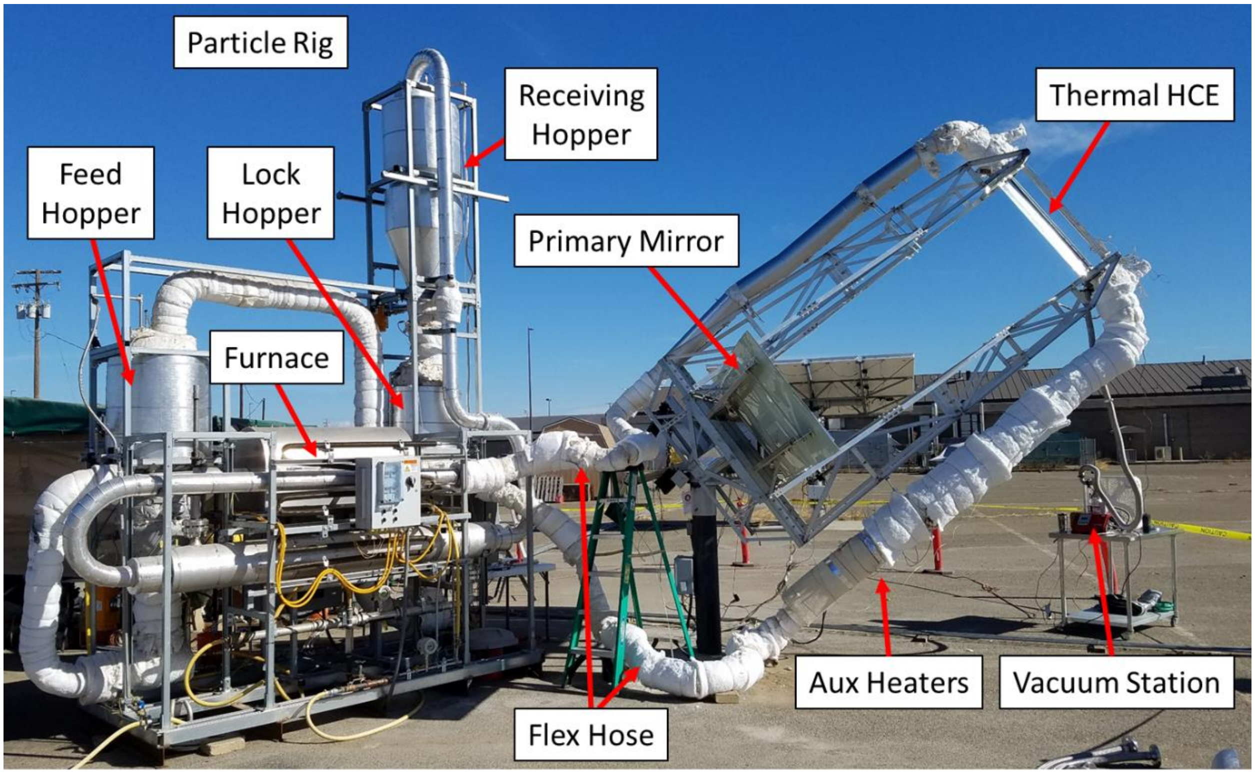

Figure 5.41 – *Testing apparatus with particle circulation rig (left) and collector (right).*

A combination of high-temperature ceramic heaters located on the rig and on the supply pipeline on the tracker (labelled as auxiliary heaters) are used to add heat into the particles to maintain desired operating temperatures. The entire piping system is insulated with 1" of aerogel insulation and external layers of FiberFrax. Temperatures across the HCE are measured by clusters of thermocouples at the inlet and outlet which have individual thermocouples inserted at various depths in the flow path between the center and the tube wall. The mass flow rate of particles is calculated by the change of the feed hopper load cell output over time, recorded every minute. The heat capacity of the particulate HTF is assumed to be a constant 0.8 kJ/kg-K. The thermal efficiency of the thermal stream is calculated from equation 5.9.

$$\eta_{thermal} = \frac{Q_{thermal}}{Q_{solar}} = \frac{\dot{m}c_p\Delta T}{A_1 DNI} \tag{5.9}$$

The cooling circuit is fed by a city-water line. The rate of water flowing through the minichannels is measured manually by recording the time it takes to fill a 5 gallon bucket (which actually contains 5.6 gallons). This was typically around 25 g/s to facilitate ~ 10 ΔT in the cooling circuit for thermocouple error reduction. Inlet and outlet temperatures of the cooling circuit are measured manually with a hand-held thermocouple reader by inserting a thermocouple probe directly into the flow. The heat capacity of water is assumed to be a constant 4.184 kJ/kg-K and the cooling circuit efficiency (or rather the fraction of incoming solar which is exhausted as waste heat) is calculated according to equation 5.9.

The performance of each strip of solar cells is quantified using a Keithley 2460 IV curve tracer. The maximum power point of each strip of cells is determined and added to estimate net solar-to-electric efficiency of the CPV subsystem according to equation 5.10.

$$\eta_{electric} = \frac{W_{system,cells}}{Q_{solar}} = \frac{\sum_{n_{strips}}^{4} I_{MPP} V_{MPP}}{A_1 DNI} \tag{5.10}$$

The vacuum in the HCE is actively maintained by a benchtop combination (turbopump + roughing pump) vacuum station. It is connected to the bottom of the HCE by 3 meters of flexible hose. At the opposite end of the HCE is a gauge to measure the vacuum pressure inside the HCE.

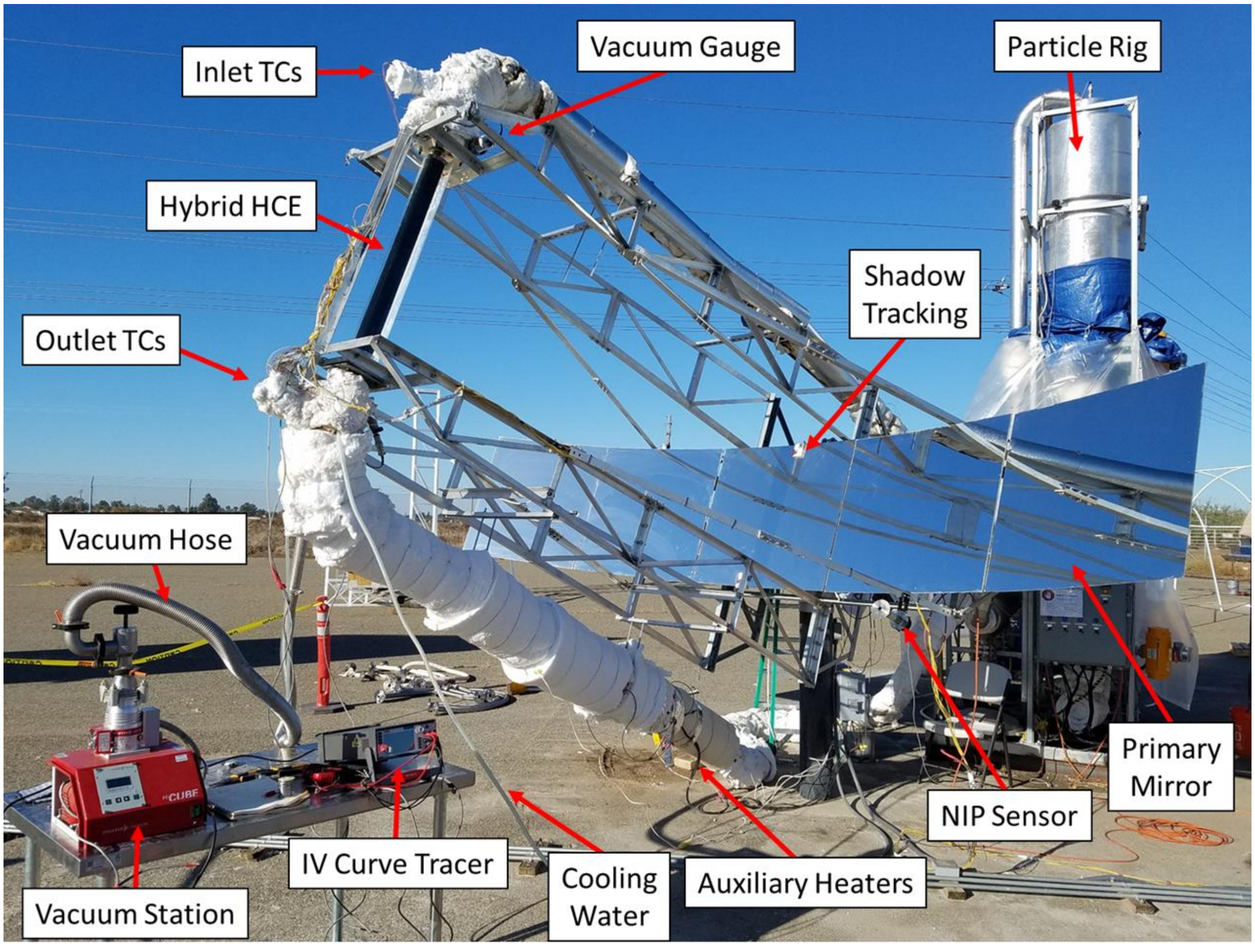

Figure 5.42 – *Experimental test platform for characterization of the hybrid collector.*

5.4 Thermal HCE Testing

5.4.1 Water Testing

Water testing was conducted between 9/30/2016 – 12/3/2016. A representative test day is shown in Figure 5.43 for the date of 10/5/2016.

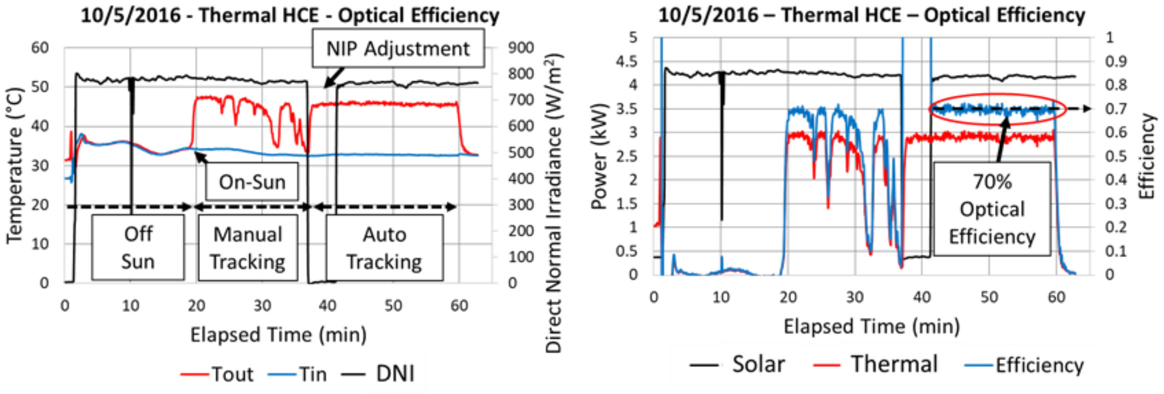

(a) (b)

Figure 5.43 – *Optical efficiency testing of thermal HCE using water*

In the first 20 minutes of data-logging the system is stowed. At approximately 20 minutes, the tracker is aligned producing a temperature difference at the HCE. For the next 15 minutes the system is manually tracked, which causes fluctuations in the outlet temperature as a result of misalignment. At about 35 minutes the automatic shadow-tracking system was engaged, resulting in a very steady and consistent temperature difference between the inlet and outlet of the HCE. At the start of automatic tracking, the NIP sensor was readjusted, after which approximately 20 minutes of steady state data are taken. In these last 20 minutes, the system demonstrated an optical efficiency of 70% which is consistent with the results of water testing on the other days and the simulated performance at low temperature.

5.4.2 Particle Testing

The first test was performed on August 31st, 2017. The system was started at 9 am and run until 2:30 pm at which point the flex hoses were stretched to their maximum by the tracker, limiting further mobility of the collector. Between 12:00 and 2:00 pm, the sun rose above the maximum elevation angle of the tracker resulting in the artificial dip in the DNI reading in Fig. 5.44. This is manually corrected for when calculating efficiency by using the dashed black line. The vacuum pressure in the HCE was initially 10^{-4} mbar prior to alignment, rose to 10^{-2} mbar once the collector was put on sun, and reduced over the course of the test to 10^{-3} mbar.

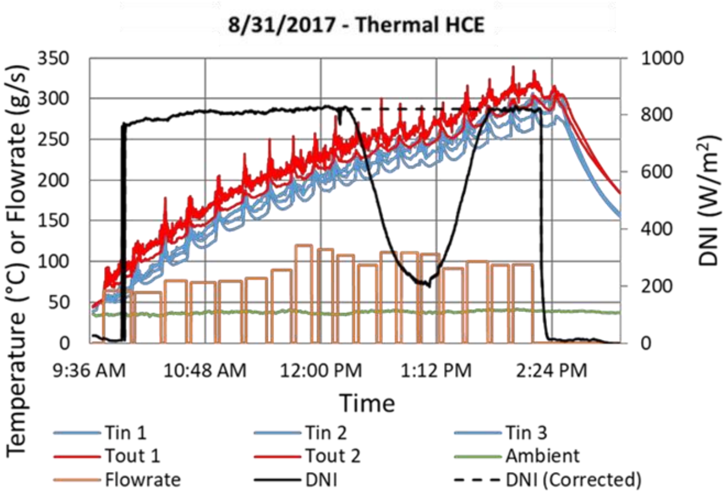

Figure 5.44 – *300 °C test of thermal HCE.*

4 kW of additional heaters (labelled as aux heaters in pictures) were installed on the pipe run just prior to the HCE and testing resumed on September 25th 2017 after making the modifications to the HCE discussed in section 5.6.4.

High temperature testing continued on October 19th, 2017, reaching a particle temperature of 550 °C at the HCE. During this test a thermal camera was used to capture the external temperature of the entire particle rig and HTF loop. The exterior of all pipe insulation was typically < 60 °C with the front side of the glass tube reaching close to 120 °C (Figure 5.45) and back side of the glass reaching approximately 50 °C. These temperatures are consistent with the temperatures measured during the vacuum bake-out test and indicate a combined loss of roughly 500 watts from convection and radiation from the glass tube.

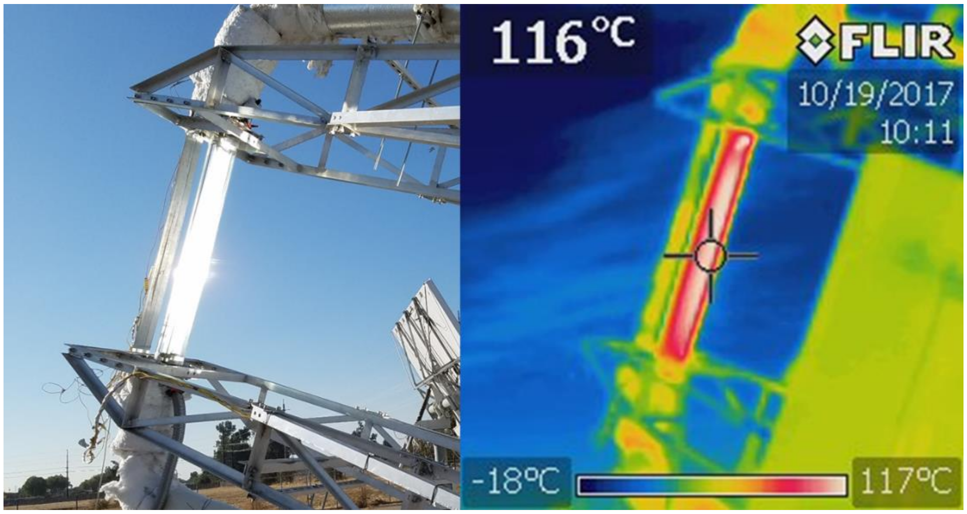

Figure 5.45 – *Thermal imaging of HCE on-sun*

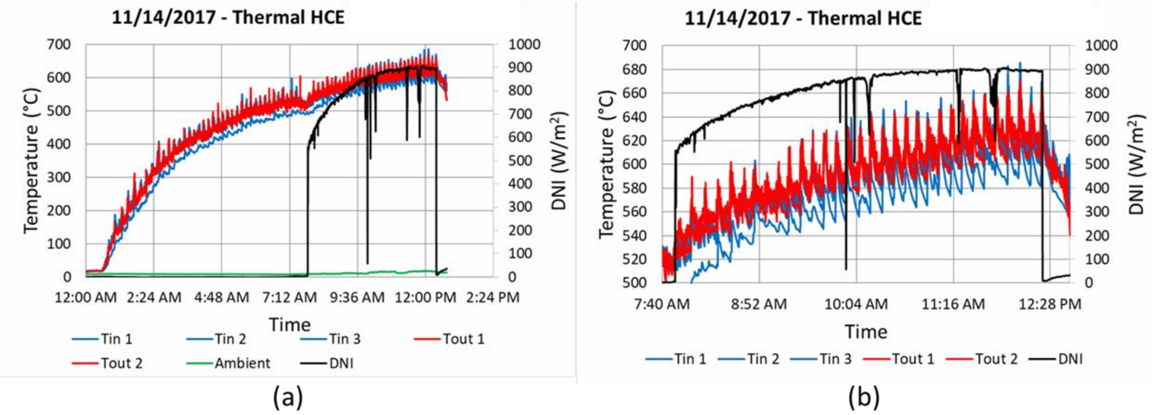

(a) (b)

Figure 5.46 – *650 °C Test*

To deliver particle HTF at 625 °C target temperature at the inlet of the absorber, additional heaters were added to the system. On November 14th, 2017 the system was started at 12:00 AM and heated until approximately 7:00 AM at which point the system was put on sun (see Fig. 5.46). By the end of testing, the HCE had reached a maximum temperature of 685 °C. At 650 °C, the collector averages roughly 40% efficiency.

On November 17th, 2017, the thermal HCE was tested again at low temperatures for two cycles (Figure 5.47) and demonstrated an optical efficiency of 60%. This indicates little to no damage or degradation to the optics, reflectance, or absorptance of the selective coating after elevated temperature testing.

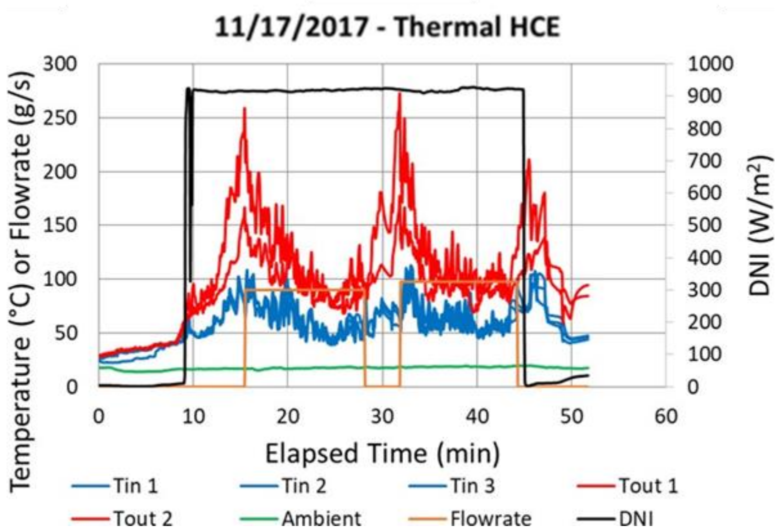

Figure 5.47 – *Optical Efficiency Test*

5.4.3 Summary

The results from all experimental performance tests are summarized in Table 5.8 and plotted in Figure 5.49 with a second order polynomial curve fit. The semi-continuous flow rate of particles causes significant temperature variation, and as a result the efficiencies from each test are estimated by visually averaging over several cycles.

Date	T_{avg}	η	**Fluid**
9/30/2016 - 12/3/2016	25	0.7	Water
9/25/2017	50	0.6	Particles
11/17/2017	75	0.6	Particles
8/31/2017	200	0.6	Particles
10/19/2017	480	0.55	Particles
10/19/2017	540	0.5	Particles
11/14/2017	600	0.4	Particles
11/14/2017	650	0.4	Particles

Table 5.8 – *Thermal-only experimental test results*

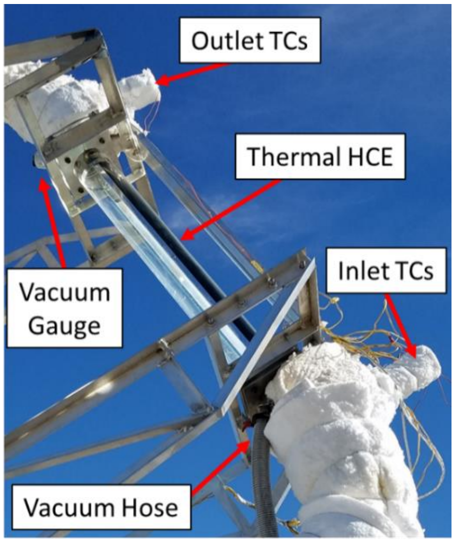

Figure 5.48 – *Thermal HCE On-Sun*

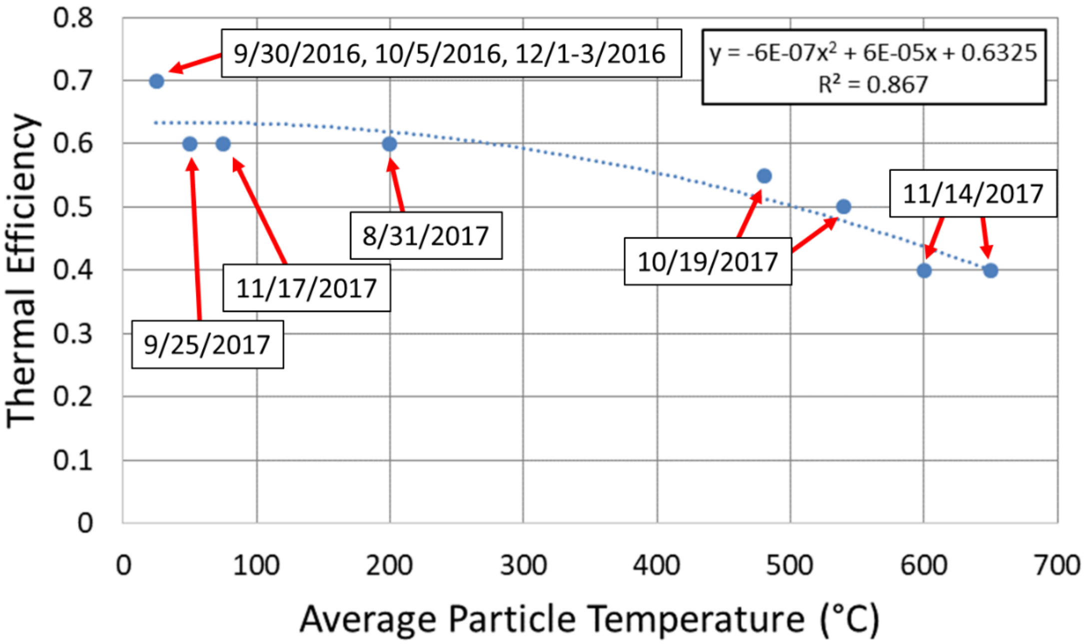

Figure 5.49 – *Experimental test results. The first point on the top left is the result of multiple optical efficiency tests using water. The remaining points are taken using the alumina particulate HTF.*

By the end of testing the thermal HCE had undergone more than 50 hours of on-sun operation. On November 17th, 2017 the HCE was dismounted from the system with no visual indication of any degradation (Figure 5.50). Based on these experimental results the collector achieves a thermal efficiency of 40% at a particle temperature of 650 °C.

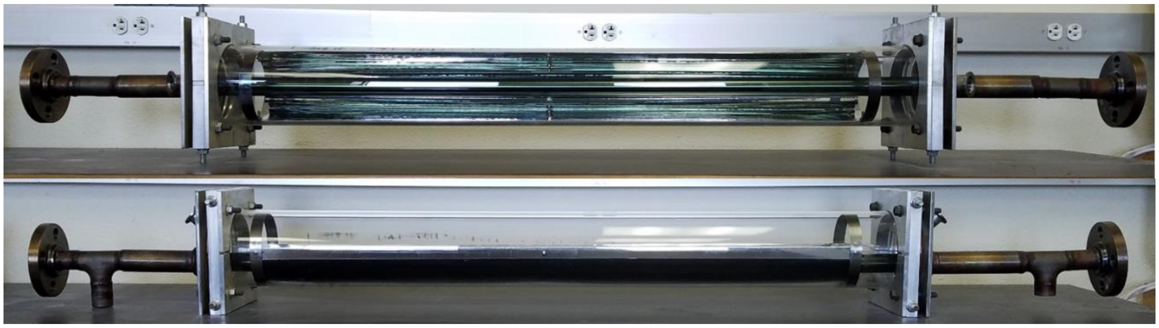

Figure 5.50 – *Dismounted HCE from top view (top) and side view (bottom).*

The experimental results of the thermal HCE are plotted against the modelled performance in Figure 5.51, and loss mechanisms are discussed in section 5.6.

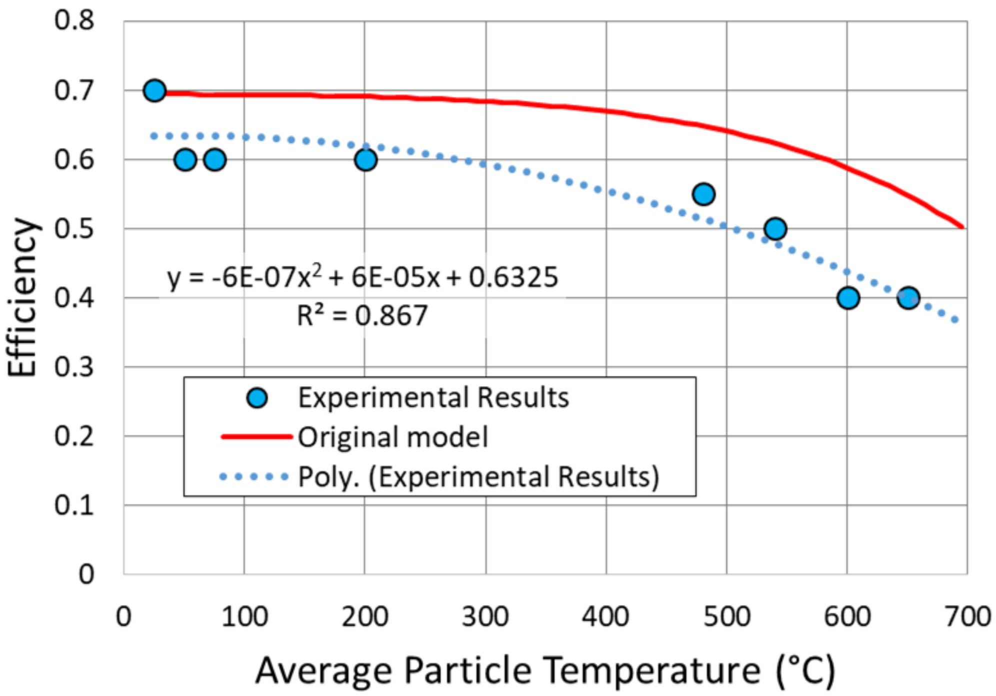

Figure 5.51 – *Modelled versus experimental data. An updated model reduces the optical efficiency to 63% with an estimated increase in absorber surface temperature of 125 °C due to poor heat transfer.*

5.5 Hybrid HCE Testing

5.5.1 Water Testing

Water testing on the hybrid HCE was conducted between 4/29/2017 – 5/17/2017. A representative water test day is shown in Figure 5.53 for the date of 5/17/2017.

Figure 5.52 – *Hybrid HCE On-Sun during May 17th optical efficiency tests using water.*

Optical efficiency testing was performed on May 17th, 2017 using water as the thermal stream HTF. There was no vacuum during this test but this should have little effect since the collector was operating near ambient conditions.

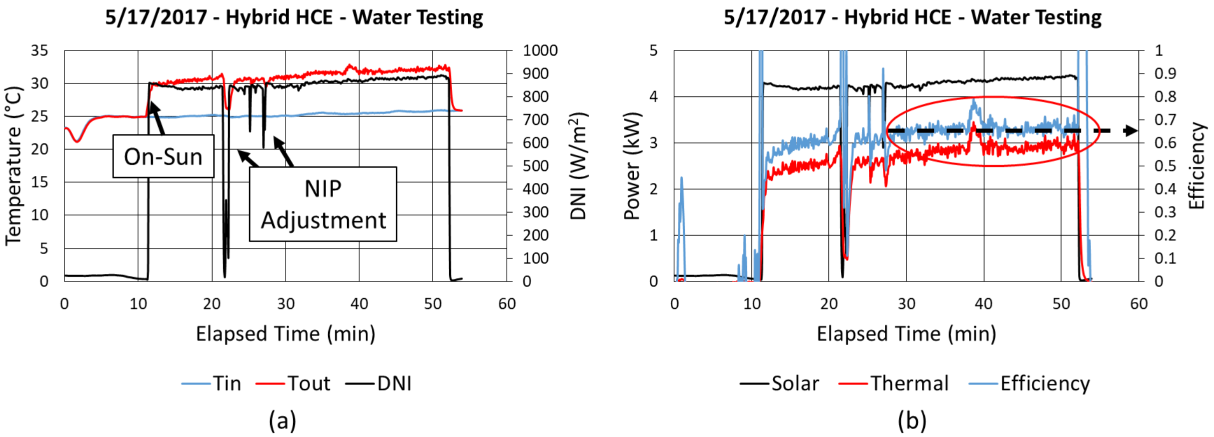

(a) (b)

Figure 5.53 – *Hybrid HCE water testing.*

IV-curve tracing was performed on all 4 strips of cells (Figure 5.54) using a manually adjusted variable resistor and measuring the voltage and current output of each strip. The resulting maximum solar-to-electric efficiency of the cell subsystem (by summing the maximum power points of each strip) is approximately 4%.

After this test, the leak which prevented a vacuum from being pulled was repaired (by disassembly, fabrication of an entirely new end-cap and all components, and re-assembly). After re-assembly, one of the solar cell strips had lost its contact. This test was beforehand, and is why all 4 strips produced a measureable IV-curve in Figure 5.54. Each color is representative of a single strip.

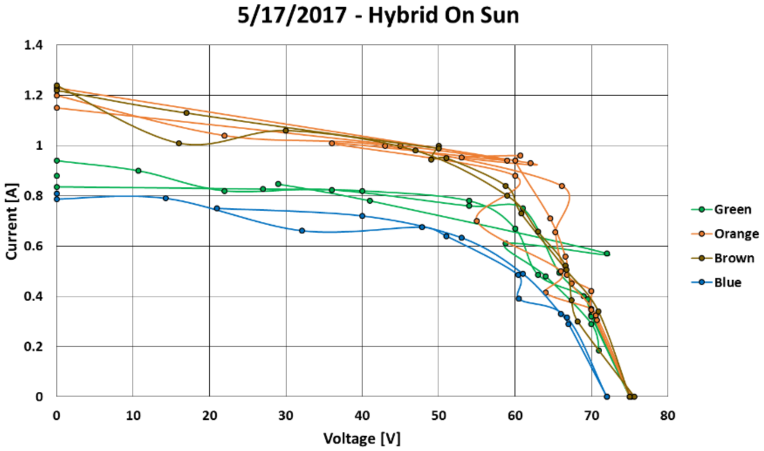

Figure 5.54 – *IV curves during water testing.*

5.5.2 Particle Testing

By November 18th, 2017 the HCE had been connected to the particle rig. Starting at midnight on November 18th, the system was heated until the HCE outlet reached a stable 600 °C by 10 am. The temperature profiles during the test are shown in Figure 5.55. The HCE was evacuated, reaching a lowest internal pressure of 1.9 e^{-3} mbar. IV-curve tracing was performed on all 4 strips of cells (Figure 5.56), however, only 3 strips were active as one strip had disconnected during a vacuum-seal repair). The maximum power for all three strips was about 42 Watts (60 V and 0.7 A) and this was assumed for the fourth strip in the estimation of cell electric efficiency. During testing, only 1 thermocouple at the outlet of the HCE was active. As a result, the thermal efficiency calculated for this test is considered uncertain.

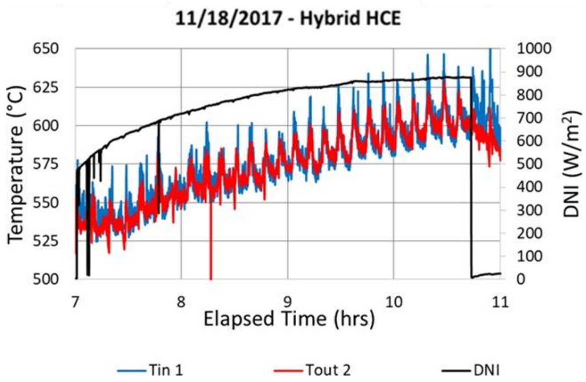

Figure 5.55 – *11/18/2017 – High temperature testing (600 °C) with particles.*

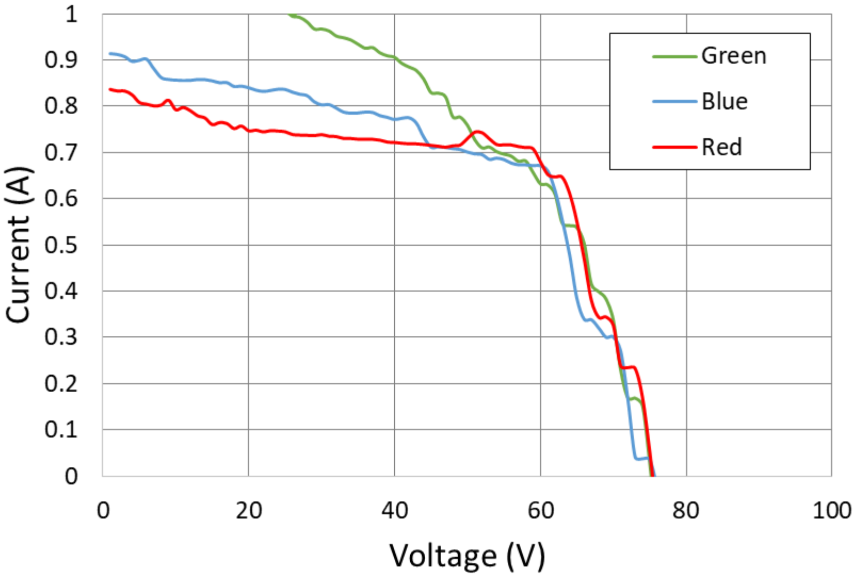

Figure 5.56 – *11/18/2017 – IV Curves during high temperature (600 °C) testing*

On December 4th, 2017 a second optical efficiency test was performed, this time using particles (Figure 5.57). The thermal efficiency with particles was nearly identical to the earlier optical efficiency tests with water, indicating little to no degradation of the hybrid HCE after elevated temperature testing.

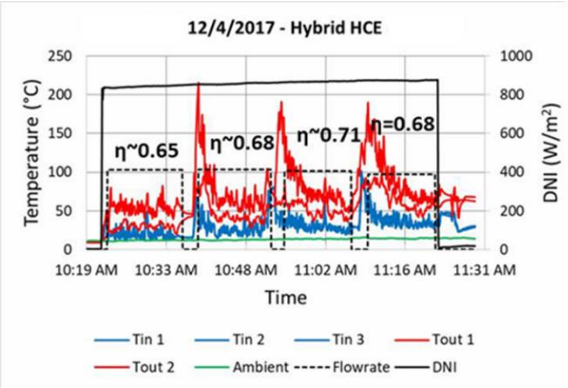

Figure 5.57 - *12/4/2017 – Optical efficiency testing with particles*

On December 5th, 2017 the hybrid HCE was operated under slowly increasing temperatures up to 250 °C peak (Figure 5.58). Cell performance was not quantified in these last two tests.

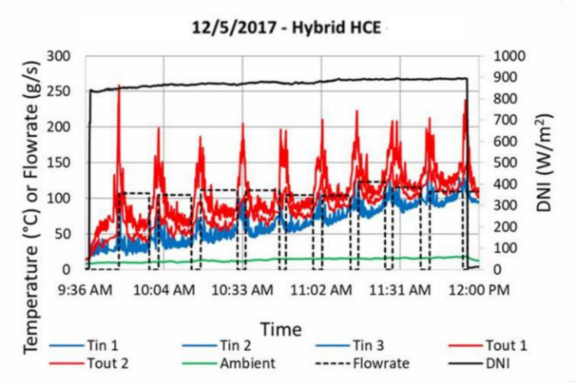

Figure 5.58 - *12/5/2017 – Low temperature testing with particles.*

5.5.3 Summary

A picture of the hybrid HCE on sun is shown in Figure 5.59 and test results summarized in Table 5.9.

Date	Duration	Thermal Stream HTF	Thermal Stream Temp	Average Thermal Efficiency	Cooling Temp	Cooling Flow rate	Cell Thermal Generation*	Cell Electric Efficiency*	HCE Internal Pressure
5/17/2017	3 hrs	Water	40 °C	64%	20-35 °C	~25 g/s	17%	4%	Atmospheric
12/4/2017	1 hr	Particles	50 °C	63%	16-26 °C	~25 g/s	16%	-	1.2 e^{-2} mbar
12/5/2017	3 hrs	Particles	100 °C	62%	23-28 °C	~25 g/s	12%	-	1.4 e^{-2} mbar

Table 5.9 – *Hybrid experimental test results*

*Unless a solar cell strip was undergoing IV curve tracing, there was not a continuous load on the solar cells. As a result, any would-be electric generation is instead converted into heat and accounted for by an increase in the "cell thermal generation" measurement. This partially explains the increase in cell thermal generation over the simulations.

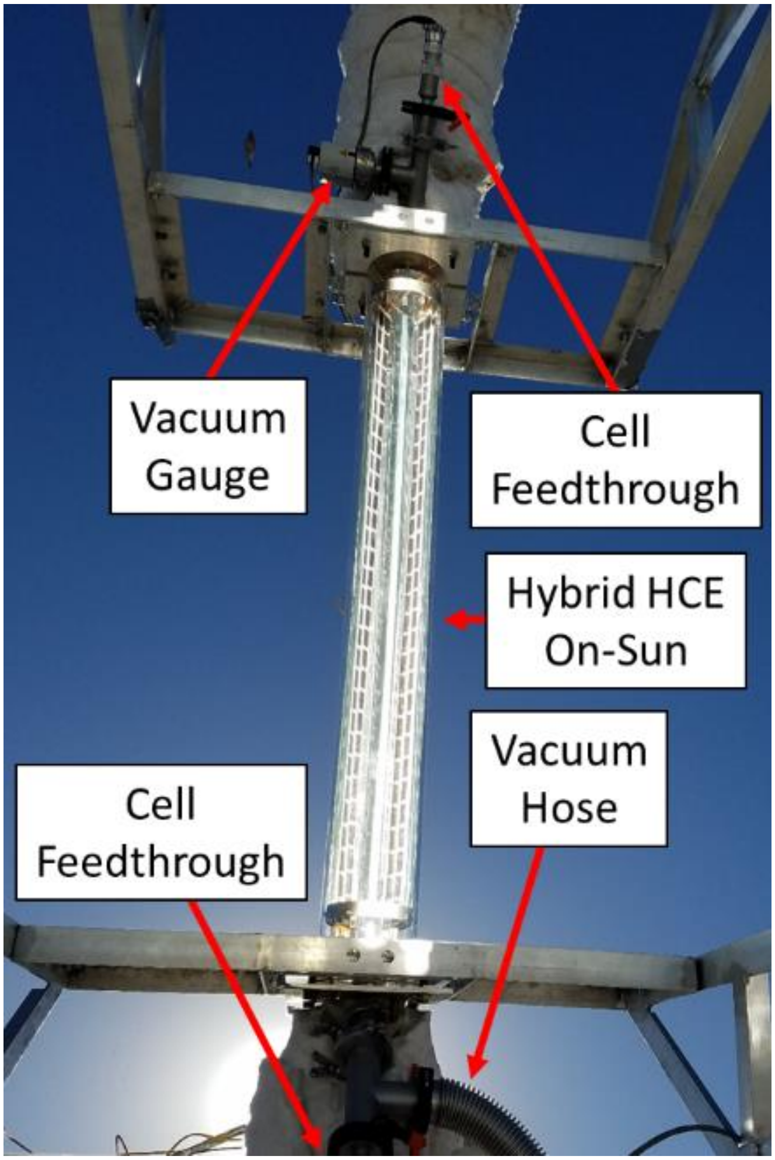

Figure 5.59 – *Hybrid HCE on-sun during 600 °C testing.*

The consistency between the simulated optical efficiency (62%) and the measured optical efficiency with water (64%) and particles (63%) indicates successful operation of the optical system, including spectrum splitting by the solar cells. Solar cell performance was about 2/3 the expected performance and factors involved in this are discussed in section 5.6.3. The high temperature thermal efficiency data point, however, was much lower than expected. As previously mentioned, only one thermocouple each at the inlet and outlet was active during this test and there may be an underestimation of performance simply based on thermocouple location since we see a significant variation in temperature between thermocouples in the other tests. The mechanisms which contribute to lower than simulated performance are discussed in more detail in the next section.

5.6 Discussion

5.6.1 Optical Losses

Several optical loss mechanisms were apparent in the experimental test (see Figure 5.60). Support rings (2.5 cm wide) at the top and bottom of the HCE shade about 5% of the aperture. Additionally, a combination of primary mirror misalignment and structural drooping of the support structure from the weight and distance of the HCE caused some light to miss the HCE aperture (mostly above the aperture). Furthermore, misalignment of the secondary reflector inside the HCE (rotation, non-uniformity along length of HCE) was apparent in both HCEs and must have contributed to some gap loss and light rejection from the primary.

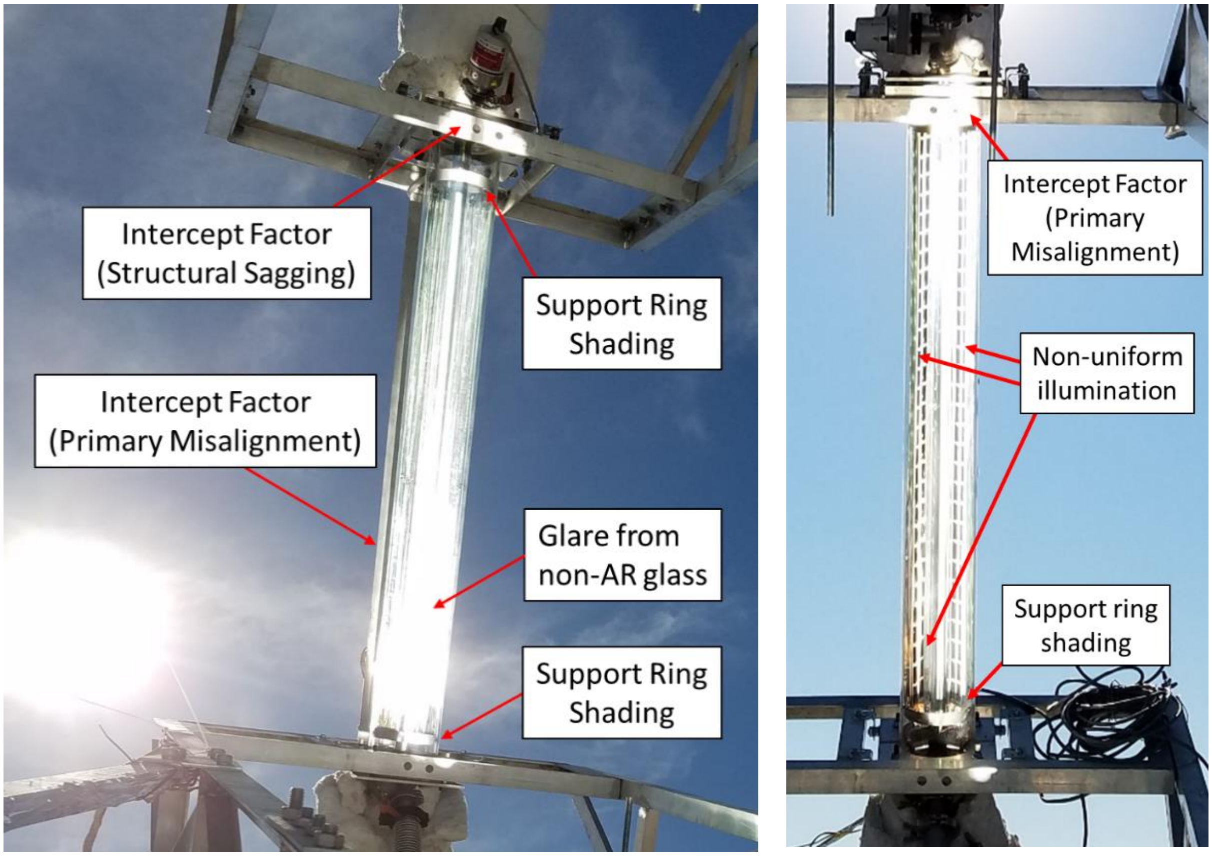

Figure 5.60 – *Optical losses in Thermal (left) and Hybrid (right) HCEs.*

Fortunately these losses are likely recoverable. The HCE assembly can be re-designed to not shadow itself by the support rings and improved precision in the assembly can reduce misalignment effects. Proper orientation in a single-axis tracking commercial system will reduce structural sagging and alignment of the primary mirrors would be standard in a commercial system. An interesting observation is that during the optical efficiency tests with water the tracker was much lighter without the pipes, insulation, or heaters installed and likely had little to no structural sagging. Additionally, during those tests the early iterations of the HCE had no support rings to shade the secondary aperture. The combination of these two effects may be the reason the optical efficiency tests consistently demonstrated 70% with water and 60% with particles. Increasing the acceptance angle of the secondary by ±5° may be an option to allow for some rotational misalignment without rejecting light from the primary. Lastly, the use of anti-reflective coatings on the glass tube (which was unavailable for the prototype) would be standard in a commercial product, improving transmittance from 92% to 96% and optical efficiency from 70% to 73%.

5.6.2 Thermal Losses

Higher than simulated thermal losses are evident in the widening gap between the results of simulation and actual tests at higher temperatures. As mentioned earlier, the secondary reflector shape of the thermal HCE prototype could be optimized to achieve a concentration ratio of 68X instead of 50X which would reduce the effects of radiative losses. Further, the particle HTF flow rates and particle to carrier air weight ratios could be optimized to increase particle HTF side heat transfer coefficients and reduce the absorber surface temperatures and radiation losses.

5.6.3 Solar Cell Losses

The solar cells generated roughly 2/3 what was expected, which can be explained in part by the following effects. Non-uniform illumination limits the current output of each strip and is evident in Figure 5.60. The internal HCE assembly has a supporting ring at the top and bottom of the tube which shades half of both the top and bottom cells. This activates the bypass diode on the top and bottom cell of each strip, dropping the number of active cells from 30 to 28 (93%). Additionally, grid contacts cover approximately 14% of the cell area and the cells themselves have approximately 97% width utilization and 81% height utilization of the strip (Figure 5.61), equivalent to approximately 79% area utilization of the strip.

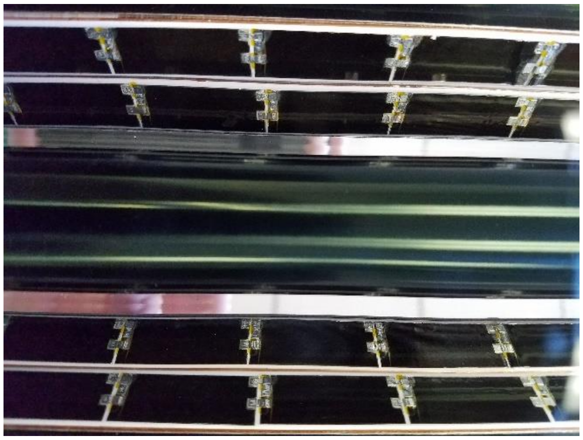

Figure 5.61 – *Solar cell assembly*

5.6.4 Reflector Deformation

Immediately following the first on-sun test thermal HCE test with particles there was visible deformation of the secondary reflector and the HCE was dismounted for inspection and repair. A few non-SS internal parts (galvanized nuts and bolts) had caused deposition on the glass tube as shown in Figure 5.62 (a) and the secondary reflector was severely deformed Figure 5.62 (b),(d). The deposition located approximately ½” from the cold resting position of the support ring Figure 5.62 (c) indicated a temperature rise (based on the expansion coefficient of aluminum) of approximately 500 °C. Further disassembly revealed the secondary reflector had been completely annealed and easily deformed to the touch, confirming an elevated temperature above 400 °C.

We can describe the heating of the reflector from the concentrated light from the primary mirror, radiation absorbed from the absorber, and account for distinct front and back emittance of the reflector to allow for the possibility of painting the backside with a highly emitting coating with Equation 5.11.

$$\underbrace{(DNI * 20X)\rho_{primary}\tau_{glass}\alpha_{reflector}}_{\text{Concentrated flux from primary}} + \underbrace{\alpha_{reflector}\varepsilon_{absorber}\sigma T_{absorber}^{4}}_{\text{Radiation from absorber}} = \underbrace{(\varepsilon_{reflector,front} + \varepsilon_{reflector,back})\,\sigma\, T_{reflector}^{4}}_{\text{Radiation from reflector}} \qquad (5.11)$$

If we assumed 900 W/m^2 DNI, a primary reflectance of 0.92, a transmittance of 0.90, 0.05 reflector absorptance, 0.25 absorber emittance, operating temperature of 650 °C, and reflector emittance (both front and back) of 0.05, we get a reflector temperature of about 275 °C. If we instead estimate the backside of the reflector has an emittance of 0.95 to account for painting it black, we get a reflector temperature closer to 35 °C. This simple calculation demonstrates the potential for passive radiative cooling of the secondary reflector and was implemented in later iterations.

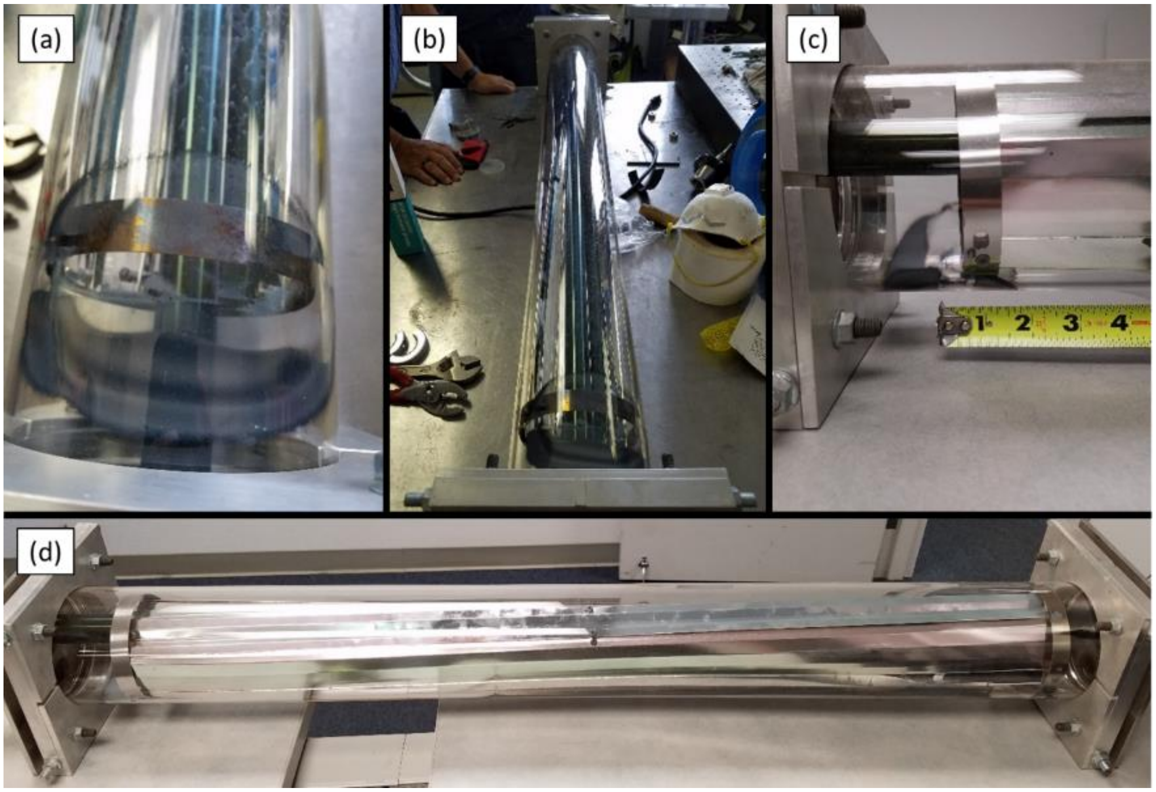

Figure 5.62 – *HCE Degradation / Deformation*

The backside of the secondary reflector (Figure 5.63 (a)) was painted black using the highly emissive Pyromark paint Figure 5.63 (b) and cured at 200 °C for 2 hours in a vacuum chamber. All nuts and bolts inside the HCE were switched to stainless steel (Figure 5.63 (c)), and a “wye” catcher (Figure 5.63 (d)) was implemented at the opposite end of the tube to restrain the secondary reflector at both ends and prevent it from twisting. The resulting HCE was tested with particles up to 685 °C at the outlet with no deformation of the secondary reflector.

There was no recorded deformation with the hybrid HCE. By the time it was fabricated and assembled, it had already had its backside painted black as a result of the deformation learnings with the thermal HCE. Furthermore, active cooling of the cells likely provides some active cooling of the reflector.

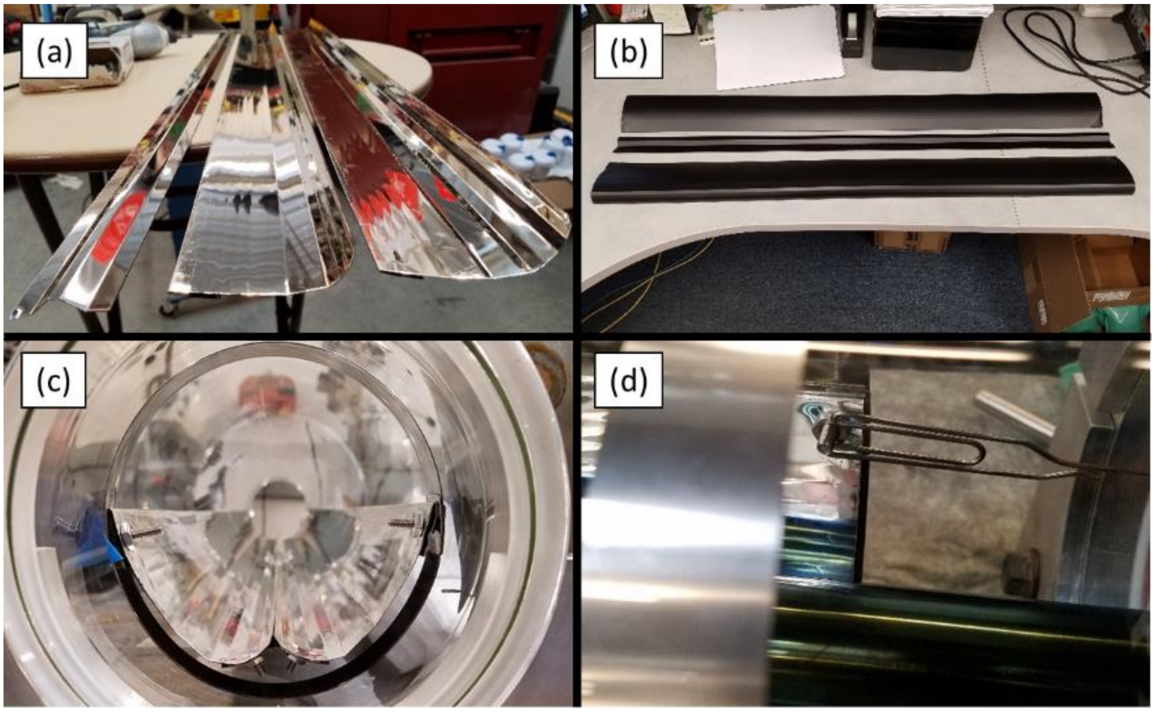

Figure 5.63 – *HCE modifications to prevent deformation*

5.7 Summary

The experimental and technical achievements of this second generation collector are listed below:

- The thermal HCE was successfully tested up to 650 °C on-sun for over 50 hours
- After painting the back-side black, there was no deformation/degradation of the thermal HCE.
- The hybrid HCE was successfully tested up to 600 °C on-sun for over 20 hours
- There was no deformation/degradation of the cells or HCE after testing
- The IV curves of cells were consistent between high and low temperature testing.
- Particle circulation was successfully achieved for over 70 hours.
- Particles were successfully operated up to 685 °C peak.

Several new concepts were developed and tested in this work.

A passively cooled secondary reflector is a viable option for providing additional concentration in a parabolic trough system. In the literature, many secondary designs avoid having the secondary reflector touch the hot absorber surface to prevent melting or degradation. There were no such issues, even up to an absorber temperature of at least 685 °C. Having a vacuum likely reduces the thermal contact between surfaces to very small “point-contacts” which reduces the area for conduction to a minimum. Passive radiative cooling of the reflector through a highly emissive back surface was key to preventing overheating and deformation under concentrated solar flux.

Back-reflecting solar cells also seem to be a viable option for spectrum splitting. They eliminates the need for additional optical or light-filtering materials, which reduces the number of components, optical interfaces, and potential losses.

The use of internally flowing particulate HTF was demonstrated for the first time in an actual prototype collector system which involved several meters of pipe and flex hoses. Solid particles allow an increase in operating temperature beyond the 400 °C limit of thermal oils and the 580 °C limit of current molten salts.

Additionally, the feasibility of a two-stage thermal-only collector was demonstrated. The current thermal-only secondary profile was made to match the hybrid profile under the constraint of integrated flat solar cell strips. Without this constraint, the concentration ratio can be improved from 50X to 67.5X. Since parabolic trough absorbers operate in evacuated conditions and can utilize selective coatings which impart a degree of "spectral" concentration, two-stage trough designs may be able to deliver high temperature thermal power at temperatures which are currently only achievable by dish or solar tower systems. This presents an exciting opportunity for situations where other technologies are less suitable (i.e. distributed, small scale, or industrial process heat).

Experimental prototype development and testing indicated a number of improvements which could be made for future collectors and also highlighted potential areas for future research:

- **Improve primary mirror assembly**: More accurate mounting of the primary mirror segments will improve the distribution and uniformity of light on the HCE.
- **Stronger support frame:** the high downward torque of the HCE as a result of the extended focal distance (~3m) caused the HCE to drop below the focused light beam from the primary. A stronger supporting structure would reduce sagging and improve optical efficiency by increasing the intercept factor.
- **Optimize HCE assembly:** Several improvements to the HCE assembly are possible, including removing the support rings to reduce cell and absorber shading and improving the accuracy and tolerances of the secondary to improve geometric efficiency.
- **AR coating:** an anti-reflective coating on the internal and external glass surface of the HCE would improve light transmission from ~92% to ~95%, improving optical efficiency and overall performance.
- **Increase cell active area:** reducing the grid contact coverage of solar cells and increasing the cell utilization of space over the minichannels will help recover some of the cell power which was lost in this prototype.
- **Improve cell connection method (leads):** one of the cell strip leads was disconnected during prototype HCE repair. The cell leads were connected using alligator clips to wire which transitioned through a vacuum feed-through to remove the lines outside the evacuated HCE. There are several points where a line can be easily disconnected and further design must be made to eliminate the risk of disconnection.
- **Particle flow characterization:** A greater understanding of particle flow is required to properly quantify the temperature distribution within the flow and calculate the "bulk" temperature for accurate thermal power calculations. Furthermore, an understanding how the different flow parameters (feed pressure, fluidization flow rate) affects the volume fraction of particles inside the absorber pipe is needed. Particle flow can then be optimized (feed pressure, fluidization flow rate) to maximize heat transfer from the inner absorber surface into the particle stream.
- **Circulation optimization:** Optimization of the particle circulation rig is also needed to reduce charge-cycle duration and reduce the amount of "down-time" to maximize particle flow and prevent absorber stagnation.

6. Dissertation Summary and Conclusions

A novel hybrid CPV/CSP solar collector using a two-stage (PTC + CPC) optical system and back-reflecting spectrum splitting solar cells has been designed and optimized for the purpose of power generation. It has currently undergone two rounds of prototype development and experimental testing.

In its current iteration, the two-stage concentrator consists of a parabolic primary and CPC secondary to achieve a geometric concentration of 50X on the thermal absorber. Modifications to the optics of the secondary CPC allowed integration of flat, back-reflecting solar cells into the secondary profile without any loss of geometric efficiency. This optimized design has the potential to achieve 40% solar-to-exergy and 23% solar-to-electric efficiency at 600 °C as a result of simulations, with a thermal fraction of 73% and an estimated mass-production install cost of $\$2.15/W_e$.

The design has been developed into multiple prototype collectors (thermal-only and hybrid configurations) which were experimentally characterized at the University of California in Merced. The novel use of suspended particles as a heat transfer medium (developed by GTI) in combination with the two-stage concentrator enabled us to reach record operating temperatures in a linear solar thermal system and performance has been successfully measured up to 685 °C. The most recent prototypes (thermal and hybrid) have undergone over 100 hours of combined on-sun testing.

These prototypes have demonstrated several novel concepts:

1. The ability of a two-stage linear trough system to generate high concentration ratios on the absorber and enabling efficient high temperature operation.
2. The use of back-reflecting solar cells to provide spectrally selective secondary concentration.
3. The potential of particulate HTFs for increasing the operating temperature in solar thermal systems above the 400 °C limit of thermal oils and the 580 °C limit of current molten salts.

As a result of these successful demonstrations, we are left with a number of takeaways:

- Two-stage linear trough systems can achieve concentration ratios 50-69X with realistic acceptance angles. When combined with selective coatings in a vacuum receiver, this enables high temperature operation (650 °C demonstrated) in the realm of tower technologies (SunShot research target of 700 °C, with most recent Ivanpah facility operating at 565 °C). This presents an exciting opportunity for bankable, distributed, or small scale trough solar thermal systems operating at high temperature where tower configurations are less suitable.
- The ability to reach high temperatures is only valuable when paired with a compatible heat transfer fluid (HTF). The particulate HTF utilized in this work has now demonstrated successful 650 °C operation, surpassing the 400 °C limit of thermal oils and the 580 °C limit of current molten salts. This presents an exciting opportunity for high temperature industrial process heat (IPH) and concentrating solar power (CSP) systems which now can potentially achieve higher solar-to-electric efficiencies as a result of high temperature operation.

The demonstrations in this work are part of the continuing development of solar and renewable technologies. It is the author's hope that the findings here will contribute to the development of new technologies and ultimately aid in the global energy transformation.

Appendix

Appendix A1 – Two-Stage Parabolic Trough Literature Review

The use of a secondary optic in tandem with a primary parabolic trough for increased concentration has been reported in the literature since the 1980s. Early on it was shown a symmetric compound elliptical concentrator (CEC) secondary optic could easily improve system concentration by more than 2X (Winston and Welford 1980). Asymmetric solutions were also reported (Mills 1980), which benefit from the fact the secondary does not shade the primary reflector (Kritchman 1982). Several secondary designs were subsequently proposed with features such as being encased in evacuated tubes and with acceptance angles to accommodate 90° rim angle parabolic trough primaries such as the asymmetric CPC (Collares-Pereira et al. 1991) and CEC (Collares-Pereira et al. 1995).

When comparing two-stage systems of different secondary concentrators (ideal, non-ideal, symmetric, asymmetric), one cannot use the geometric concentration ratio as the sole measure of performance because asymmetric collectors do not follow the ideal 2D geometric concentration and in non-ideal collectors there is a trade-off between optical transmission and geometric concentration (Mills 1995). Since flux concentration from the primary is high, high optical transmission of the secondary optic is favored at the expense of geometric concentration. Optics with somewhat less than maximal concentration, however, can still lead to compact secondary optics that collect all the radiation from the primary.

This led to the development of some non-ideal tailored edge-ray concentrators (TERC) (Friedman et al. 1993), designed according to the edge-ray principle (Ries and Rabl 1994). While simplistic, they suffered significant shading of the primary and were found to be more suitable for point-focus systems where the shaded area is highly reduced.

A second class of tailored concentrators (Ries and Sprikl 1996) were designed to sacrifice geometric concentration ratio in favor of optical transmission for reflectors comprised of an involute portion and a flat portion. The resulting "seagull" concentrators resemble birds in flight and achieve compact secondary concentration on the order of 2X for parabolic troughs of 90° rim angles (Spirkl et al. 1997).

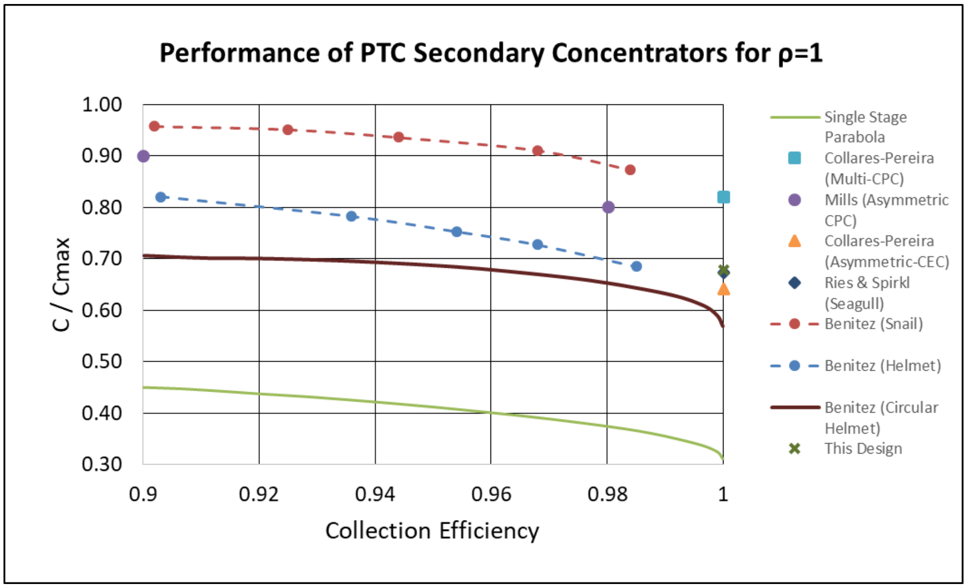

Figure A1.1 – Concentration ratio versus geometric efficiency

A class of *contactless* concentrators (asymmetric “snail design” (Benitez et al. 1997), and symmetric “helmet” design (Benitez 1998) was developed using the simultaneous multiple surface (SMS) method (Minano and Gonzalez 1992) achieving higher average flux concentrations over previous designs at similar collection efficiencies (95% maximum concentration ratio for 90% collection efficiency in the snail design). Simulations also showed concentration boosts of 1.75X were possible using simple arc-mirrors (inside surface of evacuated glass tube is coated with reflective surface) (Benitez 1998).

Asymmetric designs typically have smaller aspect ratios due to their ability to make use of larger rim angles (Schmitz et al. 2015). They also achieve higher concentration ratios by the virtue of not-shading the primary mirror. A composite “symmetric” design (by placing two asymmetric designs side by side) would incur similar shading losses to a symmetric concentrator but could make use of larger rim angles.

While previous discussions have all been based on parabolic mirrors, one can relax the requirement of a parabolic primary with the use of nonimaging optics to produce an infinite number of profiles which achieve the same geometric concentration (Cooper et al. 2014). This has led to the development of new mirror solutions, such as reflectors that are shaped by inflating metallized polymer films (Good et al. 2014).

A different secondary concentrator (XX-SMS) was proposed for large aperture *parabolic-like* primary mirrors (Canavarro et al. 2013). By moving to a rim angle of 55°, the geometric concentration was doubled compared to existing troughs, but the design suffers lower optical efficiency due to extra shading and reflection losses. In an effort to reduce these shading losses, an alternative CEC-type design (Canavarro et al. 2016) incorporating simple v-groove back reflectors (as shown in (McIntire 1980, Gee et al. 2002)) was developed for rim angles of 45° with significantly slimmer secondary profiles. While both designs suffer in optical performance compared to existing PTCs, increased concentration would theoretically enable more efficient operation at higher temperatures, with higher corresponding thermal-to-electricity conversion efficiencies. Additionally, both designs require roughly half the number of collector rows compared to existing plants (due to the larger aperture size), which should reduce the total cost of components (receivers, pipe length, heat losses, HTF quantity) and installation.

Along the same lines, a “Macrofocal” parabola has been designed and paired with an arc-Helmet type secondary which improves the concentration ratio 1.6X over traditional troughs while still allowing the use of standard commercially available 70mm diameter tubes (Bootello 2016) The two-stage system is designed for a 100% intercept factor and makes use of the simplistic design of the arc-Helmet secondary.

Additionally an investigation was done into the use of simple flat secondary mirrors placed above the absorber for traditional PTC primary mirrors, allowing increases in concentration ratio up to 1.8X (Rodriguez-Sanchez and Rosengarten 2015).

There are several alternative non-parabolic linear solutions. One solution is the two-mirror aplanat (Ostroumov et al. 2009) which achieves excellent compactness but suffers large shading losses (Schmitz et al. 2015). Another solution combines nested asymmetric concentrators with absorbers located at both ends of the primary mirror (Benitez 1998). This design achieves compact concentration without requiring a secondary support structure to hold the absorber.

There are many design options for two stage systems that achieve good optical transmission and concentration. Early development focused on optimal design of parabolic-paired secondaries, while today there is more focus on the use of simpler secondaries paired in some cases with customized primary optics. There are several strategies for reducing the LCOE of energy delivered by parabolic trough systems, the use of secondary concentration to reach higher temperatures being one. Down-selection of both strategy and design will likely be the result of practical system-level considerations combined with market and economic considerations.

Appendix A2 – Selective Coating Literature Review

Typically most coatings tested and developed for applications up to 400 °C since this was the maximum operating temperature of most CSP plants. More recently several reviews have reported the development of high temperature coatings with decent absorptance, emittance, and stability in vacuum at high temperatures (Kennedy 2002), (Selvakumar & Barshilia 2012), (Cao et al 2014). The emittance of several selective coatings reported in the literature (Selvakumar and Barshilia 2012, Kennedy 2002) and by commercial suppliers (Almeco, Himin, Siemens, Schott, Archimede Solar) are plotted in Figure A2.1. A fit-curve is estimated as a function of temperature based on these coatings.

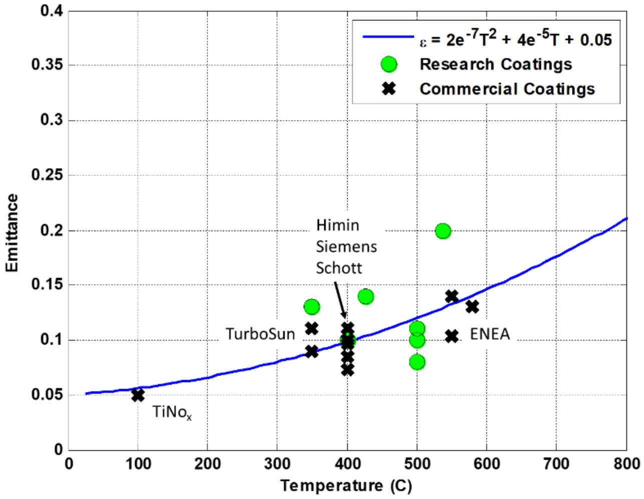

Figure A2.1 – Research & commercial selective coatings plotted against a fit curve.

References

Abdelhamid, M., Widyolar, B.K., Jiang, L., Winston, R., Yablonovitch, E., Scranton, G., Cygan, D., Abbasi, H. and Kozlov, A., 2016. Novel double-stage high-concentrated solar hybrid photovoltaic/thermal (PV/T) collector with nonimaging optics and GaAs solar cells reflector. Applied Energy, 182, pp.68-79.

Amori, K.E. and Abd-AlRaheem, M.A., 2014. Field study of various air based photovoltaic/thermal hybrid solar collectors. Renewable Energy, 63, pp.402-414.

An, W., Wu, J., Zhu, T. and Zhu, Q., 2016. Experimental investigation of a concentrating PV/T collector with Cu9S5 nanofluid spectral splitting filter. Applied energy, 184, pp.197-206.

An, W., Zhang, J., Zhu, T. and Gao, N., 2016. Investigation on a spectral splitting photovoltaic/thermal hybrid system based on polypyrrole nanofluid: preliminary test. Renewable energy, 86, pp.633-642.

Aste, N., Chiesa, G. and Verri, F., 2008. Design, development and performance monitoring of a photovoltaic-thermal (PVT) air collector. Renewable Energy, 33(5), pp.914-927.

Aste, N., del Pero, C. and Leonforte, F., 2014. Water flat plate PV–thermal collectors: a review. Solar Energy, 102, pp.98-115.

Behar, O., Khellaf, A. and Mohammedi, K., 2013. A review of studies on central receiver solar thermal power plants. Renewable and sustainable energy reviews, 23, pp.12-39.

Benítez, P., García, R. and Miñano, J.C., 1997. Contactless efficient two-stage solar concentrator for tubular absorber. Applied optics, 36(28), pp.7119-7124.

Benitez, P., Minano, J.C., Garcia, R. and Arroyo, R.M., 1997, October. Contactless two-stage solar concentrators for tubular absorber. In Nonimaging Optics: Maximum Efficiency Light Transfer IV (Vol. 3139, pp. 205-217). International Society for Optics and Photonics.

Benítez, P., 1998. Advanced concepts of non-imaging optics: design and manufacture (Doctoral dissertation, PhD Thesis, Presented in Madrid).

Benoit, H., López, I.P., Gauthier, D., Sans, J.L. and Flamant, G., 2015. On-sun demonstration of a 750 C heat transfer fluid for concentrating solar systems: dense particle suspension in tube. Solar Energy, 118, pp.622-633.

Benoit, H., Spreafico, L., Gauthier, D. and Flamant, G., 2016. Review of heat transfer fluids in tube-receivers used in concentrating solar thermal systems: Properties and heat transfer coefficients. Renewable and Sustainable Energy Reviews, 55, pp.298-315.

Bentley, R., Anstey, B., Callear, J., Chonavel, S., Clark, I., Collins, I., Ramallo, A., Scanlon, H. and Weatherby, C., 2010, October. The Whitfield Solar CPV Collector. In AIP Conference Proceedings (Vol. 1277, No. 1, pp. 167-170). AIP.

Bierman, D.M., Lenert, A. and Wang, E.N., 2016. Spectral splitting optimization for high-efficiency solar photovoltaic and thermal power generation. Applied Physics Letters, 109(24), p.243904.

Blair, N., Dobos, A.P., Freeman, J., Neises, T., Wagner, M., Ferguson, T., Gilman, P. and Janzou, S., 2014. System advisor model, sam 2014.1. 14: General description (No. NREL/TP-6A20-61019). National Renewable Energy Laboratory (NREL), Golden, CO.

Bootello, J.P.N., Price, H., Pérez, M.S. and Castellano, M.D., 2016. Optical Analysis of a Two Stage XX Concentrator for Parametric Trough Primary and Tubular Absorber With Application in Solar Thermal Energy Trough Power Plants. Journal of Solar Energy Engineering, 138(4), p.041002.

Born, M. and Wolf, E., 2013. Principles of optics: electromagnetic theory of propagation, interference and diffraction of light. Elsevier.

Branz, H.M., Regan, W., Gerst, K.J., Borak, J.B. and Santori, E.A., 2015. Hybrid solar converters for maximum exergy and inexpensive dispatchable electricity. Energy & Environmental Science, 8(11), pp.3083-3091.

Brogren, M., Nostell, P. and Karlsson, B., 2001. Optical efficiency of a PV–thermal hybrid CPC module for high latitudes. Solar Energy, 69, pp.173-185.

Canavarro, D., Chaves, J. and Collares-Pereira, M., 2013. New second-stage concentrators (XX SMS) for parabolic primaries; Comparison with conventional parabolic trough concentrators. Solar Energy, 92, pp.98-105.

Canavarro, D., Chaves, J. and Collares-Pereira, M., 2016. A novel Compound Elliptical-type Concentrator for parabolic primaries with tubular receiver. Solar Energy, 134, pp.383-391.

Cao, F., McEnaney, K., Chen, G. and Ren, Z., 2014. A review of cermet-based spectrally selective solar absorbers. Energy & Environmental Science, 7(5), pp.1615-1627.

Carroll, S.M., 2010. From eternity to here: the quest for the ultimate theory of time. Penguin.

Cespedes, E., Wirz, M., Sánchez-García, J.A., Alvarez-Fraga, L., Escobar-Galindo, R. and Prieto, C., 2014. Novel Mo–Si3N4 based selective coating for high temperature concentrating solar power applications. Solar energy materials and solar cells, 122, pp.217-225.

Charalambous, P.G., Maidment, G.G., Kalogirou, S.A. and Yiakoumetti, K., 2007. Photovoltaic thermal (PV/T) collectors: A review. Applied Thermal Engineering, 27(2-3), pp.275-286.

Chemisana, D., López-Villada, J., Coronas, A., Rosell, J.I. and Lodi, C., 2013. Building integration of concentrating systems for solar cooling applications. Applied Thermal Engineering, 50(2), pp.1472-1479.

Chendo, M.A.C., Jacobson, M.R. and Osborn, D.E., 1987. Liquid and thin-film filters for hybrid solar energy conversion systems. Solar & wind technology, 4(2), pp.131-138.

Chow, T.T., 2010. A review on photovoltaic/thermal hybrid solar technology. Applied energy, 87(2), pp.365-379.

Chow, T.T., Tiwari, G.N. and Menezo, C., 2012. Hybrid solar: a review on photovoltaic and thermal power integration. International Journal of Photoenergy, 2012.

Chun-Hui, S., Zhong-Yang, L., Tao, W., Wei-Dong, S., Gary, R., Cheng, W., Ming-Jiang, N. and Ke-Fa, C., 2011. A dielectric multilayer filter for combining photovoltaics with a Stirling engine for improvement of the efficiency of solar electricity generation. Chinese Physics Letters, 28(12), p.128402.

Collares-Pereira, M., Gordon, J.M., Rabl, A. and Winston, R., 1991. High concentration two-stage optics for parabolic trough solar collectors with tubular absorber and large rim angle. Solar energy, 47(6), pp.457-466.

Collares-Pereira, M. and Mendes, J.F., 1995, August. Novel second-stage solar concentrator for parabolic troughs. In Nonimaging Optics: Maximum Efficiency Light Transfer III (Vol. 2538, pp. 125-131). International Society for Optics and Photonics.

Cooper, T., Dähler, F., Ambrosetti, G., Pedretti, A. and Steinfeld, A., 2013. Performance of compound parabolic concentrators with polygonal apertures. Solar Energy, 95, pp.308-318.

Cooper, T., Schmitz, M., Good, P., Ambrosetti, G., Pedretti, A. and Steinfeld, A., 2014. Nonparabolic solar concentrators matching the parabola. Optics letters, 39(15), pp.4301-4304.

Coventry, J.S., 2005. Performance of a concentrating photovoltaic/thermal solar collector. Solar Energy, 78(2), pp.211-222.

Crisostomo F, Taylor RA, Surjadi D, Mojiri A, Rosengarten G, Hawkes ER. Spectral splitting strategy and optical model for the development of a concentrating hybrid PV/T collector. Appl Energy 2015;141:238–46. doi:10.1016/j.apenergy.2014.12.044.

Crisostomo, F., Becker, J., Mesgari, S., Hjerrild, N. and Taylor, R.A., 2015, May. Desing and on-sun testing of a hybrid PVT prototype using a nanofluid-based selective absorption filter. In European Energy Market (EEM), 2015 12th International Conference on the (pp. 1-5). IEEE.

Crisostomo, F., Taylor, R.A., Surjadi, D., Mojiri, A., Rosengarten, G. and Hawkes, E.R., 2015. Spectral splitting strategy and optical model for the development of a concentrating hybrid PV/T collector. Applied Energy, 141, pp.238-246.

Crisostomo, F., Hjerrild, N., Mesgari, S., Li, Q. and Taylor, R.A., 2017. A hybrid PV/T collector using spectrally selective absorbing nanofluids. Applied energy, 193, pp.1-14.

Cygan, D., Abbasi, H., Kozlov, A., Pondo, J., Winston, R., Widyolar, B., Jiang, L., Abdelhamid, M., Kirk, A.P., Drees, M. and Miyamoto, H., 2016. Full Spectrum Solar System: Hybrid Concentrated Photovoltaic/Concentrated Solar Power (CPV-CSP). MRS Advances, 1(43), pp.2941-2946.

DeJarnette, D., Otanicar, T., Brekke, N., Hari, P. and Roberts, K., 2015. Selective spectral filtration with nanoparticles for concentrating solar collectors. Journal of Photonics for Energy, 5(1), p.057008.

DeJarnette, D., Tunkara, E., Brekke, N., Otanicar, T., Roberts, K., Gao, B. and Saunders, A.E., 2016. Nanoparticle enhanced spectral filtration of insolation from trough concentrators. Solar Energy Materials and Solar Cells, 149, pp.145-153.

Delgado-Torres, A.M., 2009. Solar thermal heat engines for water pumping: an update. Renewable and Sustainable Energy Reviews, 13(2), pp.462-472.

Denholm, P., Wan, Y.H., Hummon, M. and Mehos, M., 2013. Analysis of concentrating solar power with thermal energy storage in a California 33% Renewable Scenario (No. NREL/TP-6A20-58186). National Renewable Energy Laboratory (NREL), Golden, CO.

DeSandre, L., Song, D.Y., Macleod, H.A., Jacobson, M.R. and Osborn, D.E., 1985, December. Thin-film multilayer filter designs for hybrid solar energy conversion systems. In Optical Materials Technology for Energy Efficiency and Solar Energy Conversion IV (Vol. 562, pp. 155-160). International Society for Optics and Photonics.

Dunham, M.T. and Iverson, B.D., 2014. High-efficiency thermodynamic power cycles for concentrated solar power systems. Renewable and Sustainable Energy Reviews, 30, pp.758-770.

Duquette, B. and Otanicar, T., 2013. Comparative economic analysis of concentrating solar technologies. Journal of Solar Energy Engineering, 135(2), p.024504.

Falcone, P.K., Noring, J.E. and Hruby, J.M., 1985. Assessment of a solid particle receiver for a high temperature solar central receiver system (No. SAND-85-8208). Sandia National Labs., Livermore, CA (USA).

Farr, A. and Gee, R., 2009, January. The SkyTrough™ Parabolic Trough Solar Collector. In ASME 2009 3rd International Conference on Energy Sustainability collocated with the Heat Transfer and InterPACK09 Conferences (pp. 573-580). American Society of Mechanical Engineers.

Fernandes, D., Pitié, F., Cáceres, G. and Baeyens, J., 2012. Thermal energy storage: "How previous findings determine current research priorities". Energy, 39(1), pp.246-257.

Fernández-García, A., Zarza, E., Valenzuela, L. and Pérez, M., 2010. Parabolic-trough solar collectors and their applications. Renewable and Sustainable Energy Reviews, 14(7), pp.1695-1721.

Flamant, G., 1982. Theoretical and experimental study of radiant heat transfer in a solar fluidized-bed receiver. AIChE Journal, 28(4), pp.529-535.

Flamant, G., Gauthier, D., Benoit, H., Sans, J.L., Garcia, R., Boissière, B., Ansart, R. and Hemati, M., 2013. Dense suspension of solid particles as a new heat transfer fluid for concentrated solar thermal plants: On-sun proof of concept. Chemical Engineering Science, 102, pp.567-576.

Flamant, G., Gauthier, D., Benoit, H., Sans, J.L., Boissière, B., Ansart, R. and Hemati, M., 2014. A new heat transfer fluid for concentrating solar systems: Particle flow in tubes. Energy Procedia, 49, pp.617-626.

Friedman, R.P., Gordon, J.M. and Ries, H., 1993. New high-flux two-stage optical designs for parabolic solar concentrators. Solar Energy, 51(5), pp.317-325.

Fu, R., Feldman, D.J., Margolis, R.M., Woodhouse, M.A. and Ardani, K.B., 2017. US solar photovoltaic system cost benchmark: Q1 2017 (No. NREL/TP-6A20-68925). National Renewable Energy Laboratory (NREL), Golden, CO (United States).

Gallo, A., Spelling, J., Romero, M. and González-Aguilar, J., 2015. Preliminary design and performance analysis of a multi-megawatt scale dense particle suspension receiver. Energy Procedia, 69, pp.388-397.

Gee, R., Cohen, G. and Winston, R., 2002, January. A Nonimaging Receiver for Parabolic Trough Concentrating Collectors. In ASME Solar 2002: International Solar Energy Conference (pp. 269-276). American Society of Mechanical Engineers.

Gee, R., Brost, R., Zhu, G. and Jorgensen, G., 2010, September. An improved method for characterizing reflector specularity for parabolic trough concentrators. In Proceedings of Solar PACES Conference Perpignan (France) (Vol. 2124, p. 2O1O).

Ghosal, K., Lilly, D., Gabriel, J., Seel, S., Fisher, B. and Burroughs, S., 2014, June. Semprius module and system results. In Photovoltaic Specialist Conference (PVSC), 2014 IEEE 40th (pp. 3287-3292). IEEE.

Ginley, D., Green, M.A. and Collins, R., 2008. Solar energy conversion toward 1 terawatt. Mrs Bulletin, 33(4), pp.355-364.

Gómez-Gil, F.J., Wang, X. and Barnett, A., 2012. Energy production of photovoltaic systems: Fixed, tracking, and concentrating. Renewable and Sustainable Energy Reviews, 16(1), pp.306-313.

Good, P., Zanganeh, G., Ambrosetti, G., Barbato, M.C., Pedretti, A. and Steinfeld, A., 2014. Towards a commercial parabolic trough CSP system using air as heat transfer fluid. Energy Procedia, 49, pp.381-385.

Green, M.A., Emery, K., Hishikawa, Y., Warta, W. and Dunlop, E.D., 2013. Solar cell efficiency tables (version 41). Progress in Photovoltaics: Research and Applications

Green, M.A., Emery, K., Hishikawa, Y., Warta, W. and Dunlop, E.D., 2016. Solar cell efficiency tables (version 48). Progress in Photovoltaics: Research and Applications, 24(7), pp.905-913.

Green, M.A., Emery, K., Hishikawa, Y., Warta, W. and Dunlop, E.D., 2017. Solar cell efficiency tables (version 49). Progress in Photovoltaics: Research and Applications

Hinterberger, H. and Winston, R., 1968. Use of a solid light funnel to increase phototube aperture without restricting angular acceptance. Review of Scientific Instruments, 39(8), pp.1217-1218.

Hjerrild, N.E., Mesgari, S., Crisostomo, F., Scott, J.A., Amal, R. and Taylor, R.A., 2016. Hybrid PV/T enhancement using selectively absorbing Ag–SiO2/carbon nanofluids. Solar Energy Materials and Solar Cells, 147, pp.281-287.

Horne, S., Conley, G., Gordon, J., Fork, D., Meada, P., Schrader, E. and Zimmermann, T., 2006, May. A solid 500 sun compound concentrator PV design. In Photovoltaic Energy Conversion, Conference Record of the 2006 IEEE 4th World Conference on (Vol. 1, pp. 694-697). IEEE.

Hu, P., Zhang, Q., Liu, Y., Sheng, C., Cheng, X. and Chen, Z., 2013. Optical analysis of a hybrid solar concentrating photovoltaic/thermal (CPV/T) system with beam splitting technique. Science China Technological Sciences, 56(6), pp.1387-1394.

Ibrahim, A., Othman, M.Y., Ruslan, M.H., Mat, S. and Sopian, K., 2011. Recent advances in flat plate photovoltaic/thermal (PV/T) solar collectors. Renewable and sustainable energy reviews, 15(1), pp.352-365.

Imenes, A.G. and Mills, D.R., 2004. Spectral beam splitting technology for increased conversion efficiency in solar concentrating systems: a review. Solar energy materials and solar cells, 84(1-4), pp.19-69.

Imenes, A.G., Buie, D. and McKenzie, D., 2006. The design of broadband, wide-angle interference filters for solar concentrating systems. Solar energy materials and solar cells, 90(11), pp.1579-1606.

Jacobson, M.Z., Delucchi, M.A., Bazouin, G., Bauer, Z.A., Heavey, C.C., Fisher, E., Morris, S.B., Piekutowski, D.J., Vencill, T.A. and Yeskoo, T.W., 2015. 100% clean and renewable wind, water, and sunlight (WWS) all-sector energy roadmaps for the 50 United States. Energy & Environmental Science, 8(7), pp.2093-2117.

Jafrancesco, D., Sani, E., Fontani, D., Mercatelli, L., Sansoni, P., Giannini, A. and Francini, F., 2012. Simple methods to approximate CPC shape to preserve collection efficiency. International Journal of Photoenergy, 2012.

Ji, Y., Ollanik, A., Farrar-Foley, N., Xu, Q., Madrone, L., Lynn, P., Romanin, V., Codd, D. and Escarra, M., 2015, June. Transmissive spectrum splitting multi-junction solar module for hybrid CPV/CSP system. In Photovoltaic Specialist Conference (PVSC), 2015 IEEE 42nd (pp. 1-5). IEEE.

Jiang, S., Hu, P., Mo, S. and Chen, Z., 2010. Optical modeling for a two-stage parabolic trough concentrating photovoltaic/thermal system using spectral beam splitting technology. Solar Energy Materials and Solar Cells, 94(10), pp.1686-1696.

Jiang, S.L., Hu, P., Mo, S.P. and Chen, Z.S., 2009, March. Modeling for two-stage dish concentrating spectral beam splitting photovoltaic/thermal system. In Power and Energy Engineering Conference, 2009. APPEEC 2009. Asia-Pacific (pp. 1-4). IEEE.

Johnson, D.H., 1983. Quantum and thermal conversion of solar energy to useful work (No. NREL/TP--252-2137). National Renewable Energy Lab.(NREL), Golden, CO (United States).

Jorgenson, J., Mehos, M. and Denholm, P., 2016, May. Comparing the net cost of CSP-TES to PV deployed with battery storage. In AIP Conference Proceedings (Vol. 1734, No. 1, p. 080003). AIP Publishing.

Joshi, S.S., Dhoble, A.S. and Jiwanapurkar, P.R., 2016. Investigations of different liquid based spectrum beam splitters for combined solar photovoltaic thermal systems. Journal of Solar Energy Engineering, 138(2), p.021003.

Ju, X., Xu, C., Han, X., Du, X., Wei, G. and Yang, Y., 2017. A review of the concentrated photovoltaic/thermal (CPVT) hybrid solar systems based on the spectral beam splitting technology. Applied Energy, 187, pp.534-563.

Kearney, D., Herrmann, U., Nava, P., Kelly, B., Mahoney, R., Pacheco, J., Cable, R., Potrovitza, N., Blake, D. and Price, H., 2003. Assessment of a molten salt heat transfer fluid in a parabolic trough solar field. Journal of solar energy engineering, 125(2), pp.170-176.

Kennedy, C.E., 2002. Review of mid-to high-temperature solar selective absorber materials (No. NREL/TP-520-31267). National Renewable Energy Lab., Golden, CO.(US).

Kern Jr, E.C. and Russell, M.C., 1978. Combined photovoltaic and thermal hybrid collector systems (No. COO-4577-3; CONF-780619-24). Massachusetts Inst. of Tech., Lexington (USA). Lincoln Lab..

Kinsey, G.S., Stone, K., Brown, J. and Garboushian, V., 2011. Energy prediction of Amonix CPV solar power plants. Progress in Photovoltaics: Research and Applications, 19(7), pp.794-796.

Kong, C., Xu, Z. and Yao, Q., 2013. Outdoor performance of a low-concentrated photovoltaic–thermal hybrid system with crystalline silicon solar cells. Applied energy, 112, pp.618-625.

Koshel, R.J. ed., 2012. Illumination Engineering: design with nonimaging optics. John Wiley & Sons.

Kritchman, E.M., 1982. Asymmetric second-stage concentrators. Applied optics, 21(5), pp.870-873.

Kumar, A., Baredar, P. and Qureshi, U., 2015. Historical and recent development of photovoltaic thermal (PVT) technologies. Renewable and Sustainable Energy Reviews, 42, pp.1428-1436.

Kumar, R. and Rosen, M.A., 2011. A critical review of photovoltaic–thermal solar collectors for air heating. Applied Energy, 88(11), pp.3603-3614.

Kurtz, S., 2012. Opportunities and challenges for development of a mature concentrating photovoltaic power industry (revision) (No. NREL/TP-5200-43208). National Renewable Energy Laboratory (NREL), Golden, CO..

Lasich, J.B., Cleeve, A., Kaila, N., Ganakas, G., Timmons, M., Venkatasubramanian, R., Colpitts, T. and Hills, J., 1994, December. Close-packed cell arrays for dish concentrators. In Photovoltaic Energy Conversion, 1994., Conference Record of the Twenty Fourth. IEEE Photovoltaic Specialists Conference-1994, 1994 IEEE First World Conference on (Vol. 2, pp. 1938-1941). IEEE.

Lasich, J., 2009. The design and optimisation of a reflective concentrator photovoltaic generator system (Doctoral dissertation, Victoria University).

Li, M., Ji, X., Li, G., Wei, S., Li, Y. and Shi, F., 2011. Performance study of solar cell arrays based on a trough concentrating photovoltaic/thermal system. Applied Energy, 88(9), pp.3218-3227.

Liu, Y., Hu, P., Zhang, Q. and Chen, Z., 2014. Thermodynamic and optical analysis for a CPV/T hybrid system with beam splitter and fully tracked linear Fresnel reflector concentrator utilizing sloped panels. Solar Energy, 103, pp.191-199.

Looser, R., Vivar, M. and Everett, V., 2014. Spectral characterisation and long-term performance analysis of various commercial heat transfer fluids (HTF) as direct-absorption filters for CPV-T beam-splitting applications. Applied Energy, 113, pp.1496-1511.

Luneburg, R.K. and Herzberger, M., 1964. Mathematical theory of optics. Univ of California Press.

Luque, A., Sala, G., Arboiro, J.C., Bruton, T., Cunningham, D. and Mason, N., 1997. Some results of the EUCLIDES photovoltaic concentrator prototype. Progress in Photovoltaics: Research and Applications, 5(3), pp.195-212.

Ma, Z., Glatzmaier, G.C. and Mehos, M., 2014. Development of solid particle thermal energy storage for concentrating solar power plants that use fluidized bed technology. Energy Procedia, 49, pp.898-907.

Maccari, A., Donnola, S., Matino, F. and Tamano, S., 2016, May. Archimede solar energy molten salt parabolic trough demo plant: Improvements and second year of operation. In AIP Conference Proceedings (Vol. 1734, No. 1, p. 100007). AIP Publishing.

Mason, A. and Reitze, E., 2014. Establishing bankability for high performance, cost reducing SkyTrough parabolic trough solar collector. Energy Procedia, 49, pp.155-162.

McIntire, W.R., 1980. Secondary concentration for linear focusing systems: a novel approach. Applied optics, 19(18), pp.3036-3037.

Mehos, M., Turchi, C., Jorgenson, J., Denholm, P., Ho, C. and Armijo, K., 2016. On the Path to SunShot. Advancing Concentrating Solar Power Technology, Performance, and Dispatchability (No. NREL/TP--5500-65688; SAND2016--2237 R). National Renewable Energy Lab.(NREL), Golden, CO (United States).

Mehos, M., Turchi, C., Vidal, J., Wagner, M., Ma, Z., Ho, C., Kolb, W., Andraka, C. and Kruizenga, A., 2017. Concentrating solar power Gen3 demonstration roadmap (No. NREL/TP-5500-67464). NREL (National Renewable Energy Laboratory (NREL), Golden, CO (United States)).

Michael, J.J., Iniyan, S. and Goic, R., 2015. Flat plate solar photovoltaic–thermal (PV/T) systems: a reference guide. Renewable and Sustainable Energy Reviews, 51, pp.62-88.

Mikami, R., Inagaki, M., Moriguchi, M., Kitayama, K.I., Konoka, H. and Iwasaki, T., 2016. Advantages of Concentrator Photovoltaic System in High Solar Radiation Region. SEI Technical Review, (82), p.137.

Mills, D.R., 1980. Two-stage tilting solar concentrators. Solar Energy, 25(6), pp.505-509.

Mills, D.R., 1995. Two-stage solar collectors approaching maximal concentration. Solar energy, 54(1), pp.41-47.

Mills, D.R., Schramek, P., Dey, C., Buie, D., Imenes, A.G., Haynes, B.S. and Morrison, G., 2002. Multi tower solar array project. In Paper 1b4, ANZSES Annual Conference—Solar Harvest, Newcastle.

Miñano, J.C. and Gonzalez, J.C., 1992. New method of design of nonimaging concentrators. Applied optics, 31(16), pp.3051-3060.

Modest, M.F., 2013. Radiative heat transfer. Academic press.

Mojiri, A., Taylor, R., Thomsen, E. and Rosengarten, G., 2013. Spectral beam splitting for efficient conversion of solar energy—A review. Renewable and Sustainable Energy Reviews, 28, pp.654-663.

Mojiri, A., Stanley, C., Taylor, R.A., Kalantar-zadeh, K. and Rosengarten, G., 2015. A spectrally splitting photovoltaic-thermal hybrid receiver utilising direct absorption and wave interference light filtering. Solar Energy Materials and Solar Cells, 139, pp.71-80.

Mojiri, A., Stanley, C., Rodriguez-Sanchez, D., Everett, V., Blakers, A. and Rosengarten, G., 2016. A spectral-splitting PV–thermal volumetric solar receiver. Applied Energy, 169, pp.63-71.

Mokri, A. and Emziane, M., 2011, November. Concentrator photovoltaic technologies and market: a critical review. In World Renewable Energy Congress-Sweden; 8-13 May; 2011; Linköping; Sweden (No. 057, pp. 2738-2742). Linköping University Electronic Press.

Nishioka, K., Takamoto, T., Agui, T., Kaneiwa, M., Uraoka, Y. and Fuyuki, T., 2005. Evaluation of temperature characteristics of high-efficiency InGaP/InGaAs/Ge triple-junction solar cells under concentration. Solar energy materials and solar cells, 85(3), pp.429-436.

Orosz, M., Zweibaum, N., Lance, T., Ruiz, M. and Morad, R., 2016, May. Spectrum-Splitting hybrid CSP-CPV solar energy system with standalone and parabolic trough plant retrofit applications. In AIP Conference Proceedings (Vol. 1734, No. 1, p. 070023). AIP Publishing.

Osborn, D.E., Chendo, M.A.C., Hamdy, M.A., Luttmann, F., Jacobson, M.R., Macleod, H.A. and Swenson, R., 1986. Spectral selectivity applied to hybrid concentration systems. Solar Energy Materials, 14(3-5), pp.299-325.

Ostroumov, N., Gordon, J.M. and Feuermann, D., 2009. Panorama of dual-mirror aplanats for maximum concentration. Applied optics, 48(26), pp.4926-4931.

Otanicar, T., Taylor, R.A., Phelan, P.E. and Prasher, R., 2009, January. Impact of size and scattering mode on the optimal solar absorbing nanofluid. In ASME 2009 3rd International Conference on Energy Sustainability collocated with the Heat Transfer and InterPACK09 Conferences (pp. 791-796). American Society of Mechanical Engineers.

Otanicar, T.P., Chowdhury, I., Prasher, R. and Phelan, P.E., 2011. Band-gap tuned direct absorption for a hybrid concentrating solar photovoltaic/thermal system. Journal of Solar Energy Engineering, 133(4), p.041014.

Otanicar, T.P., Theisen, S., Norman, T., Tyagi, H. and Taylor, R.A., 2015. Envisioning advanced solar electricity generation: Parametric studies of CPV/T systems with spectral filtering and high temperature PV. Applied Energy, 140, pp.224-233.

Otanicar, T., DeJarnette, D., Brekke, N., Tunkara, E., Roberts, K. and Harikumar, P., 2016. Full Spectrum Collection of Concentrated Solar Energy Using PV Coupled with Selective Filtration Utilizing Nanoparticles. MRS Advances, 1(43), pp.2935-2940.

Othman, M.Y., Ibrahim, A., Jin, G.L., Ruslan, M.H. and Sopian, K., 2013. Photovoltaic-thermal (PV/T) technology–the future energy technology. Renewable Energy, 49, pp.171-174.

Othman, M.Y., Hamid, S.A., Tabook, M.A.S., Sopian, K., Roslan, M.H. and Ibarahim, Z., 2016. Performance analysis of PV/T Combi with water and air heating system: An experimental study. Renewable Energy, 86, pp.716-722.

Palmintier, B., Broderick, R., Mather, B., Coddington, M., Baker, K., Ding, F., Reno, M., Lave, M. and Bharatkumar, A., 2016. On the Path to SunShot. Emerging Issues and Challenges in Integrating Solar with the Distribution System (No. NREL/TP--5D00-65331; SAND2016--2524 R). National Renewable Energy Lab.(NREL), Golden, CO (United States).

Perlin, J., 2013. Let it shine: the 6,000-year story of solar energy. New World Library.

Peters, M., Goldschmidt, J.C., Löper, P., Groß, B., Üpping, J., Dimroth, F., Wehrspohn, R.B. and Bläsi, B., 2010. Spectrally-selective photonic structures for PV applications. Energies, 3(2), pp.171-193.

Price, H., Lupfert, E., Kearney, D., Zarza, E., Cohen, G., Gee, R. and Mahoney, R., 2002. Advances in parabolic trough solar power technology. Journal of solar energy engineering, 124(2), pp.109-125.

Raush, J.R. and Chambers, T.L., 2014. Initial field testing of concentrating solar photovoltaic (CSPV) thermal hybrid solar energy generator utilizing large aperture parabolic trough and spectrum selective mirrors. International Journal of Sustainable and Green Energy, 3(6), pp.123-131.

Rejeb, O., Dhaou, H. and Jemni, A., 2015. A numerical investigation of a photovoltaic thermal (PV/T) collector. Renewable Energy, 77, pp.43-50.

Ricketts, M., Ferry, J., Jiang, L. and Winston, R., 2016, September. Nonimaging optics in lighting to reduce light pollution. In Nonimaging Optics: Efficient Design for Illumination and Solar Concentration XIII—Commemorating the 50th Anniversary of Nonimaging Optics (Vol. 9955, p. 99550G). International Society for Optics and Photonics.

Ries, H. and Rabl, A., 1994. Edge-ray principle of nonimaging optics. JOSA A, 11(10), pp.2627-2632.

Ries, H. and Spirkl, W., 1996. Nonimaging secondary concentrators for large rim angle parabolic troughs with tubular absorbers. Applied optics, 35(13), pp.2242-2245.

Rodriguez-Sanchez, D. and Rosengarten, G., 2015. Improving the concentration ratio of parabolic troughs using a second-stage flat mirror. Applied energy, 159, pp.620-632.

Sala, G., Arboiro, J.C., Luque, A., Zamorano, J.C., Minano, J.C., Dramsch, C., Bruton, T. and Cunningham, D., 1996, May. The EUCLIDES prototype: an efficient parabolic trough for PV concentration. In Photovoltaic Specialists Conference, 1996., Conference Record of the Twenty Fifth IEEE (pp. 1207-1210). IEEE.

Saroha, S., Mittal, T., Modi, P.J., Bhalla, V., Khullar, V., Tyagi, H., Taylor, R.A. and Otanicar, T.P., 2015. Theoretical analysis and testing of nanofluids-based solar photovoltaic/thermal hybrid collector. Journal of Heat Transfer, 137(9), p.091015.

Schmitz, M., Cooper, T., Ambrosetti, G. and Steinfeld, A., 2015. Two-stage solar concentrators based on parabolic troughs: asymmetric versus symmetric designs. Applied optics, 54(33), pp.9709-9721.

Schmitz, M., 2017. Compact high-flux solar dish systems for concentrated photovoltaics (Doctoral dissertation, ETH Zurich).

Schweizer, E. and Enecolo, A.G., 2000. LESO-PB, new generation of hybrid solar PV/T collectors. Final Report DIS, 56360(16868), pp.1-55.

Segal, A., 1994, September. Approximated secondary CPC, built of planar facets, adjustable for two solar central receivers. In Optical Materials Technology for Energy Efficiency and Solar Energy Conversion XIII (Vol. 2255, pp. 567-573). International Society for Optics and Photonics.

Segal, A., Epstein, M. and Yogev, A., 2004. Hybrid concentrated photovoltaic and thermal power conversion at different spectral bands. Solar Energy, 76(5), pp.591-601.

Selvakumar, N. and Barshilia, H.C., 2012. Review of physical vapor deposited (PVD) spectrally selective coatings for mid-and high-temperature solar thermal applications. Solar Energy Materials and Solar Cells, 98, pp.1-23.

Shockley, W. and Queisser, H.J., 1961. Detailed balance limit of efficiency of p-n junction solar cells. Journal of applied physics, 32(3), pp.510-519.

Shou, C., Luo, Z., Wang, T., Shen, W., Rosengarten, G., Wei, W., Wang, C., Ni, M. and Cen, K., 2012. Investigation of a broadband TiO2/SiO2 optical thin-film filter for hybrid solar power systems. Applied Energy, 92, pp.298-306.

Sibin, K.P., Selvakumar, N., Kumar, A., Dey, A., Sridhara, N., Shashikala, H.D., Sharma, A.K. and Barshilia, H.C., 2017. Design and development of ITO/Ag/ITO spectral beam splitter coating for photovoltaic-thermoelectric hybrid systems. Solar Energy, 141, pp.118-126.

Silverman, T.J., Deceglie, M.G., Marion, B., Cowley, S., Kayes, B. and Kurtz, S., 2013, June. Outdoor performance of a thin-film gallium-arsenide photovoltaic module. In Photovoltaic Specialists Conference (PVSC), 2013 IEEE 39th (pp. 0103-0108). IEEE.

Skoplaki, E. and Palyvos, J.A., 2009. On the temperature dependence of photovoltaic module electrical performance: A review of efficiency/power correlations. Solar energy, 83(5), pp.614-624.

Smith, D.D., Cousins, P.J., Masad, A., Westerberg, S., Defensor, M., Ilaw, R., Dennis, T., Daquin, R., Bergstrom, N., Leygo, A. and Zhu, X., 2013, June. SunPower's Maxeon Gen III solar cell: High efficiency and energy yield. In Photovoltaic Specialists Conference (PVSC), 2013 IEEE 39th (pp. 0908-0913). IEEE.

Soule, D.E., Rechel, E.F., Smith, D.W. and Willis, F.A., 1985, December. Efficient hybrid photovoltaic-photothermal solar conversion system with cogeneration. In Optical Materials Technology for Energy Efficiency and Solar Energy Conversion IV (Vol. 562, pp. 166-176). International Society for Optics and Photonics.

Soule, D.E. and Wood, S.E., 1986, September. Heat-mirror spectral profile optimization for TSC hybrid solar conversion. In Optical Materials Technology for Energy Efficiency and Solar Energy Conversion V (Vol. 653, pp. 172-181). International Society for Optics and Photonics.

Spelling, J., Gallo, A., Romero, M. and González-Aguilar, J., 2015. A high-efficiency solar thermal power plant using a dense particle suspension as the heat transfer fluid. Energy Procedia, 69, pp.1160-1170.

Spirkl, W., Ries, H., Muschaweck, J. and Timinger, A., 1997. Optimized compact secondary reflectors for parabolic troughs with tubular absorbers. Solar Energy, 61(3), pp.153-158.

Stanley, C., Mojiri, A., Rahat, M., Blakers, A. and Rosengarten, G., 2016. Performance testing of a spectral beam splitting hybrid PVT solar receiver for linear concentrators. Applied Energy, 168, pp.303-313.

Stone, K.W., Garboushian, V., Dutra, D. and Hayden, H., 2004, January. Four years of operation of the AMONIX high concentration photovoltaic system at arizona public service utility. In ASME 2004 International Solar Energy Conference (pp. 441-448). American Society of Mechanical Engineers.

Sun, X., Silverman, T.J., Zhou, Z., Khan, M.R., Bermel, P. and Alam, M.A., 2017. Optics-based approach to thermal management of photovoltaics: selective-spectral and radiative cooling. IEEE Journal of Photovoltaics, 7(2), pp.566-574.

Taylor, R.A., Otanicar, T. and Rosengarten, G., 2012. Nanofluid-based optical filter optimization for PV/T systems. Light: Science & Applications, 1(10), p.e34.

Taylor, R.A., Otanicar, T.P., Herukerrupu, Y., Bremond, F., Rosengarten, G., Hawkes, E.R., Jiang, X. and Coulombe, S., 2013. Feasibility of nanofluid-based optical filters. Applied optics, 52(7), pp.1413-1422.

Timinger, A., Kribus, A., Doron, P. and Ries, H., 2000. Faceted concentrators optimized for homogeneous radiation. Applied Optics, 39(7), pp.1152-1158.

Timinger, A., Spirkl, W., Kribus, A. and Ries, H., 2000. Optimized secondary concentrators for a partitioned central receiver system. Solar energy, 69(2), pp.153-162.

Torrey, E.R., Krohn, J., Ruden, P.P. and Cohen, P.I., 2010, June. Efficiency of a laterally engineered architecture for photovoltaics. In Photovoltaic Specialists Conference (PVSC), 2010 35th IEEE (pp. 002978-002983). IEEE.

Tyagi, V.V., Kaushik, S.C. and Tyagi, S.K., 2012. Advancement in solar photovoltaic/thermal (PV/T) hybrid collector technology. Renewable and Sustainable Energy Reviews, 16(3), pp.1383-1398.

van Riesen, S., Gombert, A., Gerster, E., Gerstmaier, T., Jaus, J., Eltermann, F. and Bett, A.W., 2011, December. Concentrix Solar's progress in developing highly efficient modules. In AIP Conference Proceedings (Vol. 1407, No. 1, pp. 235-238). AIP.

Victoria, M., Domínguez, C., Antón, I. and Sala, G., 2009. Comparative analysis of different secondary optical elements for aspheric primary lenses. Optics Express, 17(8), pp.6487-6492.

Vignarooban, K., Xu, X., Arvay, A., Hsu, K. and Kannan, A.M., 2015. Heat transfer fluids for concentrating solar power systems–a review. Applied Energy, 146, pp.383-396.

Virtuani, A., Pavanello, D. and Friesen, G., 2010, September. Overview of temperature coefficients of different thin film photovoltaic technologies. In 25th European photovoltaic solar energy conference and exhibition/5th World conference on photovoltaic energy conversion (pp. 6-10).

Vivar, M., Sala, G., Pachon, D. and Antón, I., 2006, May. Large-area Si-cell encapsulation for concentrator systems: review of critical points and new proposal for the third generation of EUCLIDES. In Photovoltaic Energy Conversion, Conference Record of the 2006 IEEE 4th World Conference on (Vol. 1, pp. 621-624). IEEE.

Vivar, M., Herrero, R., Moretón, R., Martinez-Moreno, F. and Sala, G., 2008, May. Effect of soiling on PV concentrators: comparison with flat modules. In Photovoltaic Specialists Conference, 2008. PVSC'08. 33rd IEEE (pp. 1-4). IEEE.

Vivar, M., Herrero, R., Antón, I., Martínez-Moreno, F., Moretón, R., Sala, G., Blakers, A.W. and Smeltink, J., 2010. Effect of soiling in CPV systems. Solar Energy, 84(7), pp.1327-1335.

Vivar, M., Antón, I., Pachón, D. and Sala, G., 2012. Third-generation EUCLIDES concentrator results. Progress in Photovoltaics: Research and Applications, 20(3), pp.356-371.

Vivar, M. and Everett, V., 2014. A review of optical and thermal transfer fluids used for optical adaptation or beam-splitting in concentrating solar systems. Progress in Photovoltaics: Research and Applications, 22(6), pp.612-633.

Vorobiev, Y., González-Hernández, J., Vorobiev, P. and Bulat, L., 2006. Thermal-photovoltaic solar hybrid system for efficient solar energy conversion. Solar energy, 80(2), pp.170-176.

Wang, G., Cheng, X.F., Hu, P., Chen, Z.S., Liu, Y. and Jia, L., 2013. Theoretical analysis of spectral selective transmission coatings for solar energy PV system. International Journal of Thermophysics, 34(12), pp.2322-2333.

Weinstein, L.A., McEnaney, K., Strobach, E., Yang, S., Bhatia, B., Zhao, L., Huang, Y., Loomis, J., Cao, F., Boriskina, S.V. and Ren, Z., 2018. A Hybrid Electric and Thermal Solar Receiver. Joule.

Welford, W.T. and Winston, R., 1989. High Collection Nonimaging Optics Academic. San Diego, Calif, 19892, p.55.

Widyolar, B.K., Jiang, L. and Winston, R., 2017. Thermodynamics and the segmented compound parabolic concentrator. Journal of Photonics for Energy, 7(2), p.028002.

Widyolar, B., Jiang, L. and Winston, R., 2017, September. Thermodynamic investigation of the segmented CPC. In Nonimaging Optics: Efficient Design for Illumination and Solar Concentration XIV (Vol. 10379, p. 103790L). International Society for Optics and Photonics.

Widyolar, B., Jiang, L. and Winston, R., 2018. Spectral beam splitting in hybrid PV/T parabolic trough systems for power generation. Applied Energy, 209, pp.236-250.

Widyolar, B., Jiang, L., Abdelhamid, M. and Winston, R., 2018. Design and modeling of a spectrum-splitting hybrid CSP-CPV parabolic trough using two-stage high concentration optics and dual junction InGaP/GaAs solar cells. Solar Energy, 165, pp.75-84.

Widyolar, B.K., Abdelhamid, M., Jiang, L., Winston, R., Yablonovitch, E., Scranton, G., Cygan, D., Abbasi, H. and Kozlov, A., 2017. Design, simulation and experimental characterization of a novel parabolic trough hybrid solar photovoltaic/thermal (PV/T) collector. Renewable Energy, 101, pp.1379-1389.

Winston, R., 1970. Light collection within the framework of geometrical optics. JOSA, 60(2), pp.245-247.

Winston, R., 1974. Principles of solar concentrators of a novel design. Solar Energy, 16(2), pp.89-95.

Winston, R. and Hinterberger, H., 1975. Principles of cylindrical concentrators for solar energy. Solar Energy, 17(4), pp.255-258.

Winston, R. and Welford, W.T., 1980. Design of nonimaging concentrators as second stages in tandem with image-forming first-stage concentrators. Applied Optics, 19(3), pp.347-351.

Winston, R., Miñano, J.C. and Benitez, P.G., 2005. Nonimaging optics. Academic Press.

Winston, R., 2011, September. Thermodynamically efficient solar concentrators. In Nonimaging Optics: Efficient Design for Illumination and Solar Concentration VIII (Vol. 8124, p. 812409). International Society for Optics and Photonics.

Woodhouse, M. and Goodrich, A., 2014. Manufacturing cost analysis relevant to single-and dual-junction photovoltaic cells fabricated with III-Vs and III-Vs grown on Czochralski silicon (presentation) (No. NREL/PR-6A20-60126). National Renewable Energy Laboratory (NREL), Golden, CO..

Woody, D.P. and Richards, P.L., 1981. Near-millimeter spectrum of the microwave background. The Astrophysical Journal, 248, pp.18-37.

Xu, Q., Ji, Y., Riggs, B., Ollanik, A., Farrar-Foley, N., Ermer, J.H., Romanin, V., Lynn, P., Codd, D. and Escarra, M.D., 2016. A transmissive, spectrum-splitting concentrating photovoltaic module for hybrid photovoltaic-solar thermal energy conversion. Solar Energy, 137, pp.585-593.

Yeh, P. and Yeh, N., 2018. Design and analysis of solar-tracking 2D Fresnel lens-based two staged, spectrum-splitting solar concentrators. Renewable Energy, 120, pp.1-13.

Zhang, L., Jing, D., Zhao, L., Wei, J. and Guo, L., 2012. Concentrating PV/T hybrid system for simultaneous electricity and usable heat generation: a review. International Journal of Photoenergy, 2012.

Zhang, H.L., Baeyens, J., Degrève, J. and Cacères, G., 2013. Concentrated solar power plants: Review and design methodology. Renewable and Sustainable Energy Reviews, 22, pp.466-481.

Zhao, J., Luo, Z., Zhang, Y., Shou, C. and Ni, M., 2010, March. Optimal design and performance analysis of a low concentrating photovoltaic/thermal system using the direct absorption collection concept. In Power and Energy Engineering Conference (APPEEC), 2010 Asia-Pacific (pp. 1-6). IEEE.

Zhengshan, J.Y., Fisher, K.C., Wheelwright, B.M., Angel, R.P. and Holman, Z.C., 2015. PVMirror: a new concept for tandem solar cells and hybrid solar converters. IEEE Journal of Photovoltaics, 5(6), pp.1791-1799.

Zondag, H.A., Van Helden, W.G.J., Bakker, M., Affolter, P., Eisenmann, W., Fechner, H., Rommel, M., Schaap, A., Sörensen, H. and Tripanagnostopoulos, Y., 2006. PVT roadmap. A European guide for the development and market introduction of PVT technology.